Analytical Study of Gusset Plate Joints in Steel Truss Bridges and Development of Assessment Procedures

Bo-Shiuan Wang

A dissertation
submitted in partial fulfillment of the
requirements for the degree of

Doctor of Philosophy

University of Washington

2013

Reading Committee:

Jeffrey W. Berman, Chair

Charles W. Roeder

Dawn E. Lehman

Program Authorized to Offer Degree:

Civil & Environmental Engineering

University of Washington

Abstract

Analytical Study of Gusset Plate Joints in Steel Truss Bridges and Development of Assessment Procedures

Bo-Shiuan Wang

Co-Chairs of the Supervisory Committee:

Associate Professor Jeffrey W. Berman

Civil Civil & Environmental Engineering

Professor Charles W. Roeder

Civil Civil & Environmental Engineering

Gusset plate connections are commonly used to join members in steel truss bridges. Most gusset plate connections were designed to provide sufficient thickness to resist tensile and shear forces as well as compression buckling based on simple approximations. The 2007 collapse of the I-35W Bridge in Minnesota necessitated the safety assessment of gusset plates and prompted several studies of gusset plate behavior. The complex geometry and various loading profiles make it difficult to analyze and estimate maximum stress in gusset plates and its capacity.

This research focuses on numerical simulation of steel truss bridge gusset plate connections. A simple but accurate finite element modeling methodology was developed to efficiently simulate gusset plate connection subassemblages. A rapid procedure for assessing gusset plate safety, namely Triage Evaluation Procedure (TEP), was developed to predict the onset of gusset plate yielding. This procedure considers the worst-case scenario for the interaction of stresses generated by connected truss members and conservatively identifies at risk gusset plates. A Refined Evaluation Procedure (REP) was then developed to predict stress

distributions at critical sections using simple and idealized approximate stress distribution models. By using these stress distribution models at the critical sections, the location and magnitude of the maximum stress in the gusset plate connections can be estimated. The TEP and REP are two-step evaluation procedures to provide fast and accurate estimate for gusset plate yield capacity.

In addition to the gusset plates, rivet shear resistance needs to be considered to evaluate the overall safety of gusset plate connections. Rivet shear strength, rivet ductility, connected member yielding, and the effect of connection length were identified as factors which affect joint strength. The current AASHTO bridge evaluation code does not consider all four factors and yields an overly-conservative estimate of joint shear resistance. A revised equation which considers "Strong" and "Weak" connected elements and produces a more reasonable estimate of joint shear resistance is recommended.

TABLE OF CONTENTS

LIST OF FIGURES

ACKNOWLEDGMENTS

I would like to express my deep and sincere gratitude to the people who made this Ph.D. dissertation possible. Without their support, this work would not have been accomplished.

I would like to thank my advisor, Dr. Jeffrey W. Berman, for his continued support and encouragement, guiding me through my research and dissertation writing. I would especially like to thank my committee co-chair and advisor, Dr. Charles W. Roeder, for providing his vast knowledge and expertise throughout this research. His constructive comments on this dissertation were invaluable. I would like also express my sincere gratitude to my advisor and committee member, Dr. Dawn E. Lehman, and committee member, Dr. Laura N. Lowes, for their valuable inputs and suggestions.

I sincerely appreciate the Dr. and Mrs. Paul B. Liao fellowship endowment for their financial support. They not only generously sponsored my research, but also kindly mentored my engineering career and genuinely cared about my life in the States. Their generosity and kindness is unforgettable. I would also like to acknowledge the Washington Department of Transportation for their funding and for recognizing the achievements of this research.

I would like to thank fellow graduate student, Aaron W. Olson for providing calculations for verification of the developed methods and Saura M. Jost for providing the valuable experimental data for validating the theories in this dissertation. They are not only talented colleagues but also very good friends.

My gratitude goes to the administrative staff of Civil & Environmental Engineering Department at the University of Washington, particularly Lorna Latal, for guiding me through the fulfillment of my degree requirements.

I would like to thank my colleagues and officemates: Olafur Haraldsson, Jonathan Weigand,

Patricia Clayton, Po-Chien Hsiao, Anna Birely, Mohammad Malakoutian, Max Stephens, Travis Thonstad, Tran Viet Hung, David Webster, Keith Palmer, Josh Pugh, Cal Bearman, for the vibrant discussion, inspiration and support throughout my research. I am very grateful to have shared many great times with you.

I would also thank my friends in Seattle: the Newman family, Yen-Yu, Po-Hsuan, Chun-Hao, Chia-Feng, Muning, Chieh-Lun, Henry, and alumnus Wen-Liang Huang for their generosity, care, and support.

My deepest gratitude goes to my parents, Cheng-Hsiung Wang and Mei-Hua Huang, for their belief in me and encouragement throughout my academic endeavors and my brother, Chia-Sheng, for his unselfish support overseas.

Last but not least, I would like to express my immense gratitude to my beloved wife, Chia-Pin Chen. Her love and companionship made this dissertation easier to complete. Her support and encouragement throughout the ups and downs of this research project have made this dissertation possible.

DEDICATION

To my dear parents and my beloved wife, Chia-Pin Chen

Chapter 1

INTRODUCTION AND RESEARCH OBJECTIVES

1.1 General

Steel truss bridges are common in the United States and in other industrial countries and many were built between 1900 and 1980 before other bridge types became more common. They typically consist of two planar trusses connected to each other via floor beams, lateral bracing and the bridge deck. Steel truss bridges have historically taken on many different configurations, including over-truss (also known as through truss) and under-truss configurations as illustrated in Figure 1.1 where the road deck is below or above the truss superstructure. Trusses are comprised of diagonal and chords that are primarily loaded in tension or compression and their design and analysis typically neglects any bending moment or shear force in the elements. Due to their geometry, the shear and bending moments in the diagonals and chords are typically small and trusses derive their stiffness largely from the axial stiffness of the members. Most trusses are statically determinant to prevent the development of large forces in the elements due to thermal strains. This also means that most truss bridges are non-load-path-redundant structures where the failure of a truss member or connection could cause a portion of the bridge, or the entire bridge, to collapse.

Common geometries for steel truss bridges include the Warren configuration (Figure 1.1) where alternating diagonals are in tension or compression for a uniform load and the Pratt configuration where the diagonals are all in tension for uniform loads. In all truss configurations, if the truss is represented by a beam between the supports and shear and bending moment diagrams are constructed for a given loading, it can be demonstrated that the diagonals resist this global shear force while chords resist the moment.

Truss members are typically connected at joints with gusset plates as shown in Figure 1.2.

Additional plates may also be present to help splice the chords together. Gusset plates must resist the stress resulting from axial loads in the connected elements and the stress distribution in the gusset plates is complex. Design of truss gusset plates has evolved substantially over time and recent changes have modified the load rating procedures used for gusset plates when load rating bridges.

(a) Through-truss and Warren type bridge which the deck is supported directly by lower chord and the diagonals are in tension and compression alternatively

(b) Under-truss and Pratt type bridge which the deck is supported directly by upper chord and the all diagonals are in tension

Figure 1.1: Common configurations used for steel truss bridges

1.2 Research Motivation

The collapse of the I-35W Mississippi River Bridge has aroused concerns regarding the safety of existing steel truss bridges and specifically their gusset plate connections. Inspection and load rating of all steel truss bridges has been ongoing since the collapse. At the time of the collapse, the American Association of State Highway and Transportation Officials (AASHTO) provisions for design of new gusset plate connections in trusses were somewhat vague and required that the design consider fastener strength, block shear, tensile strength, combined stresses from flexural and axial loading (where flexural stresses were computed using standard beam theory), both uniform and flexural shear stresses, and a

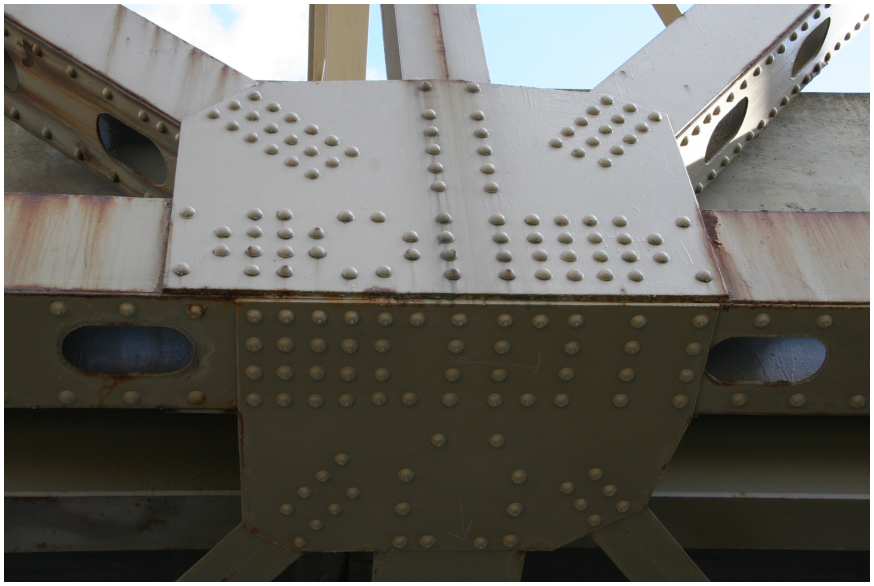

Figure 1.2: Configuration of gusset plate joint which connects planar truss member by dual gusset plates and lateral bracing by a wind gusset plate

maximum unbraced edge length requirement to prevent plate buckling (AASHTO 2007) . To clarify how the provisions were to be employed to load rate existing bridges following the collapse of the I-35W Bridge, the Federal Highway Administration (FHWA) released *Load Rating Guidance and Examples for Bolted and Riveted Gusset Plates in Truss Bridges* (FHWA [2009]), denoted the FHWA Guide hereafter. The recommendations differed from the AASHTO provisions somewhat in that they excluded the consideration of bending stress or shear stress from bending using beam analysis of the gusset plate at critical sections. Several studies have noted that many bridges in-service for years fail to meet the load rating requirements and that there is a lack of supportive evidence for the requirements from full-scale tests or detailed analyses of large bridge type gusset plate connections (Higgins et al. [2010] and Mentes [2011]).

Many truss bridges designed prior to the 1970's have gusset plate connections that were designed assuming that all fasteners connecting a member to the gusset plate carry an equal share of member load through shear forces. The number of fasteners necessary to carry

member load into the gusset plates were determined accordingly using allowable stresses. The configuration of the gusset plates were determined by the layout of the connected members and the required number of fasteners and fastener spacing. The thickness of the gusset plates were then determined using beam theory to estimate the maximum stresses at assumed critical sections or later using effective width methods, such as the Whitmore method and Thornton method (Fisher and Struik [1974]); in both cases allowable stress design was used. Later, the effects of long connections were considered and the fasteners were no longer assumed to carry the member loads uniformly. However, the gusset plate design methods remained similar until the introduction of limit state design and the block shear failure mode.

When beam theory was used in early truss bridge designs for sizing the gusset plate thickness, the procedure included selecting critical sections in the gusset plate. At each section, the axial force, shear force, and bending moment were calculated and used to compute principle stresses at the neutral axis of the section and at the edges of the section. The gusset thickness was then determined by comparing the computed stresses with allowable stresses. However, beam theory had been recognized as inaccurate by previous research (Rust [1940], Whitmore [1952], and Vasarhelyi [1971]). Whitmore found that the maximum principal stress in bridge gusset plates was located at the end of either tensile or compressive diagonals and proposed that the maximum principal stress could be evaluated by the diagonal load acting on an effective area across the end row of fasteners of the diagonal, which has become the well-known Whitmore method.

The FHWA Guide (FHWA [2009]) did not include the check of the maximum stress at the critical sections using beam theory and only employed the Whitmore method to check gross area yield at member ends and a check of uniform shear at critical sections. The latter is load case specific and requires a combination of loads in the diagonals and chords that are in equilibrium. This is difficult in bridges where moving loads necessitate the use of envelope forces for member evaluation and result in a large number of possible load cases when point-in-time combinations of loads are considered. ***Considering the large inventory of truss bridges, an approximate procedure that can rapidly identify potentially***

overstressed gusset plates using envelope member forces is desirable.

Though beam theory method and the Whitmore method are two common methods used to evaluate the maximum stress in a gusset plate, neither of them are sufficient to determine both the maximum stress and its location in the gusset plates. Many studies have been conducted on elastic and inelastic gusset plates using experimental and analytical approaches to study the stress distributions (Hardin [1958], Vasarhelyi [1971], and Yamamoto et al. [1985]) but no other design recommendations have been suggested (Fisher and Struik [1974]). Although the results from these studies indicated significant variation between observed stress distributions and maximum stress locations and those predicted by beam theory and results from these studies, those differences may not be unsafe (Fisher and Struik [1974]). It should be noted that the collapse of the I-35W Bridge was determined to be a result of an inadequate gusset plate thickness resulting from a mistake that resulted in the wrong thickness plate being employed rather than a flaw in the design methodology (Ocel and Wright [2008]). However, without a fundamental understanding of the stress distributions and stress interactions in gusset plate connections, the methods employed for gusset plate design and load rating are questionable. ***Therefore, comprehensive analysis of the stress distributions in gusset plates and the development of alternative checks for safety that build on those analysis results are warranted.***

Gusset plate buckling has also been a concern and it has been hypothesized that Joint U10's failure mode was inelastic buckling (Ocel 2012). However, very few studies prior to the collapse have investigated bridge-type gusset plate buckling (Yamamoto et al. [1988]). Recent research after the I-35W bridge collapse (Ocel et al. [2012],Mentes [2011] and Hafner [2012]) has found that gusset plate buckling may appear as a pure compression buckling, a combination of shear yielding and compression buckling, or shear yielding followed by instability at large plastic strains, depending on the thickness of the gusset plates. The buckling capacity may also be affected by the connected member's stiffness (Hafner [2012]). Today however, the Thornton method (Thornton [1984]), which uses a column analogy for an effective section of gusset plate, is generally used to check buckling of gusset plates and these more complicated factors are neglected. ***It is important that the Thornton***

method be evaluated to ensure it is conservative for a wide range of gusset plate geometries and robust for different stress states in gusset plates.

The final area of concern for gusset plate connections is the shear strength of riveted connections. Recent research has demonstrated that previous values for rivet shear strength used in the AASHTO Manual for Bridge Evaluation (MBE) were overly conservative (Olson 2010) and that unnecessary and costly rivet replacement was likely taking place. This resulted in a recent modification of specified rivet strengths in an interim revisions of the MBE (AASHTO 2011). The length of riveted connections is also known to impact their strength. In previous AASHTO design specifications, the shear capacity of connections with lengths over 50 in. were required to be reduced by 20%. This has recently been revised and now uses a reduction factor that varies continuously with connection length (AASHTO [2011]). However, the earlier research showed the reduction of connection capacity with length is not only related to the connection length but also to the ratio of connected member area to the rivet shear area (Kulak et al. [1987]). ***Therefore, it is important to investigate the effect of connection length combined with connected element strength and stiffness to determine if the current connection strength reduction approach is reasonable.***

1.3 Research Objectives and Scope of Work

This dissertation focuses on the urgent and fundamental issues of gusset plate connections motivated by the collapse of the I-35W Bridges and the necessary to bridge the discrepancy between the current codes and engineering practice. The primary research objectives are as follows:

1. Develop a rapid assessment tool for engineers to identify gusset plates that may be yielding and require additional investigation. This tool will allow Departments of Transportation to quickly identify problem gusset plates and save considerable engineering time over current evaluation procedures while being appropriately conservative.

2. Investigate the stress distributions in gusset plates for various distributions of member loads to develop more accurate methods of determining the location and magnitude of the maximum gusset plate stress.

3. Investigate single rivet shear strength affected by moderate corrosion and the effect of connection length in combination with connected element yield strength and stiffness change on the strength of riveted connections.

4. Develop appropriate analytical modeling procedure to predict gusset plate buckling. Preliminary study gusset plate buckling capacity affected by stresses in gusset plates and evaluate the effectiveness of the Thornton's method.

5. Develop preliminary method to estimate yield capacity for gusset plate critical sections.

To achieve these objectives, detailed finite element models of truss bridge gusset plate joints are developed, calibrated and analyzed. A parametric study is conducted using these models that considers basic variations in joint configuration and load distribution which are derived from actual truss bridge joints. Observations from these models are used to develop the rapid assessment procedure for gusset plate joints, denoted the Triage Evaluation Procedure (TEP), and to investigate in more detail how gusset plate stresses are generated and how they interact to develop a Refined Evaluation Procedure (REP) for determining the magnitude and location of the maximum gusset plate stress. Experiments on rivets salvaged from vintage truss bridge are then conducted and used to calibrate rivet force-deformation models that are used in detailed finite element models of riveted connections to investigate the strength of riveted connections with different connection lengths and connected element yield strengths.

1.4 Overview of Document

This dissertation includes ten chapters and five appendices. This chapter provides the introduction, a brief background of gusset plate connections and rivet fasteners and the research objectives and scope of work. A literature review of prior studies of gusset plates

connections, shear resistance of riveted connections, and current gusset plate joint design and evaluation specifications are provided in Chapter 2. Chapter 3 presents the method used to establish finite element (FE) models gusset plate joint subassemblages and the verification of the FE model with experiments and a large-scale analysis. This modeling methodology was then applied to different joints for a parametric study of gusset plate joint behavior. Chapter 4 describes the selected gusset plate joints and the steel truss bridges in Washington State to which the selected joints belong. Joint characteristics are described that were used in the selection process including geometric configurations, loading profiles, and the evaluation results using current specification. Chapter 5 defines the criteria for the onset of gusset plate yielding, proposes the TEP to predict the onset of yielding, and verifies the TEP by comparisons with FE simulations of selected joints. A few cases where the TEP is overly conservative are discussed and used to motivate the study of the stress distributions in the gusset plates.

Chapter 6 investigates the reasons the TEP provides poor estimates of the onset of yielding in a few cases and develops an approximate stress distribution model for the X-direction normal stress at the chord splice in gusset plates. The approximate stress distribution is verified for a variety of geometries. Chapter 7 discusses the stress distributions at other critical sections and presents approximate stress distribution models for these sections of the gusset plates. These critical sections and component stress distributions include the XY shear stress along the horizontal section and vertical sections, the X-direction normal stress at the chord splice, and the Y-direction normal stress along the horizontal section. An approach, denoted the Refined Evaluation Procedure, to calculate Von Mises stress at several critical points is presented and the new developed procedure is examined by several examples to demonstrate its effectiveness.

Chapter 8 presents experiments conducted to determine the shear force-displacement response of vintage rivets and a modified analytical modeling methodology that includes the fastener behavior. The impact of connection length is studied and a modified method accounting for the strength reduction of riveted joints with increasing connection length is proposed that accounts for the impact of the yield strength of the connected elements.

Chapter 9 discusses the advantage of the approach combining the TEP and REP on load rating gusset plate connections. Chapter 10 concludes with a summary of results, concise conclusions and several recommendations for future research.

In addition to the ten chapters, five appendices are provided. Appendix A documents the experimental data for the single rivet shear strength tests. Appendix B presents the plastic yield capacity of gusset plates at the chord splice. Appendix C presents the plastic yield capacity of gusset plates at critical sections using effective length methods developed for the approximate stress distributions. Appendix D presents an analytical technique to estimate gusset plate buckling and buckling capacity as affected by the stress in the gusset plates. The predicted critical buckling loads are verified with gusset plate experiments. Appendix E presents the gusset plate behavior as the external load reaches the gusset plate block shear strength.

Chapter 2

LITERATURE REVIEW

Steel or cast iron truss bridges were built in the United State as early as the end of the nineteenth century. Steel truss bridges using gusset plates as connections to join truss members became increasingly popular in the 1920's. At almost the same time, structural rivets became popular in steel structures including steel truss bridges. Today, tens of thousands steel truss bridges using riveted gusset plate joints across the US are still in service. They are required to be inspected every two years when on federal highways. The 2007 collapse of the I-35W Bridge in Minneapolis illustrated the importance of this requirement. Gusset plate connections usually consist of two steel plates joining truss members on both sides. Sometimes a wind gusset plate joining a strut and lateral braces is attached to top or bottom of the connections. Figure 1.2 shows an illustration of a typical gusset plate connection joining diagonals and hanger, and splicing chords. A wind gusset plate is attached to the bottom of joints to connect the strut and lateral bracing.

Research has been conducted for gusset plate connections and rivet behavior respectively. However, much of the pertinent research was done long after many such bridges were already constructed. Rivet behaviors were studied much earlier than the study of gusset plate connections. Riveted connections were first introduced to steam containers and ships and studies were conducted for rivets in those applications. Experiments for large structural riveted joints were not conducted until the early 1900's while the study of gusset plate behavior did not start until 1952. In this chapter, literature on the elastic stress distribution in gusset plates, the buckling and ultimate strengths for gusset plates are reviewed and discussed. Further, research on single rivet strength and the strength of long riveted connections will also be reviewed and discussed.

2.1 Elastic Stress Distribution of the Gusset Plate

2.1.1 Stress at the End of Connected Members

The elastic stress distributions of gusset plates were first investigated by Whitmore [1952] at the University of Tennessee. A Warren-type low-chord truss joint, which was made of high strength aluminum alloy was tested. The tested object was a miniature of gusset plate connection whose dimension and loads is shown in Figure 2.1. The specimen had rectangular gusset plate, continuous chords and zero-loaded vertical hanger. Diagonals and chords were simple steel bars connected to gusset plates by bolts which were subjected to double shear. Whitmore [1952] found that diagonals generated the maximum tensile/compressive principal stresses at their end at gusset plates while the maximum shear stress was found close to the top of the chord and near the middle of gusset plates. Stresses at the free edges of the gusset plate were not as significant as expected as shown in Figure 2.2.

Whitmore's tests founded the important approximation of the maximum stress at gusset plates. It was approximated that the maximum tensile/compressive stresses could be considered the diagonal loads acting on an effective width uniformly at gusset plates. This effective width, denoted Whitmore width, was taken as a section across the last row of fasteners of diagonals and was intersected by two lines drawn at 30 degrees from the outer rivets of the first row of the diagonal as shown in Figure 2.3. This approximation was initially observed suitable for diagonals by Whitmore but was extended to approximate stress at chord end at gusset plates, too. For the maximum shear stress, it was found the maximum shear stress can be approximated as 1.5 times the averaged horizontal shear stress based upon a parabolic shear stress distribution approximation for the gusset.

Two similar studies were conducted by Irvan [1957] and Hardin [1958] at the University of Kentucky on the Pratt-type joints with respective continuous chords and spliced chords. Irvan [1957] and Hardin [1958] both confirmed that the maximum tensile/compressive stress at the Pratt-type gusset plates were observed at the end of diagonals as it was found in the Warren-type joints by Whitmore [1952]. However, they both found the Whitmore's

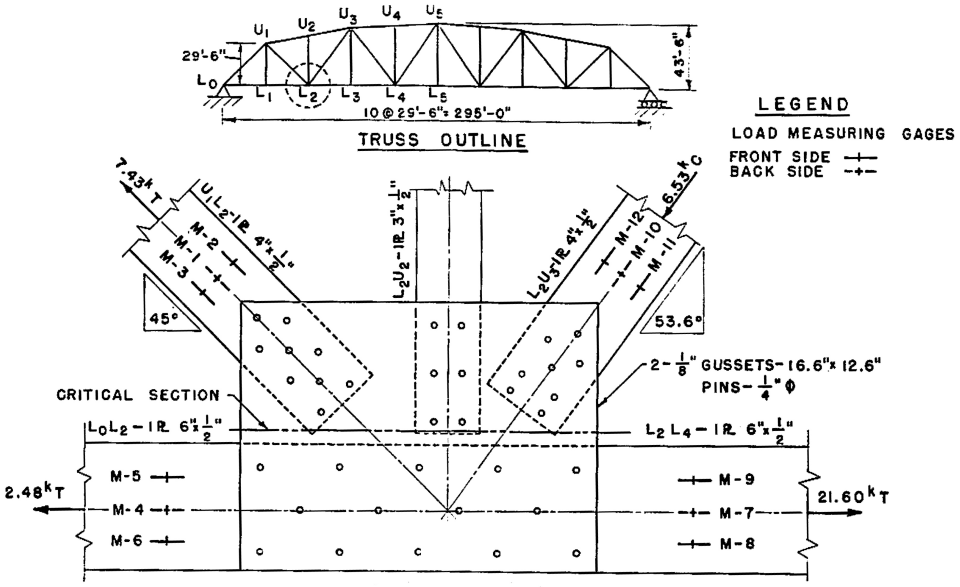

Figure 2.1: Joint L2 from a Warren-type bridge was tested by Whitmore Whitmore [1952]

approximation of the principal stress was lower than the experiments so that Irvan [1957] proposed a different procedure to determine the effective width. He proposed that the effective width was the section across the last row of fasteners and being intersected by two 30 degrees lines drawn from the center of the gravity of the fastener group. This method was also shown in the Figure 2.3 with the Whitmore [1952]'s methods.

2.1.2 Stress at Critical Sections

High stresses were found at several critical sections at gusset plates as well. High shear stress was observed above the top edge of the chord at horizontal sections on gusset plates, Whitmore [1952]. Hardin [1958] found high tensile stress at chord splice along vertical sections. Generally, the stress along these critical sections were considered using beam theory, which considers the flexure and shear stress, to formulate the stress distributions in practice. However, studies had shown that beam theory applied to gusset plate is not reliable(Hardin [1958]). As it was mentioned by Hardin [1958] that *"it is easy to see that*

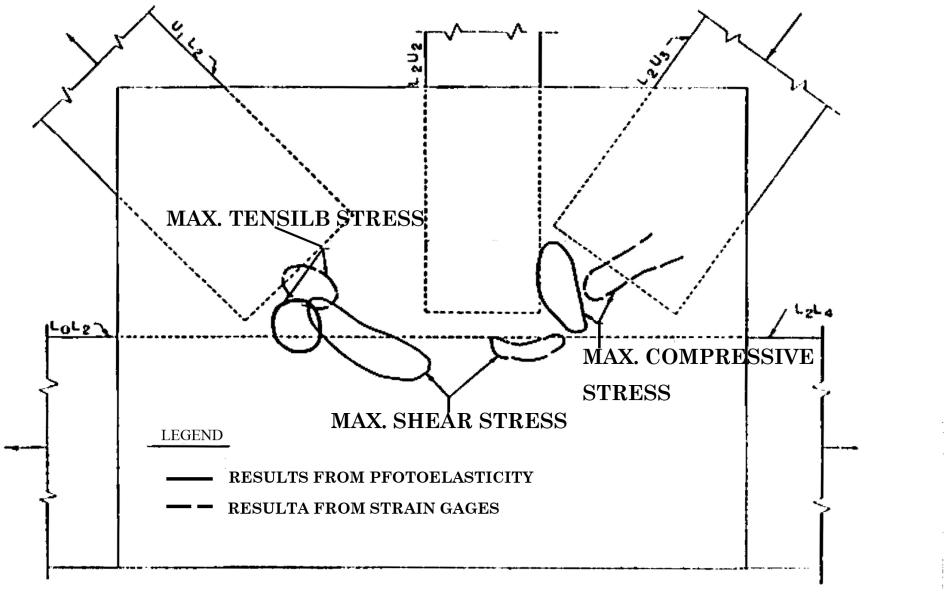

Figure 2.2: Schematic of the location of the maximum tension, compression, and shear stress Whitmore [1952]

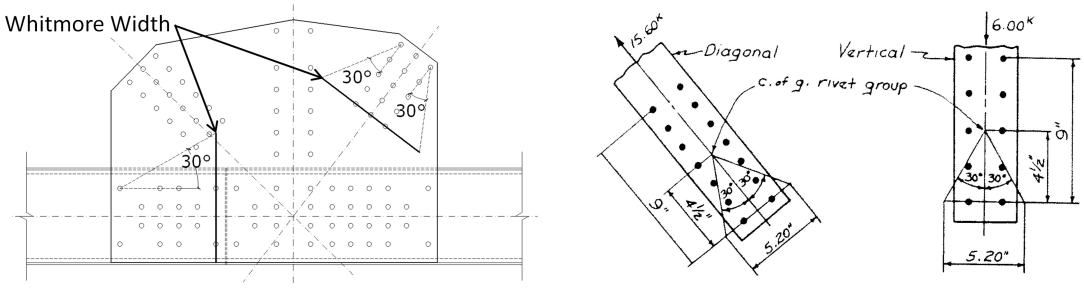

Figure 2.3: Approximations of principal stress at the end of members proposed by Whitmore [1952] and Irvan [1957]

designers do not really believe that a gusset plate acts as a beam, the assumption is still there and gusset plates are still being designed based on this assumption". Irvan [1957] and Hardin [1958] also tried to verify beam formula applied to the critical sections at gusset plates for flexure and shear stress. However, the conflicts between two experiments make

the use of beam formula on critical sections more uncertain. Hardin [1958] confirmed that beam formula is fine to approximate the tensile stress along the vertical section while Irvan [1957] found that the beam formula is not proper for gusset plate without chord splice. The shear stress in both experiments were found higher than the results using $\frac{3}{2}\frac{V}{A}$ and whole cross section but the multipliers were different in different applications.

Vasarhelyi [1971] at the University of Washington further studied the stress distributions along critical sections at gusset plates. Vasarhelyi [1971] conceived a device which could generate different loading distributions by controlling the angle of two separate ring frames to which loads from universal testing machine were applied. Figure 2.4 shows the test apparatus. Two loading distributions, one corresponding to high chord forces, denoted as loading position 1, and another corresponding to high diagonal forces, denoted as loading position 2, were considered in the tests. The test specimen was a Warren-type joint with two 45 degree diagonals and discontinuous chords. Vertical hanger and the chord splice plates were omitted to simplify the specimen and allowed the use of strain gages at splice on the gusset plates. Therefore, the gusset plates functioned not only as the connection of diagonals but also as splice plates of discontinuous chords. Photoelastic methods were used to decide the trajectories of tension, compression and shear stresses.

In addition to the experiments, four analytical methods were used to model his tests including two numerical methods, a prismatic element method by Hrennikoff [1941], and the finite plate element method. To clarify the influence of fastener force distributions to gusset plate stress distributions, four different fastener force distributions were considered for analytical studies. These four fastener force distributions were: the uniform fastener force distribution, the Type I and Type II nonlinear fastener force distributions proposed by Batho [1915], and the member force applied on the edges of the gusset plates, which was denoted "boundary" in Figure 2.5. Figure 2.5 shows the normal stress, σ_x, at referenced vertical section which passes through the center of the gusset plate and the splices, has similar stress distributions regardless of different force distributions transmitted from fastener.

The comparison of analytical and experimental results are shown in Figure 2.6. The analytical results had similar trends but was somewhat larger than the experimental results.

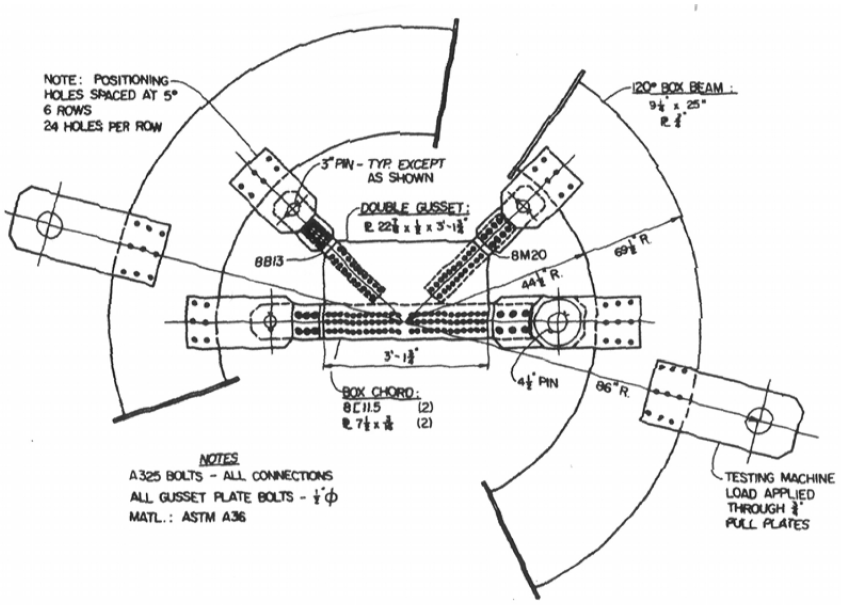

Figure 2.4: The apparatus was used byVasarhelyi [1971] to generate different loading combinations by controlling the angle of two half rims

Different stress in the double gusset plates was observed and shown by the shadow area implying that there was bending stress due to the initial imperfection. Vasarhelyi [1971] found that the maximum normal stress along vertical section did not occur at the edge of the gusset plate but rather somewhere near the center of the chord, while the maximum shear stress occurred at approximately one-third of the gusset plate depth measured from the bottom edge. Both the maximum stress and the location were observed to be affected by the magnitude of the diagonal forces. Although high chord loads occurred in loading position 1 and high diagonal loads in loading position 2, the maximum normal stresses shown in the two different loading pattern were not differed significantly. While Vasarhelyi [1971] described how the distribution of stress along the vertical section was affected by diagonal forces, the overall maximum shear and normal stresses were not reported. The mechanisms of the stresses at critical sections were still uncertain.

A comprehensive experimental study of bridge gusset plates were conducted by Yamamoto et al. [1985]. Yamamoto et al. [1985] used an apparatus similar to Vasarhelyi's device to

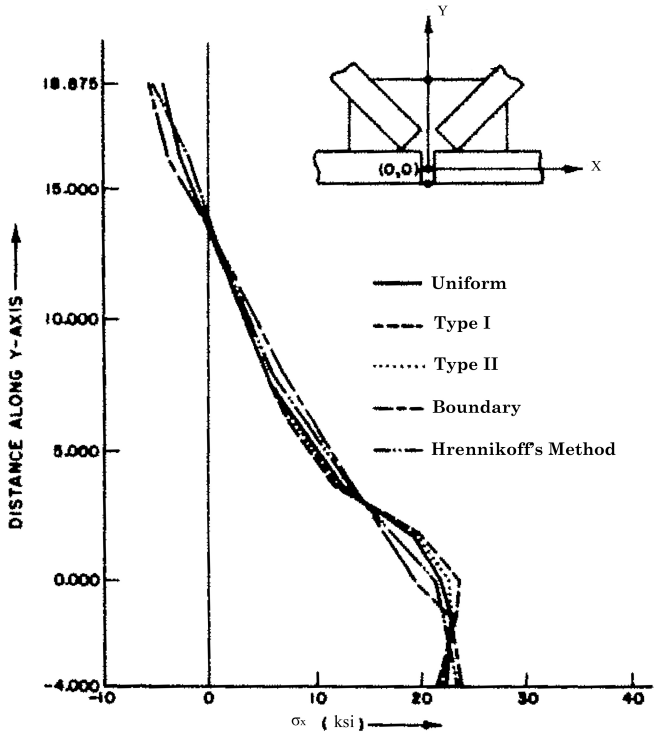

Figure 2.5: Normal stress considering four different fastener load transmitted mechanism along the critical section which passed the center of the splice of gusset plates were studied by Vasarhelyi [1971]

generate axial forces in truss members. Loads were directly applied to one diagonal and one chord, and the reactions from the ring frame balanced the axial forces for other truss members. The apparatus is shown in Figure 2.7. Eight specimens were tested using two geometries from Warren-type and Pratt-type bridges, two types of gusset plates, denoted as spliced-type and monolithic-type, and two types of loads, in-plane axial loads and in-plan bending loads. Spliced-type gusset plates were lapped and bolted to chord members, which was denoted as P2 and W2 specimen and shown in Figure 2.8. The author stated that *"in this type of gusset plate, stresses in one chord member are mainly transmitted to the other and only a small difference between them is supported by gusset plates"*. This implied that the spliced-type specimen had continuous chord members and the gusset plate did not act as

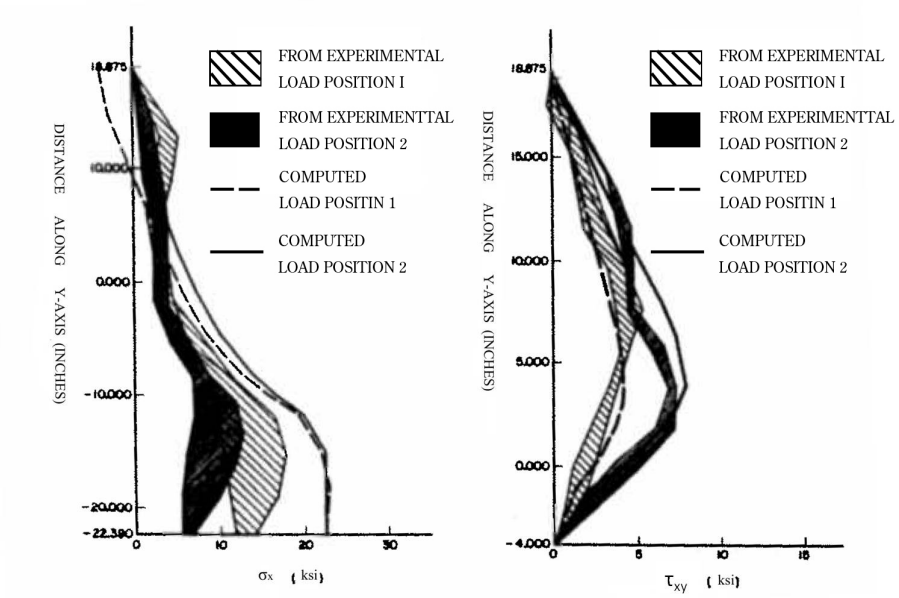

Figure 2.6: Normal stress distributions of analytical and experimental results were studied by Vasarhelyi [1971]

splice plates for chords. The term "spliced" indicated the gusset plates joined the diagonal members, not the chords. The monolithic-type specimen had the webs of the chord member expanded and become the gusset plates to connect diagonals. This configuration is seldom seen in practice. The dimensions and structural details for eight specimens of Yamamoto's testing are shown in Figure 2.8. P-2 and W-2 are spliced-type gusset plates and the other four specimens are monolithic-type gusset plates.

Although the unconventional specimens were tested, there are several important observations worthy of discussion.

- The shear stress trajectories were closely resemble the equivalent stress (Von Mises Stress) trajectories.
- For spliced-type gusset plates, which had continuous chords, the changes of chord loads had little influence to the shear stress distributions at gusset plates while in

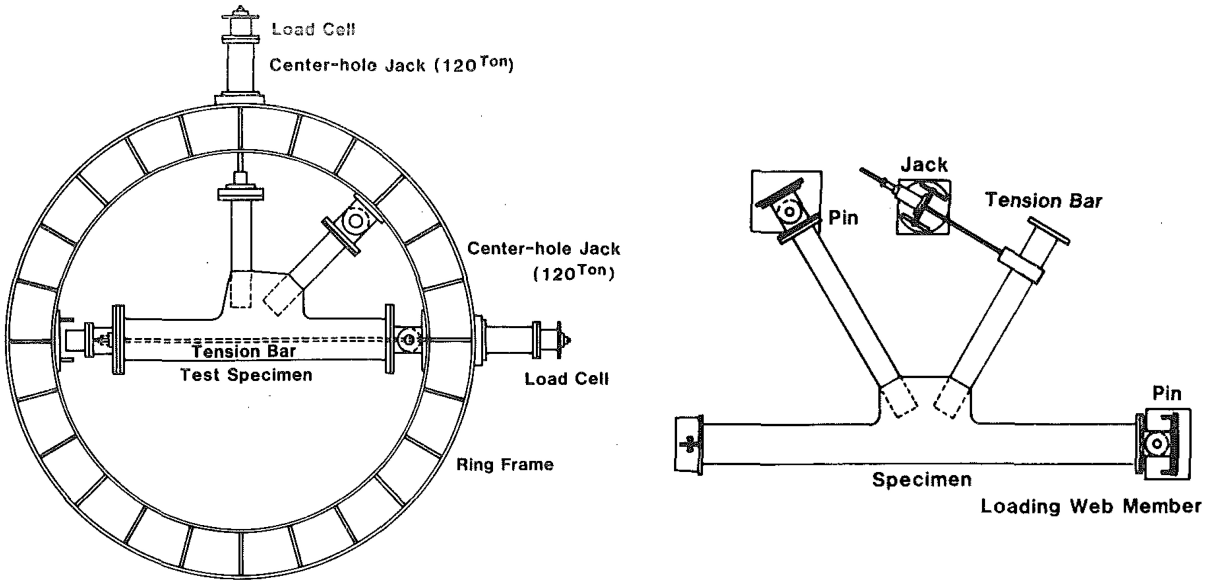

Figure 2.7: Test apparatus for axial loading and bending loading used in the tests conducted by Yamamoto et al. [1985]

the monolithic-type gusset plates, the shear stress distribution were greatly influenced by the changes of chord axial loads. This implied that the stress interaction was important at the gusset plate when gusset plates not only joint diagonals but also splice chords. However, it was not clear how the chord load interacts with the stress from diagonals.

- As in Irvan [1957] and Hardin [1958]'s tests, experimental results showed that maximum principal stress using Whitmore's method may underestimate the maximum stress. Yamamoto et al. [1985] proposed to use 22° instead of 30° to calculate principal stress at end of connected members and is given by Eq. 2.1:.

$$\frac{b_e}{b} = 1.0 + 0.8(\frac{d}{b}) \approx 1.0 + 2.0 * \tan 22^\circ * (\frac{d}{b}) \tag{2.1}$$

where b_e is the effective width, b is the connection width perpendicular to axial direction (in.), d is the connection length along the axial direction (in.)

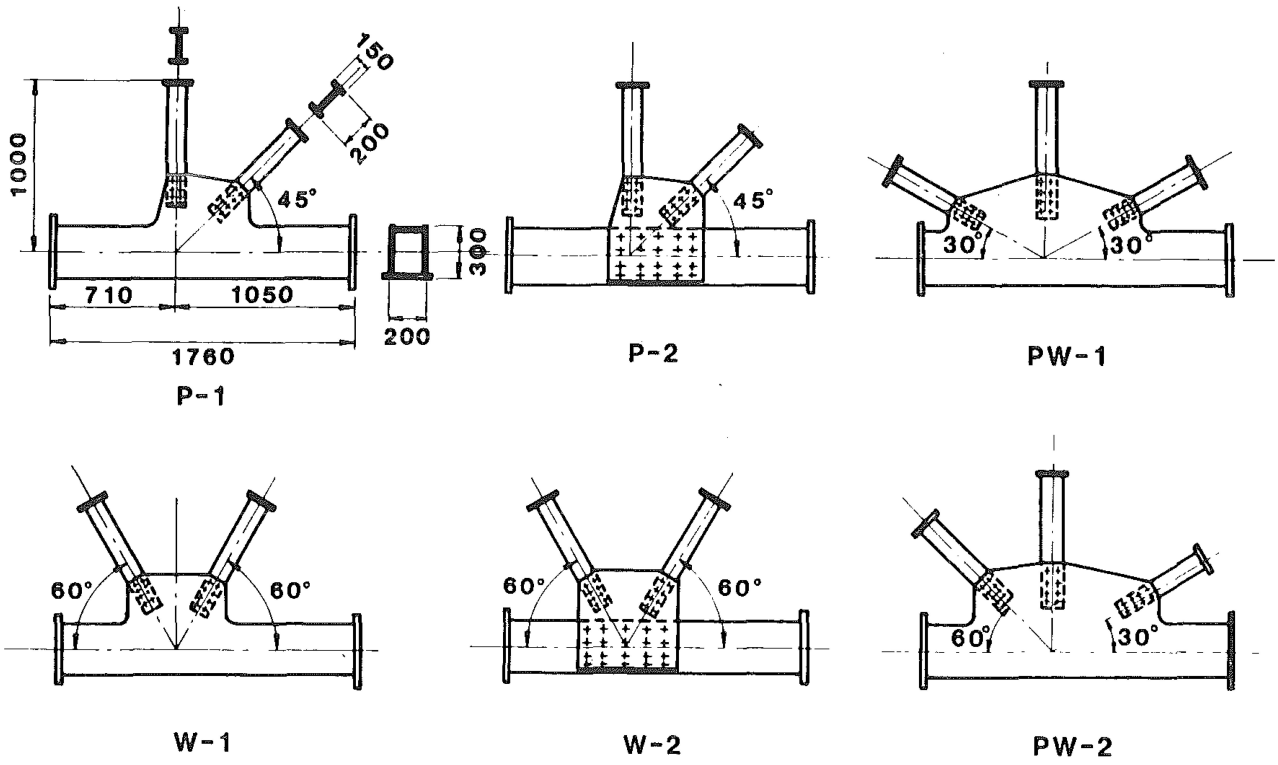

Figure 2.8: Six specimens for axial force loads were tested by Yamamoto et al. [1985] including P-2 and W-2 for spliced-type gusset plate and P-1, W-1, PW1, and PW2 for monolithic-type gusset plate

Yamamoto et al. [1985] verified the predicted stresses by Eq. 2.1 have less than 10% deviation with the experimental results.

- The secondary stresses generated by in-plane moment was considered. However, in-plane bending was found small and was about one-third of the primary stress empirically. A gusset plate thickness design equation considering primary and second stresses was proposed by Yamamoto et al. [1985].

$$t \geq \frac{P * 10^3}{b_e \sigma_a} * (\frac{1}{2} + \frac{I_w}{A_w} \frac{1}{b^2 + d^2}) \tag{2.2}$$

where t is required gusset plate thickness (in.), P is the axial force in the diagonal

member (kip), b_e is the effective width given by the Eq. 2.1, b is the connection width perpendicular to axial direction (in.), d is the connection length along the axial direction (in.), I_w is the moment of inertia of the diagonal member (in^4), A_w is the cross-sectional area of the member (in^2) and σ_a is the allowable stress of the gusset plate material (psi).

The first part of Eq. 2.2 represents the thickness of the gusset plates required to resist axial force and the second part represents the thickness required to resist in-plane moment. However, in practice, there is typically no in-plane bending exerting on the gusset plates and the second term in Eq. 2.2 is typically omitted.

In the literature review of elastic stress at gusset plates, high principal stress is generally observed at the end of diagonals at gusset plates. Studies found that 30° dispersion angle generates low estimation of the principal stress and several methods were proposed to improve Whitmore's method. High stresses are also observed at critical sections such as horizontal section along the edge of chords at gusset plates or vertical section cross chord splice but there is no effective method to estimate this stress. Beam theory is conventionally used to estimate flexure stress at these critical sections but is known to be unreliable. Shear stress at these critical sections using $\frac{3}{2}\frac{V}{A}$ as rectangular section is also found inaccurate most of time.

2.2 Buckling Strength of Gusset Plates

Buckling is one of major failure modes of steel gusset plate connections. Out-of-plane deformation at the gusset plate compressive edges was also observed in joint U10 prier to the I-35W collapse during an inspection in 2003 by URS [2003]. However, the research on the bridge gusset plate buckling is very limit. The complex stress state and boundary conditions make studies of bridge gusset plate buckling very difficult. Therefore, most of discussion of gusset plate buckling were made for gusset plates in braced frames in buildings. Gusset plate buckling was first considered by Thornton [1984] when a vertical bracing connection design philosophy was being proposed. There was no rigorous analysis or experiment conducted

for this proposal.

Thornton [1984] adapted the concept of column buckling and ignored bending resistance and post-buckling strength of plates to propose a conservative method for evaluation gusset plate buckling capacity. The proposed method considers the middle length $L2$ among the unsupported lengths $L1$, $L2$, and $L3$ measured from the Whitmore's section to the adjacent fastener lines of members as shown in Figure 2.9. The buckling mode was considered a fixed-fixed column and used the effective length factor, K, of 0.65. Thornton [1984] also suggested that the use of averaged length of $L1$, $L2$, and $L3$ may attain more reasonable buckling capacity, which is used in current code (FHWA [2009]). The column buckling equations are shown in Eq. 2.3 and 2.4 for reference. This equation simply considers the geometry of buckling area but dose not accommodate the complex stress states in this region.

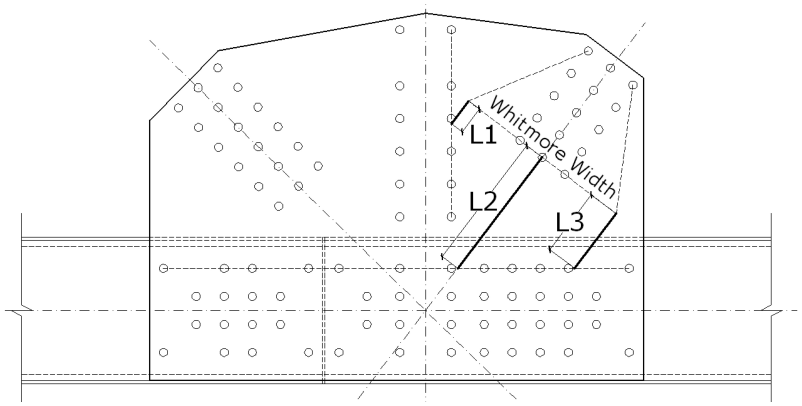

Figure 2.9: The effective length proposed by Thornton

$$\text{When } \frac{KL}{r} \leq 4.71\sqrt{\frac{E}{F_y}}\ F_{cr} = \left[0.685^{\frac{F_y}{F_e}}]\right] \text{ where } F_e = \frac{\pi^2 E}{(\frac{KL}{r})^2},\ r = \sqrt{\frac{I}{A}} \tag{2.3}$$

$$\text{When } \frac{KL}{r} \geq 4.71\sqrt{\frac{E}{F_y}}\ F_{cr} = 0.877F_e \text{ where } F_e = \frac{\pi^2 E}{(\frac{KL}{r})^2},\ r = \sqrt{\frac{I}{A}} \tag{2.4}$$

where I and A are computed for the Whimore width of the plate. Eq. 2.3 denotes the inelastic buckling and Eq. 2.4 denotes the elastic buckling.

The accuracy of Thornton [1984]'s method was validated by Dowswell [2006] for corner-brace gusset plate buckling. Dowswell [2006] analyzed 59 experimental specimens and 56 finite element models of corner-brace gusset plates from published studies. Dowswell [2006] first divided these corner brace gusset plates into three groups, compact, noncompact, and single-brace gusset plates, by considering the stiffness that the gusset plates provided. The gusset plate out-of-plane deformation stiffness is considered two parts, one is provided by the end support as a cantilever plate strip with unbraced length "l_1" and another part is provide by the bending stiffness from the lateral support as a guided cantilever with length "c" which are shown in Figure 2.10. Considering the required stiffness to prevent buckling, the required thickness for compact corner brace gusset plates was derived, $t_{beta} = 1.5\sqrt{\frac{F_y c^3}{E l_1}}$. Single-brace gusset plates is defined that brace gusset plate only connected to beam or column at one side. Dowswell [2006] found the current method is conservative for compact gusset plates, but it slightly over-estimates the buckling capacity of noncompact gusset plates. By analyzing these data, Dowswell [2006] proposed different unbraced lengths and effective length factors for brace gusset plates in the three categories. Overall, Dowswell [2006] confirmed the accuracy of Thornton's method when it was applied to brace gusset plates.

Gusset plates buckling at unbraced free edge was studied by Brown [1988]. Brown [1988] tested 24 half-scale braced gusset plates with three different gusset plate thicknesses and six different angles of the brace member. Fifteen out of 24 specimens were failed in the long free edge buckling. Brown [1988] justified that it was proper to determine the ultimate capacity of gusset plates using the buckling resistance at their longest free edge. The buckling shape of the long free edge often resembled a fix-guided column of which has an effective length factor, K, of 1.2. Brown [1988] took into account the plate buckling behavior and equated the plate buckling stress to Euler's column buckling stress to calculate equivalent slenderness ratio for the free edge length at gusset plates. However, the plate buckling coefficient, k' in Eq. 2.5a is questionable where $k' = 1.0$ is used. The minimum $k' = 4.0$ shall be considered

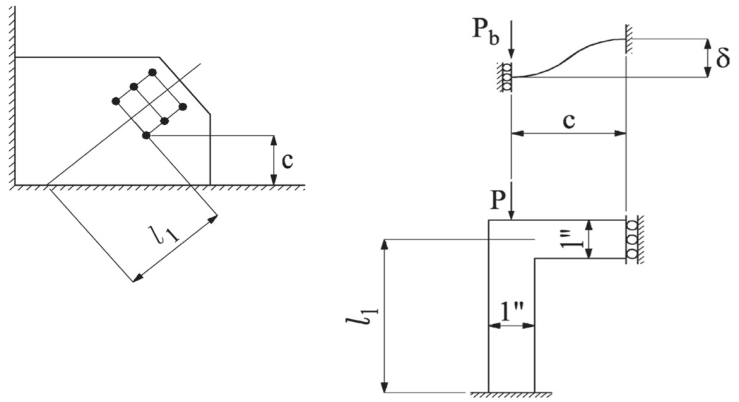

Figure 2.10: L-shape model for gusset plate buckling

according to the analytical solution of plate buckling. The critical buckling stress, F_a, then can be computed based on the equivalent slenderness from column buckling curve (Eq 2.3 and 2.4). The buckling capacity of the gusset plate at free edge is calculated by critical buckling stress time effective width, b and divided by load partition factor (LPF). LPF is a factor considering that only loads at fasteners located between buckling line and edge of gusset plate would contribute forces to this buckling mode (partitioning loads). LPF calculates ratio of the length in fastener contributed area to the whole connected length. Each fastener takes even load is assumed. Therefore, the buckling loads that member can take is larger than the load just buckle the plates.

The derivation is shown in Eq.2.5. The dimension of brace frame gusset plate is shown in Figure 2.11.

$$\sigma_{cr} = \frac{\pi^2 E}{(\frac{kl}{r})^2_{equiv}} = \frac{k'\pi^2 E}{12(1-\nu)^2(\frac{a}{t})^2} \text{ use k=1.2 } \nu = 0.3 \text{ k'=1} \tag{2.5a}$$

$$\frac{kl}{r}_{equiv} = \frac{2a}{t}$$

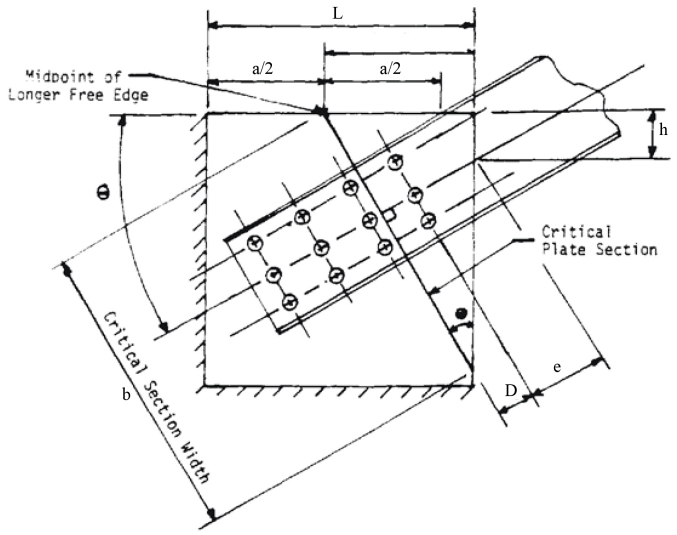

Figure 2.11: The dimension used to calculate the gusset plate buckling capacity

$$LPF = \frac{acos\theta + 2(p-e)}{2np} \tag{2.5b}$$

$$b = \frac{L - a/2}{\sin\theta} \tag{2.5c}$$

$$P_b = F_a bt/LPF = F_a \frac{L-a/2}{\sin\theta} t \frac{2np}{acos\theta + 2(p-e)} = \frac{F_a(2L-a)tnp}{(acos\theta + 2(p-e))sin\theta} \tag{2.5d}$$

where a is the length of the unsupported edge of gusset plate, t is the thickness of gusset plate, θ is the angle from the direction of loading to the free edge of gusset plate, n is the number of bolt rows in the direction of loading, p is bolt pitch, and e is the edge distance

Hu and Cheng [1987] and Cheng et al. [1994] examined elastic buckling capacity of thin brace gusset plates by experiments and FE analyses. Four specimens with two thin plates, 3.11mm (1/8") and 6.7mm (1/4"), and two different free edge lengths were tested with either fixed or free out-of-plane movement of the brace which was controlled by the testing frame. A sway buckling mode was found if brace frame allowed moves out-of-plane and a

fixed-guided column buckling mode was found if the frame was fixed. Local buckling of the free edge at gusset plate was found in the frame fixed situation and it buckled resembling to the fixed-fixed column. These tests obviously showed that the buckling mode is governed by the boundary conditions set for the experiments but it is not clear which buckling mode shall be considered for common braced gusset plates. In general, for elastic buckling, the Whitmore method was found to overestimate the strength of gusset plates.

Yam and Cheng [1993] and Yam and Cheng [2002] studied the inelastic buckling behavior of brace gusset plates. Thirteen full-scale tests were conducted with various parameters. A sway buckling mode was generally found to be the failure mode and significant yielding was observed before the ultimate load. Yam and Cheng [1993] and Yam and Cheng [2002] found the Whitmore width and the Thornton method were conservative for estimating the ultimate strength due to their neglect the stress redistribution after yielding. A modified Thornton method was proposed that uses a 45° dispersion angle and the maximum of the lengths $L1$, $L2$, and $L3$ to compute the effective width. Sheng et al. [2002] evaluated the Thornton methods, and the modified Thornton method and concluded that the methods are still conservative for estimating the ultimate strength of gusset plates. Sheng et al. [2002] developed a design method for rectangular type gusset plates subjected to compression based on the theoretical plate buckling equations.

However, these gusset plate buckling studies mentioned above were done for typical brace frame gusset plates. There was little study on buckling of bridge gusset plate connection. Yamamoto et al. [1988] conducted eight Warren-type gusset plate joint specimens to study buckling mode and buckling loads. The parameters include gusset plate types, materials, and thickness. Seven out of eight were monolithic-type gusset plates and one was spliced-type gusset plate which is most commonly used in U.S.. Three important phases, initial yielding, local buckling, and overall failure were recorded of the tests. Yamamoto et al. [1988] found the initial yielding was first found at the end of compression member, zone B, while the vertical and horizontal free edge, zone A and B, was still in the elastic state. In the spliced-type gusset plate, all zone were observed local buckling as the initial yielding starts. A design thickness, t_{cr}, for local buckling presuming that buckling occurs when the

stress in zone A reaches the allowable stress of the material was proposed.

$$t_{cr} = 1.10 L_1 \sqrt{\frac{\sigma_a}{E}} \tag{2.6}$$

where σ_a is the allowable stress of the material (about 0.58 times yielding stress and $L1$ is the length of the vertical free edge of zone A shown in Figure 2.12

Yamamoto et al. [1988] indicated that local buckling in one zone does not mean the failure of the system because other zones and post-buckling strength would provide supporting capacity. The ratios of the ultimate load to the buckling load range from 1.2 to 1.7 and have nothing to do with gusset plate type, material, or thickness. For the spliced-type gusset plate, it is worthy to note the local buckling at the vertical free edge almost happens simultaneously after the initial yielding and the overall failure happens when the horizontal section along top chords yielded.

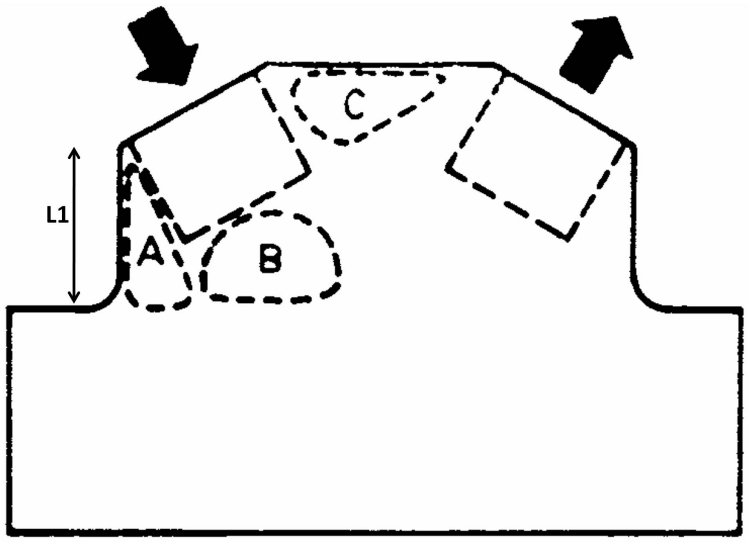

Figure 2.12: Buckling area and buckling mode on the gusset plate

2.3 Rivet Connection Strength

In additional to the failure of gusset plates, fastener failure in gusset plate connections is another important failure mode. There are many more studies on rivets and riveted joints compared to the studies on gusset plates, mainly because of the broad applications for riveted connections. In recent research, Olson [2010] showed that rivet capacity in the current gusset plate connection check often determines the capacity of riveted joints. This was mainly because of the use of conservative rivet shear strengths used in the current AASHTO specifications. Additionally, long connections require the rivet strength to be reduced by up to 20% when the connected length is over 50 (in) (*AASHTO* [2007] *and FHWA* [2009]). To understand the background of these requirements for riveted joints, dedicated literature reviews were conducted by Olson [2010] and Jost [2012]. Those reviews along with some additional experimental and theoretical studies will be summarized and discussed here. Literature studying factors affecting rivet strength and the behavior of long connections effect will be of particular interest.

2.3.1 Single Rivet Shear Strength

Rivets used to join two pieces of materials was a cutting-edge technology in the beginning of the 20^{th} century. They were commonly used in metal containers and ships. At this time, many studies focused on the performance of single rivet, small joints and properties such as rivet yielding, tensile and shear strength, initial clamping force, rivet slip, friction coefficient, rivet deformation, and plate efficiency through many tests (*Richard deJonge* [1945]). These tests were undertaken for different rivet materials, riveting tools, riveting procedures, and with different plate materials. Some research also studied the theoretical behaviors of rivets in riveted joints such as Batho [1916] and Hrennikoff [1934]. However, riveted joints used in civil engineering are usually much larger in size than the joints used in containers or ships and require higher strength..

AREMA [1905] reported a riveted joint study specific to rivets used in civil engineering, which was conducted at Cornell University in 1903 and reported by the committee of iron

and steel structures in the proceedings of the American Railway Engineering and Maintenance Way of Association (AREMA). AREMA [1905] studied open-hearth steel rivet joints where rivets and plates consisted of the same materials. They tested 90 different specimens. These specimens included lap and butt joint specimens with one to four rivets in a row and rivet patterns of one to three full rows or staggered arrangement. As a follow up, Talbot and Moore [1911] conducted the same test using nickel and chrome-nickel steel rivets. In total, 90 nickel steel joints and 54 chrome-nickel steel joints were tested by Talbot and Moore [1911]. The tests from AREMA [1905] and Talbot and Moore [1911] established the basic understanding of the properties of riveted joints used in civil engineering; such as rivet yielding, slip, clamping force, rivet grip length, and ultimate strength. In addition, an important finding was that the rivet joint ultimate shear strength was not determined solely by the rivet strength but was also related to the plate material in the joint. A statistical assessment result of rivet strength and the test variables drawn from these two sets of tests and other literature was developed by Olson [2010] and modified here and is shown in Table 2.1. This table includes several studies of riveted joint and the resulting rivet shear strength for connections with different rivet materials, plate materials and joints patterns.

Table 2.1: Rivet ultimate shear strength from the literature (modified from Olson [2010]

Reference	Steel Material	Rivet Mat. Properties		Ultimate Shear Strength(ksi)	
		F_y (ksi)	F_u (ksi)	Mean	Std. Dev.
AREMA [1905]	OH Steel	35.4	60.3	48.5	2.8
Talbot and Moore [1911]	Nickel Steel	45	68.5	56.6	1.8
	Chrome-Nickel Steel	38.4	59	52.8	2.5
Davis et al. [1940]	Carbon Steel	39.8	57.6	53.2 (60.03) [1]	2.5
	Manganese Steel	54.6	81	75.1 (79.15)[2]	2.5
Wilson and Thomas [1938]	Carbon Steel	37.9	47.9	60.0	N/A
	Manganese Steel	57.6	80.0	80.5	N/A
Wilson et al. [1942]	Low-Alloy A	52.4	74.1	63.9	2.0
	Low-Alloy B	42.9	65.6	64.8	0.8
	Low-Alloy C	49.1	76.3	74.0	3.8
Munse and Cox [1956]	ASTM A141	42.9	57.8	52.7 (61.6) [3]	3.86
Dlugosz [1962]	ASTM A141	N.A.	N.A	55.3	N.A.

[1] value in parentheses only considers short joints

[2] value in parentheses only considers short joints

[3] preliminary test results

Talbot and Moore [1911] conducted the first riveted joint test at the University of Illinois. Consecutive riveted joint tests at the University of Illinois using different rivets including rivets made by carbon-steel, manganese-steel, and three other low-alloy were conducted by Wilson and Thomas [1938] and Wilson et al. [1942]. Their reports broadly discussed the parameters that might affect the rivet strength. These parameters include double/single shear loading, driven/undriven rivets, pneumatic/machine riveting, heat temperature, grip length and plate materials. From these test results, it was found that the driving of rivets most significantly affected the rivet strength. Driven riveted joints had rivet tensile strengths that were 20% larger than the undriven rivet joints. Since there is a ratio between tensile and shear strength, Schenker et al. [1954], it is reasonable to expect that the shear strength in driven rivets is increased as well. Tables 2.2 and 2.3 compare tensile and shear strength of driven and undriven rivets with two different grip lengths tested by Wilson and Thomas [1938] and Wilson et al. [1942]. The tensile strength of driven rivets is shown to increase more over than undriven rivet where grip is shorter. Driven rivets were also shown to have larger strength in single shear as shown in Table 2.3, but the difference was less than 10% as shown in Table 2.4. It is worth noting that the sterngth listed here is nominal strenght which considers the original or specified rivet diameter while some discussions in the literature may use the actual strength computed using the deformed rivet diameter or rivet hole diameter. The rivet shear strength was also observed affected by the rigidity of the connected plates. Schenker et al. [1954] examined the rivet test literature and had similar discussions.

Table 2.2: Nominal ultimate tensile strength with parameters of grip length and driven/undriven condition

Rivet Type	Grip Length (in)	Carbon-steel [1](ksi)	Manganese-steel (ksi)	Low-alloy steel A [2] (ksi)	Low-alloy steel B (ksi)	Low-alloy steel C (ksi)
Undriven	3	57.62	79.75	74.43	67.35	78.92
	5	57.72	79.75	74.43	67.35	78.92
Driven	3	76.80	107.58	94.75	95.45	104.3
	5	70.23	96.885	86.50	84.35	98.95

[1] Wilson and Thomas [1938]

[2] Wilson et al. [1942]

Table 2.3: Nominal single ultimate shear strength with parameter of driven/undriven rivets

Rivet Type	Carbon-steel [1](ksi)	Manganese-steel (ksi)	Low-alloy steel A [2] (ksi)	Low-alloy steel B (ksi)	Low-alloy steel C (ksi)
Driven shear	59.96	80.52	63.92	64.82	75.96
Undriven shear	46.28	66.26	50.18	50.13	56.94
Difference	21.51%	17.71%	21.50%	22.66%	25.04%

[1] Wilson and Thomas [1938]

[2] Wilson et al. [1942]

Table 2.4: Undriven nominal ultimate shear strength with parameter of single/double shear

Rivet Type	Carbon-steel [1](ksi)	Manganese-steel (ksi)	Low-alloy steel A [2] (ksi)	Low-alloy steel B (ksi)	Low-alloy steel C (ksi)
Single shear	46.28	66.26	50.18	50.13	56.94
Double shear	42.14	54.52	48.64	47.34	54.44
Difference	8.95%	17.72%	3.07%	5.57%	4.39%

[1] Wilson and Thomas [1938]

[2] Wilson et al. [1942]

Finally, from Table 2.1, carbon-steel rivets, i.e. ASTM A141 rivet after 1932, are found to have a nominal ultimate shear strength of about 60 (ksi) in small and driven riveted connections considering all reviewed literature. Jost [2012] tested older ASTM A141 riveted connections salvaged from decommissioned truss bridge and reported the ultimate shear strength was approximately 60 (ksi), as well.

2.3.2 Impact of the Connection Length on Riveted and Bolted Connections

The load on a joint is often assumed to be uniformly distributed to each rivet. Batho [1916] and Hrennikoff [1934] theoretically studied this issue and found that the rivet in the end of a lap joint had higher loads than rivets in the middle of the joint. Their discussion was limited to the riveted joints in the elastic state. Davis et al. [1940] of the University of Illinois was the first to systematically test long and large connections until joint failure. Davis et al. [1940] tried to include several factors such as variations in the connection length, type of splice, plate and rivet steel, pitch, and rivet pattern into his test programs. A premature failure mode, where the joint shear capacity was less than the sum of each rivet shear capacity, was implicitly observed with some long connection joints. The failure mode showed the

first row of rivets failing in shear and consecutive shear failure in the successive rows of rivets of a joint, which is denoted an "unbuttoning failure". The tests conducted by Davis et al. [1940] included many variables and these variables may not be independent to each other. Nevertheless, the unbuttoning failure was observed in all long connections. Davis et al. [1940] concluded that: *"In general, at the ultimate load the greater the length of the joints the lower was the rivet strength. However, it was found that the usual assumption of equal distribution of load among rivets is satisfactory for design purpose."* Dlugosz [1962] commented on this work saying that *"Their tests show the unbuttoning trend but the joint configuration raises some questions as to the influence of other variables."* However, Davis et al. [1940] provided considerable and important test results for verifying the analytical study. His test results will be discussed again in Chapter 7.

The most cited studies investigating the effect of connection length on joint strength focused mostly on bolted joints and was conducted at Lehigh University and led by Prof. Rumpf and Prof. Fisher, beginning in 1958. A test program was carefully designed to include different variables and a theoretical solution for the joint behavior covering both the elastic and inelastic states was developed. Their preliminary tests documented in Foreman and Rumpf [1958], tested several small bolted connections consisting of A7 steel plates and A325 high strength bolts.

Foreman and Rumpf [1958] established baseline load-deformation behavior for A7 plates and A325 bolts and formulated the tension-shear ratio, which was the ratio of allowable tensile stress, T, of connected elements to the allowable shear stress, S, of fasteners. Using specific tension-shear ratios, a balanced design could be produced where failure in the plates or fasteners was equally likely. For A7 plate and A325 bolts, T/S was found to be $1 : 1.10$ and $1 : 0.75$ for A7 plate and A141 rivets. For a T/S of $1 : 0.75$, the ratio of net section area of the plate to the fastener shear area is $A_n/A_s = 0.75 : 1$

Building on the previous work, Bendigo and Rumpf [1960] tested two series of long bolted joints and several compact joints with different bolt pattern. Two series joints included variations in the plate width and in the plate thickness to achieve balanced design. The unbuttoning phenomenon was observed in all specimens where the connected length longer

was than 21 (in), or 7 bolts in a row. Hansen and Rumpf [1960] extended this test series to a 52.5 (in) connection length with 16 rivets in a row. It was determined that the unbuttoning phenomenon was occurred in long connections even when ductile fasteners were used. Dlugosz [1962] revised the plate specimens used in the test by Bendigo and Rumpf [1960] and fastened this specimens with A141 7/8" diameter rivet. The results showed that although the stress redistribution in riveted joints was more apparent than in bolted connections, the long riveted joints still failed in an unbuttoning mode. In addition, although the rivets were more ductile, the bolted connection of of the same size had higher capacity. Other details of the work by Dlugosz [1962] will be discussed later and used for verifying finite element simulations.

The unbuttoning failure mode was also observed in the additional tests in which A440 plates were joined by either A325 bolts or A490 bolts. These tests were documented by Fisher et al. [1963], Sterling and Fisher [1965], and Sterling and Fisher [1965]. In addition to the materials, the ratio of the net section tensile area to fastener shear area, A_n/A_s, was the main variable being studied in these tests. These tests were designed "unbalanced" to a A_n/A_s from 0.8 to 1.3. It was found that the larger ratio of A_n/A_s, the higher the average rivet shear strength observed at joints failure. The results from varying the tension-shear ratio agreed with the observations in previous studies that for a long riveted joint, rivet strength was not solely proportional to the single rivet strength and area but related to the rigidity of the connected plates.

A theoretical solution was developed by Fisher [1964] and Fisher and Rumpf [1967] to study the effect of high strength materials and other variables that could influence the strength of long joints. The solution considered the elastic and inelastic behavior of the plate and fasteners. The joint was treated as a statically indeterminate structure, and therefore, the equilibrium of load distribution to the fasteners and compatibility between the main plate and lap plates were coupled with load-deformation relationships from typical tension tests on plates with holes and fastener. The success of this theoretical solution mainly relied on the accuracy of the nonlinear stress-strain relationship of standard plate coupons for different materials and thicknesses, and single fastener double shear tests. The parameters

in those load-deformation relationships were from a regression analysis resulted from the test conducted at Lehigh University. The most important findings regarding that of long joints behavior can be concluded as follows and shown in Figure 2.13.

- The unbuttoning is apparent in long connections where the end fasteners take higher loads than fasteners in the middle. Connections having lower connected element yield stress had lower average rivet load at the time of unbuttoning. Joints with higher yield stress connected element material had more uniform rivet load distribution. This is shown in Figure 2.13(a).

- With increasing the net plate area, the average shear strength of the fasteners for the long joints was increased. As the A_n/A_s approached infinity, the load would fully re-distribute to all fasteners and the joints would not fail in an unbuttoning mode. The higher strength of the connected elements would mitigate the decrease in average fastener load at failure with increasing connection length. At $A_n/A_s = 1.0$, the average fastener shear stress was below 60 (ksi) for connected lengths over 40 (in) in joints with A440 connected element material, while for joints with A7 connected element material that occurred at around 25 (in) in length.

2.4 Research after I-35W Bridge Collapse

Much research on gusset plate connection behavior has been conducted since the collapse of the I-35W bridge. First, the reasons cause the bridge collapse were investigated by the National Transportation Safety Board (NTSB) and the Federal Highway Administration(FHWA). Then, methods to identify potential "at risk" gusset plate joints and comparisons of older and recent design philosophies were developed (Berman et al. [2012] and Higgins et al. [2010]). Additionally, studies of general gusset plate behavior considering factors, such as compressive buckling, yielding capacity, fracture at fastener holes, effect of corrosion and gusset plate retrofits have been performed (Kay [2011], Mentes [2011], Ocel et al. [2012] and Hafner [2012]). This research has mostly focused on the effect of gusset plate and connected member geometry and none of them have studied the complex stress

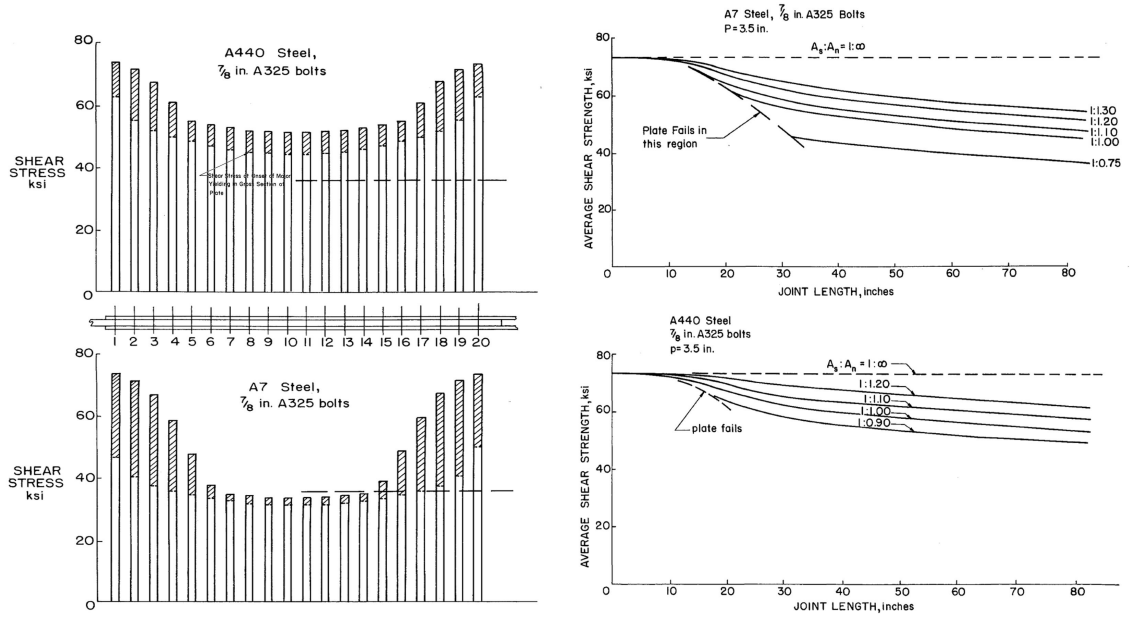

(a) Shear stress in individual fastener as plate gross area yields as shown the white bar and joint fails as shown hatched area

(b) The effect of A_n/A_s to the long connection effect

Figure 2.13: Theoretical fastener behavior in joints derived by Fisher [1964]

state in gusset plates.

2.4.1 Investigation of the Minnesota Bridge Collapse

The collapse of the I-35W Bridge (also known as Minn BR9340), carrying Interstate 35W across the Mississippi River, on August 1st, 2007 generated concerns regarding the safety of gusset plate connections. The initial onsite investigation, conducted by the NTSB, indicated that failure initiated at Joint U10 and L11, and caused the progressive collapse of the bridge. The I-35W Bridge was designed according to the 1961 American Association of State Highway and Transportation Officials (AASHTO) *Standard Specification for Highway Bridges* AASHTO [1961] using allowable stress design philosophy. An investigation team commissioned by the FHWA was assigned to review and assess the original bridge plan,

which was designed by Sverdrup & Parcel originally. In the resulting report, Holt and Hartmann [2008] performed design calculation similar to the original design draft and indicated the inadequate design at several gusset plates, highlighting this as a potential cause of the collapse. Further, a more detailed and comprehensive FE analysis was conducted by Ocel and Wright [2008]. Ocel and Wright [2008] used ABAQUS to analyze I-35W bridge behaviors during four different loading stages. Their FE model was mainly built by beam elements for most of the truss superstructure with shell elements for the deck and a detailed shell element model for Joint U10 that was embedded in the global truss bridge model. Rigid link elements represented rivets connecting gusset plates with members and contact element with compression only property were used at the edges of the plates to prevent unrealistic intrusion from one plate into another.

They analyzed the response of the bridge under different historic loading stages and simulated possible impacts from corrosion, thermal effects, and the gusset plate imperfection which was identified from photographs taken before the collapse. The loading stages and corresponding axial loads in the members of Joint U10 were as listed in Table 2.5. Ocel and Wright [2008] concluded: 1) the gusset plates at Joints U10 and L11 joints were underdesigned, 2) significant yielding along the horizontal shear plane was observed and the likely failure was due to inelastic gusset plate buckling, 3) the likely extent of corrosion was a significant factor in the failure, and 4) Joint U10 joint yielded under dead loads when the bridge had just been constructed. The work by Ocel and Wright [2008] is important not only for providing information and data on the bridge collapse but also allowing for comparisons to be made with simplified FE modeling methodology.

Liao et al. [2011] also investigated the possible failure causes of the I-35W Bridge Joint U10 gusset plate. Liao et al. [2011] used ABAQUS and developed a FE model with eight-node solid elements to observe the detailed behavior in the vicinity of rivet holes on the gusset plates. Liao et al. [2011] found that the high stress concentration around the rivet holes may have caused fracture prior to the compression demand reaching its capacity. Liao et al. [2011] indicated that the interaction between gusset plate tensile and shear stress decreased the gusset plate stiffness significantly.

Table 2.5: Four Stages of Loading Change

Member	After Step 1 (Steel +wet concrete)	After Step2 (Add original barriers)	After Step3 (Add deck thickness and modified barriers)	After Step4 (Add construction and traffic loads)	Design Load on design plan
U10U9W	1420	1560.2	1926.1	1989.4	2179
U10L9W	-1593	-1747.6	-2163.2	-2388.6	-2288
U10L10W	243.8	264.8	333.1	398.8	540
U10L11W	1333	1458.4	1796.7	1933.1	1975
U10U11W	-407.9	-436	-520.3	-647.6	-972

2.4.2 Research on the Improvement of Current Evaluation Methods

Higgins et al. [2010] discussed the discrepancy of evaluating existing gusset plates that were designed using the Whitmore section and allowable stress methods with the current block shear and load and resistance factored design methods. They identified vintage gusset plates that were properly designed as those having a rating factor equal to 1.0 or greater using the older approaches. The researchers found the rating factor calculated with modern load and resistance factored methods are often less than 1.0 meaning inadequate capacity of these vintage gusset plates. However, errors in gusset plate design were only identified when the actual rating factor was much smaller than the expected rating factor accounting for the differences between older and modern rating method. In order to have an economic and systemic way to examine vintage gusset plates, Higgins et al. [2010] proposed a prioritization method. The method is based on evaluation of the fastener capacity, and gusset plate tension, compression, and shear strengths. These four checks are very simplified, conservative and are limited to the diagonals to speed the calculation and filter the most vulnerable gusset plates.

Hafner [2012] tested six full-scale truss bridge joints specimens at Oregon State University to study gusset plate sway-buckling, plate imperfection, the effect of corrosion, and retrofit strategies. Sway-buckling was found in all tested specimens and the plate imperfection and the stiffness of the compressive diagonal were the main parameters studied for buckling. Plate imperfection was found to have significant impact on the plate buckling capacity as was the compression diagonal's stiffness. Hafner [2012] showed that the current effective length factor suggested by FHWA, $K = 1.2$, underestimates the buckling capacity and an effective upper bound of unity for K was suggested. The use of a lower effective length factor is consistent with the observation of a fixed-fixed buckling mode rather than a sway mode. Notably, the buckling failures observed by Hafner [2012] were generally elastic buckling which may not often be observed in existing gusset plates. The specimens studied by Hafner [2012] mainly featured thin plate with large unbraced lengths under the compression diagonal.

One of the full-scale steel truss bridge gusset plate joint specimens tested at Oregon State University was investigated further by Kay [2011] using finite element simulation. Four analytical modeling techniques for fasteners were studied prior to conducting a parametric study of gusset plates. Kay [2011] found that though a more complex fastener model simulating fasteners as radial springs deployed around the hole has better performance in the vicinity of the fastener hole, the simple rigid link model for fasteners is proper to study the gusset plate stress away from the holes and also to study gusset plate buckling. A study of gusset plate buckling showed that the gusset plate bucking capacity is not determined solely by the gusset plates but also is affected by the stiffness of the connected members.

Comprehensive and full-scale experiments on truss bridge joints were also performed in the FHWA laboratory at the Turner-Fairbank Highway Research Center recently. Test specimens were designed using a collection of typical steel truss bridge joints from across the U.S. The standoff length, which describes the length from the compressive diagonal's end to the horizontal chord fastener line, free edge length and the thickness of gusset plate were the parameters studied. The tests are reported in Ocel et al. [2012] and Mentes [2011]. Buckling capacity, shear resistance at critical sections, and stress at the chord splice were

also studied and several recommendations were made. Mentes [2011] reported the buckling capacity of the gusset plates can be calculated by Thornton's method using middle length from Whitmore section to adjacent fastener line and effective length factor K=0.35 for unchamfered gusset plates. The use of a lower effective length factor is consistent with Hafner [2012]'s study, but a K factor less than 0.5 is theoretically unsound by buckling theory. In addition, the slenderness check of the free edges currently required by AASHTO [2007] current regulation was found to have little impact on the buckling capacity and its removal was suggested.

For gusset plate shear resistance, though the results calculated by the current evaluation were found to be not fully consistent with test results, no changes to the current methods were recommended but further study of the resistance factor was suggested for shear resistance. A pseudo-plastic section approach was proposed to estimate capacity of chord splice in both compression and tension.

The comprehensive study of gusset plate behavior by FHWA provides key test data for future validation of numerical gusset plate studies and examines many of the important gusset plate issues reported by previous studies. However, it still lacks discussion of the impact of the stress state on the gusset plate behavior, which was also reported as having a significant impact in previous studies. The lack of insight into the interaction of stresses generated from various connected elements and the stress state itself in gusset plate behavior remains absent in recent gusset plate research.

2.5 Current AASHTO and FHWA Guidelines for Gusset Plates Design and Evaluation

Prior to the collapse of I-35W, the 2007 AASHTO LRFD Bridge Design Specification (AASHTO [2007]) requires that the gusset plate shall be designed as tensile connection where gross section yield, net section fracture, and block shear are considered. In addition, the gusset plate is required to provide enough thickness to prevent yielding from combined flexural and axial stress and uniform or parabolic shear stress at critical sections. A limit of the unsupported length at gusset plate edges to prevent gusset plate buckling and sufficient

fasteners symmetric to the center line of connected members to provide enough fastener shear resistance are required. The 2012 AASHTO code (AASHTO [2012]) does not revise the text for gusset plate design but suggests that designers shall consider the evaluation guidance, *"Load Rating Guidance and Examples For Bolted and Riveted Gusset Plates in Truss Bridges"* published in 2009 by FHWA.

The method included by the design specification (AASHTO [2007]) to consider the combined axial and flexural stress, denoted the "Method of Section" and also referred to as the method using beam theory, and the methods in the FHWA guidance, denoted the FHWA Guide, will be discussed in the following sections.

2.5.1 "Method of Section"–Axial and Flexural Stress on Gusset Plates

This method considers arbitrary sections such as horizontal and vertical gusset plate sections like beam sections as shown in Figure 2.14. On those sections, the axial, shear forces and bending moment are calculated using the loads from connected members acting on the free-body-diagram of these sections. The combined stresses on these section are required not to exceed $\phi_f F_y$. Eq. 2.7 shows the calculation of these stresses. The corresponding limits of the maximum stress are listed below:

- The maximum stress from combined factored flexural and axial forces shall not exceed $\phi_f F_y$ where $\phi_f = 1.0$ and F_y is the yield stress of the gusset plates.
- The maximum shear stress on a section due to the factored shear force divided by the gross shear area shall not exceed $\phi_v F_y/\sqrt{3}$ for uniform shear or $\phi_v 0.74 F_y/\sqrt{3}$ for shear from flexure, where $\phi_v = 1.0$.

$$f_a = \frac{P}{A} \tag{2.7a}$$

$$f_b = \frac{M}{S} \tag{2.7b}$$

$$f_v = 1.5\frac{V}{A} \tag{2.7c}$$

$$f_{comb} = \frac{f_a + f_b}{2} \pm \sqrt{\frac{f_a + f_b}{2}^2 + f_v^2} \tag{2.7d}$$

where P, M, and V are axial force, bending moment, and shear force, $S = \frac{bh^2}{6}$ is rectangular section modulus, A is gross section area, and f_v is the shear stress, f_a is the axial stress, and f_b is the bending stress.

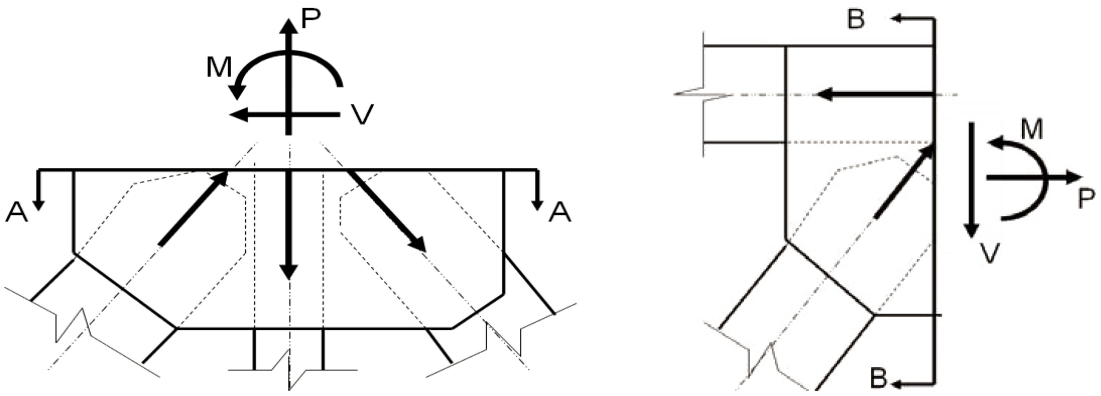

Figure 2.14: The horizontal section A-A and vertical section B-B are considered for combined stress in gusset plate (Holt and Hartmann [2008])

2.5.2 FHWA Gusset Plate Load Rating Guidance

The "Load Rating Guidance and Examples for Bolted and Riveted Gusset Plate in Truss Bridges", which was published in 2009, is FHWA's response to the 2007 Minnesota I-35W Bridge collapse. This guidance was developed for two methods of bridge load rating in current use: Load and Resistance Factor Rating (LRFR) and Load Factor Rating (LFR) respectively. Gusset plate joint capacity is taken as the smaller of the capacity between connecting gussets and fasteners in these methods. The considerations for both methods

are very similar, but the equations are somewhat different. The procedures are described below and both methods are listed side by side for reference.

2.5.2.1 Fastener Shear Resistance

$$\phi R = \phi F m A_r \tag{2.8}$$

when connection length is over 50 in, a reduced factor of 0.8 is used to calculate total rivet strength where

m = the number of shear face

A_r = cross-sectional area of the rivet before driving

ϕF = Factored shear strength of one rivet suggested in Table 2.6

Table 2.6: Rivet shear strength suggested by the FHWA Guide FHWA [2009]

Rivet Type	LRFR ϕ F(ksi)	LFR ϕ F(ksi)
Constructed prior to 1936 or of unknown origin	18	18
Constructed after 1936 or of unknown origin	21	21
ASTM A502 Grade I	27	N/A
ASTM A502 Grade II	32	N/A

[1] A141 rivet shear strength is updated in AASHTO [2011]

2.5.2.2 Gusset Plates in Tension

The effective sections using Whitmore method at the end of tensile members are considered to calculate the capacities of gusset plates in tension. Gross section yielding is considered by LRFR and LFR methods. Net section fracture is only considered by LRFR method. Table 2.7 shows the calculation equations for both methods and Figure 2.15 again demonstrates the Whitmore sections considered for the hanger, diagonals, and chords.

Table 2.7: Gusset plates tension yielding or rupture capacity

	LRFR	LFR
Gross Section Yielding Resistance	$P_r = \phi_y P_{ny} = \phi_y F_y A_g$ (2.9)	$R_r = A_e F_y$ (2.10)
Net Section Fracture Resistance	$P_r = \phi_u P_{nu} = \phi_u F_u A_n U$ (2.11)	N/A

where

ϕ_y = resistance factor for tension yielding = 0.95

ϕ_y = resistance factor for tension fracture= 0.8

P_{ny} = nominal tensile resistance for yielding in gross section

A_n = net cross-section area of the plates as specified in AASHTO LRFD Article 6.8.3 for LRFR and specified in AASHTO Article 10.16.14 for LFR

A_g = cross-section area of the plates

P_{nu} = nominal tensile resistance for fraction on the net section

F_y = yielding strength of the plates

U = reduction factor to account fir shear lag = 1.0 for gusset plates

A_e = effective gross cross-sectional area taking into account the possibility of net section fracture

$A_e = A_n + \beta A_g \leq A_g$

β = 0.0 for M270 grade 100/100W steels, or when holes exceed $1\frac{1}{4}$ in diameter

= 0.15 for all other steels and when holes are less than or equal to $\frac{1}{4}$ in diameter

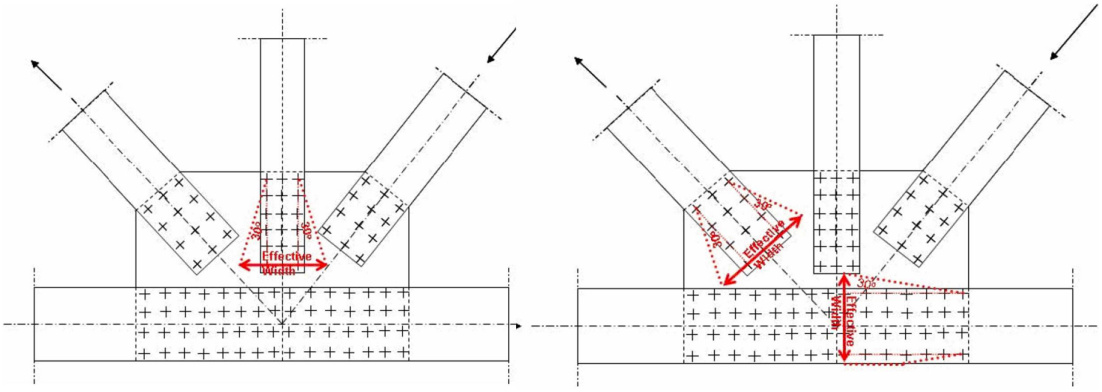

Figure 2.15: Effective section for tensile strength check using the Whitmore section in the FHWA Guide

2.5.2.3 Block Shear Rupture Resistance

Block shear in tension members or gusset plates considers several failure planes to find the governing plane as shown in Figure 2.16. Eq. 2.12 shows the calculation of the block shear capacity considering combinations of tensile planes and shear planes.

$$\text{If} \quad A_{tn} \geq 0.58A_{vn} \quad \text{then} \quad R_r = \phi_{bs}(0.58F_yA_{vg} + F_uA_{tn}) \tag{2.12a}$$

$$\text{Otherwise} \quad R_r = \phi_{bs}(0.58F_uA_{vn} + F_yA_{tg}) \tag{2.12b}$$

where

ϕ_{bs} = resistance factor for block shear = 0.8 for LRFR; = 0.85 for LFR

A_{vg} = gross area along the plane resisting shear stress

A_{tg} = gross area along the plane resisting tension stress

A_{vg} = net area along the plane resisting shear stress

A_{tg} = net area along the plane resisting tension stress

F_y = specified yield stress for LRFR and minimum yield stress for LFR

F_u = specified tension stress for LRFR and minimum yield stress for LFR

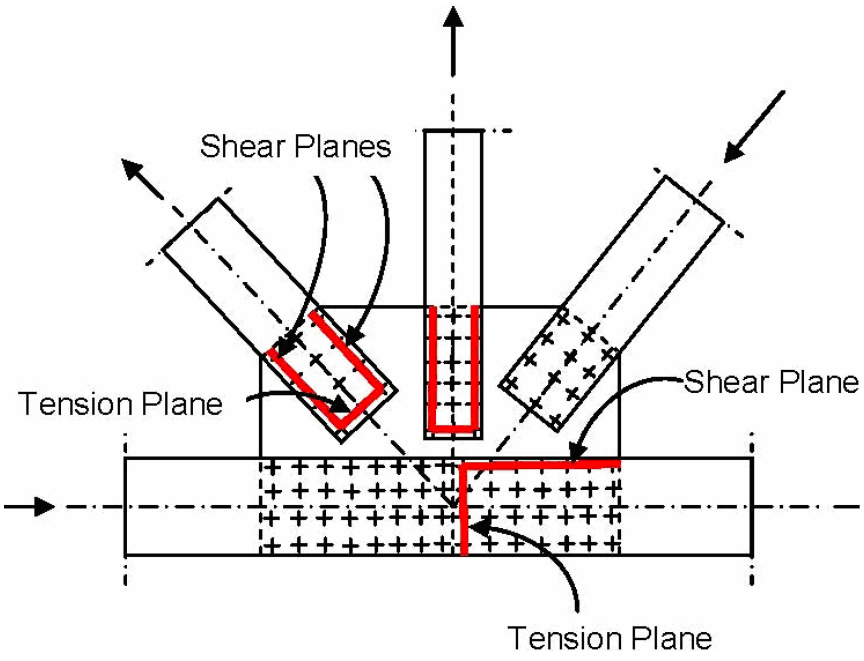

Figure 2.16: Block shear for gusset plate checking for a combination of shear and tension planes (FHWA [2009])

2.5.2.4 Gusset Plates Subjected to Shear

The factored shear resistance for gusset plates subjected to shear considers several critical sections, mainly along horizontal and vertical lines beside the chord rivet line and the hanger rivet lines, as shown in Figure 2.17. Both LRFR and LFR methods consider gross section shear yielding and net section fracture as given by Eqs. 2.13a and 2.13b. A reduction factor, Ω, is applied to Eq. 2.13 to ensure the development of plastic shear section before gusset plate buckling.

$$V_r = \phi_{vy} = \phi_{vy} \times 0.58 \times F_y A_g \times \Omega \tag{2.13a}$$

$$V_r = \phi_{vu} = \phi_{vy} \times 0.58 \times F_u A_n \times \Omega \tag{2.13b}$$

where:

ϕ_{vy} = resistance factor for shear yielding on the gross section=0.95 for LRFR

ϕ_{vy} = resistance factor for shear yielding on the gross section=1.0 for LFR

ϕ_{vu} = resistance factor for shear fracture on the gross section=0.8 for LRFR

ϕ_{vu} = resistance factor for shear fracture on the gross section=0.85 for LFR

A_g = gross area of the plates resisting shear

A_n = net area of the plates resisting shear

F_y = minimum yielding stress of the plates

F_u = minimum yielding stress of the plates

Ω = reduction factor taken as $\Omega = 1.00$ when the gusset plates are of ample stiffness to prevent buckling and develop the plastic shear force of the plates or 0.74 in the absence of a more rigorous analysis or criterion to assure and quantify the stiffness requirement to develop the plastic shear force of the plates

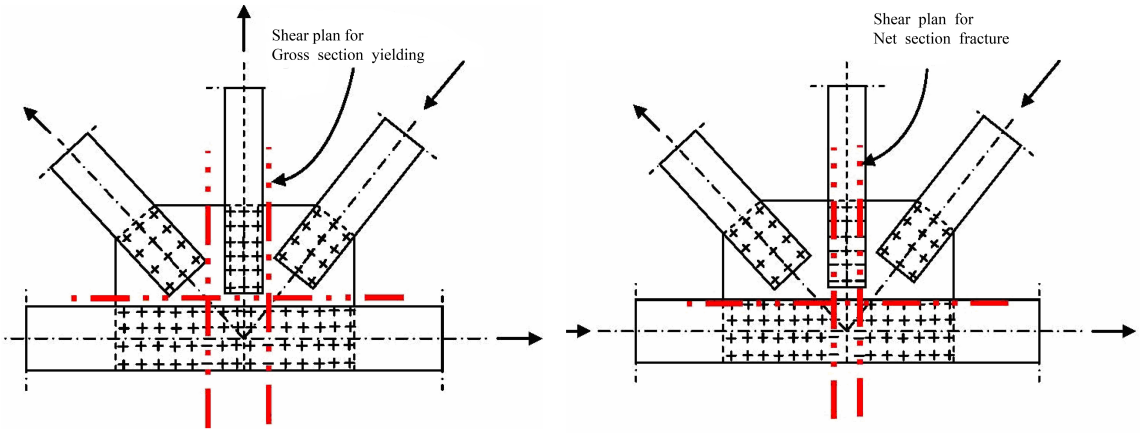

Figure 2.17: Critical sections for checking gusset plate shear capacity (FHWA [2009])

2.5.2.5 Gusset Plate Buckling

In the absence of rigorous analysis, the FHWA Guide suggests gusset plate buckling be evaluated using the column buckling formula. The averaged unbraced length, instead of using the middle unsupported length proposed by Thornton [1984], is used as the effective length and is shown in Figure 2.18. The effective length factor is chosen according to the possible buckled shape of gusset plates from 2.19. When lateral sway of gusset plates is possible, the effective length factor, K, was chosen from cases(d), (e), and (f) of Figure 2.19. When lateral sway is not possible, the effective length factor, K, is chosen from cases (a), (b), and (c) of Figure 2.19.

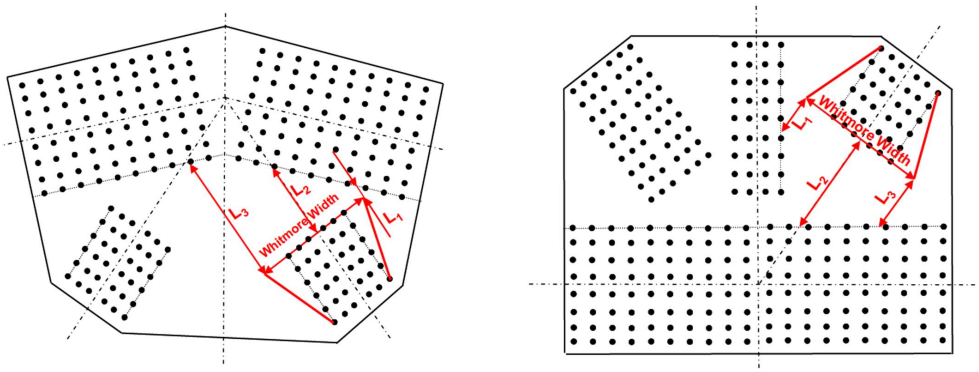

Figure 2.18: Effective length is calculated based on the Thornton method

Buckled shape	(a)	(b)	(c)	(d)	(e)	(f)
Theoretical *K* value	0.5	0.7	1.0	1.0	2.0	2.0
Design *K* value	0.65	0.80	1.0	1.2	2.1	2.0

Figure 2.19: Effective length factor,K, for different buckling shape

Chapter 3

ANALYTICAL MODELING OF STEEL TRUSS BRIDGE JOINTS

3.1 Overview and Motivation

To investigate the behavior of gusset plate Joints U10 and L11 affected by various factors such as loading history, corrosion, thermal effect, imperfection and so forth, Ocel and Wright [2008] conducted Finite Element Analysis (FEA) using ABAQUS v.6.6 establishing a comprehensive finite element bridge model. This model consisted of all structural components of the bridge, where the truss members were modeled with beam elements, the bridge deck was modeled with shell elements, and gusset plate Joints U10 and L11 were modeled with shell elements and were embedded into the global bridge model. In addition, compression-only contact element were used between gusset plates and connected truss members. However, building this kind of model is time-consuming and is not feasible for performing parametric studies to investigate gusset plate behaviors more broadly.

In order to analyze gusset plate joints with various geometries and study various parameters, a method of modeling a subassemblage of the gusset plate joints was developed using the finite element software ANSYS (64-bit v11). In this section, the development of the methodology to simulate the behavior of the joint subassemblage accurately and efficiently is described. This method considers modeling of correct geometries of gusset plate, nonlinear material behavior, initial imperfection of the gusset plates, mesh density for solution convergence, assumptions used for modeling the rivets, second-order deformation, and appropriate boundary conditions. This methodology will be employed to model several joint subassemblages with different geometries and loading profiles for parametric studies which will be discussed in Chapters 4 and 5. Joint U10 of the I-35W Bridge was used to develop the method and the results were verified against Ocel and Wright [2008]'s analytical results.

Verification of the modeling method was also dine using Whitmore's experiments.

3.2 General FE Model Description and Modeling Process

The FE model building method started with a Computer Aided Design (CAD) drawings of the truss joints, which were developed from original shop and as-built drawings. The original drawing were typically hand drawn, blurred or smeared, and some interpretation was required. Information such as gusset plate thickness, rivet pattern, splice thickness, connected member dimensions, and layout of additional wind gusset plates is important to accurately re-build the gusset plate joint geometry. In all cases it is ensured that all members were directed to a single work point and each rivet group was taken to be symmetric about the center line of connected member. Some minor assumptions were necessary such as spacing and edge distance of fasteners, dimensions of splice plates or additional plates, and sections of built-up member. Once the CAD drawing of each joint was completed, the coordinates of the geometry were exported to a text file and input as *KEY* points of the geometry in ANSYS. This allowed the joint geometry to be generated accurately and efficiently. Geometry modification and model manipulation was then conducted in the ANSYS input file rather than using the graphical user interface (GUI). The input file approach has several advantages, including flexibility for modification and maintenance, small and portable file size, compatibility to access parallel computation and batch file scripts, and feasibility to be controlled and manipulated through external programs, such as *Matlab*.

3.2.1 Joint Subassemblage Model and Boundary Conditions

Two joint subssemably types were considered to simplify the modeling of gusset plate joint in steel truss bridges. The first type modeled joint subassemblages including gusset plates, splice plates, wind gusset plates, connected members covered by gusset plates and short extensions of connected members beyond gusset plates approximately two times the depth of member section. By St. Venant's principle, this arrangement allows the truss members

to develop reasonable stress distributions over the shelled gross section before intersecting the gusset plate. The whole subassemblage model is modeled using shell elements. Surface pressure corresponding to the direction of member axial force was applied on the edges of the shell elements at the end of the short member extension. The pressure was applied normal to the connected member section even when the deformation is large. This physical problem can be solved as long as applied loads are in equilibrium. However, to avoid numerical rigid body motion in the FEA, several nodes of the shell elements on the short member extension were restrained against translation in all directions except the direction parallel to the applied pressure, i.e., the member's longitudinal direction. The results were examined to determine if there were stress concentrations around the restrained nodes, and if the sum of reaction forces on the restrained nodes maintained equilibrium. The boundary condition at the short extension end of a truss member for this model type is shown in the left of Figure 3.1.

The second type of subassemblage model also consisted of gusset plates, splice plates, wind gusset plates, connected members covered by gusset plates and short extensions of connected members beyond gusset plates approximately two times the depth of member section using shell elements and extends the connected member to the next joint of steel truss bridge using beam element. The axial forces are applied to the end point of the extended truss members and the translational and rotational Degrees of Freedom (DOFs) other than the axial direction are restrained at this end node as shown on the right side if Figure 3.1. Figure 3.2 shows this type of subassemblage for an entire joint. The sum of the reaction forces from all restrained DOFs should be zero to ensure global equilibrium. The connection of the shell elements of short member extension and the beam element of the member extension is made by constraining the six DOFs of shell element nodes at the edge of short extension to the beam element node at the center of the member section.

Both methods showed good agreement in terms of stress along the horizontal critical section when compared with results from Ocel and Wright [2008]. However, because large deformation and buckling of the gusset plate may be affected by the stiffness of the truss members, the latter method was used for modeling of all truss joints considered in this research.

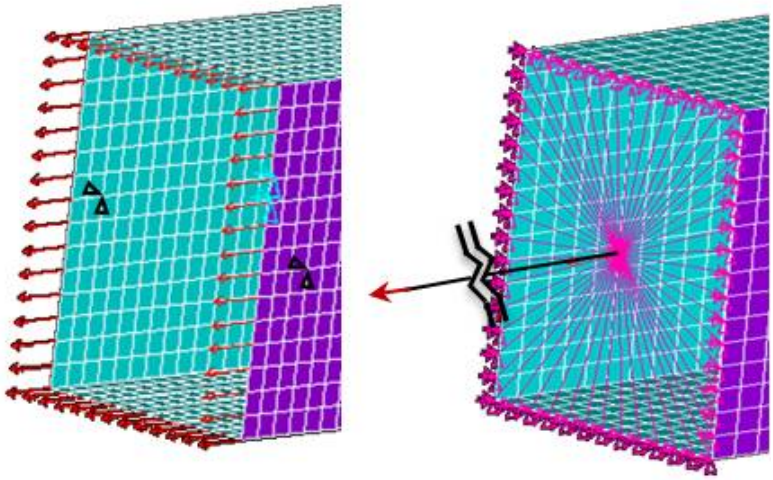

Figure 3.1: Two ways of applying boundary conditions, from left to right, surface pressure applied on the member section and force applied on the far-end joint

3.2.2 Elements Types

The SHELL181 element was used to model major parts of the joint subassemblages, including the gusset plates, splice plates, wind gusset plates, and the short extension of the members connected to the gusset plates. The rest of the connected members, extending to the joint adjacent to the one being modeled, were modeled with as shown in Figure 3.2. As described above, the DOFs of shell element at the edge of the short extension of the connected member are constrained to the node of the beam element at the center of the member section. The node on the beam element is regarded as master node. The model of the I-35W Bridge Joint U10 used for model development is shown in Figure 3.2.

The SHELL 181 element is a 4-node element with six degrees of freedom at each node, translations in the x, y, and z directions, and rotations about the x, y, and z-axes. The 1x1 in-plane reduced integration scheme is used in the element domain with hourglass control. THE SHELL 181 element allows several layers through the the thickness for modeling laminated composite material but only a single layer is considered here. Five integration

points through the thickness are used to calculate the stress at different locations through the thickness. The integration points through the thickness are located at the top and bottom surface and the quarter and mid the thickness to account for nonlinear bending in large deformation analysis. The SHELL 181 element accounts for shear between layers using Mindlin-Reissner shell theory.

BEAM188 is a two-node quadratic element based on Timoshenko beam theory to account for shear deformation. Each node have six degrees of freedom, translations in the x, y, and z directions, and rotations about the x, y, and z-axes. A third point is required to define the orientation of beam section.

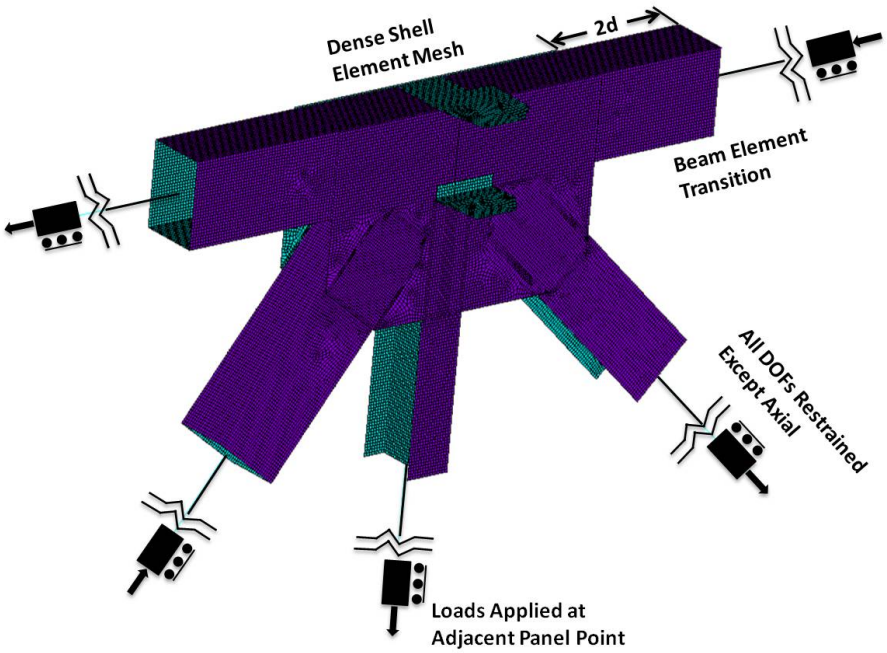

Figure 3.2: Pilot FE model of Joint U10 gusset plate connection

3.2.3 Material Model

The FE stress analyses of the gusset plate joint subassemblage employed an elastic-plastic material model. The plastic response of steel was modeled using the Von Mises yield cri-

terion, the bilinear kinematic hardening, and an associated flow rule. The plastic tangent modulus for the uniaxial stress-strain behavior was 3% of the elastic modulus. This bi-linear material model is consistent with the material coupon test reported by Ocel and Wright [2008] for the investigation of the I-35W Bridge Joint U10. Note that loading in the analyses will be monotonic, resulting in little difference in behavior between kinematic and isotropic hardening.

3.2.4 Large Deformation Formulation

A large deformation formulation was employed for the ANSYS Finite Element Analysis. Specifically an updated Lagrangian was employed for element formulation which true (Cauchy) stresses and logarithmic (Hencky) strains were defined and shown for output results in rotated element coordination system.

Nweton-Raphon algorithm with enhanced converge approach, line search, was used to solve large deformation nonlinear problems.

3.2.5 Element Size for Finite Element Analysis

The stress distributions in elastic range are used to study the mesh convergence of FEA to provide a proper mesh size for joint subassemblage modeling methodology. The XY shear stress distribution on the horizontal section, section A-A in Figure 3.8, and the X normal stress distribution along the chord splice, section B-B in Figure 3.8, were studied because those two stress distributions significantly dominate the stress magnitude in these sections. Stress distributions with mesh size 2.5", 1.5", 1.25",1.0", 0.75",0.5", and 0.25" in width are plotted in Figure 3.3 and 3.4 respectively. FEA stress distributions on the sections are sampled every 0.125" where the stress is the interpolation from adjacent nodes. The stress at nodes is the average of neighboring Gaussian integral points which are located at the middle of shell element for reduced integration. Since reduced integration is used to calculate the stiffness matrix in the weak form of governing equation, as the mesh is refined,

the system becomes stiffer and approaches to the exact solution. Therefore, the stress is expected to be higher in analyses using finer mesh.

For the XY shear stress distribution on the horizontal section, Figure 3.3 shows that the apparent local kinks decrease as the mesh size was reduced below 0.5" in width. For the X normal stress distribution on the chord splice location, Figure 3.4 shows that the stress kinks decrease when the mesh size was reduced below 1.25". As the mesh refinement continues, the X normal stress is increased gradually. The kinks in the stress distributions are resulted from the load discontinuity from the model of rivets and will be explained in the next section. The stress appears to converge quickly with mesh refinement for both XY shear stress and X normal stress, indicating the coarse mesh size used in the beginning of the refinement study is enough for studying the stress distributions. The 0.5" mesh size, which shows reasonably smooth stress distributions for both the XY shear and X direction normal stress distribution, is used for shell elements in the gusset plate joint modeling method.

3.2.6 Initial Imperfection of Gusset Plates

To initiate the gusset plates imperfection for buckling failure mode, a small out-of-plane deformed shape is applied to the gusset plates in the out-of-plane direction prior to conduct large deformation analysis. The small out-of-plane deformed shape is generated by a combination of the first five elastic buckling modes and applies the maximum out-of-plane displacement as $\frac{1}{500}$ of gusset plate thickness for the combined deformed shape. The elastic buckling shapes are attained by using eigenvalue buckling analysis. However, if the gusset plate joint has unbalanced load from attached floor beam at one side of the gusset plate, the imperfect disturbance can be attained without elastic buckling analysis. The unbalanced floor beam load in the out-of-plane direction is enough to trigger the gusset plate buckling failure.

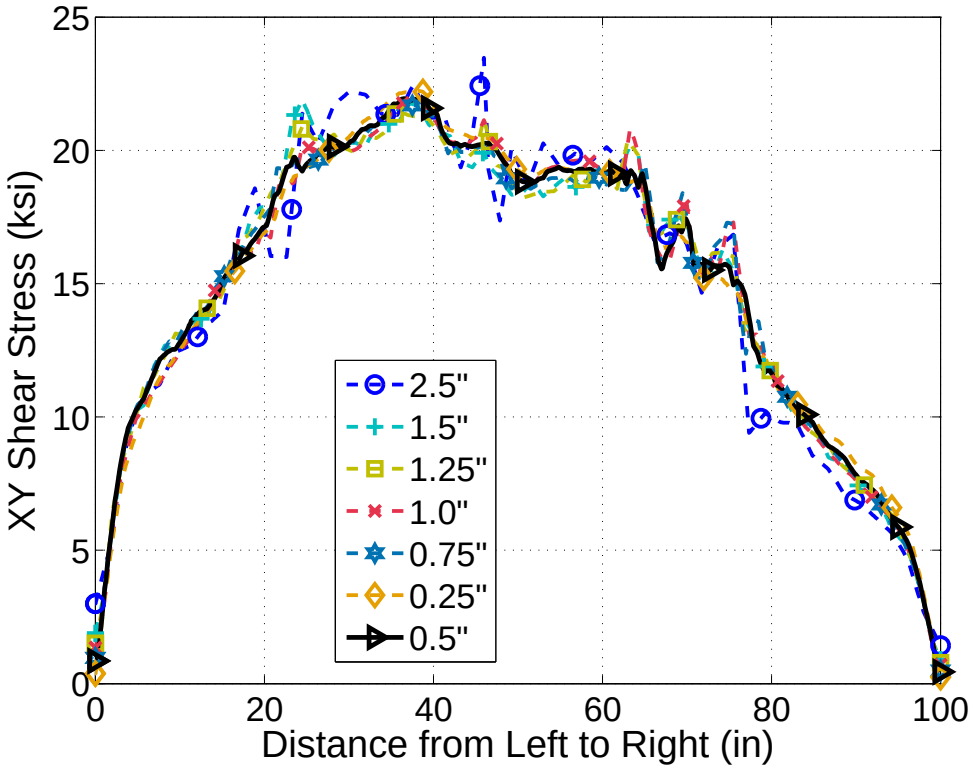

Figure 3.3: Mesh convergence study for XY shear stress along the horizontal section

3.2.7 Modeling of Rivet Connectors

All rivets were modeled as rigid connectors and rivet holes were not modeled. Kay [2011] verified that methods of modeling connectors do not significantly influence the stress generated on gusset plates away from the fasteners. Therefore, it is acceptable to just use rigid connector instead of modeling rivet's shear behaviors and interaction between rivet holes. The nodes for shell elements were deliberately deployed at the location of the rivets when the geometry was built. In other words, the location of the rivet in the gusset plates, truss members, splice plates, and any other connected plates had the same in-plane coordinates but different coordinates in the out-of-plane direction. All six DOFs of the connected nodes in the plates were constrained to one node and formed a rigid link between the plates. If a rivet connects several layers of plates, the nodes at each layer shall be included in the

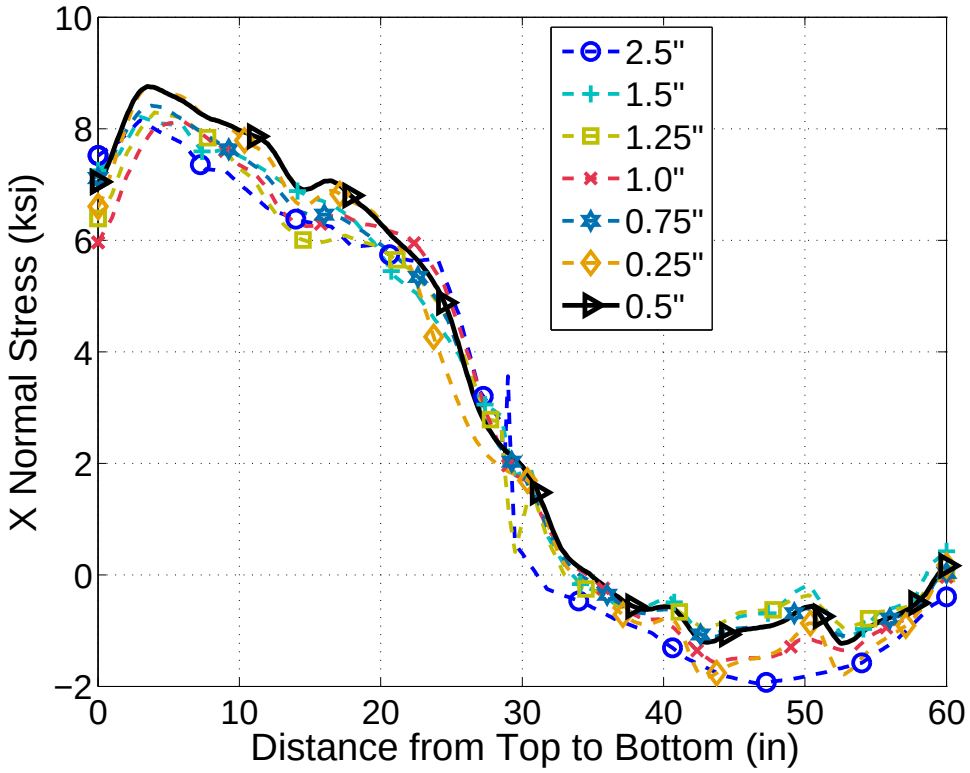

Figure 3.4: Mesh convergence study for X normal stress along the chord splice section

constraint formulation. No elements were used to model rivets, only mathematical DOFs constraints. Because the forces are transmitted between modeled steel plates, i.e. gusset plates and connected member, through signal node, stress discontinuity is observed near the rivet location. Between different plates, i.e., the gusset plates and truss members, no contact effect was modeled so that the unrealistic phenomenon of the edge of one plate moving through an adjacent plate was possible. However, this phenomenon only occurs after large deformations of yielding and buckling of the gusset plate have already initiated. Thus, it is likely to have limited impact and lead to slightly conservative estimates of buckling capacity.

3.3 Validation of the Modeling Method

The method used to simulate Joint U10 was validated with the results from previous experiments and analytical studies. The elastic stress distribution from the experiments performed by Whitmore [1952] and the analytical analysis results from the complete I-35W Bridge model developed by Ocel and Wright [2008] were used for validation. Whitmore's findings of the elastic stress distribution in gusset plates, and the resulting method of calculating the maximum stress in the gusset plates were discussed in Chapter 2. His experimental specimen was modeled in ANSYS using the method described above.

The test specimen used by Whitmore [1952] was a quarter-scale Warren-type bridge truss gusset plate joint model using two 66 in. $\times$ 50 in. rectangular plates as gusset plates. The gusset plate thickness was scaled down to $\frac{1}{8}$ in.. A low modulus of elasticity but high strength aluminum alloy 61-ST was used so that the strains would be larger and more easily observed while keeping the yield stress high to represent a similar strength to structural steel. This aluminum alloy was used for whole joints including the members, gusset plates and pin-fasteners. The material properties were given as follows: modulus of elasticity is 10,000 ksi, Poisson's ratio is 0.33, yield strength is 39 ksi, and ultimate tension strength is 45 ksi.

As described in Chapter 2, the test specimen was simplified relative to the prototype to provide clearer indications of the stresses. The hanger was assumed to be a near zero-force member and was not modeled in the physical experiment. The chord was continuous without a splice at the joint to eliminate any additional stresses generated at the splice. The diagonals were arranged at 45° and 53.60° to the horizontal chord and were modeled by two solid rectangular plates to provide a sufficient capacity for applied axial load. The geometry of the joint was given in the Figure 2.1. All of these simplifications were also applied to the analytical model developed here.

The contours plotted for different stresses were compared between the FE analysis results and Whitmore's experiment. They are shown in Figures 3.5 to 3.7. Whitmore's experimental results are shown by solid lines and the FE analysis results are shown by the gray-scale contours. Figure 3.5 shows the first principal stress in tension, Figure 3.6 shows the third

principal stress in compression and Figure 3.7 shows the stress intensity and the maximum shear stress. It should be noted that the FE analysis results in Figure 3.7 show the stress intensity given by $|\sigma_1^p - \sigma_3^p|$, where σ_1^p is the first principal stress and σ_3^p is the third principal stress, whereas the results from Whitmore [1952] are expressed by the maximum shear stress, τ, which is given by $\frac{1}{2}|\sigma_1^p - \sigma_3^p|$. Therefore, the magnitude of the FE analysis contour should be compared with two times the magnitude of the contour from Whitmore [1952]. The three figures show reasonable agreement between the value of contours and the locations of the maximum stress. The lower stress contours ranging from 1 ksi to 2.5 ksi in all three figures were almost coincident with the experimental results, but the higher stresses show some variation between the FE analysis results and experimental results. As shown, the FE analysis results predict larger localized stresses than the experimental results indicate. One reason for this is that the FE analysis results show the stresses in much greater detail than what Whitmore [1952] was able to produce using a mix of limited strain gages and other methods. This results in the FE analysis showing stress concentrations near rivets that would have been very difficult to detect using the technology available at the time of the experiments. It is also acknowledged that modeling the rivets with rigid nodal constraints probably increased the stress concentration around the rivets. However, given the limitations of the experimental data and the reasonable agreement with the FE analysis results, the FE modeling method seems appropriate for determining the stress magnitude and distribution away from rivets.

The FE modeling method was also validated via comparison with the finite element analysis conducted by Ocel and Wright [2008]. Their investigation of the collapse of the I-35W Bridge over the Mississippi River in Minnesota was also discussed in Chapter 2. Since the detailed model of Joint U10 was embedded in the global model, it is assumed that Ocel and Wright [2008] had a more accurate representation of the boundary conditions for the joint than the subassemablage method that will be used here and was described above. Therefore, the distribution of normal stress, shear stress and equivalent stress (Von Mises stress) with the loads at the time of collapse were compared at the critical sections A-A and B-B, which are shown in Figure 3.8. The comparison of those stresses between the Joint U10

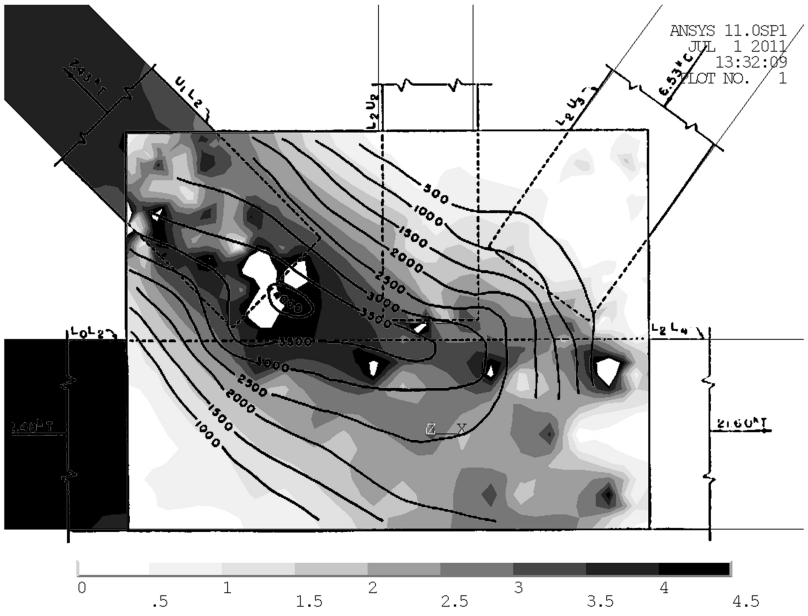

Figure 3.5: Comparison of tension principal stress with experimental results from Whitmore [1952]

model developed here and the results from Ocel and Wright [2008] are given in Figures 3.9 and 3.10. Both figures show a good agreement in the stress distribution along the critical sections.

In summary, the results of the validation of the developed joint subassemblage FE modeling method using pilot Joint U10 shows the method produces results that are in good agreement with both experimental and analytical results from the literature. This efficient and reliable modeling method is employed in the next chapters to conduct the parametric studies to understand the complicated behavior of steel truss bridge joints and the stress distribution in gusset plates.

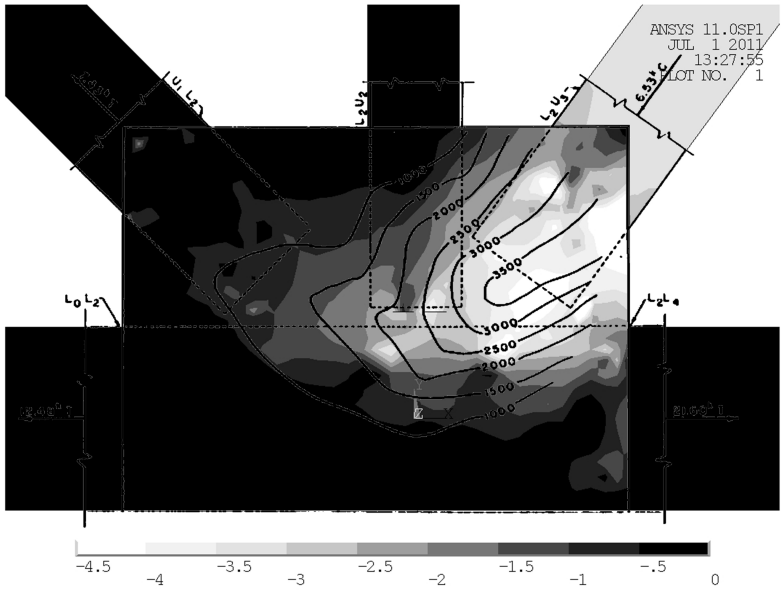

Figure 3.6: Comparison of compression principal stress with experimental results from Whitmore [1952]

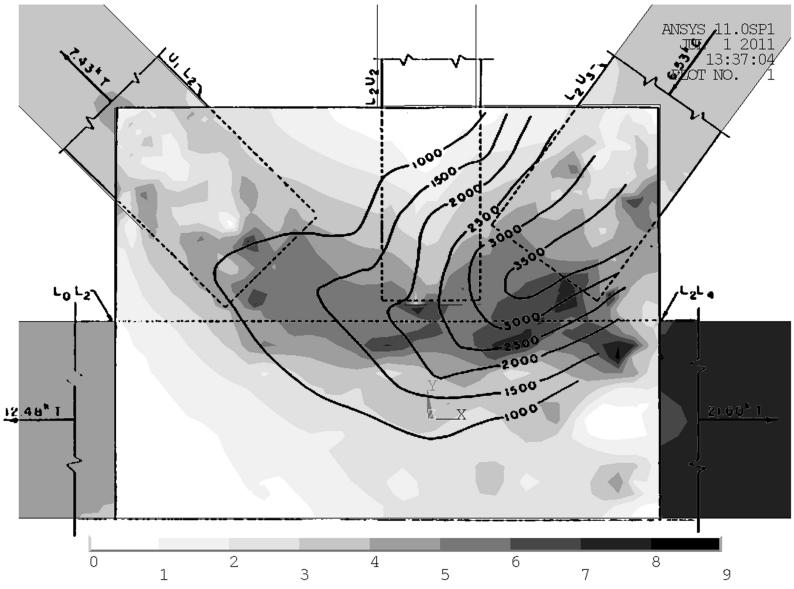

Figure 3.7: Comparison of shear intensity, which is two times of the maximum shear stress, with the maximum shear stress of Whitmore [1952] experiment

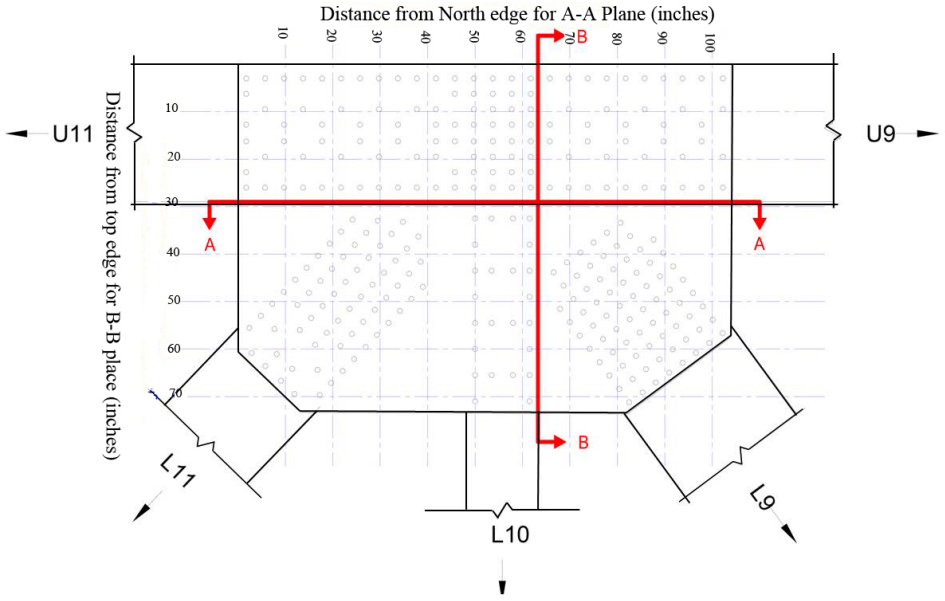

Figure 3.8: The schematic of the horizontal and vertical critical section used to validate the developing subassemablange model with results from Ocel and Wright [2008]

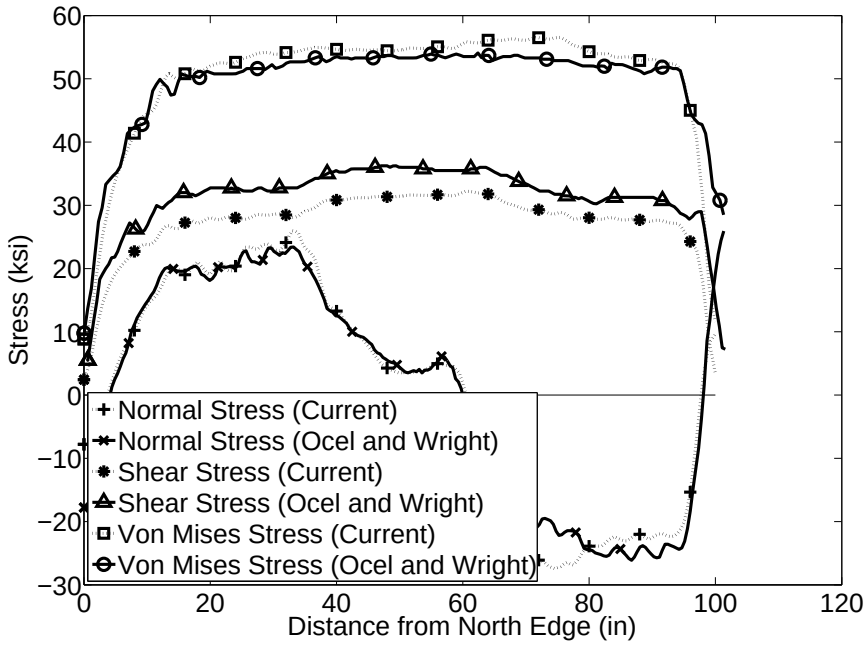

Figure 3.9: Comparison of three stress distribution along horizontal section A-A between current methodology and global FEA by Ocel and Wright (2008).

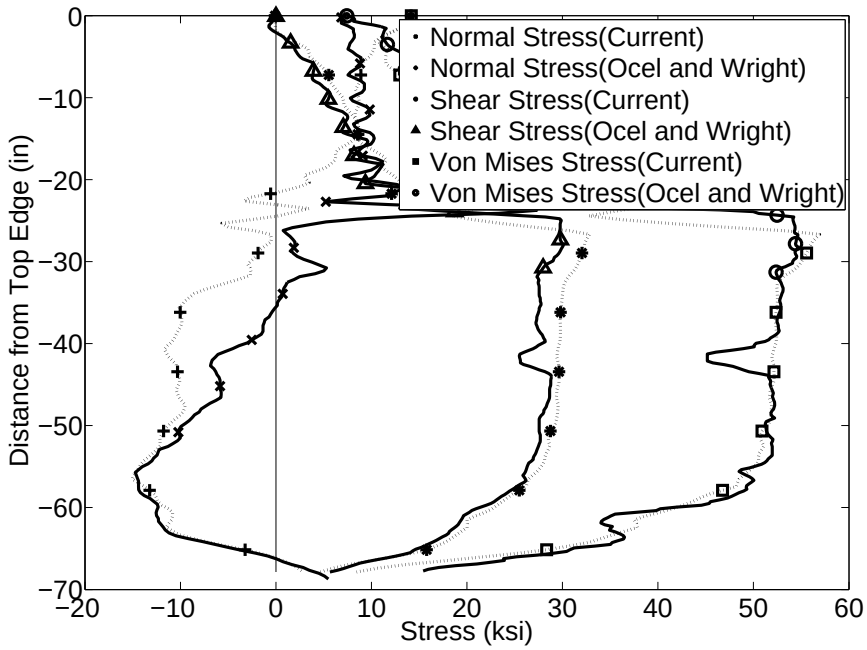

Figure 3.10: Comparison of three stress distribution along vertical section B-B between current methodology and global FEA by Ocel and Wright (2008)

Chapter 4

CHARACTERISTICS OF SELECTED TRUSS BRIDGE JOINTS

The method of building joint subassemblage FE models developed in Chapter 3 was used to model several critical joints from steel truss bridges in Washington State for parametric studies. The parameters considered important with respect to joint behavior are joint geometry, load distribution, gusset plate thickness, and location of chord splices. Therefore, these selected joints for parametric studies shall include the variation of possible load distributions at joints, i.e. the maximum corresponding loading demands on the joints, the variation of geometric configuration, i.e., joints from Warren or Pratt truss bridges, the variation of thickness buckling, i.e. elastic or inelastic gusset plate buckling, and the variation of chord splice location, i.e. the influence of interaction between normal and shear stress on gusset plates. Several joints were chosen from selected steel truss bridges in Washington State and the collapsed I-35W Bridge. The selected joints also had relative high demand-to-capacity ratios as evaluated using the FHWA guide. Three steel truss bridges selected by Washington State Department of Transportation (WSDOT) were BR. 90/134N, BR. 31/36, and BR. 101/217. In addition, to conduct the FEA for these specific joints, the axial loads are necessary information. In this chapter, the characteristics of these steel truss bridges and selected joints are introduced and the fundamental bridge structural analysis for the joint load demands will be discussed.

4.1 Fundamental Bridge Structural Analysis for Selected Bridges

4.1.1 Global Analysis of Steel Truss Bridges

For most bridges, the design member loads for truss bridges had been specified on the shop drawings. However, these member loads are enveloped loads, which are not in equilibrium

and can't be used directly for FE joint subassemblage model. To acquire axial member loads in equilibrium at a joint, a two-dimensional bridge structural analysis was conducted using SAP2000 (CSI 2008). These analyses were conducted and documented by Olson [2010]. Models in SAP2000 were developed considering both pin-ended truss members and fully restrained truss members. The resulting member axial forces from the two model types were then compared with each other and with the enveloped member loads given on the original shop drawings. It was determined that the two-dimensional plane truss model with pin-ended members was adequate for use in determining the member loads in equilibrium at joints.

The bridges were analyzed for dead load and live load. Unit weights for the structural steel and the concrete used in the dead load determination were $490(\frac{lb}{ft^3})$and $150(\frac{lb}{ft^3})$ respectively. The dead loads from decks and other super structural elements were calculated and distributed to the proper joints. The live load used in the analysis was the HS20 truck and lane load, which is described in the WSDOT Bridge Design Manual LRFD, WSDOT [2010]. The HS20 truck load consists of three point loads representing a three-axle truck with the location of the trailing axle being variable so that it will produce the largest possible loads on the bridge. For each truss member, the HS20 truck is positioned to cause the maximum axial load. The HS20 lane load consists of a distributed load of 640 $(\frac{lb}{ft})$ with two different point loads, only one of which is applied for each truss bridge member. The first point load, known as the moment rider, is an 18 kip load associated with moments and will be carried by chord members, and the second point load, known as the shear rider, is a 26 kip load associated with shear and will be carried by diagonal members. The distributed load and one appropriate point load are positioned along the bridge to cause the maximum axial force in a particular truss member. The larger live load between the HS20 truck load, and uniform land load with a point load will be used to develop concurrent loading cases for FE subassemblage joints. Three selected Washington bridges were analyzed to acquire loading distributions at joints. The characteristics of selected steel truss bridges and joints will be described in the next section.

4.1.2 Loading Distribution on the Selected Joints

The concurrent load distributions used in this study were calculated from a combination of factored dead load and factored live load based on three different load rating specifications. The considered specifications were: 1) the Load and Resistance Factor Rating (LRFR) described in the Manual for Bridge Evaluation (MBE) published by AASHTO [2008], referred to as AASHTO-LRFR; 2) the Load Factor Rating (LFR) also described in the MBE in AASHTO [2008], referred to as AASHTO-LFR; and 3) the Load and Resistance Factor Rating (LRFR) described in the WSDOT Bridge Design Manual (BDM) WSDOT [2010], referred to as WSDOT-LFR. These three load rating equations were given in Eqs. 4.1, 4.2, and 4.3. To find the factored load combinations acting on the selected joints, the Rating Factor (RF) in Eqs. 4.1, 4.2, and 4.3 is assumed equal to one that postulates the demands equals to the capacity, and calculate the demands in different limit states using factors tabulated in Table 4.1. The use of unfactored deal load is calculated from decks and other super structures, and the use of unfactored live load considering the larger one of HS20 truck load and land load with one point load as described in previous section.

- For the AASHTO-LRFR, the rating factor is equated as:

$$RF_{AASHTO\_LRFR} = \frac{\phi_c \phi_s \phi R_n - \gamma_D DC - \gamma_{DW} DW}{\gamma_{LL}(LL + IM)} \tag{4.1}$$

  where ϕ_c is the condition factor, ϕ_s is the system factor, R_n is nominal resistance of a member, ϕ is the LRFD resistance factor, DC is the dead load effect due to structural components and attachment , DW is the dead load effect due to wearing surface and utilities, γ is the load factor for each particular load effect, and IM is the dynamic load allowance.

- For the AASHTO-LFR, rating factor is calculated as:

$$RF_{AASHTO\_LRF} = \frac{C - A_1 D}{A_2 L(1 + I)} \tag{4.2}$$

where I is the live load impact factor given by $I = \frac{50}{125+L}$, C is capacity of member, A_1 is the factor for dead load, A_2 is the factor for live load, D is the dead load effect on the member, and L is the live load effect.

- For te WSDOT-LFR, rating factor equation is:

$$RF_{WSDOT\_LRFR} = \frac{\phi R_n - \gamma_D D}{\gamma_L L(1+I)} \tag{4.3}$$

where ϕ is the resistance factor per AASHTO [1989], R_n is nominal resistance, γ_D and γ_L is load factor for dead load and live load respectively, D is the dead load, L is the live load, and I is dynamic impact factor

Table 4.1 shows the different factors for dead load, live load and dynamic impact factor used in these load rating evaluations. For AASHTO-LRFR, two load combinations for different limit states were considered. The strength I load combination indicates basic load combination relating to the normal vehicular use of the bridge without wind loading. The service II load combination is intended to control yielding of steel structure and slip of slip-critical connection due to vehicular live load under normal service. For AASHTO-LFR the strength limit state is considered because AASHTO-LFR uses the maximum load for the load combination. The inventory and operating load refer to the level of design live load. The inventory load is the load that fully complies with the design load using the new specification and HL-93 loading. Therefore, the bridge has an adequate capacity for heavy vehicles no matter in AASHTO or State legal load level. The operating load level is the lower level load than inventory load. It allows the pass of heavy vehicles in AASHTO load level but not allow the heavier vehicles in State load level. The load combinations used in this analysis was conducted by Olson [2010].

For each joint, the number of different load case is equal to the number of members. Each load case was chosen to provide the maximum force in one of the member connected in the truss joint. To calculate the maximum concurrent load distributions for each member, the influence line for each connected member of a joint was plotted using SAP2000. The maximum live load position for one member can be determined from the influence line, and

Table 4.1: Load factor for three kinds of load rating methods

ASSHTO MBE-LRFR				
	StrengthI		ServiceII	
Load Factor	Inventory	Operating	Inventory	Operating
γ_{DC}	1.25	1.25	1.0	1.0
γ_{DW}	1.5	1.5	1.0	1.0
γ_{LL}	1.75	1.35	1.3	1.0
ASSHTO MBE-LFR				
Load Factor	Inventory		Operating	
A_1	1.3		1.3	
A_2	2.17		1.3	
WSDOT BDM-LRFR				
Load Factor				
γ_D	1.3			
γ_L	1.8			

the corresponding loads in other members can be calculated accordingly. Olson [2010] gives examples on how to calculate the various load distributions and the use of influence lines in the process. The calculated load distributions for different limit states and load rating methods for Washington bridge joints are tabulated in Tables 4.3 through 4.7. Due to the lack of original design information for the entire I-35W bridge, the five loading cases for the Joint U10 were calculated by increasing the load on each individual member one at a time by 20% in turns and then applying equilibrium to the joint to compute the corresponding loads for other members. The baseline for the member loads for Joint U10 was the load denoted the Stage 4 loading by Ocel and Wright [2008], which were the estimated loads

at the time of the collopse. This procedure created the load distributions that are smiliar to those developed by moving line loads on the WSDOT bridges. For Joints U3 and L5, there are only four members because of only four members in Pratt-type joint. Two load distributions were quite similiar in those four load distributions, so that only three cases were considered and are listed in Tables 4.6 and 4.7.

Table 4.2: Loading Case for Joint U10 (Kips)

Case No.	U9-U10	L9-U10	L10-U10	L11-U10	U11-U10
Case1	2379.81	-2525.44 [1]	514.67	2075.09	-652.62
Case2	2355.40	-2600.00	550.46	2107.23	-745.96
Case3	2079.40	-2360.85	566.89	1818.57	-652.62
Case4	2294.40	-2391.49	367.94	2133.94	-696.62
Case5	1969.40	-2300.34	493.22	1855.60	-768.32

[1] Minus sign means compression force

Table 4.3: WSDOT-BDM-LRFR Loading Case for Joint L2 (Kips)

Case No.	L3-L2	U3-L2	U2-L2	U1-L2	L1-L2	Floor Beam
Case1	747.44	-142.75	43.08	272.92	467.20	125.30
Case2	765.21	-133.58	44.82	329.13	450.88	174.54
Case3	779.04	-126.42	46.17	321.69	474.86	176.23
Case4	719.19	-192.99	39.01	288.11	399.07	92.28
Case5	780.92	-173.38	44.12	305.53	458.54	125.40

Table 4.4: WSDOT-BDM-LRFR Loading Case for Joint L9 (Kips)

Case No.	L8-L9	U8-L9	U9-L9	U10-L9	L10-L9
Case1	-579.12	448.39	-83.68	-449.26	0.00
Case2	-540.42	457.00	-135.70	-381.91	0.00
Case3	-516.56	450.77	-150.31	-351.75	0.00
Case4	-557.63	434.24	-83.97	-430.37	0.00

Table 4.5: AASHTO-MBE-ServiceII Loading Case for Joint L1 (Kips)

Case No.	L0-L1	U0-L1	U1-L1	U2-L1	L2-L1
Case1	0.00	407.33	-181.95	-125.07	379.71
Case2	0.00	278.14	-187.73	4.83	195.08
Case3	0.00	353.76	-67.56	-233.76	418.31
Case4	0.00	372.40	-82.83	-229.33	429.08

Table 4.6: AASHTO-MBE-ServiceII Loading Case for Joint U3 (Kips)

Case No.	U2-U3	L2-U3	L3-U3	U4-U3	Floor Beam
Case1	-465.33	141.47	-156.56	554.20	-46.93
Case2	-356.34	183.36	-197.28	471.60	-55.19
Case3	-368.48	148.91	-217.26	462.06	-101.87

4.2 Introduction of Selected Washington Bridges

4.2.1 Bridge 90/134N

Bridge BR 90-134N is a 220 ft. long single span Warren-type through-truss bridge carrying four lanes over the Cle Elum River; a photo of which can be seen in Figure 4.1. The shop drawings for BR 90-134N are dated 1949, and ASTM A7 steel was specified for the members

Table 4.7: WSDOT-BDM-LRFR Loading Case for Joint L5 (Kips)

Case No.	L4-L5	U4-L5	U5-L5	L6-L5
Case1	-804.74	209.39	-259.22	-679.45
Case2	-713.52	245.45	-290.67	-571.03
Case3	-803.05	200.54	-250.12	-682.41

and ASTM A94-46 steel (ASTM 1946) with a specified yield stress of 45 ksi was specified for the gusset plates and splice plates. Figure 4.2 shows the naming convention used for each of the nodes on the bridge. At the support node L0, the design drawings show a pinned support and at support node L8 there is a roller support.

Figure 4.1: Photo of BR 90/134N over Cle Elum River

Along the lower chords of the two identical trusses span floor beams which support the bridge deck and vehicular traffic. These floor beams frame directly into the joints of the main bridge trusses and so dead and live loads from the bridge deck are modeled as point loads at the bridge panel points. Similarly, along the top chord of the truss, wind bracing

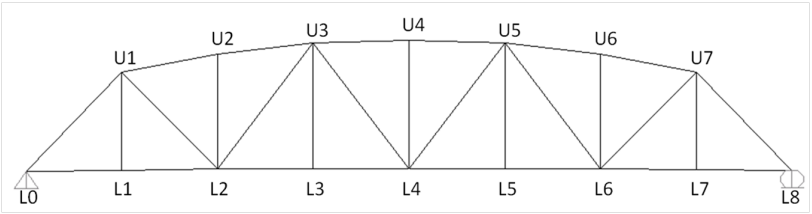

Figure 4.2: Schematic of BR 90/134N

frames into the panel points and dead loads associated with these members are modeled as point loads at the nodes. See Olson [2010] for additional details.

4.2.2 Bridge 31/36

Bridge BR 31-36 is an Warren-type deck-truss bridge that has two cantilever spans supporting a simple drop-in span in the middle. The bridge is 524 ft. long and has two main support piers approximately 142 ft. measured from each end of the bridge, as seen in Figure 4.3. BR 31-36 was built in 1950 and all steel was specified as ASTM A7 which was taken to be ASTM A7-39 (ASTM 1939) with a specified yield stress of 33 ksi, Brockenbrough [2002]. Figure 4.4 shows the naming convention for the nodes; however, in the interest of space only half of the bridge is shown.

The design drawings indicate a pin support at node L7 and a roller support at node L0. Boundary conditions for this bridge were assumed to be symmetric, so similar support conditions were assigned to the corresponding nodes on the remaining half of the bridge. Sliding pin assemblies are present between nodes U10-U11 and nodes L9-L10 to allow for thermal movement of the drop-in simple span. These pin assemblies ensure no axial force is transmitted along these members, effectively making them zero-force members. To model these sliding pin assemblies, axial force releases were assigned at the ends of the frame members where each assembly is located.

The roadway is carried by floor beams that span across the two top chords of the identical main bridge trusses. These floor beams rest directly on top of the chord at each panel point

Figure 4.3: Photo of BR 31/36 over Metalin Falls River

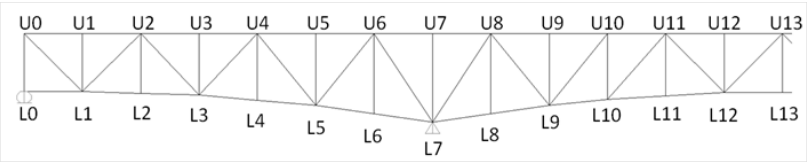

Figure 4.4: Schematic of BR 31/36

and so dead and live loads attributed to the road deck are modeled as point loads at the nodes. Dead loads associated with wind bracing and other structural elements that act along the bottom chord are also modeled as point loads at their corresponding nodes. See Olson [2010] for additional details.

4.2.3 Bridge 101/217

Bridge BR 101-27 is a Pratt-type deck-truss bridge with two cantilever spans that support a simple drop-in span in the middle. It is 392 ft. long with two main support piers approximately 71 ft. measured from each end of the bridge. Bridge 101-217 was built in 1931 and

all steel was specified as "Structural O.H. Steel" on the drawings, which stands for open hearth steel, and was taken to be ASTM A7 (ASTM 1924) with a specified yield stress of 30 ksi given the 1930 vintage. Figure 4.5 shows a photograph of the bridge and Figure 4.6 shows a schematic of half with the naming convention for the nodes. Note that the bridge is symmetric about the center of the span.

Figure 4.5: Photo of BR 101/217 over Hor River

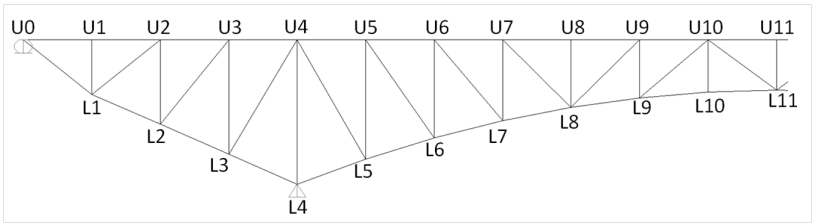

Figure 4.6: Schematic of BR 101/217

A pin support was assigned to node L4 and a roller support was assigned to node U0 consistent with the drawings. Boundary conditions were assumed to be symmetric, so

similar support types were assigned to the support nodes for the other half of the bridge. Similar to BR 31-36, BR 104-217 has a drop-in simple span that requires the need for an expansion joint. This joint is accommodated by sliding pin assemblies, as described above. These assemblies are located on the members spanning between nodes L8-L9 and U9-U10. Loads from the road deck are transferred from floor beams spanning between the main trusses to the panel points along the top chord and are modeled as point loads at the bridge nodes. Dead loads along the bottom chord attributed to wind bracing or other structural members are also modeled as point loads at the nodes.

4.3 Joints Selected for Detailed Modeling

At least one joint was selected from each selected bridge for detailed FE analysis. They were selected on the basis of unique geometry and relative large Whitmore stress on the gusset plate generated by at least one member as described in Olson [2010]. Whitmore section stresses were calculated for the factored loads at the Strength I Load Combination per the AASHTO [2008] Bridge Evaluation Manual. The strength I load combination indicates basic load combination relating to the normal vehicular use of the bridge such as live load, vehicular dynamic load,vehicular breaking, vehicular centrifugal force, and so forth but excludes wind loading. The characteristics of these selected gusset plate joints are discussed in the following section.

4.3.1 Joint L2 from BR 90/134N

From BR 90/134N, Joint L2 was selected for detailed analysis as it had somewhat large stresses at the Whitmore section associated with a chord member and a fairly common geometry. Joint L2, as it will be described herein, is a typical Warren-type gusset joint with two 1/2 in. thick gusset plates located at outer face of connected member shown in Figure 4.7. These gusset plates were specified as silicon steel and taken to be ASTM A94-46 steel (ASTM 1946), for which a specified yield stress of 45 ksi was assumed. Built-up box sections were used for both tension chords, L1-L2 and L3-L2, and tension and compression

diagonals respectively, U3-L2 and U1-L2. A built-up I section were used for the tension hanger, U2-L2. A floor beam was connected to the inner side gusset plate through a web angle connection and a wind gusset plate was attached to the bottom of chord members and also served as slice plate. The chord splice was not located at the work point and instead was shifted toward Joint L1. The other splice plate was attached on the top of the chord members so that the the top splice plate, two gusset plates and the bottom wind gusset plate formed the splice for the discontinuous chord members.

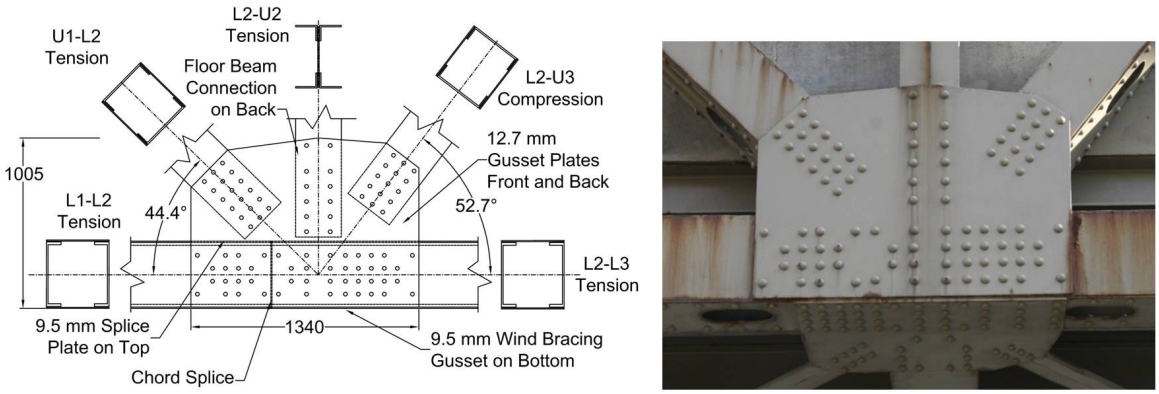

Figure 4.7: Joint L2 from BR90/134N

4.3.2 Joint L9 from BR 31/36

Joint L9 from BR 31-36, denoted Joint L9 here, was selected for detailed analysis as it had a relatively large stress of 13.9 ksi at the Whitmore section of member L8-L9 and a unique geometry as shown in Figure 4.8. This joint is at a hinge location in the truss and has a zero force chord member attached (L9-L10) with a large pin where secondary plates increase the bearing strength of the pin hole. Joint L9 has a unique chord member configuration (L8-L9) whose web was built up with a channel and a 1/2" thick plate attached to the channel as the outer layer of the chord web. The outer layer plate discontinued before it enters Joint L9, a 1/2" thick gusset plate was developed at the joint to connect the hanger and diagonals, and the outer layer plate and the gusset plate were spliced with an additional plate. The

configuration resembles to the monolith-type gusset plates illustrated by Yamamoto et al. [1985]. No additional top or bottom splice plates were attached. Since the flange and channel web of the chord member (L8-L9) was continuous through wind gusset area, the wind gusset does not provide any function as splice plates and the wind gusset is only attached to a small part on the bottom of chord member (L8-L9). The loaded chord is a compression member (L8-L9) and has a built-up box cross-section composed of channels and outer layer plates with riveted top and bottom plates. The compression diagonal (L9-U10) is also a built-up box section, the tension diagonal (L9-U8) is a built-up I-shape of angles and plate, and the vertical hanger is a rolled W12x53. All steel for this bridge was specified as ASTM A7-39(ASTM1939) with a specified yield stress of 33 ksi.

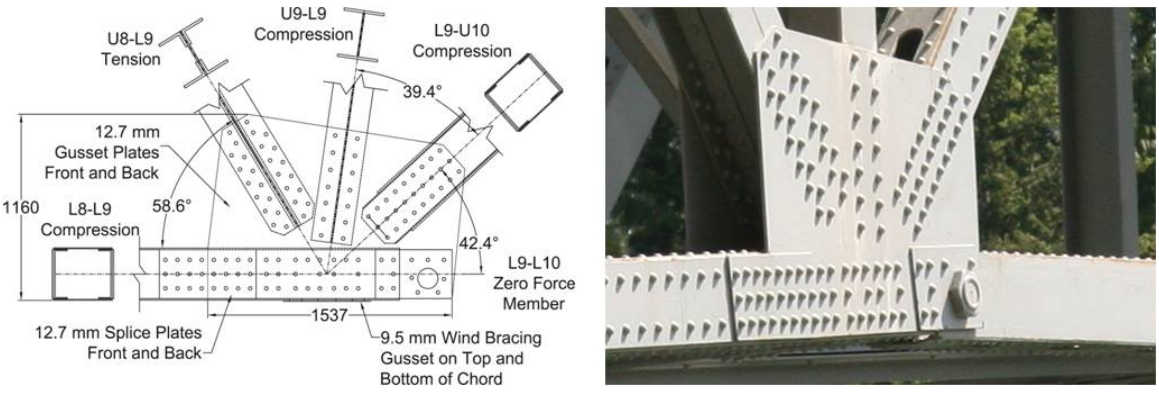

Figure 4.8: Joint L9 from BR31/36

4.3.3 Joint L1 from BR 31/36

Joint L1 from BR 31/36, denoted Joint L1 herein, was also selected for detailed analysis. Unlike Joint L9 which had unique geometry, Joint L1 is a typical Warren-type joint with a distinctive load distribution on connected members. The chord member (L0-L1) is a zero force member and the diagonal (L1-U2) had relative small loading, and has either a compression or tension member depending on the live load location. The chord is a built-up box section while the diagonals and the hanger were rolled I-shapes. The material used

in Joint L1 was the same as Joint L9 with a specified yield stress of 33 ksi. Two 3/8 in. thick main gusset plates and one 3/8 in. thick top splice plate connect the chords, which are spliced at the work point of the joint. A 5/16 in. thick wind gusset plate is also attached to the bottom of chord members as shown in Figure 4.9. Joint L1 was selected for modeling after a low rating factor in application of the Triage Evaluation Procedure (TEP) as discussed in Olson [2010].

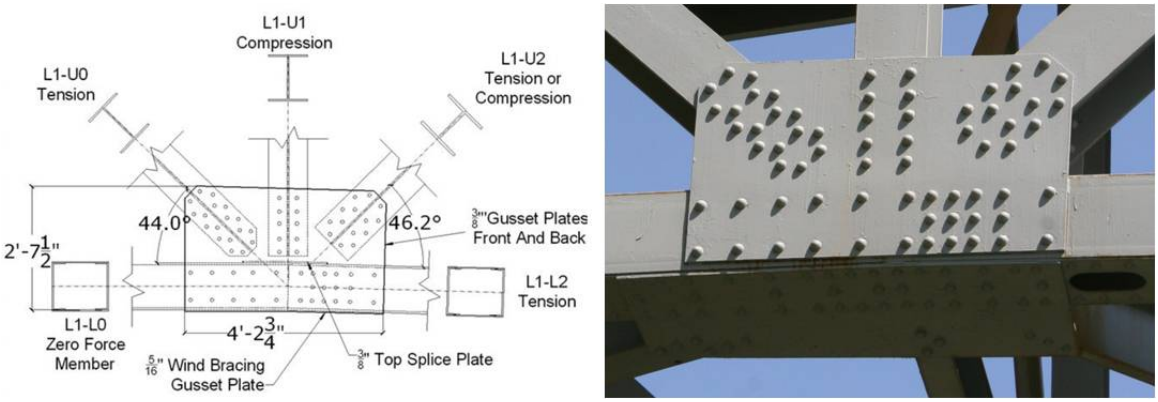

Figure 4.9: Joint L1 from BR31/36

4.3.4 Joint U3 from BR 101/217

Joint U3 was selected from BR 101/217, denoted by Joint U3 herein, due to its unique configuration. Joint U3 is a Pratt-type gusset plates with four members located between the inner face of chords and the outer face of diagonals or hanger, i.e. chord members and diagonal members were attached to outer and inner faces of gusset plates respectively. Both chords, U2-U3 and U4-U3, are in tension as well as the diagonal, L2-U3. The vertical hanger, U3-L3, is in compression and continues through whole gusset plate depth. The chords are built-up using channels back-to-back, separated by the depth of the diagonal, with lacing plates attached at the top and the bottom of the channel flanges. The 3/8" thick gusset plates are attached to inside the channel web as shown in Figure 4.10. The chord splice is offset from the work point of the joint toward Member U2-U3. Two 11/16"

thick splice plates are attached to the front of the channel webs and the inner side of gusset plate. A 3/8" thick plate is connected the flange of channels at the splice location. The diagonal and hanger are rolled I-shapes. The steel used for Joint U3 is ASTM A7-24(1924) with specified yield stress of 30 ksi.

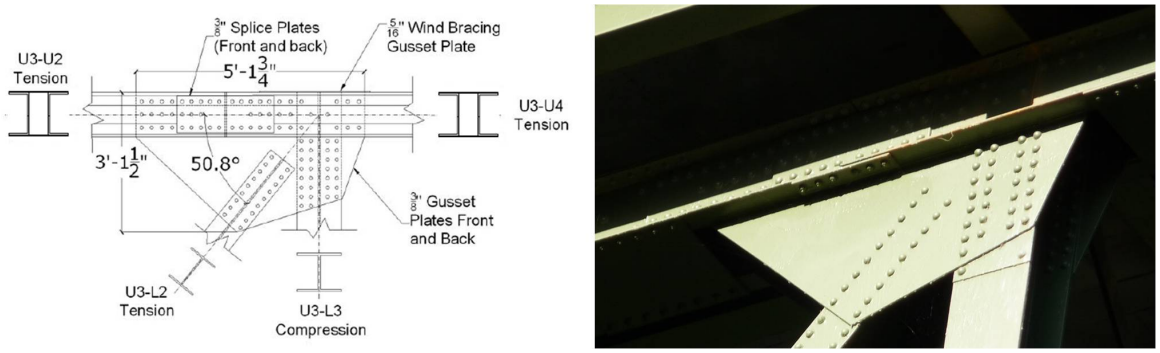

Figure 4.10: Joint U3 from BR 101/217

4.3.5 Joint L5 from BR 101/217

Joint L5 is similar to Joint U3, but is a lower chord connection form a Pratt truss and was selected from BR 101/217 because of relatively high stress at the Whitmore section and is denoted Joint L5 herein. The chords L4-L5 and L5-L6 are built up by angles, fill plates and web plates as shown in Figure 4.11. The chords are compression and are spliced at the center of the work point by 3/8 in. thick splice plates on the webs. One 3/8 in. thick wind gusset was attached to the bottom of chords across both built-up channels and one 3/8 in. strip connected to the top flange of each built-up channel, both working as splice plates. However, the splice connection was also designed to be "milled-to-bear", so the compression force could be transmitted by the direct bearing of the chords. The 3/8 in. thick main gusset was attached between the webs of the built-up chord members. The diagonal U5-L5 and the hanger U6-L5 are composed of rolled I-shapes and are in tension and compression respectively. The material used in Joint L5 was assumed to be ASTM A7-24(1924) with a specified yield stress of 30 ksi.

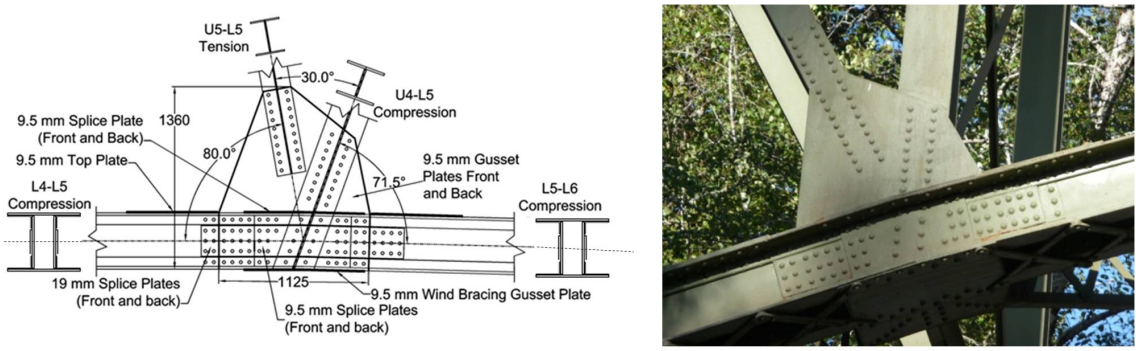

Figure 4.11: Joint L5 from BR 101/217

4.3.6 Joint U10 from BR 9340 (the I-35W Bridge)

Joint U10 from the collapsed I-35W Bridge, denoted Joint U10 herein, was also included in the parametric study and the geometry is shown in Figure 4.12. It was described in detail in Ocel and Wright [2008]. The joint is a Warren-type joint with five-finger geometry and 1/2 in. thick gusset plates with yield stress of 51.5 ksi. This joint was located near an inflection point in the bridge and had one chord in compression (U9-U10) and the other one in tension (U10-U11). Both chords were built-up box shapes and were spliced at the work point of the joint. The splice consisted of 1/2 in. thick plates attached inside the chords and 3/8 in. thick plate at the top and bottom of chords as well. The gusset plates provided additional strength for the chord splice. The compression diagonal (L9-U10) was a built-up box shape and the tension diagonal (U10-L11) and hanger (U10-L10) were rolled I-shapes. Two win gusset plate were used to connect lateral bracing. One wind gusset was jointed to the inside gusset plate by an angle attachment and the other wind gusset was riveted to the top of the chords. A floor beam rested on the top of the chords.

4.4 FE Models for Selected Joints

The FE models of selected joints were developed using the joint subassemblage modeling method described in Chapter 3. The FE models of these selected joints are illustrated and

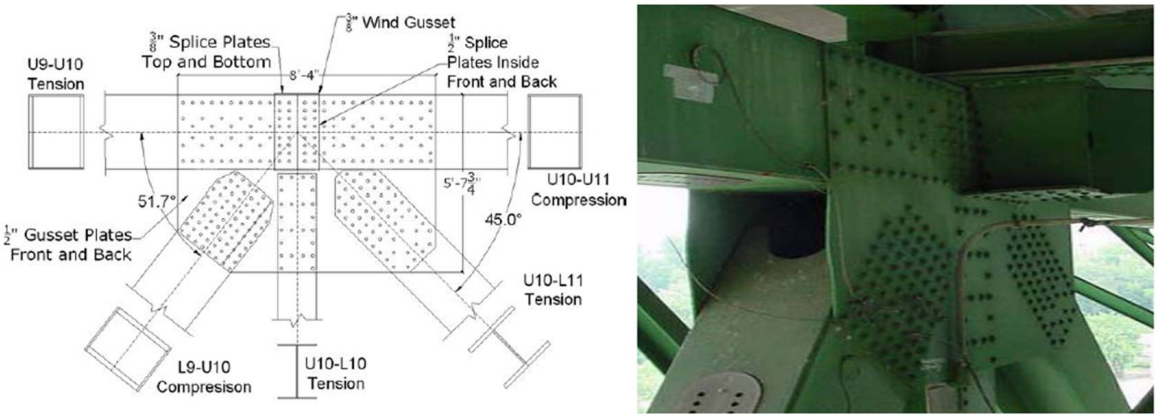

Figure 4.12: Joint U10 from I35W Bridge

pointed out the characteristics of each model in this section.

The FE model for Joint L2 is shown in Figure 4.13. This Joint L2 FE model includes two main gusset plates, one bottom wind gusset, two lateral spliced plates, two supporting angles for the floor beam attachments and five truss members that extended to the adjacent joints. The extended truss members were modeled by beam element and one end of beam element was connected to the master node of a rigid surface where the nodes of the shell elements were regarded as slave nodes. The master node was located at the centroid of the member section. Axial forces were applied to the other far-ends of the beam elements. Out-of-plane restraints were assigned to nodes along the edge of wind gusset plate and the floor beam attachment angles to simulate the out-of-plane restraint provided by the floor beam and wind bracing. The vertical load from the floor beam acted on the rivets of the angle attachment, and the resulting out-of-plane eccentricity provided the necessary trigger for buckling so that no initial out-of-straightness of the gusset plates were required.

The FE model for BR Joint L9 is shown in Figure 4.14. Joint L9 FE model includes two main gusset plates, continuous chord flanges and chord channel webs, two small wind gusset plates for strut, two angle attachments for sway bracing, inner and outer splice plates that connect main gusset plates and outer chord web plates, and five truss members that extended to the adjacent joints. Axial loads were applied to the far-end joints of the beam elements.

Master-slave rigid surfaces are used to interface the shell elements and beam elements. Because all applied loads were in-plane loads on this joint, an linear eigen-value buckling analysis was conducted before the non-linear large deformation analysis was proceeded to initiate buckling failure and determine the buckling shapes. The first five modes of buckling shape were combined and used to generate an out-of-plane imperfection with the maximum deformation of 0.001 in.. Out-of-plane restraints were applied along the edge of the wind gusset plates and the the angle attachments.

The FE model for Joint L1 is shown in Figure 4.15. Joint L1 FE subassemblage was modeled with two main gusset plates, a bottom wind gusset plate and angle attachments for strut and bracing, and the chord splice which was located on the work point of the joint. The main gusset plates, the top splice plate, and the bottom wind gusset plate formed the chord splice. The center line of the right lower chord was extended from work point with a small angle to the horizontal line. In-plane loads were applied on the far-end of the connected truss members at the adjacent joints. As no out-of-plane loads acted on the joint, an linear eigen-value buckling analysis was conducted to generate slight imperfection on the gusset plates. The maximum initial imperfection was 0.00075 in.. Out-of-plane restraints were assigned along the angle attachment and the edge of the wind gusset plate.

The FE model for Joint U3 is shown in Figure 4.16. Joint U3 has two main gusset plates and additional dual plates at chord web, both working as main splice plates for the chord splice. Top and bottom steel bars jointed the channel flanges. A wind gusset plate sit on the top of the channel flanges where floor beam load was applied. Outside the joint, top and bottom chord channel flanges were covered by steel plates. Loads were applied on the far-end of members and at the location of the floor beam. The compression hanger extends through the entire vertical depth of the joint between the gusset plates. Therefore, gusset plate buckling is not possible for Joint U3. Out-of-plane restraints were applied on the edge of the wind gusset plate.

The FE model for Joint L5 is shown in Figure 4.17. Joint L5 subassemblage modeled two main gusset plates, four truss members, two wind gusset plates on the top and bottom of the chord, and two angle attachments on the compression hanger for swing bracing. Away

from the joint, the built-up channel for the chord was covered with steel plates on the top and bottom. The main gusset plates, the dual inner reinforced plates on channel web, the bottom wind gusset plate, the top wind gusset plate and the top steel bar form the chord splice system at the work point of the joint. Loads were applied on the far-ends of the connected members. The compression hanger extended the entire vertical depth of the joint between the main gusset plates so that there was no potential for buckling failure of this joint. Out-of plane restraints were assigned along the edge of wind gusset plates.

The FE model for Joint U10 is shown in Figure 4.18 and consisted of two main gusset plates, two chord web splice plates, one bottom flange splice plate, one wind gusset plate on the top of the chords, one wind gusset plate near the bottom of the chord attached only to the inner main gusset plate by angles for struts, and two angle attachments for sway bracing and in-plane truss members that extended to the adjacent joints. The splice was located at the work point of the joint. Out-of-plane restraint was assigned to the angle attachments and the edge of wind gusset plates. An eigen-value buckling analysis was performed before non-linear large deformation analysis and generated the 0.001 in. of the maximum initial gusset plate imperfection.

The geometric characteristics considered important and described above were tabulated in Table 4.8 for the selected gusset plate connections from Washington bridges and I-35W bridges. These geometric parameters will be examined their influences when different loading combinations were applied to the joints in the next chapter. The loading combinations used in this study will be discussed in the next section.

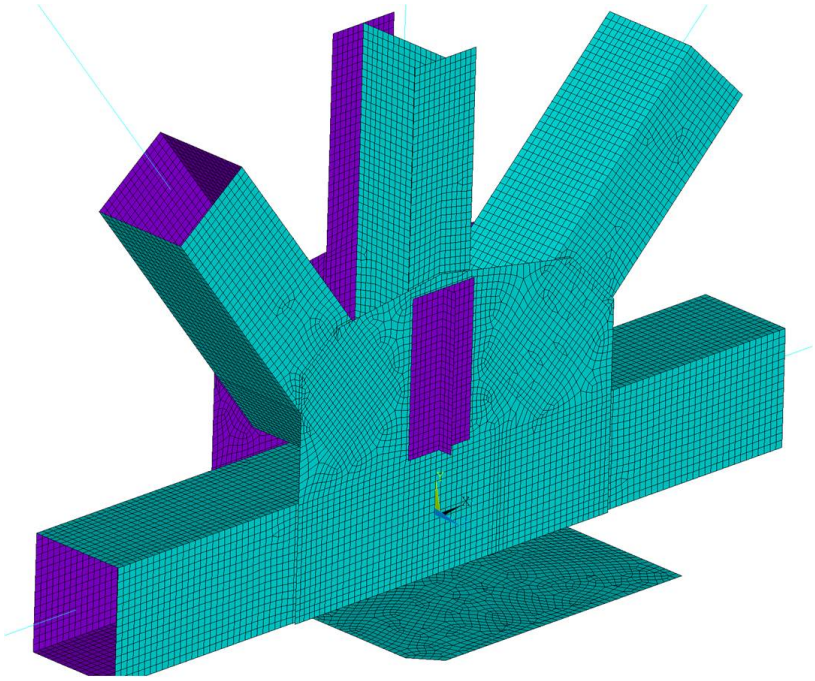

Figure 4.13: FE Model for BR90/134N Joint L2

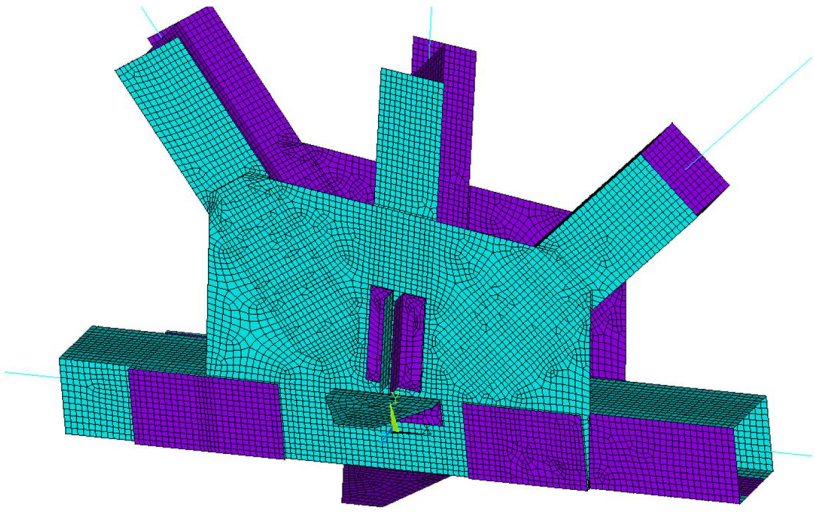

Figure 4.14: FE Model for BR31/36 Joint L9

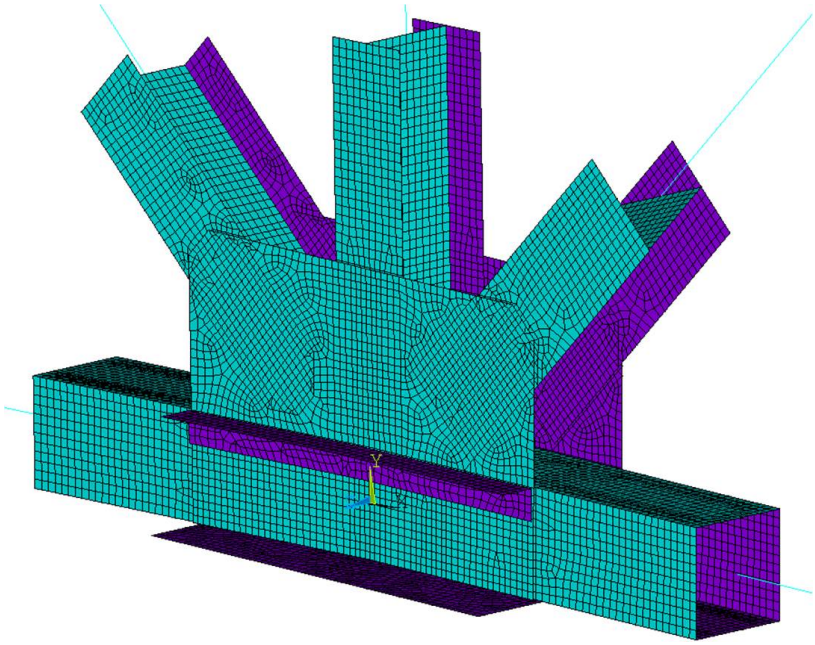

Figure 4.15: FE Model for BR31/36 Joint L1

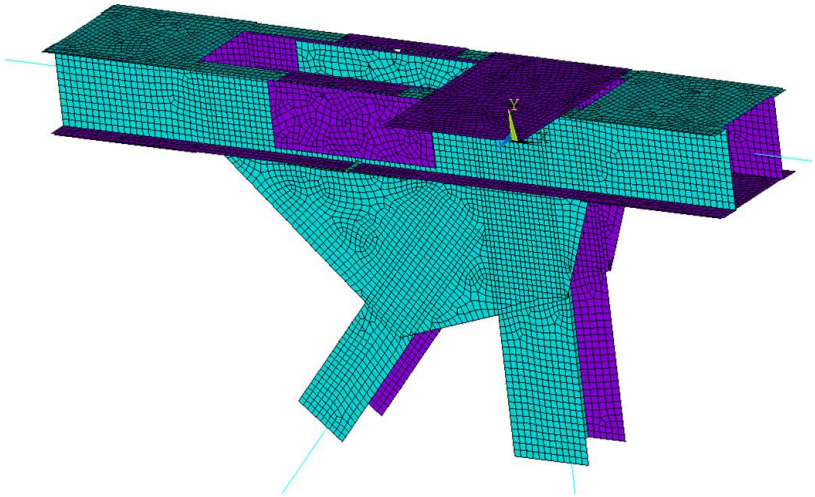

Figure 4.16: FE Model for BR 101/217 Joint U3

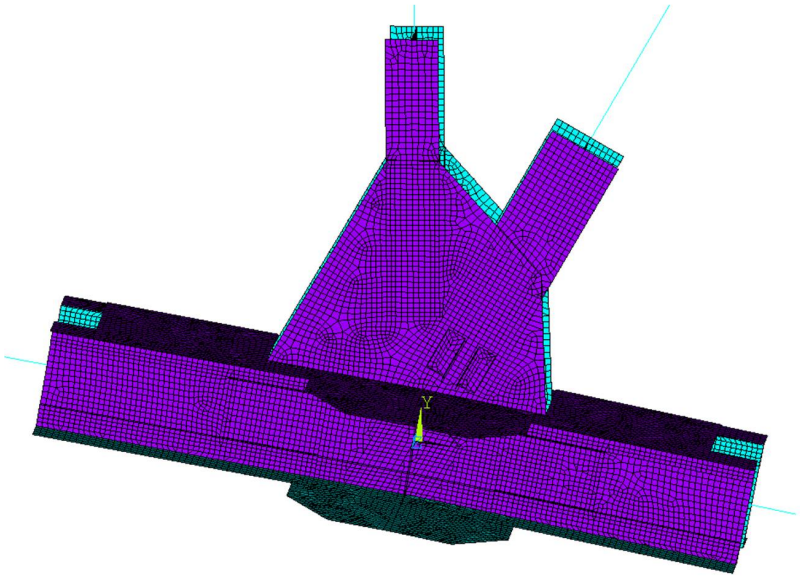

Figure 4.17: FE Model for BR 101/217 Joint L5

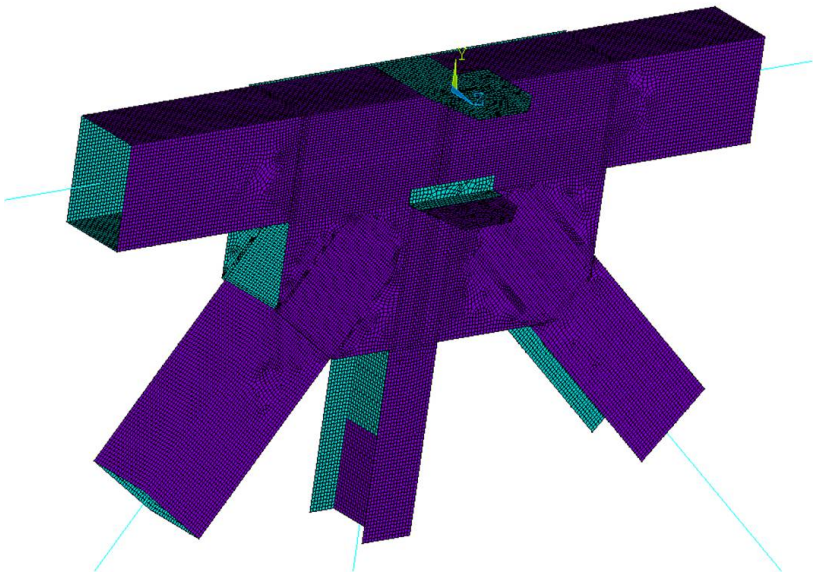

Figure 4.18: FE Model for BR 9340(I35W) Joint U10

Table 4.8: Characteristics of selected gusset plate joints

Joint	Bridge Type	Location	Gusset Plate Type	Splice Location	Gusset Plate Thickness	Steel Yielding Stress(ksi)	Splice Condition
U10@BRI35W	Warren-Type	Upper Chord	Splice-Type	Middle	1/2”	51.5	Main gusset plates, web splice plates, and flange splice plates
L2@BR90/134N	Warren-Type	Lower Chord	Splice-Type	Offset	1/2”	45	Two main gusset plates, top flange plate, and wind gusset plate form splice
L9@BR31/36	Warren-Type	Lower Chord	Monolithic-type	Offset toward zero force member and pin	1/2”	33	Continuous chords with web splice plate connecting gusset plates and out-layer web plate; continuous chord terminated before pin
L1@BR31/36	Warren-Type	Lower Chord	Splice-Type	Middle	3/8”	33	Two main gusset plates and web splice plates
U3@BR101/217	Pratt-Type	Upper Chord	Splice-Type	Offset	3/8”	30	Two main gusset plates, web splice plates and flange splice bar
L5@BR101/217	Pratt-Type	Lower Chord	Splice-Type	Middle	3/8”	30	Two main gusset plates, web splice plates, bottom wind gusset plate and flange splice bar

Chapter 5

DEVELOPMENT OF RAPID ASSESSMENT METHOD: TRIAGE EVALUATION METHOD

5.1 Analysis Procedure

Using the modeling methodology and the selected gusset plate joints described in Chapters 3 and 4, analyses were performed to investigate the truss bridge joint behaviors. To study the gusset plate behaviors the loading was increased from zero until the FE analysis failed to converge with member loads proportional to the load distributions described in Chapter 4. To maintain these desired load distributions, the analyses were conducted under force control. The failure of convergence implies a sudden large deformation caused by buckling or high stress or strain concentration over a certain area of the gusset plate that prevents equilibrium from being satisfied. Sufficient data is necessary for capturing the joint behavior, especially for identifying the onset of yielding and buckling. Considering the required data and the necessary efficiency of computation, two hundred loading steps were specified from zero to the maximum load, which was typically set as four times the design load. Convergence failure of the FE analysis was expected before that maximum load was achieved. For Joint U10, two times the Stage 4 loading was used as the maximum load because that load was the estimated collapse load. Careful attention was given to the analysis results at the onset of gusset plate yielding in this chapter. A simple and rational method, denoted by Triage Evaluation Procedure, to evaluate the safety of truss bridge joints is then developed from those observations to predict the onset of yielding. The developed method was then compared with the current FHWA inspection procedure with the selected bridges and joints.

5.2 Yielding Behavior

5.2.1 Observation of Yielding

Gusset plate yielding usually starts in the area confined by the diagonals, chords, splices, and hanger and then spreads along the horizontal section on gusset plates along the chord edge, or the vertical section along the edges of the hanger. The onset of gusset plate yielding is found to prior to other failure modes for most gusset plates, such as buckling and block shear failure modes. Thus using the onset of yielding as a limit state may be an efficient method to rapidly assess gusset plates. The Von Mises failure criterion is used here as the yield criterion and is suitable for ductile materials such as steel.

The onset of yielding must be clearly defined before developing a capacity check based on that limit state. The area of yielding must be large enough to avoid influence from high stress concentration due to the element and configuration irregularities and high density of the FE mesh but small enough that it still represents the onset of yielding. A simple algorithm was developed to compute the ratio of the yielding area compared to the whole gusset plate area. First, two-color contour plots of the Von Mises stress in the gusset plates, where red indicated areas that were elastic and gray indicated areas that were yielded, were exported from the FEA result files. Then an algorithm in *Matlab* computed area by means of examining each pixel of the contour plot's digital image, recognizing their RGB color and summing the pixels with the same color to calculate the ratio of yield area to total area of the gusset plates. Contour plots were saved and exported for each small loading step as the loading was proportionally increased until the converge failure. To ensure consistent results, all contours were saved as uncompressed tiff files with the same dimension of 2143x1610 pixels. Using the developed Matlab program, large amounts of image data can be processed quickly and a figure represents yielding area percentage to the loading levels of the joints can be plotted. The loading level of a joint is represented by the load of compressive diagonal member.

Figures 5.1(a) to 5.1(d) demonstrate the progression of yielding area in contour plots for

Joint U10, and Figure 5.1(e) shows the increase in the load level, which is represented by the compressive diagonal load, versus the increase in the ratio of yielded gusset plate area of Joint U10. Figure 5.1(e) also shows that the onset of gusset plate yielding may be taken as the point when 0.5% of the entire gusset plate has yielded. After this point the yielded area spreads along horizontal section rapidly for only small increases in the loading. The two-color stress contours for the point when 0.5% of gusset plate area has yielded for Joint U10, L2 , L1 and U3 are illustrated in Figure 5.2.

When the procedure above was applied to examine the progression of yielding for Joint U10 for the four loading stages considered in Ocel and Wright [2008], significant yielding was observed in Load Step 2, which represented only the design dead load on the bridge when it opened in 1965. At the same time, the current gusset plates checks recommended by the FHWA guide don't indicate any problems with the gusset plate safety at that load level. The maximum Whitmore section stress at the end of compression member (L9-U10) was 33ksi, 36% less than yield, and horizontal shear stress was 21ksi [1] , which is 32% less than the shear yield stress. This result demonstrates the need for a method to predict the onset of yielding in steel truss bridge gusset plates.

[1]shear stress was calculated by the total shear force divided by the total horizontal area without the 1.5 factor assuming parabolic stress distribution

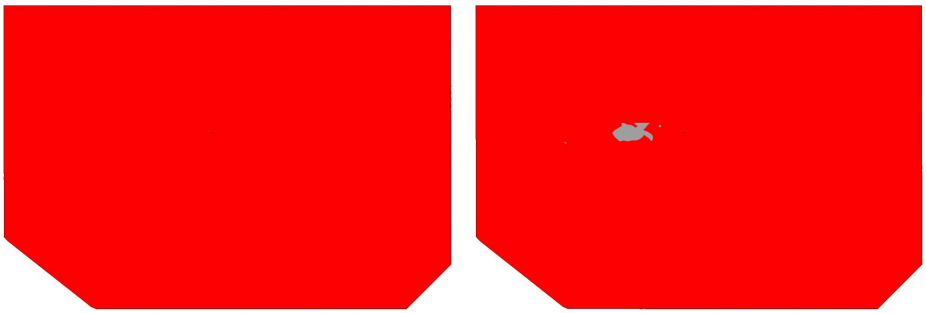

(a) 0.0% area yielding of Joint U10

(b) 0.4% area yielding of Joint U10

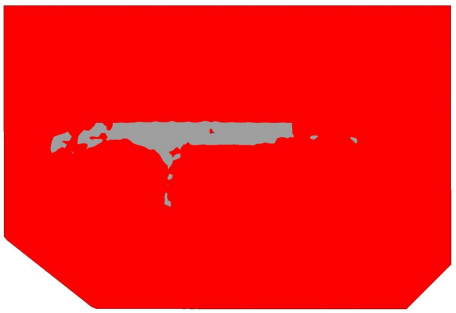

(c) 3.8% area yielding of Joint U10

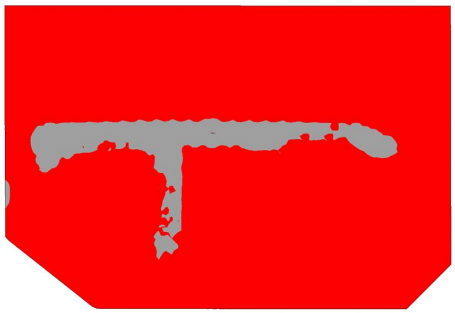

(d) 8.8% area yielding of Joint U10

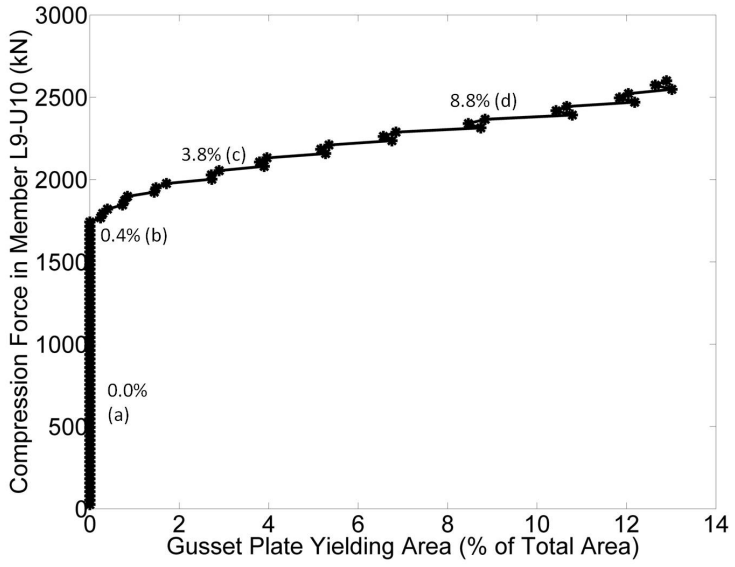

(e) yielding area vs. compression force

Figure 5.1: Progression of gusset plate yielding area with increasing joint load level represented by the axial force in the compression diagonal

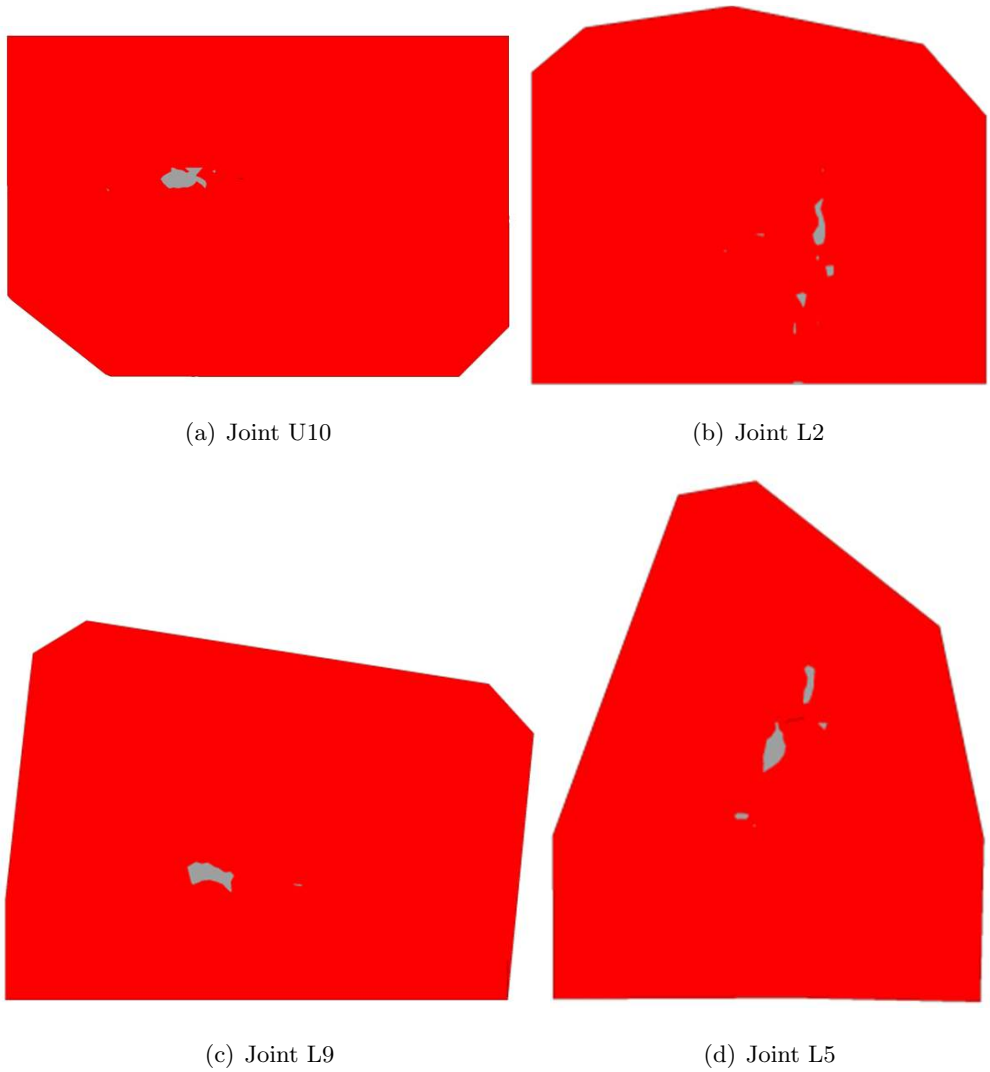

(a) Joint U10

(b) Joint L2

(c) Joint L9

(d) Joint L5

Figure 5.2: Gusset plates showing 0.5% of their area yielding

5.2.2 Development of Triage Evaluation Method for Onset Yielding

In most cases, the onset of gusset plate yielding is observed in the interference zone which is a region bounded by diagonals and chords as shown in Figure 5.3, and yielding is not particularly found at the end of diagonals as described by Whitmore [1952] and other literature. Additional stresses must be considered to interact with the stress generated at diagonal ends and result in yielding initiating earlier than only predicted with the Whitmore

stress considered at the member end. The Triage Evaluation Method (TEP) consider a plane stress problem in the interference zone on the gusset plate connection. Von Mises yielding criterion in a plane stress problem shows that the equivalent stress is a function of two principal stress components, σ_{11} and σ_{22}, at one point as shown in Eq. 5.1a. To find the maximum Von Mises stress in Eq. 5.1a, the calculation of the gradient of Eq. 5.1a is considered. The maximum equivalent stress is found when $\sigma_{11} = -\sigma_{22}$ as shown in Eq. 5.1b and 5.1c. Eq. 5.1c indicates that the maximum equivalent stress is found when a equal and opposite principal stress is generated from other interacting elements in the gusset plates.

$$\sigma_v = \sigma_{11}^2 - \sigma_{11}\sigma_{22} + \sigma_{22}^2 \tag{5.1a}$$

$$\nabla\sigma_v(\sigma_{11}, \sigma_{22}) = 2\sigma_{11} - \sigma_{22} - \sigma_{11} + 2\sigma_{22} = 0 \tag{5.1b}$$

$$\sigma_{11} = -\sigma_{22} \tag{5.1c}$$

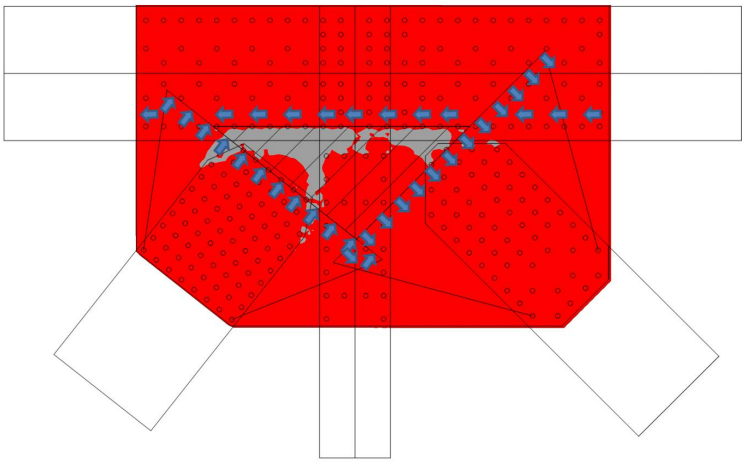

Figure 5.3: Interference zone was enclosed by diagonals, hanger and chords

In common gusset plate configurations, the two diagonals often form an orthogonal geometry and carry loads in opposite directions as shown in Figure 5.4(a). It can be conservatively assumed that diagonal configurations create a condition similar to the scenario derived in Eq. 5.1 in the interference zone. To prevent the initiation of yielding on the gusset plates, the maximum equivalent stress is assigned to be less than uniaxial yielding stress, σ_y. Therefore Eq. 5.2 is used to check the onset gusset plate yielding.

The concept of Eq. 5.2 can be applied to the stresses generated at chords and hanger as long as the member terminates inside the interference zone. Though the configuration of the chords and hanger deviates from the worst scenario, the unknown interacting stress σ_{22} may not be orthogonal, equal, and opposite to Whitmore stress, σ_{11}, the use of Eq. 5.2 will result in a conservative estimate in these conditions, but the Triage method is intended to be a conservative method. Another implicit requirement to ensure that Eq. 5.2 is conservative is that there is no stress due to moment in the interference zone. Since all the member forces meet at work point, and no moment occurs on the gusset plates, this requirement is assumed satisfied.

$$\sigma_{v,max} = \sqrt{3}\sigma_{11} \leq \sigma_y \tag{5.2}$$

Eq. 5.2 described that the maximum equivalent Von Mises stress in gusset plates can be estimated by the maximum uniaxial Whitmore stress multiplied by a factor $\sqrt{3}$. This calculation directly uses the individual member force so that the envelope truss member forces can be applied to this yielding check without the need of calculating concurrent forces in equilibrium at the joints. Since most bridge analysis software and shop drawings provide envelope forces for each member, this check for gusset plate yielding provides a simple and fast alternative to evaluate gusset plate safety in practice as along as all the members terminate inside the interference zone and no additional stress is caused by moment or torsion.

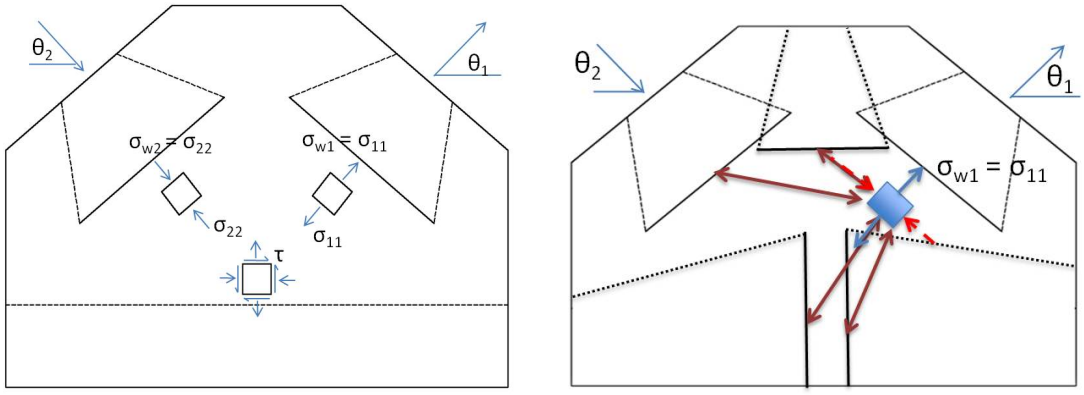

(a) Principal stresses from diagonals calculated by Whitmore's method

(b) Interacting stress, σ_{22}, generated from other elements interacting with end member stress σ_{11}

Figure 5.4: Schematic of derivation of the TEP and application to all connected members

5.3 Observations from the Application of the TEP

5.3.1 Validation of the TEP at Onset Yielding of Loads

The TEP is validated with the selected gusset plates at the onset yielding conditions. Both the TEP and FHWA methods were compared to determine their adequacy in predicting the onset of gusset plate yielding. To do this, demand-to-capacity ratios at the load level corresponding to the onset of yielding were evaluated for selected joints. The demand of the onset yielding is the load level from FEA when gusset plate has 0.5% area exceeding the yield stress, and the capacity of the gusset plate is calculated from the TEP and current FHWA evaluation method. The successive grey-red contour plots for gradually increasing load steps were plotted, saved, and used to calculate the corrosponding ratios of the yielded area. Since the loads were uniformly and linearly increased in the FEA, the load level at the 0.5% yielding gusset plate area was linearly interpolated between two load levels where the yielded area ratio were close to 0.5% of the gusset plate area. The load level when 0.5% of the gusset plate area yielded, was then used as the demand for the gusset plate at the onset yielding. The capacity for the TEP was computed by using the Whitmore width multiplied by the thickness of the gusset plates and $F_y/\sqrt{3}$ for each member and the least

one is regarded as gusset plate onset yielding capacity. The FHWA capacity considered only limit states of the tension yielding at the end of members and the shear yielding along critical sections with $\Omega = 0.74$.

For the Joint L5, there were only two distinct loading cases, so that the demand/capacity calculation was only applied to these two cases. The FHWA shear check did not apply to Joint L5 since the hanger continues through to the bottom of the joint and no horizontal cut can be made without cutting through a member. The demand-to-capacity (D/C) for Joints L2, U10, L9 and L5 are tabulated in Table from 5.1 to 5.4. From each loading case in these tables there is at least one instance of the TEP resulting in a D/C over 1.0, indicating that the TEP is correctly predicting that some part of the gusset plate has yielded. Most of the cases that the D/C ratios over 1.0 are from a diagonals. This result confirms that the TEP is conservative with respect to indicating the onset of gusset plate yielding. On the contrary, the results for the D/C ratios computed with the FHWA procedures result in significant yielding of the gusset prior to achieving their rated capacity. Only for Joints U10 and L9, the FHWA check shows that the D/C ratios are below 1.0 but close to 1.0. The variations of the D/C ratios for the FHWA check show that this evaluation is not consistent and not suitable for predicting the gusset plate yielding.

Table 5.1: Demand/Capacity ratio for I35W U10 Gusset plates

Joint ID	Load Case No.									
	Case1		Case2		Case3		Case4		Case5	
	Triage D/C	FHWA D/C	Triage D/C	FHWA D/C	Triage D/C	FHWA D/C	Triage D/C	FHWA D/C	Triage D/C	FHWA D/C
U10-U9	0.62		0.6		0.6		0.67		0.57	
U10-L9	1.01		1.02		1.05		1.06		1.02	
U10-L10	0.23	1.0	0.24	0.99	0.28	1.00	0.18	1.00	0.24	0.98
U10-L11	0.76		0.76		0.74		0.87		0.75	
U10-U11	0.16		0.18		0.18		0.19		0.21	

Table 5.2: Demand/Capacity ratio for BR 90/134N L2 Gusset plates

Joint ID	Load Case No.									
	Case1		Case2		Case3		Case4		Case5	
	Triage D/C	FHWA D/C	Triage D/C	FHWA D/C	Triage D/C	FHWA D/C	Triage D/C	FHWA D/C	Triage D/C	FHWA D/C
L2-L1	1.31		1.21		1.20		1.15		1.23	
L2-U1	1.08		1.25		1.15		1.17		1.15	
L2-U2	0.14	0.59	0.14	0.53	0.15	0.47	0.13	0.81	0.14	0.68
L2-U3	0.66		0.60		0.53		0.92		0.76	
L2-L3	1.46		1.44		1.38		1.45		1.46	

5.3.2 Validation of the TEP with Load Rating

The TEP was shown to conservatively predict the onset of yielding in truss bridge gusset plates in the previous section. The following validation of the TEP is to use the TEP with load rating procedures to evaluate the safety of existing steel truss bridges. For this application, the TEP was used to calculate the gusset plate nominal strength, R_n or joint capacity, C, in the load rating procedures described in Eqs. 4.1,4.2, and 4.3. These evaluations and comparisons were conducted by Olson [2010]. Olson [2010] tabulated the load demands as well as the Rating Factors (RF's) for all joints of the selected WSDOT bridges using these three load rating procedures in combination with the TEP and FHWA Guide methods for determining gusset plate resistance. Olson [2010] found that none of the joints had RF's that were less than 1.0 for the AASHTO-MBE-LRFR Service II load combination at the operating load level using the TEP while 3 out of the 35 joints had RF's less than 1.0 in the AASHTO-MBE-LRFR Service II load combination at the inventory load level. These three joints were Joint L9 of BR 31/36, and Joints L3 and U2 of BR 101/217. Thus these joints require additional investigation and will be further discussed below. Olson [2010] also showed that a number of joints had RF's less than 1.0 using the TEP and the AASHTO-

Table 5.3: Demand/Capacity ratio for BR 31/36 L9 Gusset plates

Joint ID	Load Case No.							
	Case1		Case2		Case3		Case4	
	Triage D/C	FHWA D/C	Triage D/C	FHWA D/C	Triage D/C	FHWA D/C	Triage D/C	FHWA D/C
L9-L8	1.01		1.01		0.97		1.01	
L9-U8	1.93	0.98	1.02	0.98	1.01	0.81	0.95	0.98
L9-U9	0.17		0.31		0.35		0.19	
L9-U10	0.96		0.87		0.8		0.95	

MBE-LRFR Strength I load combination at the inventory and operating load levels. This result was expected because the TEP is developed to consider the onset of yielding while the strength load combination are calibrated against ultimate failure. The rating factor comparisons conducted by Olson [2010] demonstrated that although the TEP is derived based on conservative assumptions, i.e. equal and opposite principal plane stresses interact in the interference zone, the TEP can be reliably used to quickly establish that a large proportion of gusset plate connections have adequate resistance.

5.3.3 Examination of TEP Results for Load Rating with Service II Loads

The application of the TEP on load rating with Service II loads showed three examples of gusset plates having a rating factor less than 1.0, Joint L9 of BR 31/36, and Joints L3 and U2 of BR 101/217. To examine these cases, the geometric configurations and loading distributions are re-considered for these joints. The FEA for these joints were intended to be conducted to understand the stress distributions on these joints. However, because of the difficulty in deciphering the details of Joints U2 and L3 of BR 101/217 on the vintage design drawings, Joints U3 and L5, which had similar geometries and load distributions to Joints U2 and L3, were used to build the FE models and investigate their stress distributions. In

Table 5.4: Demand/Capacity ratio for BR 101/217 L5 Gusset plates

CJoint ID	Load Case No.			
	Case1		Case2	
	Triage D/C	FHWA D/C	Triage D/C	FHWA D/C
L5-L4	1.48	0.68	1.24	0.71
L5-U4	1.12		1.24	
L5-U5	0.93		0.31	
L5-L6	1.29		0.87	

additional to the similarity of these joints, Joints U3 and L5 had RF's that were close to 1.0 yet were above 1.0.

In Joint L3, the RF less than 1.0 resulted from the L3-L4 compression chord, which had a splice connection specified as "milled-to-bear" to the L2-L3 chord on the drawings as shown in Figure 5.5(a). Since joints with "milled-to bear" compression chords, the compressive forces is transferred continuously between the chords, there is only a small stress that would be transferred into the gusset plates. Thus, the TEP check on these chords can be omitted and the RF's for the joint would be greater than 1.0. for the diagonals. The FE results for Joint L5, whose configuration is similar to Joint L3, also confirmed that the load transfer at the "milled-to bear" chord connection does not produce a high gusset plate stress and instead the highest stress occurs at the end of the diagonal which interacts with stress from the hanger.

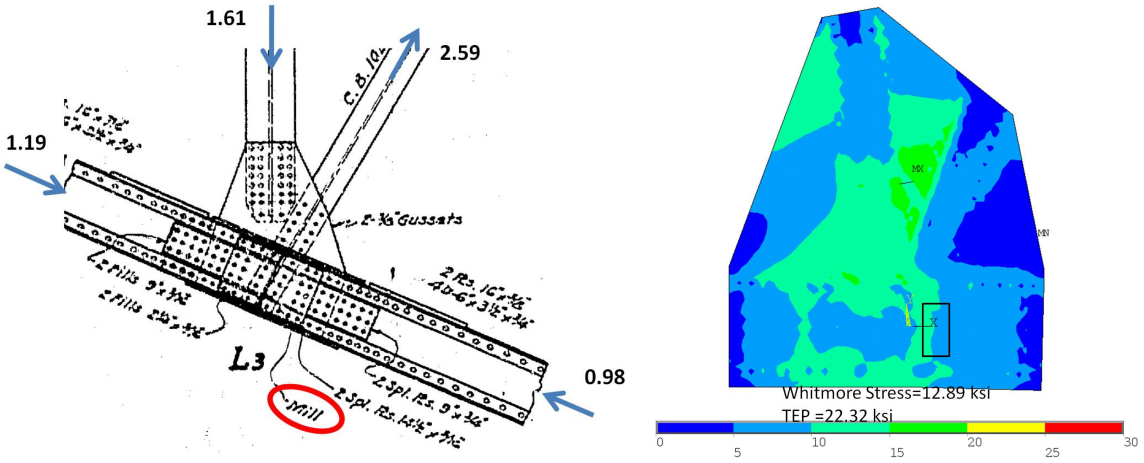

(a) Configuration of Joint L3 of BR 101/217 with milled-to-bear compressive chords showing that the RF less than 1.0 is generated by the chords

(b) Joint L5, which is similar to Joint L3 in geometry and loads, shows that highest stress incurred by the diagonal and chord

Figure 5.5: RF's of Joint L3 and FEA results of the similar Joint L5

In Joint U2, the RF less than 1.0 were also caused by the chords. Joint U2 has a chord splice that is offset from the interference zone as shown in Figure 5.6(a). Thus, in Joint U2, the stresses in the gusset plate generated from the chord do not interact with the stresses from other members in the way assumed in the TEP. It is reasonable not to consider the chord loads in the TEP check and only consider diagonals in the TEP. Once the chords are removed from consideration in the TEP, the RF's for Joint U2 have values greater than 1.0. Comparing Joint U2 with the FE analysis of the Joint U3, whose configuration is similar to the Joint U2, shows that the stresses from the chord splice do not appear to be affected by other stresses. Outside the interference zone, the stress decreases gradually but an abrupt high stress zone is present at the chord splice as shown in Figure 5.6(b). However, the stress at the chord splice was less than the TEP prediction but much larger than Whitmore stress, and the location of the high stress at the chord splice is closer to the outer edge of the chord, which is different from the location of the high stress found when the chord splice is located inside the interference zone. This observation results in a question about how the stress at chord splice outside the interference zone differs from that when chord splice located inside

the interference zone. The fundamental behavior of chord splice will be discussed in the next chapter.

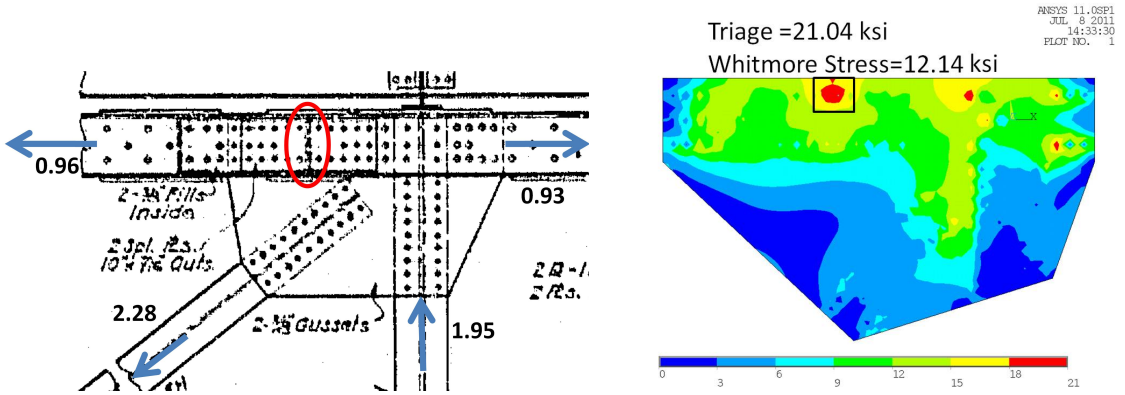

(a) Configuration of Joint U2 of BR 101/217 with chord splice outside the interference zone showing that the RF less than 1.0

(b) Joint U3, which is similar to Joint U2 in geometry and loads, shows that the chord stress was higher than Whitmore stress but smaller than the TEP

Figure 5.6: RF's of Joint L3 and FEA results of the similar Joint L5

For Joint L9, the TEP in the chord also resulted in RF's less than 1.0. The L8-L9 chord passes through the work point, terminated in the interference zone, and spliced with a zero force chord member as shown in Figure 5.7(a). The L8-L9 chord carried a relative high load to the diagonal loads but the FEA result shows that there was no significant stress observed at the L8-K9 chord end. The derivation of the TEP shows that the TEP produces conservative results if the stress interaction does not comply with the worst scenario, which means equal, opposite, and orthogonal stress interaction. Therefore, in certain conditions, the TEP will be overly-conservative and an a refined method of analysis is necessary for these cases.

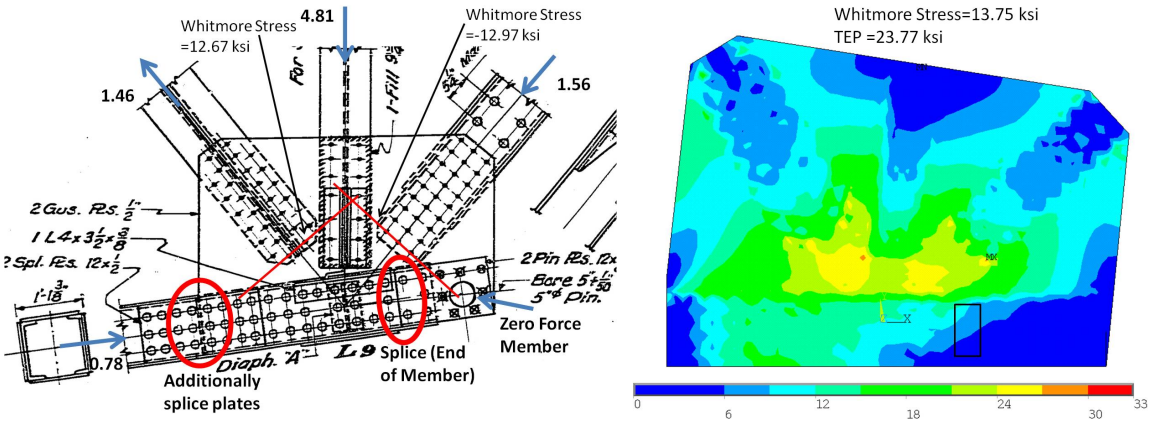

(a) Configuration of Joint L9 of BR 31/36 with chord splice in the interference zone showing that the RF less than 1.0 (b) FEA of Joint L9 showing small stress at chord which has high load

Figure 5.7: RF's and FEA results of Joint L9

The TEP was found to reliably estimate initiation of gusset plate yielding through the validation of the demand/capacity ratios at the gusset plate onset of yielding and the Rating Factors at the Service II load combinations. In a few cases the TEP was found to be overly-conservative: when the chord is in not terminated in the interference zone or when compressive chords were designed "milled-to-bear". The cases of chord members terminated outside the interference zone seem to have characteristics that result in neither Whitmore or the TEP accurately estimating the stress in these joints. Therefore, the chord splice behavior needs further study. In addition, though the TEP has been demonstrated to be advantageous for rapid assessment of the initiation of gusset plate yielding, the TEP does not provide information such as the location of the high stress area, the possible maximum stress, and the gusset plate capacity at yielding or buckling limit states. A refined method will be developed to provide solutions to these questions. In Chapter 6, the behavior of gusset plate chord splices will be studied. In Chapter 7, the stress components generated from different connected members will be explored to develop a refined evaluation procedure which is expected to be capable to estimate the magnitude and the location of the maximum gusset plate stress.

Chapter 6

STRESSES AT THE CHORD SPLICE OF GUSSET PLATE CONNECTION

In the previous section, the TEP was found to be a quick and reliable method to identify the gusset plate connections with stresses larger than the yield stress in the interference zone. In some cases, the maximum stress was not found in the interference zone, and the TEP is overly-conservative in predicting when gusset plates yield. These cases often have chord splices located outside the interference zone or at its edge. Joint U3 in Hor River bridge (BR101/217) and Joint L2 in Cle Elum bridge (BR 90/134N) are examples of joints that have chord splices located outside the interference zone and have maximum stresses in these locations. Figure 6.1 shows that in these examples, high stresses are generated at the chord splice location and in the case of Joint L2, they trigger larger interference zone stresses.

Chord splices, unlike diagonals and hangers, have unique asymmetric load-dispersion geometry and a small gap between chord ends which can narrow the dispersion angle and increase the stress in the elements that connect the chords. The chord splice may be reinforced differently by splice plates in addition to the gusset plates, and the chords may be heavily loaded, with loads exceeding those in the diagonals when the connection is located in the mid-span of bridges. Conventionally, the calculation of stresses on gusset plates at the ends of chord member are computed similarly to the stresses at end of diagonals., i.e. by using Whitmore's method. However, the findings in Figure 6.1 suggest that the stress at the chord splice may need be considered differently from the stress at the ends of diagonals and hangers. In this chapter, the stress distribution at chord splices and the impact of the splice location on that stress distribution are studied; then a model for the stress distribution in gusset plates at chord splices is proposed and its robustness is demonstrated for a range of

splice locations and gusset plate geometric parameters.

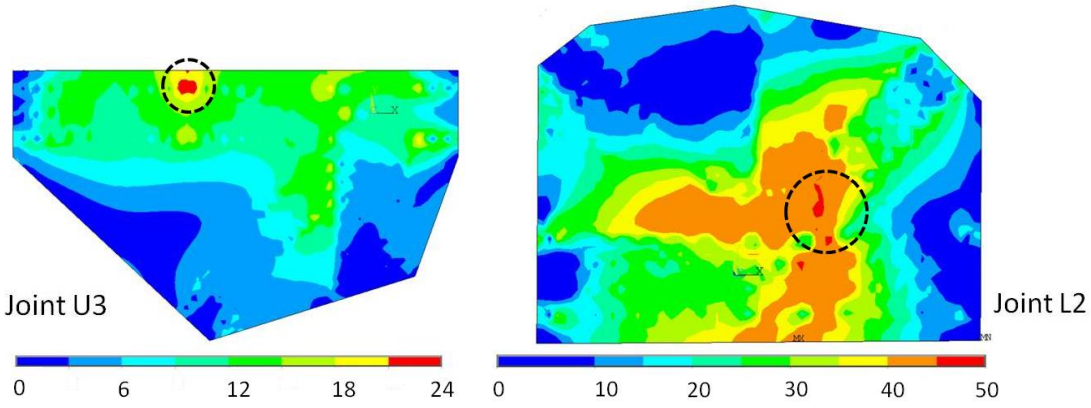

Figure 6.1: Relatively high gusset plate stresses at the chord splice location and their impact on the interference zone

6.1 Observations about the Gusset Plate Stress Distribution at Chord Splices

To study stress distributions at a chord splice, a typical Warren type gusset plate connection whose dimensions and finite element model are generally based on Joint U10 of I35W bridge is used. In this connection, the diagonals are below the chords, so the chord splice is asymmetric in that there is more gusset plates area below the chords than above the chords. To observe the changes in the stress distribution at the chord splice, the gusset plate area above the chords was gradually increased to decrease the splice's asymmetry as shown in Figure 6.2. In this initial study, the splice plates are not modeled to highlight the stress distribution in the gusset plates. An equal and opposite load of 600 kips in tension is used in the chords at far-end connections. The loads in diagonals are set to zero and the hanger is not modeled to isolate the stress at the chord splices without influence by other gusset plate stresses. The connection length is 41.25 in. for the left chord and 48.75 in. for the right chord. Gusset plates have 0.5 in. thickness. The principal stress contours of those four gusset plate studied are shown in the Figure 6.3.

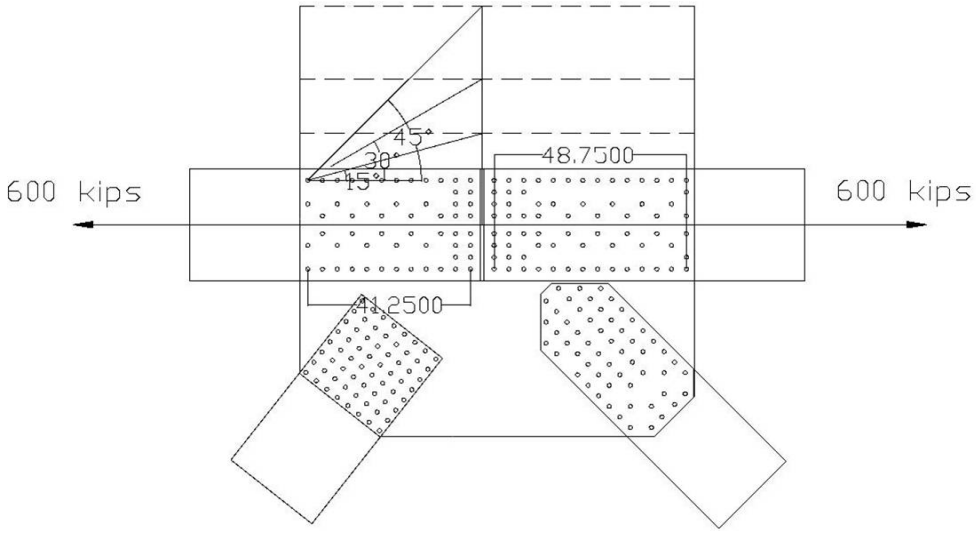

Figure 6.2: A basic Warren type gusset plate used to study stress distribution at chord splice

6.1.1 Presence of a Trapezoidal Stress Distribution

The principal stresses along the chord splice for the geometries of Figure 6.3 are plotted in Figure 6.4 with the origin of the x axis set at the top rivet line extending positively below the chord and negatively above chord for all cases. The stress at the chord splice of the original geometric configuration is shown as a solid line in Figure 6.4 and marked as original configuration in the legend. As shown, this stress distribution varies linearly, between the area of outer and inner rivet rows and then sharply drops when it leave this area. This linear variant principal stress distribution implies that it is due to combined axial loads and bending on the gusset plate at the chord splice. It seems that the loads transmitted from the chords to the gusset plates follow a certain dispersion angle in one side of the chords that there is not enough space to fully develop the same dispersion angle on another side, resulting in an unbalanced normal stress in the gusset plate chord end. This unbalanced normal stress distribution can be presumed to be generated by a bending moment due to the asymmetric gusset plate area at the chords splice.

Figure 6.4 also shows that as the asymmetry of the chord splice is decreased, the linear distributed stress between the outer rivet rows of the splice decreases as well and the stress distributions become more symmetric about the longitudinal axes of the chord. Once enough gusset plate is added such that a 30° angle on both sides of chord are possible, Figure 6.3(c), the gusset plate stress distribution at the chord end reaches a symmetric state and additional area added above the top chord no longer impacts the stress distributions. Figure 6.4 also shows that the peak of the stress at the chord splice is much larger than the calculated Whitmore stress that is shown as a horizontal line in the figure. The peak stress from these analyses occurs around the location of outer rivet line of the chords and its magnitude could be twice the Whitmore stress. This observation shows the additional normal stress generated by a bending moment due to the connection asymmetry is important and should be included in the calculation of stress at the chord splices.

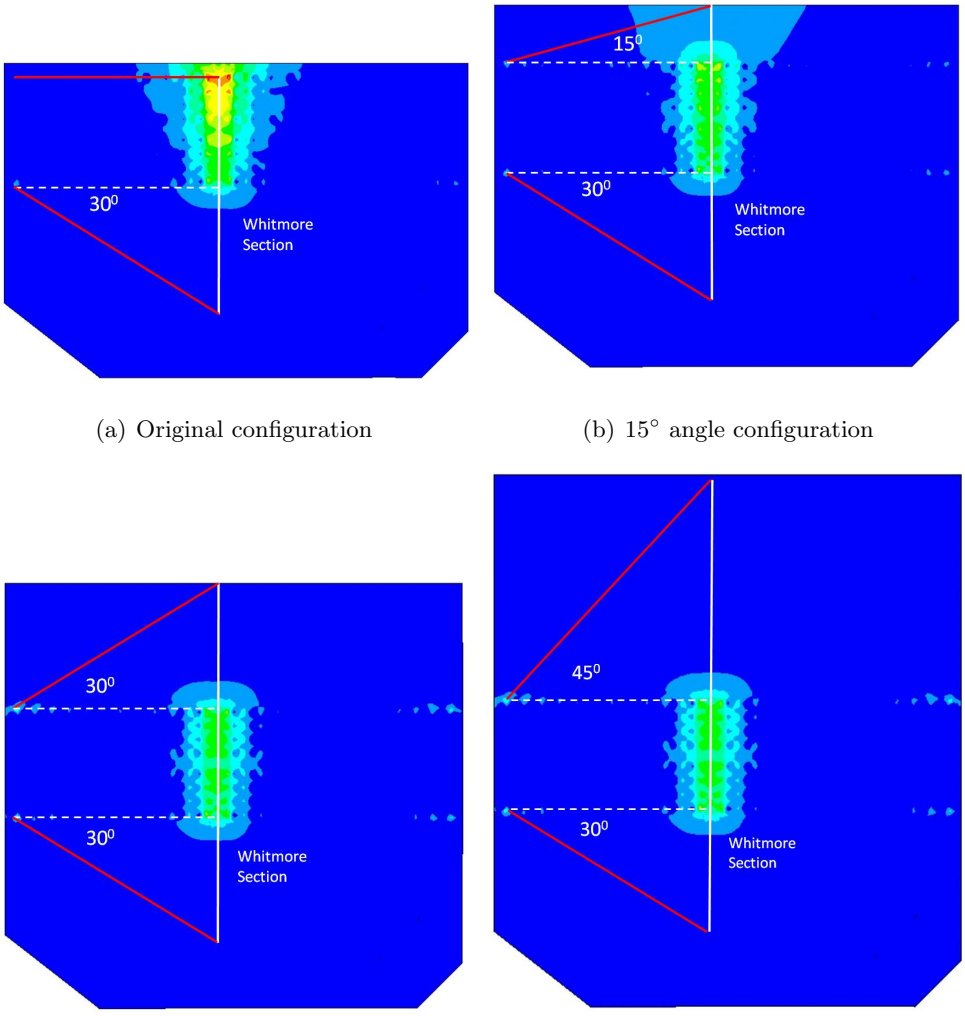

(a) Original configuration

(b) 15° angle configuration

(c) 30° angle configuration

(d) 45° angle configuration

Figure 6.3: Gusset plate geometric configurations used to study the effect of chord splice asymmetry

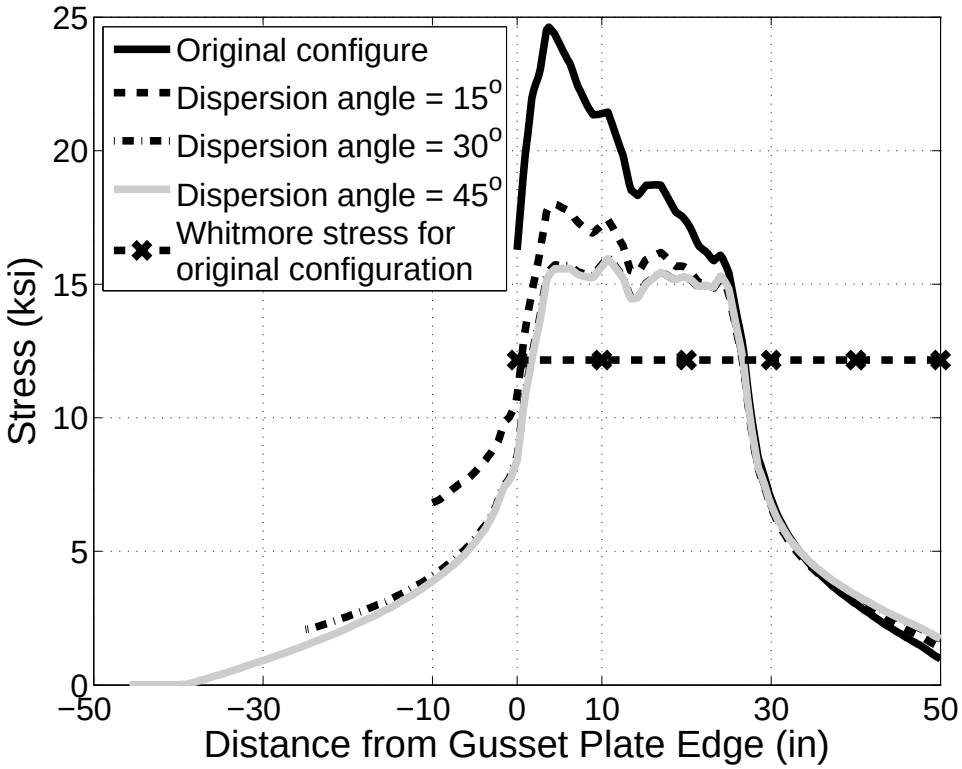

Figure 6.4: Moments due to the asymmetry of chord splices may cause additional stresses than pure axial normal stress

6.1.2 Presence of a High Stress Plateau

Even though the linear variation of the peak of the trapezoidal stress distribution in the gusset plates at the chord splice is eliminated by changing the gusset plate geometry, the stress at the chord splice is still larger than expected. The stress at the plateau in Figure 6.4 is about 1.5 times the magnitude of the Whitmore stress using a 30° dispersion, considered a good estimation for the maximum stress at the end of diagonals Whitmore [1952]. This shows that the unique geometry of the chord splice seems to be inappropriate for application of Whitmore's method. To understand the higher stresses caused at the chord splice, even when bending is eliminated by modifying gusset plate geometry, two-dimensional elasticity problems in the literature were examined to postulate the fundamental differences between

forces transferring into the gusset plate at the end of diagonals and at the chord splice. Two classic plane stress problems from the literature were found to have similar characteristics as the problems of the forces transferring into gusset plates at diagonal ends and at chord splices. In a diagonal connection to a gusset plate, there is typically a somewhat large distance between the end of the diagonal and the edge of the plate. This is similar to the classic problem of point load applied to an infinite-half-plane as shown in Figure 6.5(a). At the chord splice, there are often large forces applied to the gusset plate in opposite directions a small distance apart. This configuration is similar to the classical problem of equal-and-opposite forces acting on an infinite strip which has a limit thickness as shown in Figure 6.5(b).

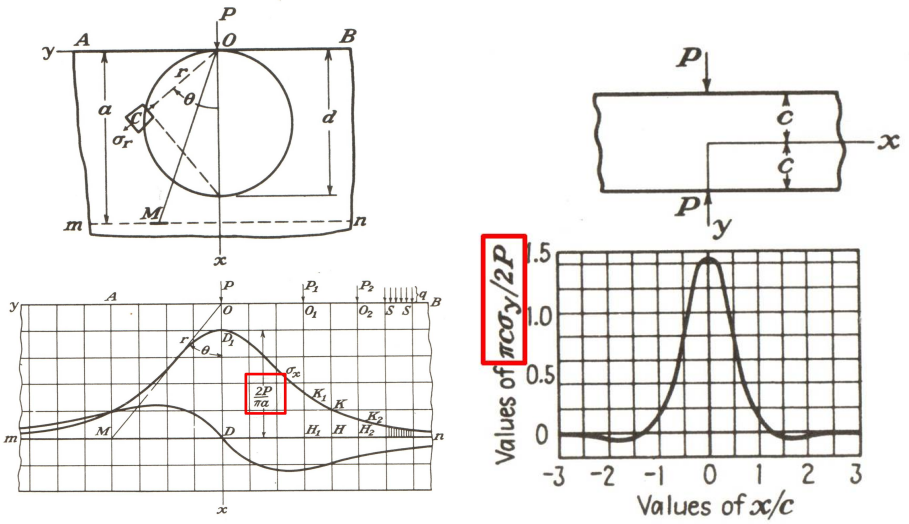

(a) Stress distribution of infinite-half-plane problem; maximum stress $= \frac{2P}{\pi a}$

(b) Stress distribution of infinite-strip problem; maximum stress $= \frac{3P}{\pi c}$

Figure 6.5: Theoretical elasticity Timoshenko [1970] similar to diagonal to gusset plate and chord splice connections.

The solutions for both of the plane stress problems in Figure 6.5(a) can be found in Timoshenko [1970]. While these somewhat complex solutions may not be directly applied in for gusset plates, the analogy provides insight into these two different load-transfer mechanism.

From Timoshenko [1970], the maximum normal stress in a distance a from the applied force in the infinite-half-plane problem can be approximated as $\frac{2P}{\pi a}$ whereas the maximum normal stress at a distance c from the applied force in the infinite-strip problem can be approximated as $\frac{3P}{\pi c}$. Setting $a = c$ shows that the peak stress in the the infinite-strip-problem is 1.5 times the peak stress from the solution of the infinite-half-plane problem at the same distance away from the applied forces. Therefore, proximity of the two chord forces at the chord splice seems to make the application of Whitmore's method at chord splices inappropriate. Recall that in the original tests conducted by Whitmore [1952], the chords were continuous through the joints. Below, an alternative method to estimate stresses in gusset plates at chord splices is proposed.

6.1.3 The Impact of Chord Splice Location on Gusset Plate Stresses

6.1.3.1 Approach to Study the Impact of Splice Locations

The chord splice is not always located at the work point as it is in Joint U10. For joint locations near the mid-span of bridges where the chords resist positive global bending moment or at the supporting piers where global negative bending occurs, large chord tensile or compressive forces are generated as in Joint L2 in BR 90/134N. The large chord forces loads may not be equal and opposite in the two chord members at a joint; therefore requiring one chord member to have a longer connection length than the other another to accommodate the necessary number of fasteners. Thus, the chord splices are often located away from the work point of the joint and may be located near the edge of or even outside the interference zone. The stress distribution in Joints L2 and U3, as shown previously in the beginning of this chapter, that the splice location is an important factor affecting the magnitude and location of the maximum gusset plate stress and the accuracy of the TEP.

To study the effect of the chord splice location, the chord splices were moved in a generic gusset plate joint from the work point by changing the connected length of both connected chord members. Chord splices were moved from left to right at increment of about two rivet spacings (7.5 in) and a total of 11 cases were included. These cases include the possibility

that the chord splice is located inside and outside the interference zone. The chord splice locations considered are shown in Table 6.1 relative to the x-axis illustrated in Figure 6.6. Zero on the x-axis represents the splice located at the work point of the connection and is denoted Case 6. The typical configuration of the gusset plate connection used to study the impact of splice location is illustrated in Figure 6.6 with 11 splice location cases. Note that chamfered diagonals have been removed from the model to have a more general connected member geometry and ease the implementation of the Matlab code that generated the gusset plate geometric input files for ANSYS. Both chords have the same connection length, 51.75 in., from the first row of rivets to the work point. Unless otherwise noted, 0.5 in think gusset plates are used for all analysis in this chapter. The loading profiles for all analyses in this chapter are limited not to generate equivalent stresses over the Von Mises yield stress, which is 51.5 ksi for the steel used here. The rivet pattern simply assumes all rivets are positioned in an uniform grid points.

Considering one target of this study is to understand the stress distributions with the interaction of all connected members and calculate the possible maximum Von Mises stress, a clear picture of individual stress component generated by connected members is necessary before applying the Von Mises criterion to calculate equivalent stress. Therefore, X-direction normal stress distributions in the gusset plate at the chord ends will be used to examine the impact of the chord splice hereafter.

Table 6.1: Splice locations

	Case1	Case2	Case3	Case4	Case5	Case6	Case7	Case8	Case9	Case10	Case11
Chord Splice Location	-37.5	-30	-22.5	-15	-7.5	0	7.5	15	22.5	30	37.5

A mesh refinement study for the baseline geometric configuration of Figure 6.6 shows that a mesh size consisting of 1 in. elements for the entire gusset plate may not be refined enough to represent the normal stresses at the chord splices. A mixed mesh of 0.5 in. average element size at the chord splices and 1.0 in. average element size covering the remainder of

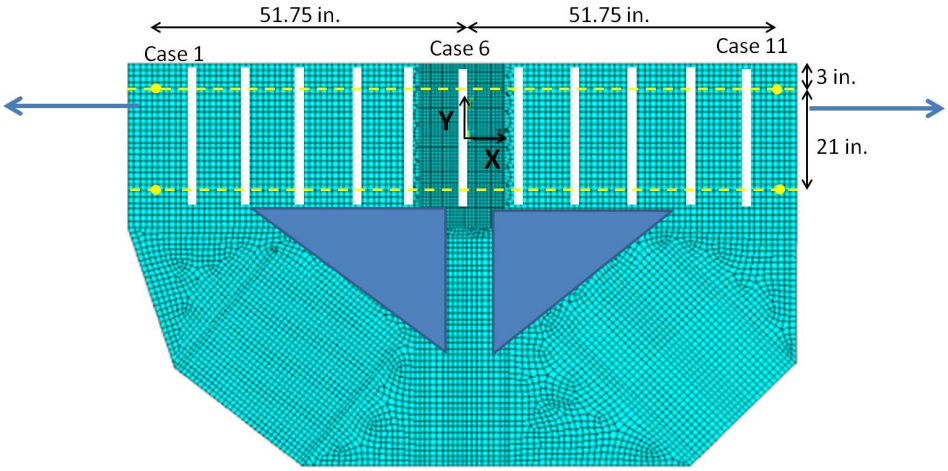

Figure 6.6: Typical Warren type gusset plate with finer mesh in chord splice and a total of 11 cases of splice location

the gusset plate area provide adequate accuracy to study the stress distribution. The mixed mesh has an error percentage of about 1.7% at the maximum stress and has a closer overall distribution to the finest mesh size considered, which was a uniform mesh of $\frac{1}{8}$ in. element size, as shown in Figure 6.7.

6.1.3.2 The Effect of Splice Location on the Stress Distribution

Applying the load, 1190 kips in tension equal and opposite at chord members, to the total 11 cases of splice location gusset plate joints, the X-direction normal stress distributions at the splice for each case were plotted in Figure 6.8. Figure 6.8 shows there is a negligible impact of the splice location on the X-direction normal stress distributions. Only the normal stress distributions at the outermost splice locations, Case 1 and Case 11, have slight differences from other normal stress distributions. This result is counter to the assumptions of Whitmore's method which implies that the connected length and width of a member will determine the maximum stress at the member end. For comparison, the stresses at the chord splice estimated by Whitmore's method are also plotted in Figure 6.8. The shorter

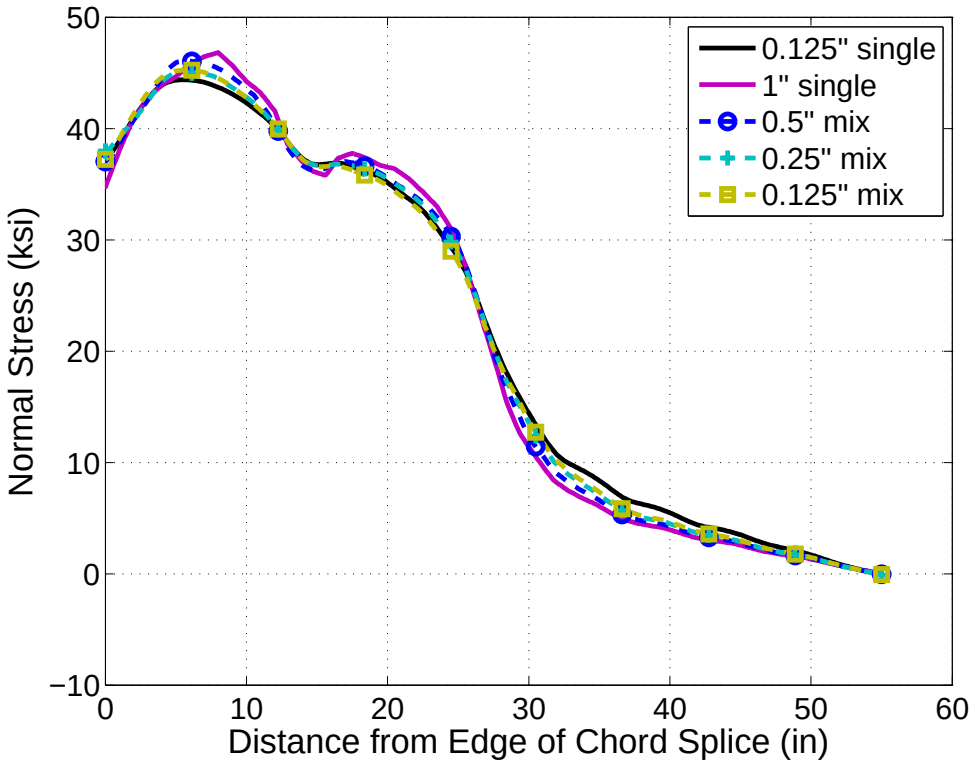

Figure 6.7: Mesh refinement study for normal stress at chord splice which use $\frac{1}{8}$ in. average element size as a baseline and is compared with single 1", mixed 0.5", and mixed 0.25" average element size mesh

connected length of two chords and a 30° dispersion angle are used to calculate Whitmore stress for each case. Figure 6.8 shows the calculated Whitmore stress changes with the splice location while the stress distributions from analyses do not. Further, Whitmore's method also underestimates the maximum stress.

In short, the observation of a trapezoidal stress distribution with a high plateau stress and independence of the distribution to the splice location suggest the application of the Whitmore's method at the chord splice is inappropriate. Another procedure for calculating the stress at gusset plate chord splices is necessary.

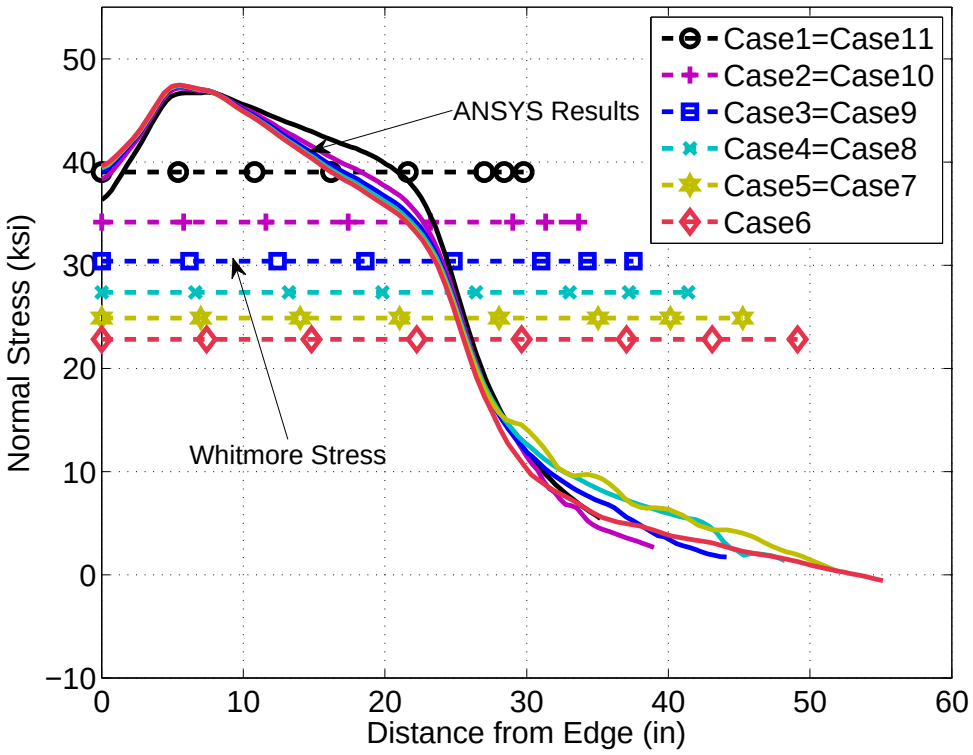

Figure 6.8: Gusset plate normal stresses at different chord splice locations and the calculated Whitmore stresses for each case

6.2 Development of a Model for the Stress Distribution at Gusset Plate Chord Splices

The process of developing a new model to estimate stress at chord splices contains two steps. The first step is to find an acceptable stress distribution representing the characteristics of the stress at chord splices. The second step is to enforce equilibrium on the stress distribution to calculate the required stress values. This is an application of using lower bound plasticity theorem.

Three characteristics of the stress distribution at the chord splice described above are used to develop a model. These are: 1) the linear distributed stress at chord splice is generated by the eccentricity between the axial force at the centroid of the chord and the gusset plate

reaction force that acts a distance away from the chord centroid, 2) the maximum stress of the trapezoidal stress distribution is larger than the Whitmore stress because of the effect of small gap between attached chord members 3) a sharp drop in gusset plate normal stress occurs outside the lines of fasteners at the end of the chord splice.

A possible model for the normal stresses in gusset plates at the ends of chord connections based on the above observations and equilibrium considerations is shown in Figure 6.9. This model assumes that the chord axial force is counteracted by normal stresses from axial force and bending on the gusset plate to satisfy equilibrium. The axial normal stress from axial load in the gusset plate is assigned a trapezoidal distribution with a plateau between the the inner and outer rivet lines of the chord and declines with equal gradient when it is outside of the connected width. The normal stress will decrease to zero at a distance from the fastener line determined by the connected length, L_c and the dispersion angle θ_1 as shown in Figure 6.9. Due to the connection asymmetry, the normal stress away from the inner fastener line can be fully developed while the normal stress away from the outer fastener line will abruptly not be fully developed. This normal stress distribution then causes an eccentricity between the chord axial force and the resulting normal stress distribution in the gusset plates. Therefore, the second part of this model includes a normal stress from gusset plate bending to compensate for the eccentricity. This bending stress may not act over the same width of gusset plate as the normal stress from axial loads and instead assumes a dispersion angle θ_2, as shown in Figure 6.9. The sum of the normal stresses from axial and bending stress will satisfy both force and moment equilibrium with the axial force.

6.2.1 Determination of θ_1 and θ_2 in the Proposed Chord Splice Stress Distribution Model

Dispersion angles θ_1 and θ_2 in the proposed chord splice normal stress distribution model need to be determined and may depend on the connection geometry. To find parameter θ_1, the geometric parameter L/W, connected length over connected width of a chord, is considered to be the critical variable and their relationship is plotted in Figure 6.10(a). Figure 6.10(a) is developed by extending the outer part of a generic gusset plate geometry

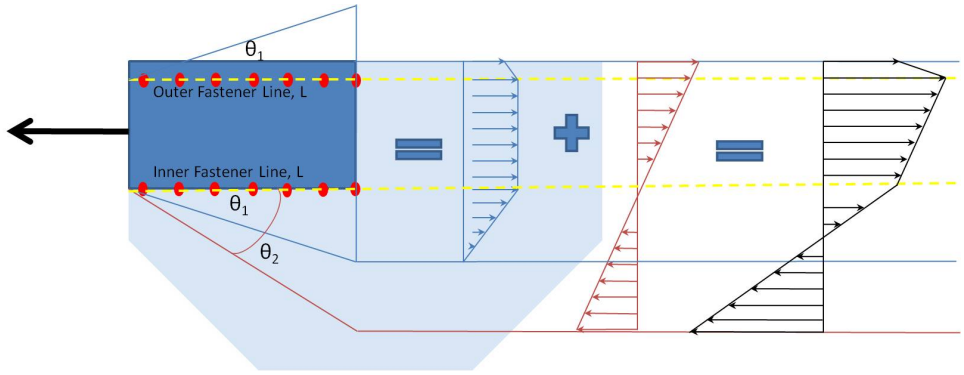

Figure 6.9: Proposed model for normal stress distribution in gusset plates at the chord splices

for different L/W as shown in Figure 6.15; making the connection more symmetric and the normal stress distribution essentially trapezoidal when equal and opposite chord loads are applied. Note that only the chord loads are loaded in this cases. One of the geometries is shown in Figure 6.10(b). The maximum x normal stress along the middle of chord splice is recognized for each L/W and a proper dispersion angel θ_1 for each L/W can be calculated by using the trapezoidal model described above. Figure 6.10(a) shows the dispersion angle θ_1 is not a constant for any cases but decreases with the increase of parameter L/W. For the most common configurations in chord connections, the L/W ranges from 1.5 to 5 where the dispersion angles varies from $\theta_1 = 19°$ to $\theta_1 = 15.5°$. A constant dispersion angle $\theta_1 = 15°$ is suggested such that a conservative estimate of the maximum normal stress at chord splices is obtained and the stress distribution is more approximated independent of connection geometry.

For dispersion angle θ_2 which determines the area over which bending stress are applied, values of 15° or 30° are considered. The choice of these two dispersion angles is based on observations from analyses. In Figure 6.3 and Figure 6.8, the normal stresses in the gusset plate drop close to zero at the edge of the traditional Whitmore's width. This indicates that bending normal stresses act on the area no larger than that found with $\theta_2 = 30°$. On the other hand, for simplicity it would be convenient for the bending stress to act over the

same area as the axial stress and there are no clear reasons why it should not. Therefore, dispersion angles of $\theta_2 = 15°$ and $\theta_2 = 30°$ are regarded as the upper and lower bounds for θ_2.

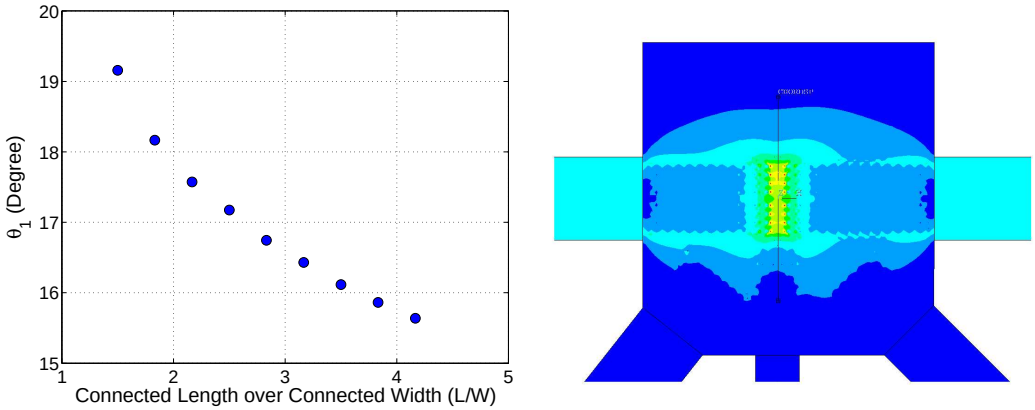

(a) Dispersion angle θ_1 versus L/W geometric parameter

(b) Illustration of model geometry used to study $\theta 1$ dispersion angle

Figure 6.10: Study of the θ_1 in trapezoidal splice stress distribution model

Using the chord splice stress model in Figure 6.9, the normal stresses caused by axial forces and eccentric bending moment can be calculated individually and superimposed. Two cases of dispersion angle θ_2 of 30° and 15° are considered along with the dispersion angle θ_1 of 15° to estimate the normal stress distributions and compare them with the results of finite element analyses in Figures 6.11 and 6.12. The figures show results for the various chord splice locations shown in Figure 6.6. Note that calculating the proposed stress distribution uses the connection length for one of the two connected chords. For splice location Cases 1 through 11 the connection length used in the proposed model and shown in Figures 6.11 and 6.12 is always that for the chord on the left of Figure 6.6. Therefore, the connection length used in the proposed model is the shorter one for Cases 1 through 5 and the longer one for Cases 7 through 11. Because of the symmetry of the splice locations, Cases 1 and 11 are similar but Case 1 uses the short connection length and Case 11 uses the long length in the proposed model in order to distinguish the calculated stress distributions. Figure 6.11 shows the proposed model with $\theta_1 = 15°$ and $\theta_2 = 30°$. As shown the proposed

model does simulate the trend of the stress distributions at the chord splice well while Whitmore's method does not estimate the stress adequately as shown in Figure 6.8. Further observation of Figure 6.11 shows that though the proposed model with $\theta_1 = 15^\circ$ and $\theta_2 = 30^\circ$ better estimates the stress distribution than Whitmore's method, the maximum stress is still underestimated. Additionally, proposed model estimates the slope of the stress distribution outside the connected width of the chord well but underestimates the slope in the connected width of the chord. The different slopes inside and outside the connected width apparently indicate that linear bending curvature is not enough to describe the flexural behavior of the gusset plate at a chord splice. This represents a limitation in the proposed model. This is because the gusset plate is more like a deep beam in which the plane does not remain plane under the flexural load and using constant curvature can not capture this behavior. This indicates that there must be a trade-off between a good estimate of bending stress in the high stress area or in the low stress area if a constant curvature model is used to calculate the gusset plate bending stress.

To improve the estimate of bending stress in the high stress area of the chord splice, the proposed model with $\theta_1 = 15^\circ$ and $\theta_2 = 15^\circ$ is used to calculate the stresses at the chord splice and the results are plotted in Figure 6.12 along with the FE analysis results. A small dispersion angle θ_2 generates smaller area for bending stress and increases the magnitude of the stress at the chord splice. The stress distributions in the high stress area are significantly improved where the maximum stress from the proposed model for different cases of splice location converge to one value to the stresses in a manner similar to the FE solutions. Further, the slopes of the stress distribution in the high stress area is much closer to the FE solution than when $\theta_1 = 15^\circ$ and $\theta_2 = 30^\circ$ are used. Only Case 1 that has a poor estimate for $\theta_1 = 15^\circ$ and $\theta_2 = 15^\circ$ than $\theta_1 = 15^\circ$ and $\theta_2 = 30^\circ$. However, Case 1 is the outermost splice location where the shorter connection length was used in the proposed model. Case 11 is essentially that the same cases but where the longer connection length was used in the model and it shows good agreement with the FE analysis results. Note that using the longer connection length consistently provides a better approximation of the stress distribution as observed by comparing Case 3 with Case 9 and Case 4 and Case 8 in addition to Case 1 and

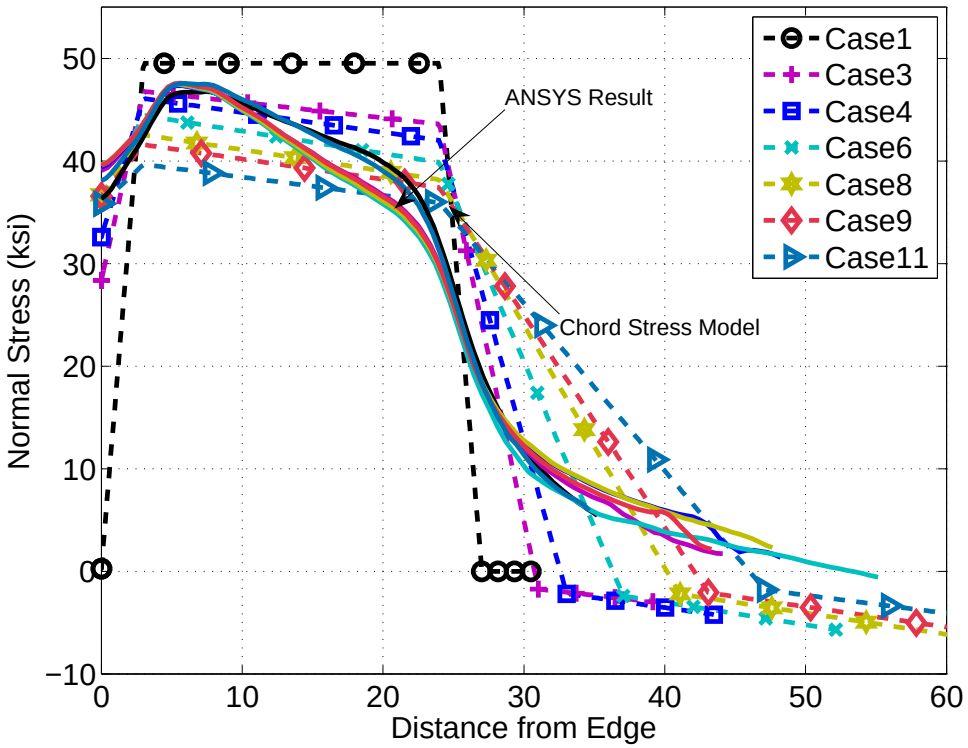

Figure 6.11: Comparison of normal stress at chord splice with analytical results and approximation model using $\theta_1 = 15°$ and $\theta_2 = 30°$

Case 11. Therefore, use of the longer connection length of the two chords is suggested in the proposed gusset plate stress distribution model at chord splice. In addition, the reasonably approximating the maximum stress, the proposed model with $\theta_1 = 15°$ and $\theta_2 = 15°$ also reasonably approximates the stress at the edge of the chord connection where the slope of the stress distribution changes.

Based on the comparison of the proposed model for gusset plate stress distribution at chord splices with $\theta_1 = 15°$ and $\theta_2 = 15°$ or $\theta_2 = 30°$ with FE analysis results, it is recommended that $\theta_1 = 15°$ and $\theta_2 = 15°$ be used.

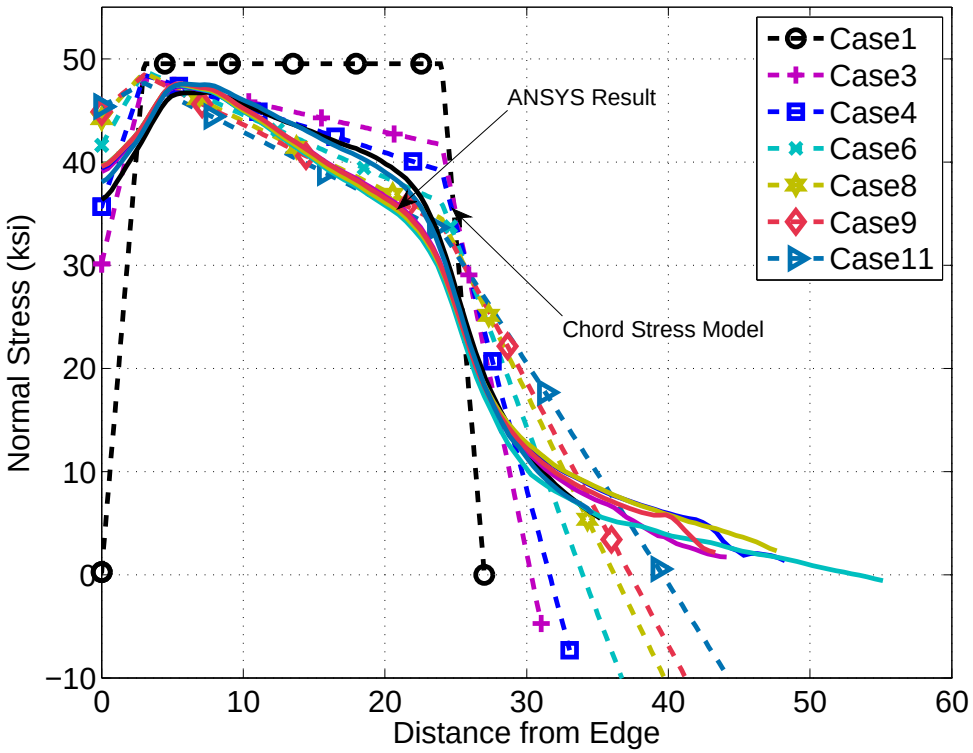

Figure 6.12: Comparison of normal stress at chord splice with analytical results and approximation model using $\theta_1 = 15°$ and $\theta_2 = 15°$

6.2.2 Verification of Normal Stress Distribution at Chord Splice with Gusset Plate Thickness and Rivet Model

Because of the assumption of rigid fasteners in the FE model, the normal stress at the chord splice from the FEA results might be affected by the modeling method. The rigid fastener assumption may cause the stress more concentrated at the end of the chord and generate higher normal stress at the chord splice especially when the gusset plate is thin and more deformable than the connected elements. To verify the rigid fastener model does not affect the stress distribution at the chord splice, the gusset plate thickness was increased to 1.0 in. in the FE model, and additionally, the rigid fasteners were replaced by a deformable rivet spring model, which is developed and verified in Chapter 8, to examine the stress

distributions at the chord splice. Although the rivets were modeled by deformable spring models, the rivet holes were not modeled in the FEA. The $\theta_1 = 15°$ and $\theta_2 = 15°$ trapezoidal stress distribution model was used to predict the stress distribution and was shown with the FEA results in Figures 6.13 and 6.14. Figure 6.13 shows the stress distribution shape is not affected by the thickness of the gusset plates when it is compared with the result using 0.5 in thick gusset plate model as shown in Figure 6.12. The trapezoidal stress distributions have good agreement with the FEA results. The magnitude of the stress in the FEA results of the 1 in. thick gusset plate is about the half of the results for the 0.5 in. thick gusset plate, indicating that the stress decreases proportionally as the thickness increases.

Figure 6.14 shows the FEA results have slightly lower stresses and the stress distributions becomes more nonlinear when the rivets are modeled as deformable springs. However, the difference is not significant and the trapezoidal stress distribution model shows more conservative estimates of the stress distribution at the chord splice in the deformable rivet model. It worthy noting that the deformable springs are designed to exceed its yield stress at this load level. From the study in Chapter 8, when the rivets yield but the connected members and gusset plates are still elastic, the force in each rivet is distributed more uniform along the connection length. This makes the less stress concentration at the end of the connected member which is contrast to the rigid rivet link where the forces taken by the rivets along the connection length is more uneven and higher forces are taken by rivets at end rows. Therefore, as the fastener is elastic in the FEA, the FEA results will approach to the FEA results using rigid fastener model. However, the effect is slight to the stress distribution in the gusset plates. These two cases verify that the current finite modeling methods and the trapezoidal stress distribution model is proper to study the X-direction normal stress at the chord splice.

6.3 Verification of Proposed Stress Distribution Model for Various Chord Connection Geometries

The proposed gusset plate stress distribution model at chord splice uses two constant dispersion angles to describe the axial stress and bending stress at the chord splice. An important

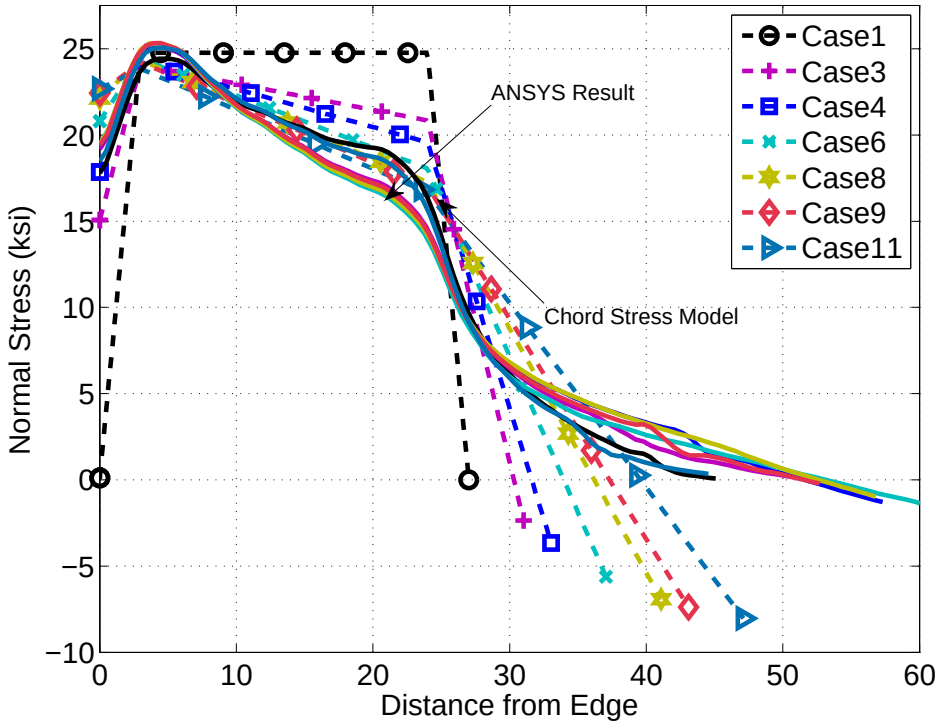

Figure 6.13: Stress distribution at chord splice when the FE model using 1.0 in. think gusset plates

question is if these two constant parameters are suitable for most chord connection geometries which can be represented by the ratio of the connected length to the connected width, L/W. The range of the ratio L/W considered here from 1.0 to 4.0, which covers most gusset plate chord connection geometry encountered in steel truss bridges. The connection ratio L/W are varied by changing the connected length or connected width from the baseline configuration used and described in previous section. Approach 1 varies L/W from 1.8 to 3.8 by fixing the connected width and increasing the connected length while approach 2 varies L/W from 2.0 to 0.9 by fixing the connected length and increasing the connected width. The two approaches are sketched in Figure 6.15 and the exact ratios of L/W considered are listed in Table 6.2.

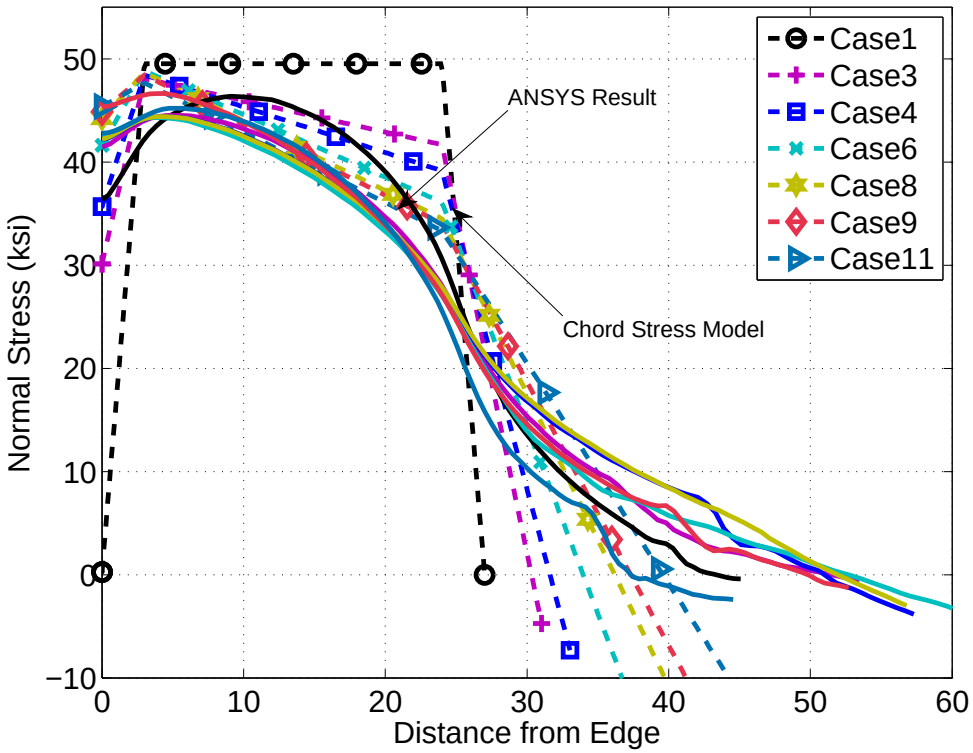

Figure 6.14: Stress distribution at chord splice when the FE model using deformable rivet model developed in Chapter 8

The computed stress distributions from the proposed model with $\theta_1 = 15°$ and $\theta_2 = 15°$ and the FE analyses are shown in Figure 6.16. There are no splice plates attached to the chord splice and the chord loads are only undertaken by gusset plates.

In the approach 1, the range of the high stress is kept constant since the connected width is fixed, whereas the high stress area decreases in approach 2 because the ratio L/W is varied by increasing the connected width. Both approaches together cover the ratios of L/W seen in most gusset plate connections. Figure 6.16 shows that for the studied range of geometry, the proposed stress distribution model provides a reasonable estimate for the stress distribution at the chord splice. Since the dispersion angles θ_1 and θ_2 used in the proposed model are both constant, the proposed model is slightly unconservative when L/W is less 1.5 and slightly

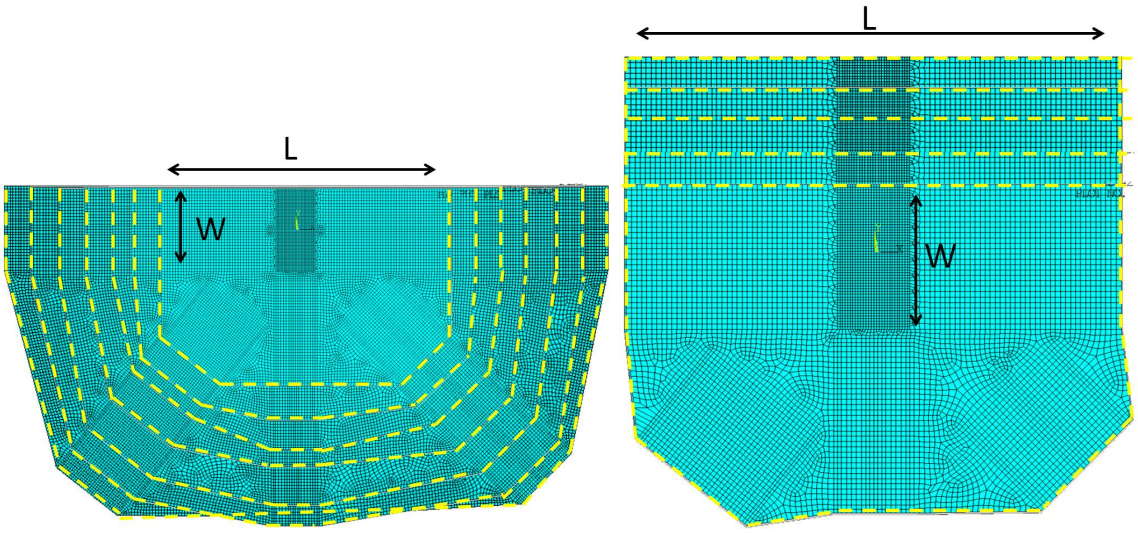

(a) Approach 1: increase connected length and keep the connected width

(b) Approach 2: increase connected width and keep the connected length

Figure 6.15: The gusset plate configuration changes shown as yellow dash line when varying the geometric parameter L/W

Table 6.2: Parameter L/W used to verify the mechanical model

Approach 1(L/W)	1.8	2.2	2.5	2.8	3.2	3.5	3.8
Approach 2(L/W)	2.0	1.5	1.3	1.1	0.9		

conservative when L/W is over 2.5. However, from an engineering point of view, having some conservatism is good when assessing safety and where the model is unconservative, ie. when L/W is less than 1.5, are geometries that are seldom seen in the gusset plate connections. In summary, the study of the geometric parameter L/W demonstrates the proposed trapezoidal model for gusset plate stress distribution at chord splices provides better accuracy for the evaluation of the stress at chord splices than Whitmore's method does.

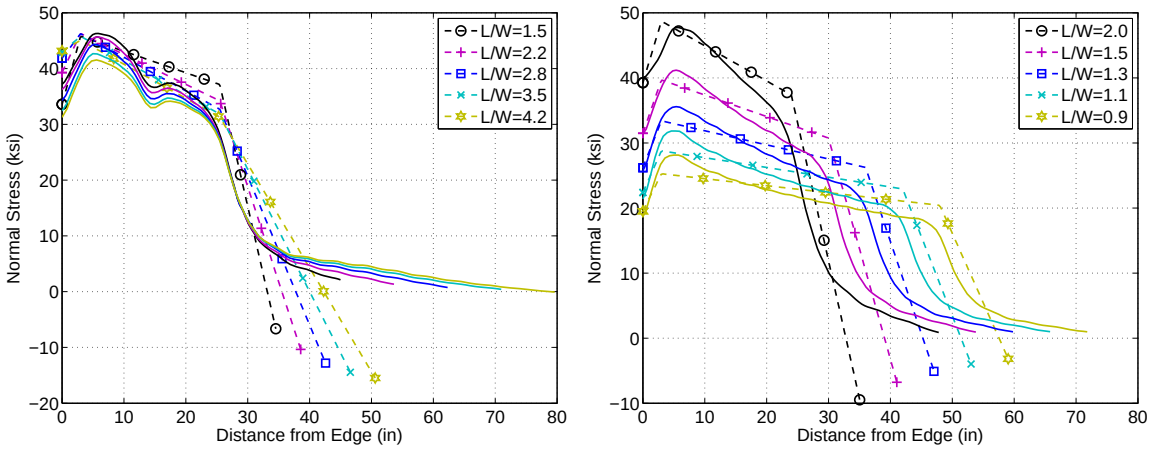

(a) L/W from 1.5 to 4.0

(b) L/W from 0.9 to 2.0

Figure 6.16: Comparison of stress distribution at chord splices between FE analyses, plotted with solid lines, and estimates from the proposed model, plotted with dashed lines. There are no splice plates in these cases

6.3.1 Proposed Model Including Splice Plates

To highlight the stress distributions in gusset plates at chord splices, the gusset plate models used in the previous sections had chords that were only connected through gusset plates at chord splices. Thus, the chord loads were completely transferred by the gusset plates. However, many gusset plate connections have additional splice plates connecting either the top and/or bottom flange of the chords or even connecting the chord webs. Gusset plates, top and bottom flange splice plates, and web splice plates collectively form the so-called chord splice. In this section, the stress distribution model for the stresses in all splice elements will be discussed.

The addition of splice plates into the stress distribution described previously requires several steps which are listed below.

1. Calculate the axial force considered to be undertaken by gusset plates and splice plates

2. Calculate the eccentricity of reacting forces from gusset plates and splice plates relative

to the chord load

3. Calculate the moment using axial force from Step 1 and the eccentricity from Step 2
4. Calculate the neutral axis location using the first moment of area: $\bar{y} = \frac{\sum y^i * A^i_{eff}}{\sum A^i_{eff}}$
5. Calculate the moment of inertia to relative the neutral axis for the gusset plates, and whatever web splice plates, and flange splice plates are present at the chord splice
6. Calculate normal stress along the chord splice by superimposing the normal stress from axial forces and bending moment

In Step 1, deformation compatibility is considered between gusset plates and additional splice plates to be included in the stress distribution model. The first assumption is that the gusset plates and web splice plates have the same deformation in the chord's direction since they are fastened by the same fasteners. Thus, the maximum normal stresses, σ in the gusset plates and web splice plates are assumed to be the same. Second, for compatibility between the flange splice plates and gusset plates, they could be assumed to have a small relative displacement to each other. Based on these two different assumptions, two different approached can be used to calculate the axial force as described below.

If no relative displacement between the gusset plates and flange splice plates is assumed, the flange splice plates have the same stress distribution as the web splice plates and gusset plates. This results in Eq. 6.1a, where the chord load, F_{chord}, is assumed to result in equal axial stress, σ_{axial} in the gusset plates, web splice plates, and flange splice plates. The effective areas for these plates, A_{eff} considers trapezoidal stress distribution for the gusset plates, and rectangular stress distributions for all splice plates. A schematic of this axial stresses at a chord splice for these three components is shown in Figure 6.17. For the compatibility condition discussed above and in 6.1a, the stresses σ_1 and σ_2 are equal to σ_{axial}.

The second approach assumes that there may be small relative displacements between flange splice plates and gusset plates due to the flexibility of the chord section so that only forces carried through the chord webs would be transmitted through the gusset plates and web

splice plates. Thus, stresses in the flange splice plates result from the forces in the chord flanges and may be different from the stress in the gusset plates which undertake load from chord web. Eq. 6.2a describes this compatibility condition, where $\frac{A_{web}}{A_{chord}}$ is the ratio of the chord web area to the total chord area and F_{gp} and F_{websp} are the forces carried by the gusset plates and web splice plates.

The remaining Steps 2 through 6 are accomplished using Eqs. 6.1b through 6.1d or Eqs. 6.2b through 6.2d for the two different assumptions regarding the relative displacement between the flange splice plates and gusset plates. In these equations, it is assumed that the splice plates and gusset plates all contribute to resisting the moment resulting from eccentricity between the chord centroid and the neutral axis of the combined splice and gusset plates.

$$F_{chord} = \sigma_{axial} * (A_{eff}^{gp} + A_{eff}^{websp} + A_{eff}^{flsp}) \tag{6.1a}$$

$$e = (y_{chord} - \bar{y}) = y_{chord} - \frac{\sum y^i * f_{eff}^i}{\sum f_{eff}^i} \quad i = 1, 2, 3 \tag{6.1b}$$

$$M = F_{chord} * e \tag{6.1c}$$

$$\sigma = \sigma_{axial} + \frac{My}{I_{eff}^{gp} + I_{eff}^{websp} + I_{eff}^{flsp}} \tag{6.1d}$$

$$F_{chord} * (\frac{A_{web}}{A_{chord}}) = F_{gp} + F_{websp} = \sigma_{axial} * (A_{eff}^{gp} + A_{eff}^{websp}) \tag{6.2a}$$

$$e = (y_{chord} - \bar{y}) = y_{chord} - \frac{\sum y^i * f_{eff}^i}{\sum f_{eff}^i} \quad i = 1, 2 \tag{6.2b}$$

$$M = F_{chord} * (\frac{A_{web}}{A_{chord}}) * e \tag{6.2c}$$

$$\sigma = \sigma_{axial} + \frac{My}{I_{eff}^{gp} + I_{eff}^{websp} + I_{eff}^{flsp}} \tag{6.2d}$$

The variables of Eqs. 6.1 and 6.2 are defined as follow: where A_{eff}^{gp} is the effective gusset plate area considering the trapezoidal axial stress distribution for the gusset plates which has been described previously, $A_{eff}^{websp} = t_{websp} * w_{websp}$ where t_{websp} is the thickness and w_{websp} is the width of web splice plates and $A_{eff}^{flsp} = t_{flsp} * w_{flsp}$ where t_{flsp} is the thickness, w_{flsp} is the width of flange splice plates, A_{web} is the web area of the chord section, A_{chord} is the total area of the chord section, f_{eff} is the internal stress in the splice elements times their areas, e is the eccentricity between chord centroid to center of the axial stresses in the gusset and splice plates, M is the eccentric bending moment, and I_{eff} is the moment of inertia to the neutral axis for individual chord splice elements.

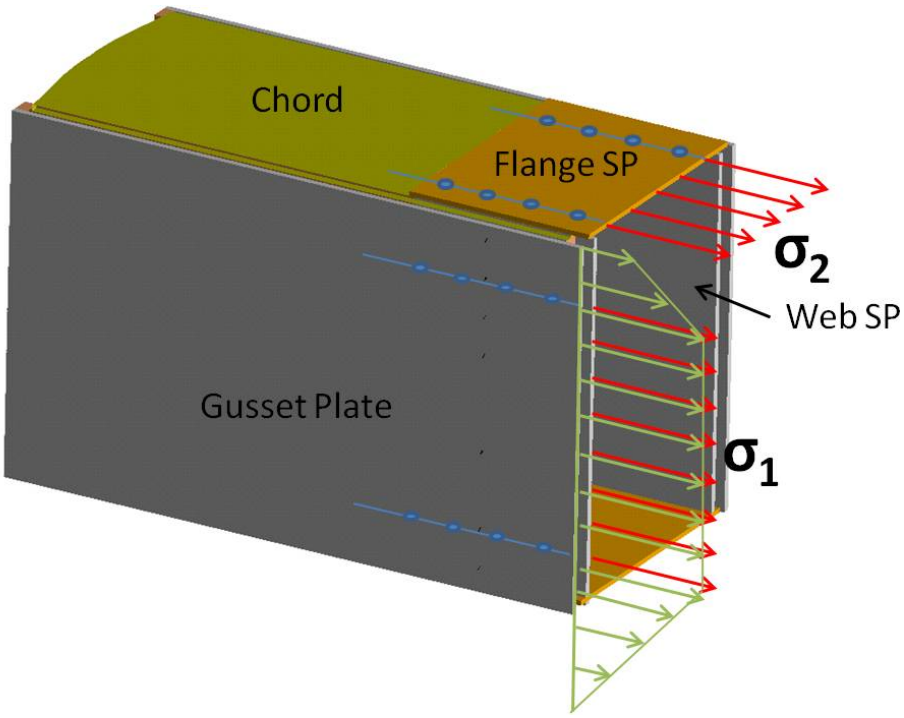

Figure 6.17: Schematic of the stress from gusset plate, web splice plates, and flange splice plates

To verify these two approaches for the trapezoidal stress distribution model including splice plates at the chord splice, Eqs. 6.1 and 6.2 are used for calculating the stress distributions at chord splice considering two gusset plate models with: 1) 3/8" thick flange splice plates and 2) 3/8" thick flange splice plates and 1/2" thick web splice plates. The computed results for the normal stress in the gusset plates at chord splices are compared with the FE analysis results shown in Figure 6.18 and Figure 6.19 for the range of L/W described in Table 6.2.

In Figure 6.16, the gusset plate stress distribution model in the cases of no splice plates showed generally a conservative estimates for L/W larger than 1.5, which covers most of gusset plate connections. Figures 6.18 and 6.19, however, show the simplifying assumptions used to consider the presence of chord splice plates may slightly change the results. Eq. 6.1 appears to be more conservative when the flange and web plates are included in a chord splice but less conservative when only flange splice plates are used; Eq. 6.2 appears to have the opposite results. The real situation seems to be between the assumptions used in Eq. 6.1 and Eq. 6.2. It is difficult to determine whether one method is superior to the other from these comparison since the FE models used here neglecting fastener deformations and assumed rigid link between plates. Overall, the stress distribution model provides a reasonably good estimate of the gusset plate stress at the chord splice even when additional splice plates are present. Eqs. 6.1 and 6.2 provide better estimates in different conditions, but the errors in both cases are tolerable. Eq. 6.1 is suggested for engineering practice for two reasons: 1) it has better performance when the stress interaction from diagonals is considered in the next section and 2) it considers all possible connected splice plates at the same time whether calculating the axial stress or the bending stress which is a simpler and more succinct solution for practice.

6.4 Impact of Adjacent Member Forces on Gusset Plate Stress at the Chord Splice

The gusset plate stress distribution at the chord splice discussed in this chapter has been limited to the stresses incurred by equal and opposite chord loads. In most gusset plate connections, chord loads are not equal and diagonal loads could have significant impacts on

the stress distributions at chord splices. Figure 6.20 shows the gusset plate stress distributions at chord splices when the chord splice is located in different positions and all other members attached to the gusset plates are loaded. The stress distributions shown do not share a single shape as observed when only the chords are loaded and the splice location is varied (Figure 6.8). The changes in the stress distribution show a significant influence from the diagonal loads and the unequal chord loads. The understanding of how other loads interact and affect the stress at the chord splice is key to understanding the overall stress distributions in gusset plates. Therefore, to study the interaction of these effects at chord splices in gusset plates, the traits of each stress distribution generated by the individual member loads need be inspected carefully and approximated stress models for each stress component and critical sections also need to be developed. This is the topic of the next section.

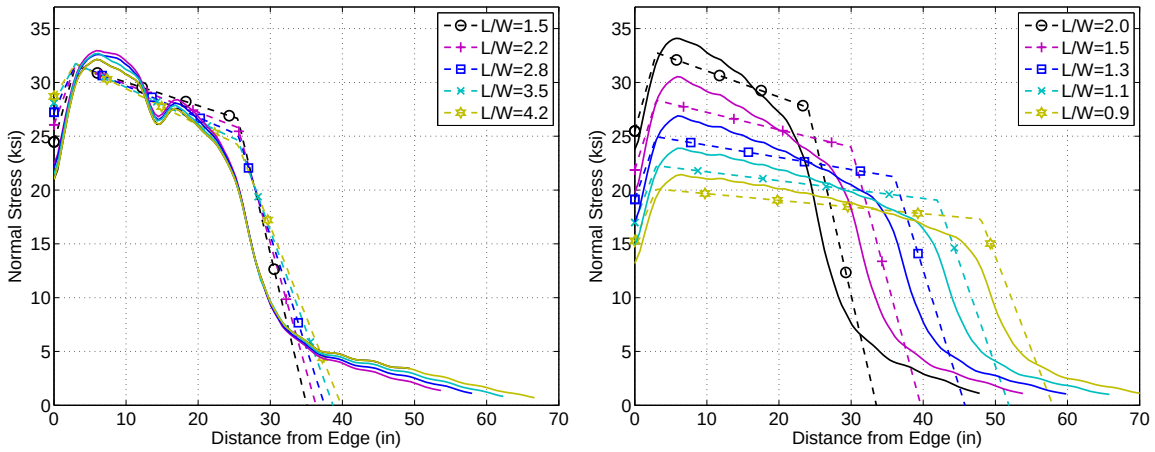

(a) L/W from 1.5 to 4.0 using Eq. 6.1

(b) L/W from 0.9 to 2.0 using Eq. 6.1

(c) L/W from 0.9 to 2.0 using Eq. 6.2

(d) L/W from 0.9 to 2.0 using Eq. 6.2

Figure 6.18: Comparison of the gusset plate stresses from FE analyses, represented by solid lines, with those from the chord splice stress distribution model, represented by dashed lines, for the case of 3/8" thick flange splice plates

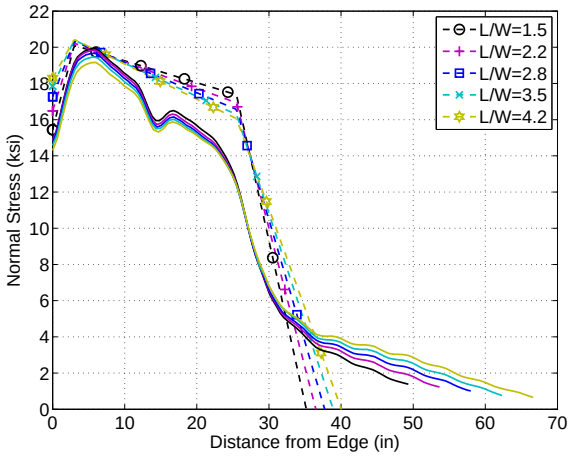

(a) L/W from 1.5 to 4.0 using Eq. 6.1

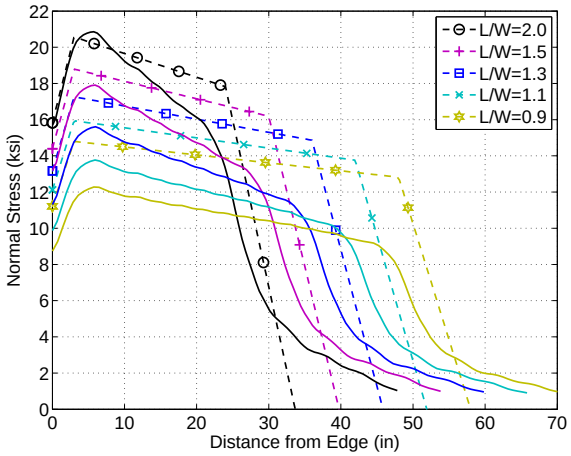

(b) L/W from 0.9 to 2.0 using Eq. 6.1

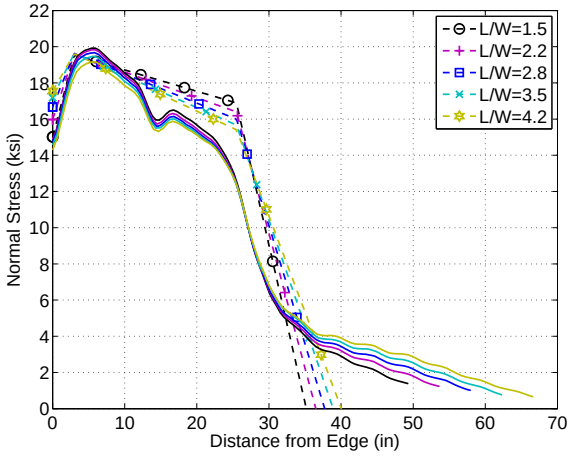

(c) L/W from 0.9 to 2.0 using Eq. 6.2

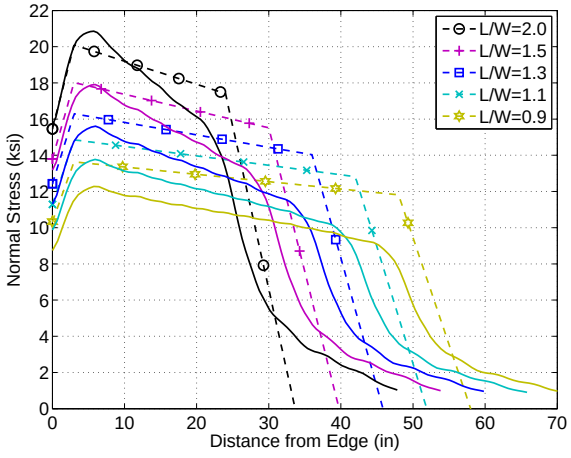

(d) L/W from 0.9 to 2.0 using Eq. 6.2

Figure 6.19: Comparison of the gusset plate stresses from FE analyses, represented by solid lines, with those from the chord splice stress distribution model, represented by dashed lines, for the case of 3/8" thick flange splice plates and 1/2"′ thick web splice plates

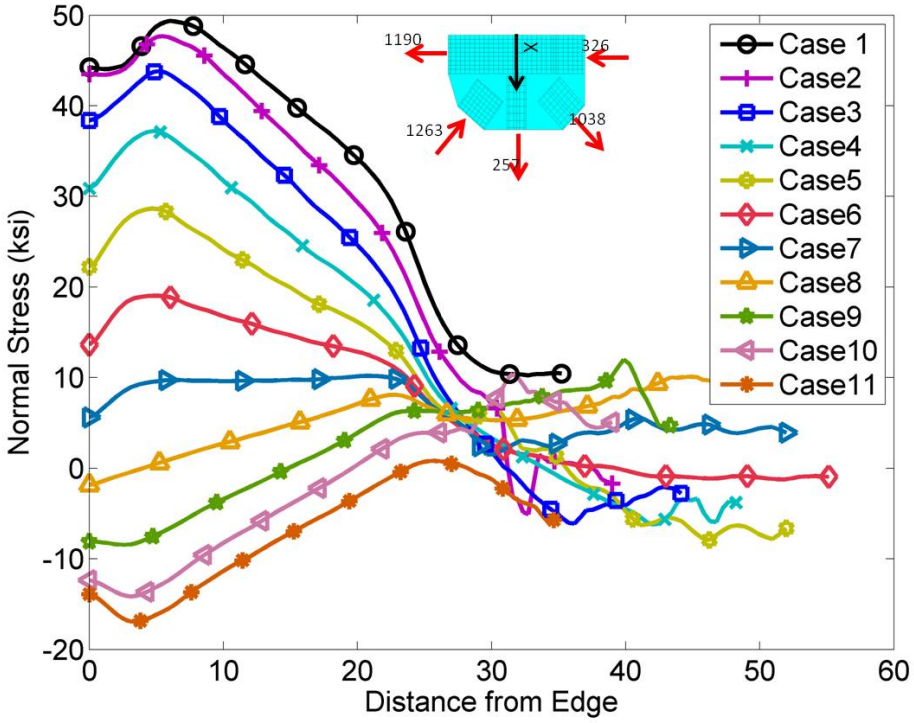

Figure 6.20: Stress distributions at 11 chord splice locations with all attached members loaded in the same loading distribution

Chapter 7

APPROXIMATION OF ELASTIC STRESS DISTRIBUTIONS AT CRITICAL SECTIONS AND EQUIVALENT MAXIMUM STRESS IN GUSSET PLATES

7.1 Introduction

This chapter examines the distributions of stress components, i.e. shear and normal stresses, at critical sections of steel truss bridge gusset plates. Observations are made about the stress distributions at the critical sections, and simple approximated stress distribution models for predicting them are developed. The geometric parameters considered are discussed below but in general the gusset plate geometry used here is that of Joint U10 from the I-35W Bridge. In the end of this chapter the methods developed here for computing stress components are used to predict the maximum stress at critical locations in several of the gusset plate configurations discussed in previous chapters.

7.2 Consideration of Gusset Plate Parameters

Previous studies including the analyses discussed in previous sections have shown the maximum stress in steel truss bridge gusset plates can occur at several critical locations (Whitmore [1952], Vasarhelyi [1971], and FHWA [2009]). These critical locations include the Whitmore section at the end of diagonals, the end of chords at splices, along horizontal sections between chords and diagonals or along vertical sections on both sides of hangers. The maximum stress at these critical sections may result from an individual member force or the interactions of several member forces. The stresses incurred at the end of diagonals were explicitly discussed by Whitmore [1952] whereas the other interaction of stresses from several elements are implicitly referred to in other studies. High stresses at chord splices were observed by Vasarhelyi [1971]. The global shear force along the horizontal section is

regarded as the interaction of diagonal member forces in the FHWA guide (FHWA [2009]). A schematic shows possible critical sections of a gusset plate in Figure 7.1 including sections at the chord splice, along the horizontal section, and the vertical sections. However, the lack of comprehensive analysis of the contribution of all the stress components generated by each member force make the estimate of the stress distributions at these critical section and the maximum stress in gusset plates difficult. The two main reasons that a comprehensive analysis is difficult and has not been performed to date are the diversities of 1) geometries and 2) loading profiles.

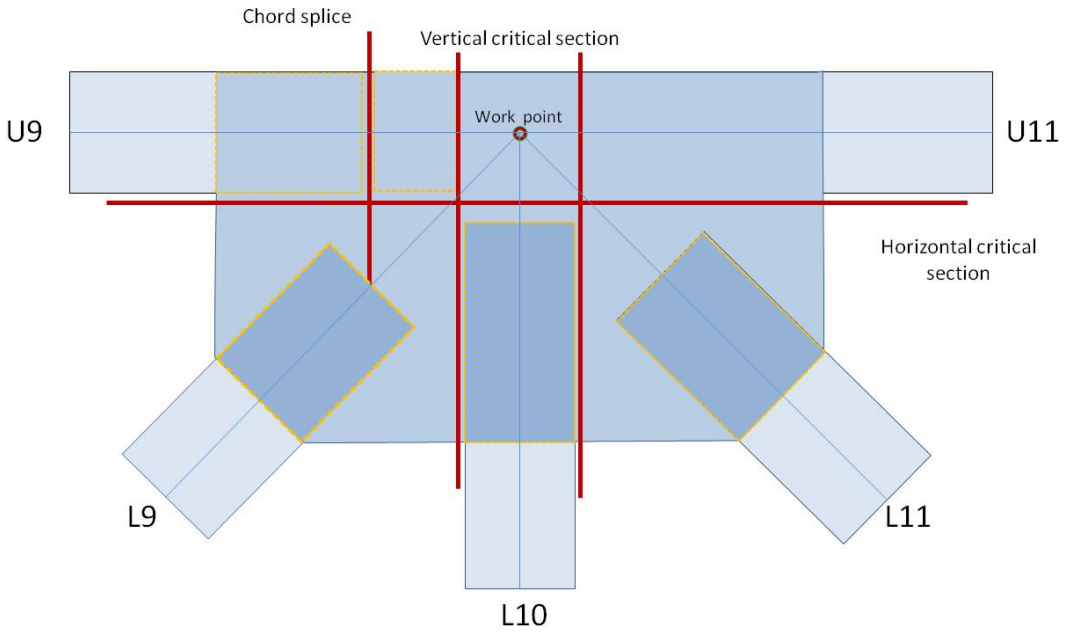

Figure 7.1: Illustration of critical sections in gusset plate

Geometric parameters such as the location of the chord splice in a gusset plate have significant impact on gusset plate stress distributions even for the same loading profiles as shown in Figure 6.20. In addition, geometric parameters such as the angles of the diagonals, the rivet arrangement, and the overall connection types also complicate the geometry and stress distributions. Additionally, the connections in different locations of a bridge may generate very different gusset plate loadings such as high diagonal forces, high chord forces, or the

presence of zero-force members. Thus, distilling the key parameters that affect the stress distributions in gusset plates and studying the interaction of theses stresses is critical for developing a simple yet more refined model than the TEP for estimating maximum gusset plate stress.

In this chapter, these parameters are considered and their influence on the stress at several critical sections of gusset plates are studied. Nevertheless, it is difficult to design a study matrix to include all these parameters at the same time since their correlations are not clear. Therefore, among these geometric parameters, the chord splice location is regarded as the most important geometric factor and also has not been studied thoroughly in previous research. Here the splice locations from Chapter 6 described in Figure 6.6 and Table 6.1 are used. The loading profiles are regarded as an independent variable to the splice location and are described in the following sections. Both parameters are used to study stress components at the critical sections in gusset plates using the FE models described and validated in previous sections.

At the critical sections, as shown in Figure 7.1, stresses generated by individual forces will be considered,

- XY shear stress at the horizontal section generated by diagonals and chords,
- Y-direction normal stress at the horizontal section generated by diagonals and the hanger,
- X-direction normal stress at the chord splice generated by chords and diagonals,
- XY shear stress at the vertical section generated by diagonals and the hanger.

On these critical sections, component stress distributions might be affected by several member forces. It is therefore proposed that if the stress distributions generated by individual member forces can be estimated through simple mechanical models, meaning the effective magnitude and range of the individual stress distributions, the resulting complete stress distributions can be acquired by superimposing those individual stress distributions, enabling the maximum stress on these critical section to be estimated. To achieve this task,

specially designed loading profiles, i.e. distributions of forces in connected truss members, are used to isolate the stresses from individual members at certain gusset plate sections. These specially designed loading profiles are used as parameters in the matrix for this study.

Four loading profile subsets are used: 1) chord loads are varied and loads in the diagonals and hanger are maintained constant 2) loads in the diagonals and hanger are varied and loads in the chords are maintained constant 3) the ratio of the chord load to the diagonal load is varied, and 4) the diagonal and chord loads on one side of gusset are varied and the chord and diagonal loads on the other side are maintained constant. Each loading profile subset is used to study one or two specific stress distributions at the critical gusset plate sections and contains several loading cases to generate the resulting trends in stress distribution change with respect to the loading changes. The details of these loading profiles and the resulting observations of the stress component distributions at critical sections are described in later sections of this chapter.

The parameter used to study the stress distributions are organized in the study matrices shown in Figure 7.2.

7.3 Correlation of Stress Distributions

Prior to the discussion of the stress distributions resulted from the parametric study of the intended studied matrix, methods to evaluate the variability and similarity of stress distributions are necessary. Statistical tools are introduced here to quantify the correlation between stress distributions. The coefficient of variation, C_v is used to measure the variance of a data set and is defined as the ratio of the standard deviation σ to the mean μ. The correlation coefficient, R, is used to measure the similarity between two data sets (random variables) and is defined as the covariance of two data sets divided by the square root of the product of the two variances from the two data sets, i.e. product of standard deviation of the two data sets. The equations of coefficient of variation and the correlation coefficient are shown in Eq. 7.1 and 7.2 respectively:

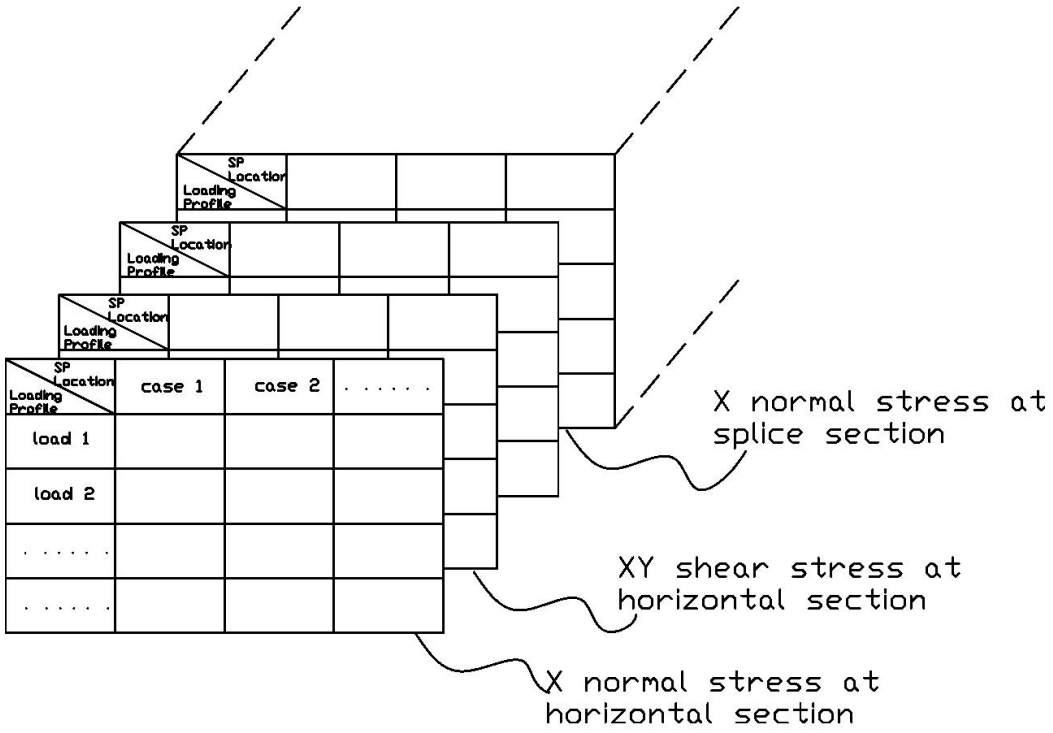

Figure 7.2: Schematics of parameter study matrices

$$C_v = \frac{\sigma}{\mu} \tag{7.1}$$

where σ is the standard deviation and μ is mean value of the distribution across the parameter to study

$$R = \frac{Cov(x,y)}{\sqrt{Var(x)Var(y)}} = \frac{Cov(xy)}{\sigma_x \sigma_y} \tag{7.2}$$

where x and y is two data sets or two random variables, $Cov(x,y)$ is covariance of the two data sets, and $Var(x)$ and $Var(y)$ is variance of the data sets.

To apply these statistical tools to our comparison of stress distributions, the stress data are arranged in the following format. Sampled stress point along a distribution at a certain

section is denoted $\mathbf{a} = [a_1 a_2 \cdots a_n]^T$, $\mathbf{b} = [b_1 b_2 \cdots b_n]^T$ and so on where a_i and b_i is the stress at the same location along the section. Each data set is inserted in a data matrix as a column data set where $X \in \Re_{m \times n}$, m in rows indicates the number of stress sample points in a distribution, and n in columns indicates the number of data sets:

$$X = \Big(\mathbf{a}, \mathbf{b}, \mathbf{c}, \cdots\Big)$$

In the application of the above, Eq. 7.1 will compute the coefficient of variation for each row of X to evaluate the variability of stress at each stress sample location in the range of the stress distribution. Directly using the maximum value of the coefficient of variation may not be proper if the sampled point has mean value, μ, close to zero and therefore, have a very large coefficient of variation. To avoid this condition and focus the concern on the maximum stress along the distribution, Eq 7.3 considers the coefficient of variation at the sampled location having the maximum absolute mean value and is denoted by C_v^{max}.

$$C_v^{max} = \frac{\sigma}{\mu_{max}} \text{ at the maximum absolute mean} \tag{7.3}$$

In the application of correlation coefficient, Eq. 7.2 can be calculated using matrix form. For a $m \times n$ data matrix X, the correlation coefficient matrix is $n \times n$. The matrix R_{ij} is a symmetric matrix. The diagonal of the correlation coefficient matrix is always 1, and the off-diagonal term R_{ij} represents the strength of relation between data column i and data column j in the X data matrix. The off-diagonal term will always between -1.0 and 1.0. R_{ij} close to 1.0 represents a strong positive linear relationship between the data columns i and j, R_{ij} close to -1.0 represents a strong negative linear relationship between the data columns i and j, and R_{ij} close or equal to 0 suggest there is no linear relationship between the data columns. Since the strength of the relation is the concern, the correlation coefficient can be taken absolute value for convenience. Therefore, the minimum value of a correlation coefficient matrix is used to represent the least relation for a group of stress distributions generated by a studied parameter, i.e. geometric parameters or loading parameters.

In general, C_v^{max} is used to evaluate the fluctuation of stress at the location of the highest stress magnitude from several distributions and a small number represents each distribution

has similar maximum stress. The minimum R_{ij}^{min} in the correlation coefficient matrix represents the least relation between any two distributions in a several stress distributions along the critical sections and a number close to 1.0 represents similar stress distributions of the stress distributions in the group. A number of correlation coefficient close to 0.0 represents the shape of the stress distributions in the group significantly very and are affected by the studied parameter.

When the approximated stress distributions calculated using new developed methods or current code are compared with the FEA results, the data matrix X will only have two or three columns of stress distribution data and the value from the FEA results will be regarded as a "correct" answer for comparison. Similar to the C_v^{max}, the error percentage R_{err} is used to consider the difference of the stress between the approximated stress and the FEA results at the maximum stress from the distribution of the FEA results. Simply, the correlation coefficient R will represent the similarity of stress distribution shape between approximated stress and the FEA result.

7.4 Loading Profiles

This section describes four loading profiles that will be designed to reveal the impact of specific effect that different member forces have on the stress distribution at a critical section. Each subsection describes a loading profile type, each containing several actual load distributions.

The basic loading profiles considered are variations of the loads for Joint U10 of the I35-W bridge. The original distribution for the loads estimated at the time of failure of the bridge had traits of near equal yet opposite diagonal forces, high tension in one chord, low compression in another chord, and light tension in hanger. This loading profile is normalized by its shear force along a horizontal line between the chords and diagonals, i.e. the sum of the chord forces, to provide more detail for the profile's characteristics. The loads for each member at Joint U10 can be represented by the ratio of the member force to the horizontal shear force and would be: load $U9 = 0.78V_h$, load $L9 = -0.52V_h/cos\alpha$, load $L10 = 0V_h$, load

$L11 = 0.48V_h/cos\beta$, load $U11 = -0.22V_h$, where $V_h = 1516kips$, $\alpha = 51.70°$ and $\beta = 45°$. A schematic demonstrating the symbols used in loading profiles is shown in Figure 7.3.

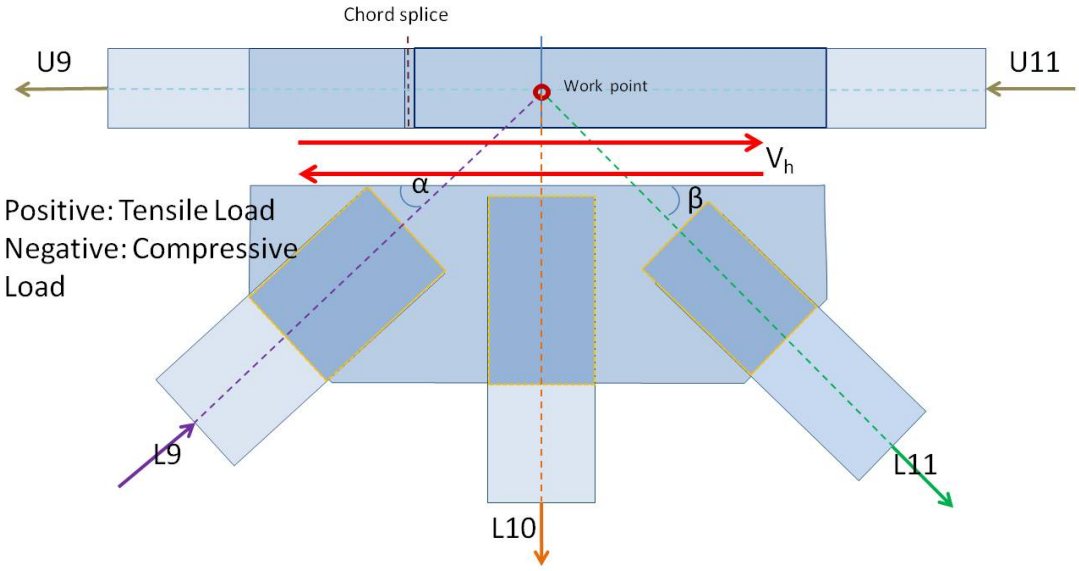

Figure 7.3: Illustration of symbols used in loading profiles

7.4.1 Type I Loading Profiles

Type I Loading Profiles are designed to examine the effect of changes in the chord loads on the stress distributions at the critical sections. The XY shear stress at the horizontal critical section and the X-direction normal stress at chord splice are assumed to be affected by the load changes in the chords. In these loading profiles, the loads in the diagonals and the hanger are kept constant and the loads in the chord member U9 are varied from $1.0V_h$, $0.5V_h$, $0V_h$, and $-0.5V_h$. Then the loads in the member U11 are varied to maintain joint equilibrium. Since the intention is to study the elastic stress distributions, it was ensured that all loading profiles do not yield the gusset plate anywhere. The four loads in Type I Loading Profiles are denoted by Load 1, Load 2, Load 3, and Load4,and are listed in Table 7.1.

Table 7.1: Type I Loading Profiles include four loads

	Load 1 (kips)	Load 2 (kips)	Load 3 (kips)	Load 4 (kips)
U9	909.73	454.87	0	-454.87
L9	-757.63	-757.63	-757.63	-757.63
L10	154.40	154.40	154.40	154.40
L11	622.53	622.53	622.53	622.53
U11	0	-454.87	-909.73	-1364.59

[1] Negative sign means compression loads

7.4.2 Type II Loading Profiles

The Type II Loading Profiles include five loads developed by varying the diagonal loads and fixing the chord loads. Diagonal load is important to the stress on the gusset plates and is assumed to affect all the considered critical sections. Type II Loading Profiles will be used to study the diagonal load influence on the XY shear stress along the horizontal and vertical sections and on the X-direction normal stress at the chord splice. Loads in the Type II Loading Profile is named from Load 5 to Load 9. Load 5 to Load 9 in the Type II Loading Profiles have fixed chord loads of $0.785V_h$ and $0.215V_h$ for the Chord U9 and U11, where V_h is the shear force at the horizontal critical section. The diagonal load of Member L9, the left diagonal, changes from $-1.0V_h/\cos\alpha$, $-0.5V_h/\cos\alpha$, $0V_h/\cos\alpha$, $0.3V_h/\cos\alpha$, where α is the angle from the diagonal to the chord, while the loads at Member L11 vary from $0V_h/\cos\beta$, $0.5V_h/\cos\beta$, $1.0V_h/\cos\beta$, $1.3V_h/\cos\beta$, where β is the angle between Members L11 and U11. The Load 9 has the same diagonal loads as Load 6 but has slightly adjusted chord loads to have equal and opposite loads of $0.5V_h$ and $-0.5V_h$. In all Type II Loading Profiles, the load in the hanger is adjusted to maintain the equilibrium of the joint. Each load of the Type II Loading Profiles is listed in Table 7.2.

Table 7.2: Type II Loading Profiles

	Load 5 (kips)	Load 6 (kips)	Load 7 (kips)	Load 8 (kips)	Load 9 (kips)
U9	475.96	475.96	475.96	475.96	303.24
L9	-978.61	-489.31	0	293.58	-489.31
L10	768.02	80.77	-606.49	-1018.84	80.77
L11	0	428.85	857.70	1114.86	428.85
U11	-130.52	-130.52	-130.52	-130.52	-303.24

[1] Negative sign means compression loads

7.4.3 Type III Loading Profiles

The Type III Loading Profiles is used to study the shear stress distributions interacted between the diagonal and chord loads along the horizontal section. Because the shear stress along the horizontal section could be affected by loads from both members, the Type III Loading Profiles are designed to vary the load ratio between the chord load and the horizontal component of the diagonal load. The chord load was gradually increased to have the six times magnitudes of the horizontal component of the diagonal loads. There are a total of seven Type III Loading Profiles which have the ratio of the chord load to the horizontal component of diagonal load on the same side ranging from 0.5 to 6.0. The diagonal and hanger loads are kept constant and load in the opposite chord is used to balance the equilibrium of the joint. To keep the overall gusset plate behavior in the elastic range, the overall load levels are decreased to have the total horizontal shear force equal to 266.56 kips which is less than previous loading profiles.

7.4.4 Type IV Loading Profiles

The Type IV Loading Profiles are designed to investigate the impact of the diagonal load from the other side on the XY shear stress distributions at the vertical critical section shown in Figure 7.1. The vertical sections between the diagonals and hangers are important

Table 7.3: Type III Loading Profiles

	Load 10 (kips)	Load 11 (kips)	Load 12 (kips)	Load 13 (kips)	Load 14 (kips)	Load 15 (kips)	Load 16 (kips)
U9	78.26	156.51	313.02	469.53	626.04	782.55	939.06
L9	-252.54	-252.54	-252.54	-252.54	-252.54	-252.54	-252.54
L10	88.15	88.15	88.15	88.15	88.15	88.15	88.15
L11	155.63	155.63	155.63	155.63	155.63	155.63	155.63
U11	-188.30	-110.05	46.46	202.97	359.48	515.99	675.5
$U9/L9cos\alpha^2$	0.5	1	2	3	4	5	6
$U11/L11cos\beta^{2,3}$	1.7	1	-0.42	-1.84	-3.27	-4.69	-6.14

[1] Negative sign means compression loads

[2] α is the angle between U9 and L9 and β is the angle between U11 and L11

[3] Negative ratio indicates the same loading direction of chord and diagonal in one side of the gusset plate

locations where yielding can initiate in certain cases. The Type IV Loading Profiles are developed by fixing the loads in the chord and diagonal on the left part of the gusset plate connection, Members U9 and L9, and varying the right diagonal loads, L11. The right chord and hanger are used to keep the joint in equilibrium. The Type IV Loading Profiles are listed in Table 7.4.

7.5 Splice Locations and FE Model

The FE model used in the analyses in this chapter is the same model in Chapter 6 Section 6.1 but includes variation of loading profiles dscribed above. The gusset plate is 0.5 in. thick and the chord splice location is regarded as an important parameter and varies the location from the left side of the gusset plate to its right side, denoting SP1, SP2, SP3...etc. The eleven splice locations are again shown in Figure 7.4. Each splice location is 7.5 in. away from the previous splice location in the gusset plates. The splice locations are listed in Table 6.1. The length from the work point to the end row of rivets near the gusset plate

Table 7.4: Type IV Loading Profiles

	Load 17 (kips)	Load 18 (kips)	Load 19 (kips)	Load 20 (kips)	Load 21 (kips)
U9	475.96	475.96	475.96	475.96	475.96
L9	-978.61	-978.61	-978.61	-978.61	-978.61
L10	768.02	537.62	384.01	230.41	0
L11	0	325.85	543.08	760.31	1086.15
U11	-130.52	-360.93	-514.54	-668.14	-898.55

[1] Negative sign means compression loads

edge is 51.75 in. for both sides. SP6 represents the splice location passes through the work point. SP5 and SP 7 are close to the critical section along the left and right sides of the hanger. SP1 and SP11 are the outermost splice locations. The mesh size in the chord splice is 0.5 in. for the element edge length and is 1 in. the element edge length elsewhere in the gusset plates.

7.6 XY Shear Stress Distribution at the Horizontal Section

7.6.1 Observations of the XY Shear Stress at the Horizontal Section

7.6.1.1 Observations of the XY Shear Stress at the Horizontal Section for Type I Loading Profiles

The XY shear stresses along the horizontal section are plotted in Figures 7.5 and 7.6, the former grouped by splice location and the latter grouped by loading profiles. The horizontal section is located 3 (in) below the inner rivet line of the chord member to avoid local stress effects due to the rivets. Mid-thickness stress at sampled points is interpolated and averaged from the node stresses at elements which the horizontal section passes. Figure 7.5 shows the shear stress plateau at the middle of the gusset plate does not change much with either chord

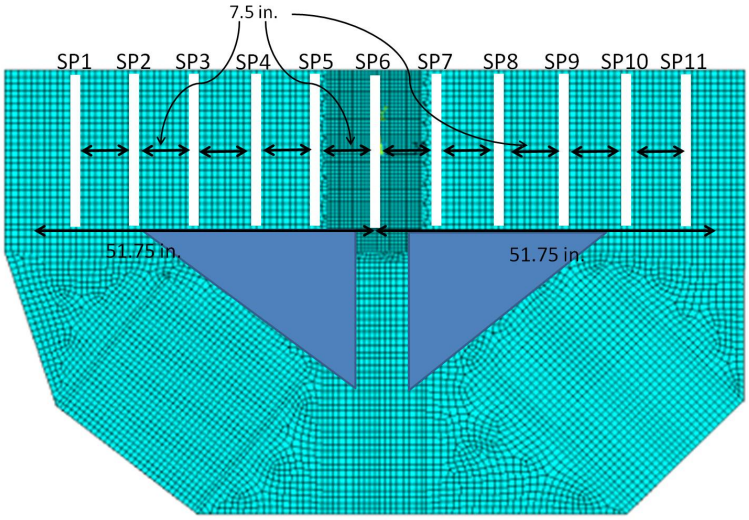

Figure 7.4: Illustration of the 11 chord splice locations used in the parameter study

loads or splice locations. However, the shear stress varies slightly around the beginning and end of the horizontal section when the chord loads change with different loads in Type I Loading Profiles. Additionally Figure 7.6 shows that for a given load profile, the splice location has little impact on the shear stress distribution. From Figure 7.5 and 7.6, two conclusions can be drawn. First, the vary of chord loads mostly affect the XY shear stress at the horizontal section near the edges of gusset plate but the effect is small since the location and magnitude of the maximum XY shear stress distributions are not changed. Second, the splice location has very little influence to the XY shear stress, therefore it is reasonable to be neglected in developing a method to estimate the stress distribution.

To simplify the figures representing stress distributions, Figures 7.5 and 7.6 only show results for selected splice locations, SP1, SP4, SP6, SP7, and SP10. The comprehensive results for all parameter values are discussed using statistical tools. The results for C_v^{max} and R_{ij}^{min} are listed in Tables 7.5 and 7.6. Table 7.5 presents the results for the variation of the stress distribution with loading profiles for fixed splice locations. While Table 7.6 presents results for the variation of the stress distribution with splice locations for fixed loading profiles. In both cases the tables contain data for all splice locations considered. The statistical

tools also support the conclusions drawn from Figures 7.5 and 7.6. The smallest correlation coefficient, R_{ij}^{min}, is about 0.7 from Tables 7.5 and is near to 1.0 from 7.6 which indicates the stress distributions are not affected by the splice location but a little affected by the loading profiles. Similarly, the coefficients of variation for the maximum stress, C_v^{max}, again reinforce the conclusion that both parameters have little impact on the variation of the maximum XY shear stress on the horizontal section.

Table 7.5: C_v^{max} and R_{ij}^{min} for the loading parameter Type I Loading Profiles over all considered splice locations

	SP1	SP2	SP3	SP4	SP5	SP6	SP7	SP8	SP9	SP10	SP11
C_v^{max}	0.002	0.009	0.019	0.004	0.044	0.062	0.069	0.052	0.038	0.03	0.026
R_{ij}^{min}	0.75	0.75	0.75	0.74	0.73	0.72	0.71	0.71	0.70	0.69	0.69

Table 7.6: C_v^{max} and R_{ij}^{min} for the splice location parameter over the Type I Loading Profiles

	Load 1	Load 2	Load 3	Load 4
C_v^{max}	0.05	0.04	0.05	0.06
R_{ij}^{min}	0.97	0.98	0.98	0.96

7.6.1.2 Observations of the XY Shear Stress at the Horizontal Section for the Type II Loading Profiles

The results for the XY shear stress distributions for the Type II Loading Profiles are shown in Figures 7.7 and 7.8. Figure 7.7 shows that varying the diagonal loads dramatically changes the XY shear stress distribution at the horizontal critical section while Figure 7.8 shows the splice locations have very little impact on the stress distribution. As the force in the left diagonal, L9, changes from compression, to zero, and then to tension, the XY shear stress in the left part of the graph in Figure 7.7 changes as well no matter where the chord

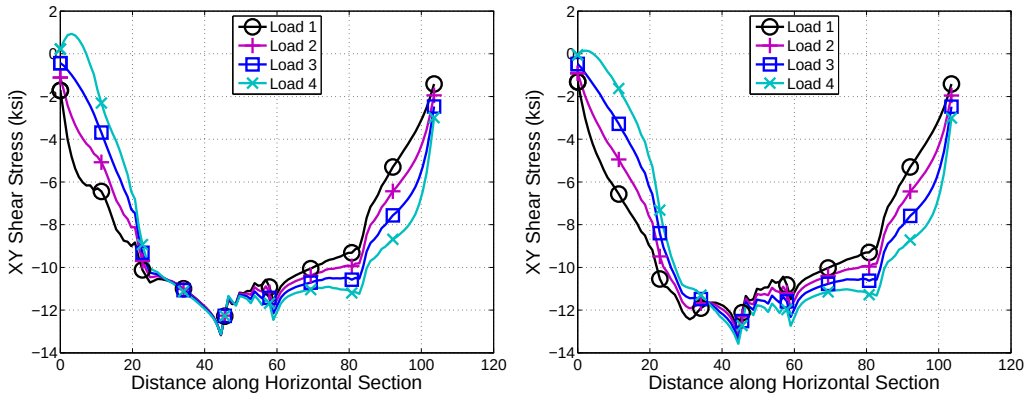

(a) Type I loads with SP1: $C_v^{max} = 0.002$ and $R_{ij}^{min} = 0.75$

(b) Type I loads with SP3: $C_v^{max} = 0.019$ and $R_{ij}^{min} = 0.75$

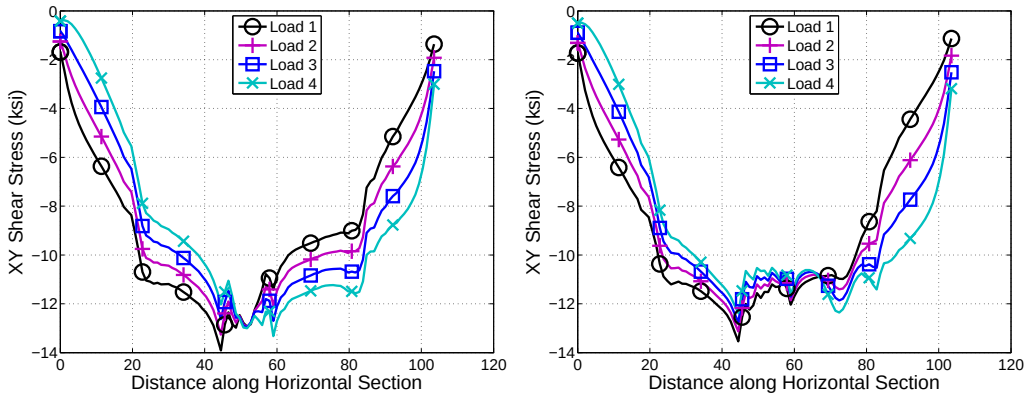

(c) Type I loads with SP6: $C_v^{max} = 0.062$ and $R_{ij}^{min} = 0.72$

(d) Type I loads with SP9: $C_v^{max} = 0.038$ and $R_{ij}^{min} = 0.70$

Figure 7.5: XY shear stress distributions along the horizontal section when the four loads in the Type I Loading Profiles apply to gusset plates with the splice locations at SP1, SP3 SP6, and SP9

splice is located. When the force in L9 is zero in Loading 7, the magnitude of the XY shear stress is also close to zero. Similarly, when the force in the right diagonal, L11, is zero, the XY shear stress is small as observed for Load 5 at the right side of the graph in Figure 7.7. This observation demonstrates that considering the total shear force acting on the whole horizontal section may only be suitable for some loading cases such as Load 6, where both

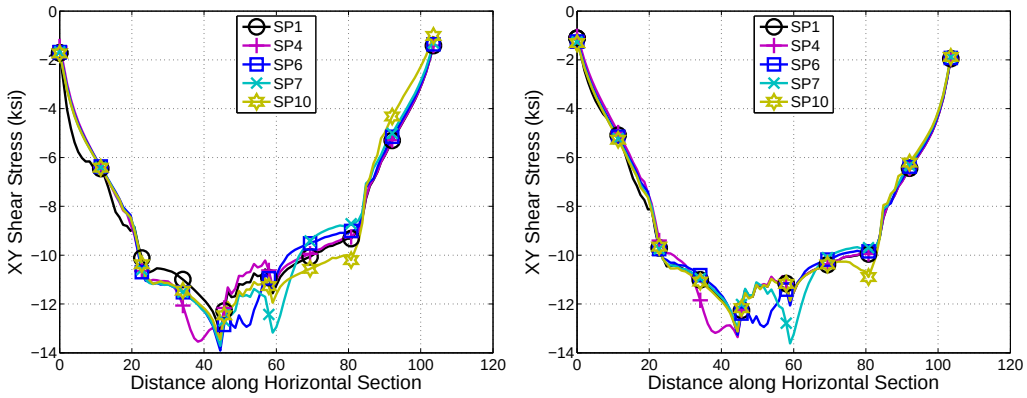

(a) Load 1 of Type I Loading Profiles, $C_v^{max} = 0.05$ and $R_{ij}^{min} = 0.97$, for all splice locations

(b) Load 2 of Type I Loading Profiles, $C_v^{max} = 0.04$ and $R_{ij}^{min} = 0.98$, for all splice locations

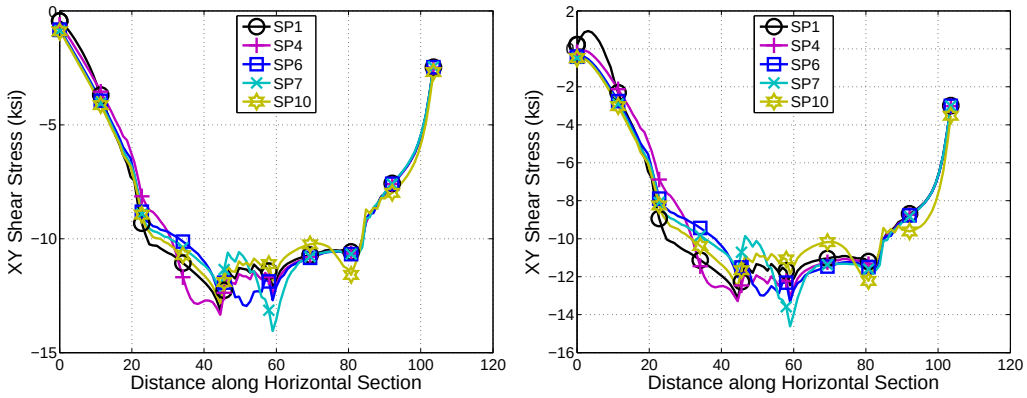

(c) Load 3 of Type I Loading Profiles, $C_v^{max} = 0.05$ and $R_{ij}^{min} = 0.98$, for all splice locations

(d) Load 4 of Type I Loading Profiles, $C_v^{max} = 0.06$ and $R_{ij}^{min} = 0.96$, for all splice locations

Figure 7.6: XY shear stress distributions along the horizontal section for selected chord splice locations for each load in Type I Loading Profiles

diagonals have equal and opposite loads and generate a stress plateau in the middle of the horizontal section. The stress generated by Load 9, which has the same diagonal loads as Load 6 yet different chord loads verifies the conclusion that the chord loads only influence the XY shear stress near the edges of the gusset plates as discussed in the previous section. The observation for the shear stress distributions for the Type II Loading Profiles leads to the conclusion that the XY shear stress at the horizontal sections is mostly affected by the

near-side diagonal load.

The C_v^{max} and R_{ij}^{min} for Type II Load Profiles and 11 splice locations, shown in Tables 7.7 and 7.8, lead to the same conclusions as those above. Table 7.7 shows little similarity found for the stress distributions when the load is varied as indicated by large C_v^{max} values and and small R_{ij}^{min} values. On the contrary, Table 7.8 demonstrates that the splice location again has no impact to the XY shear stress since the C_v^{max} values are small and the R_{ij}^{min} values are close to one when the splice location is varied.

Table 7.7: C_v^{max} and R_{ij}^{min} for the loading parameter Type II Loading Profiles over all considered splice locations

	SP1	SP2	SP3	SP4	SP5	SP6	SP7	SP8	SP9	SP10	SP11
C_v^{max}	0.43	0.42	0.42	0.42	0.41	0.42	0.46	0.43	0.43	0.43	0.43
R_{ij}^{min}	0.15	0.14	0.13	0.12	0.13	0.15	0.19	0.20	0.22	0.22	0.21

Table 7.8: C_v^{max} and R_{ij}^{min} for the splice location parameter over the Type II Loading Profiles

	Load 5	Load 6	Load 7	Load 8	Load 9
C_v^{max}	0.037	0.045	0.042	0.037	0.042
R_{ij}^{min}	0.99	0.98	0.99	0.99	0.98

7.6.1.3 Observation of the XY Shear Stress at the Horizontal Section for the Type III Loading Profiles

Several XY shear stress distribution interactions between the chord load and diagonal load for Type III Loading Profiles are observed and plotted in Figures 7.9 and 7.10.

1. The influence of the chord load on the XY shear stress is not significant until the ratio of the chord load to the horizontal component of the diagonal load exceeds four and

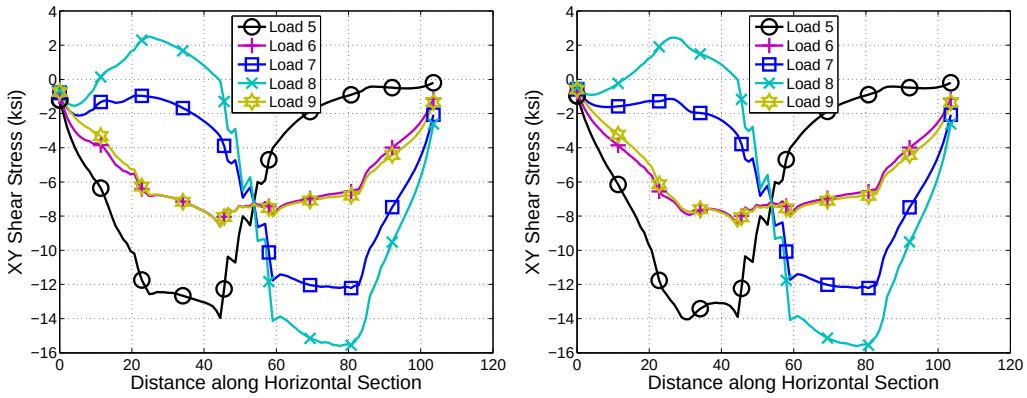

(a) Type II loads with SP1: $C_v^{max} = 0.43$ and $R_{ij}^{min} = 0.15$

(b) Type II loads with SP3: $C_v^{max} = 0.42$ and $R_{ij}^{min} = 0.13$

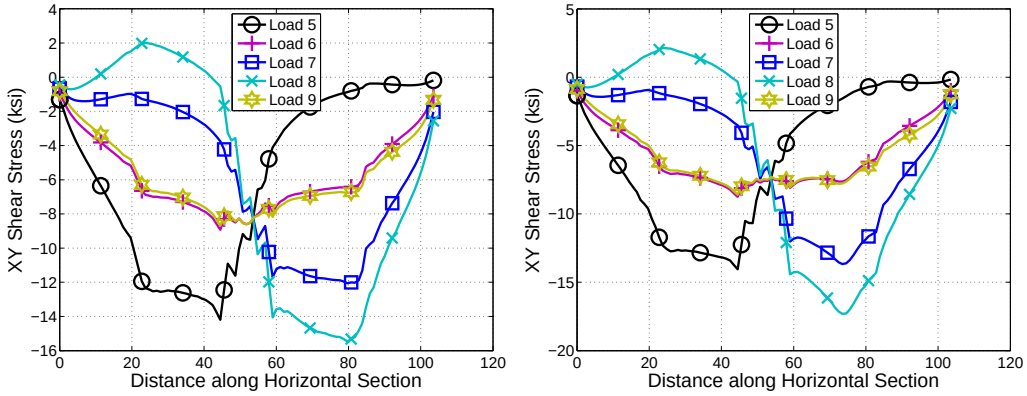

(c) Type II loads with SP6: $C_v^{max} = 0.42$ and $R_{ij}^{min} = 0.15$

(d) Type II loads with SP9: $C_v^{max} = 0.43$ and $R_{ij}^{min} = 0.22$

Figure 7.7: XY shear stress distributions along the horizontal section when the five loads in the Type II Loading Profiles apply to gusset plates with the splice locations at SP1, SP3 SP6, and SP9

the degree of influence may depend on the splice location.

2. The chord load may increase or decrease the magnitude of the shear stress generated by the diagonal load depending on the direction of the chord and diagonal loads. In Type III Loading Profiles the left side of the gusset plate has chord and diagonal loads that oppose each other and as shown in Figure 7.9 the XY shear stresses increase as

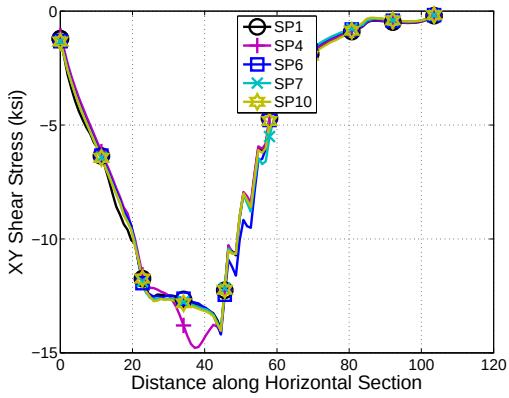

(a) Load 5 of Type II Loading Profiles, $C_v^{max} = 0.037$ and $R_{ij}^{min} = 0.99$, for all splice locations

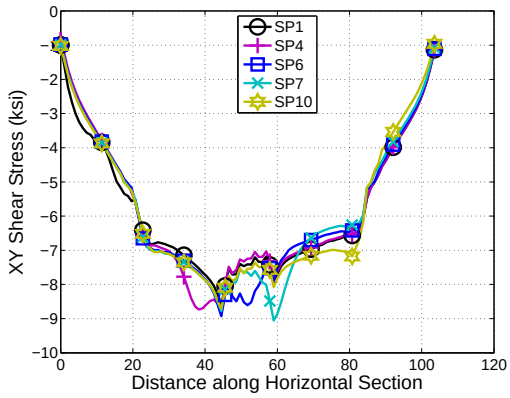

(b) Load 6 of Type II Loading Profiles, $C_v^{max} = 0.045$ and $R_{ij}^{min} = 0.98$, for all splice locations

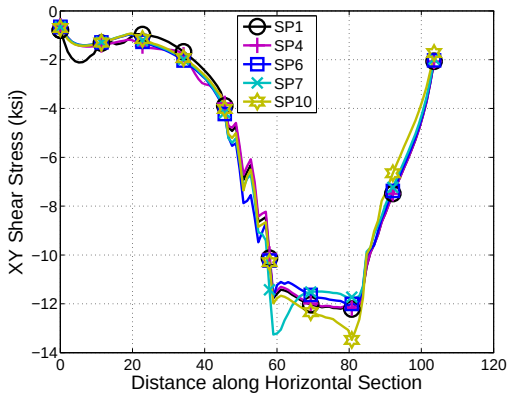

(c) Load 7 of Type II Loading Profiles, $C_v^{max} = 0.042$ and $R_{ij}^{min} = 0.99$, for all splice locations

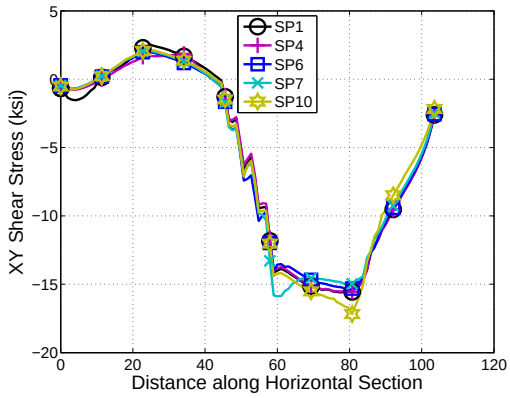

(d) Load 8 of Type II Loading Profiles, $C_v^{max} = 0.037$ and $R_{ij}^{min} = 0.99$, for all splice locations

Figure 7.8: XY shear stress distributions along the horizontal section for selected chord splice locations for each load in Type II Loading Profiles

the chord load increases. Conversely, the right side of the gusset plate has chord and diagonal loads in the same direction and as shown in Figure 7.9 the magnitude of the XY shear stresses decrease as the chord load increases.

3. The chord splice location slightly affects the influence of the chord load on the horizontal XY shear stress as observed in the Type I Loading Profiles. The effect of the chord splice location may more significant as the ratio of the chord load to the horizontal

component of the diagonal load becomes large as shown in Figure 7.10. The splice location also causes different impact on the XY shear stress distribution. As shown in Figures 7.9, in the Case SP1, the splice location is far outside the interference zone and the chord load changes the stress only around splice location and does not influence the peak stress which is located at the middle of the horizontal section and is still generated by the diagonal load. As the splice location moves closer to the interference zone or to the work point, such as Cases SP3 and SP6, the peak shear stress in the middle of the horizontal section is influenced by the increased chord loads and the move of the splice location, yet this influence is varied and difficult to estimate.

Overall, the shear stresses from the chord and the diagonal loads interact in a complicated way at the horizontal section. However, the impact of these stresses generally occurs along different regions of the horizontal section, where the diagonal loads mainly generate shear stress at the interference area while the chord load mostly affects the shear stresses near the edges of the gusset. In addition, the magnitude of the influence of the chord and diagonal loads on the XY shear stress is very different. The chord loads must be much larger than the diagonal loads to generate the same level of shear stresses.

The statistical calculations show the correlation of the shear stress distributions with the Type III Loading Profiles in Table 7.9 and the correlation of the shear stress distributions with the 11 splice locations in Table 7.10. Table 7.9 shows that R_{ij}^{min} becomes smaller as the chord loads increase as expected and Table 7.10 shows the splice location has little influence for the stress distributions. Tables 7.9 and 7.10 again verify the results observed from Figures 7.9 and 7.10.

7.6.2 Development of Approximating Method for the XY Shear Stress Distribution at the Horizontal Section

In the previous section, it was shown that the XY shear stress at horizontal critical section is controlled largely by the diagonal loads. It was also found that the chord loads have minor

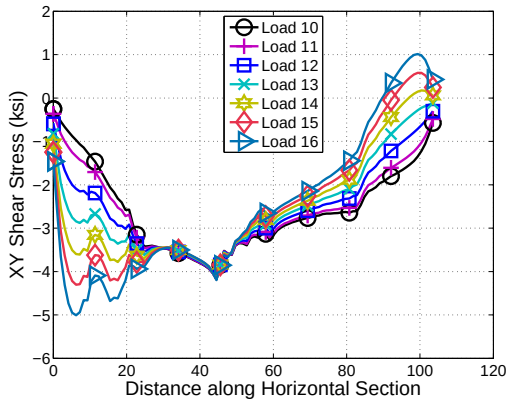

(a) Type III loads with SP1: $C_v^{max} = 0.002$ and $R_{ij}^{min} = 0.32$

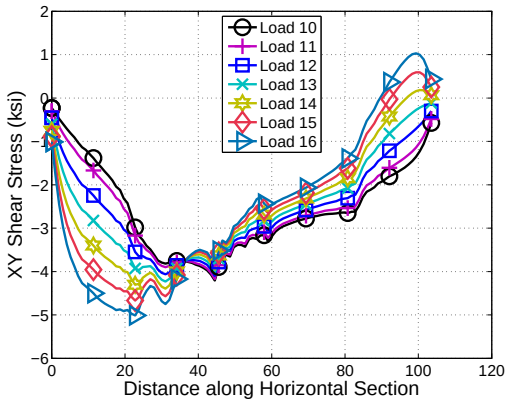

(b) Type III loads with SP3: $C_v^{max} = 0.032$ and $R_{ij}^{min} = 0.38$

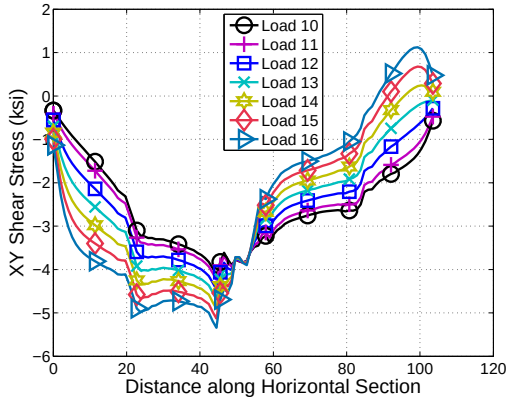

(c) Type III loads with SP6: $C_v^{max} = 0.109$ and $R_{ij}^{min} = 0.54$

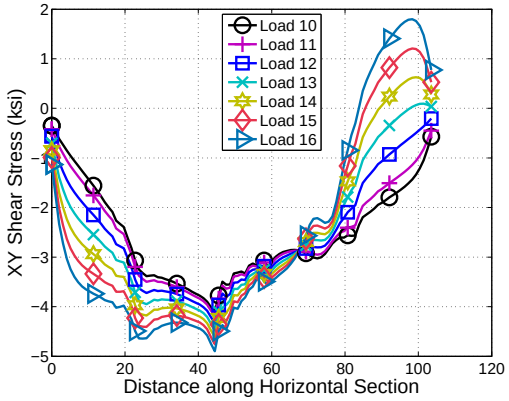

(d) Type III loads with SP9: $C_v^{max} = 0.07$ and $R_{ij}^{min} = 0.60$

Figure 7.9: XY shear stress distributions along the horizontal section when the seven loads in the Type III Loading Profiles apply to gusset plates with the splice locations at SP1, SP3 SP6, and SP9

influence on the horizontal shear unless they are large relative to the diagonal loads. Therefore, the shear stress on the horizontal section generated by chord loads will be neglected in the proposed approximate distribution and it will only consider the diagonal loads.

To approximate the shear stress distribution along the horizontal section generated by the

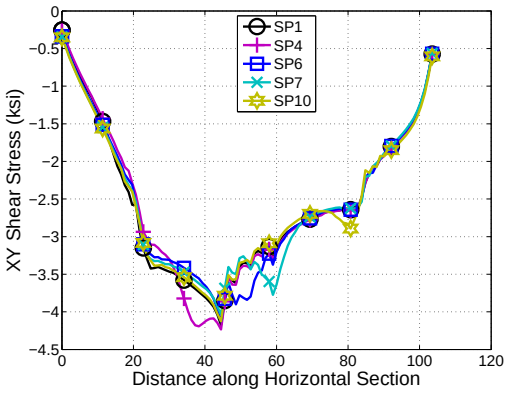

(a) Load 10 of Type III Loading Profiles, $C_v^{max} = 0.040$ and $R_{ij}^{min} = 0.98$, for all splice locations

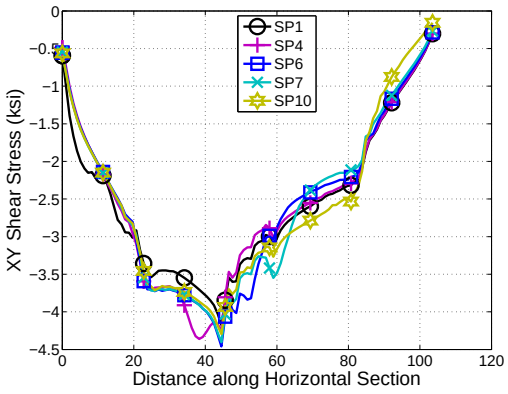

(b) Load 12 of Type III Loading Profiles, $C_v^{max} = 0.049$ and $R_{ij}^{min} = 0.98$, for all splice locations

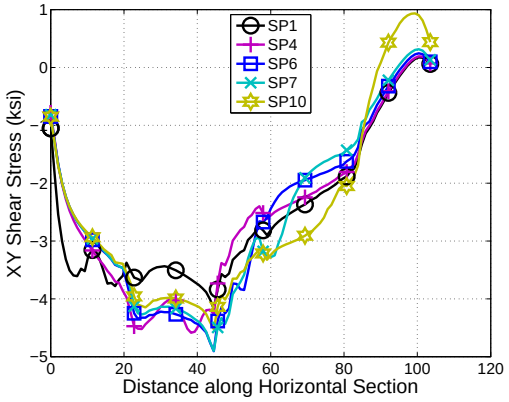

(c) Load 14 of Type III Loading Profiles, $C_v^{max} = 0.086$ and $R_{ij}^{min} = 0.94$, for all splice locations

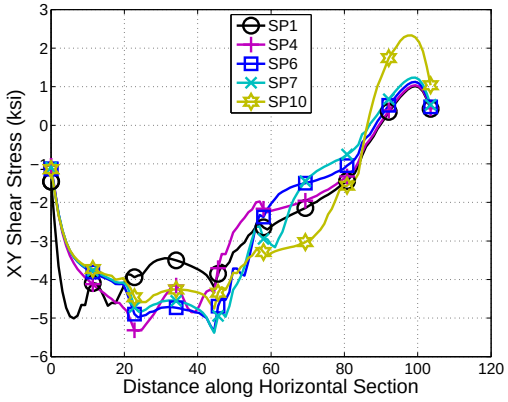

(d) Load 16 of Type III Loading Profiles, $C_v^{max} = 0.080$ and $R_{ij}^{min} = 0.92$, for all splice locations

Figure 7.10: XY shear stress distributions along the horizontal section for selected chord splice locations for each load in Type III Loading Profiles

force in the diagonals, the effective shear length is defined along the horizontal section and shown in Figure 7.11. As shown, the effective shear length for each diagonal is taken as the length along the chord rivet line between where the 30 ° dispersion angle line from the diagonal and a vertical line extending from the work point intersect the horizontal section. As Figure 7.11 shows, each connected diagonal has a separate effective shear length. The

Table 7.9: C_v^{max} and R_{ij}^{min} for the loading parameter Type III Loading Profiles over all considered splice locations

	SP1	SP2	SP3	SP4	SP5	SP6	SP7	SP8	SP9	SP10	SP11
C_v^{max}	0.002	0.014	0.032	0.009	0.079	0.109	0.121	0.092	0.070	0.056	0.049
R_{ij}^{min}	0.32	0.34	0.38	0.45	0.51	0.54	0.57	0.60	0.60	0.59	0.58

Table 7.10: C_v^{max} and R_{ij}^{min} for the splice location parameter over the Type III Loading Profiles

	Load 10	Load 11	Load 12	Load 13	Load 14	Load 15	Load 16
C_v^{max}	0.040	0.039	0.049	0.067	0.086	0.105	0.080
R_{ij}^{min}	0.98	0.98	0.98	0.96	0.94	0.93	0.92

use of individual effective shear lengths results from the observation of the XY shear stress distributions with the variation of Type II Loading Profiles in Section 7.6.1.2 that when one diagonal has zero load, there is a near zero shear stress on that side.

The shear stress distribution is assumed to be uniform distribution over each diagonal's effective shear length. Thus, the shear stress over this effective shear length can be calculated by dividing the horizontal component of the diagonal axial force by the effective shear area as shown in Eq. 7.4.

$$\tau_{xy} = \frac{F * cos(\alpha)}{2 * (L_{effect}) * t} \tag{7.4}$$

where α is the angle between chord and diagonal, L_{effect} is the effective shear length and t is the thickness of the gusset plates.

This approximate shear stress distribution provides a relatively simple and quick calculation while keeping force equilibrium at the horizontal section and capturing the primary observation that the the shear stress is not uniformly distributed along the entire horizontal section.

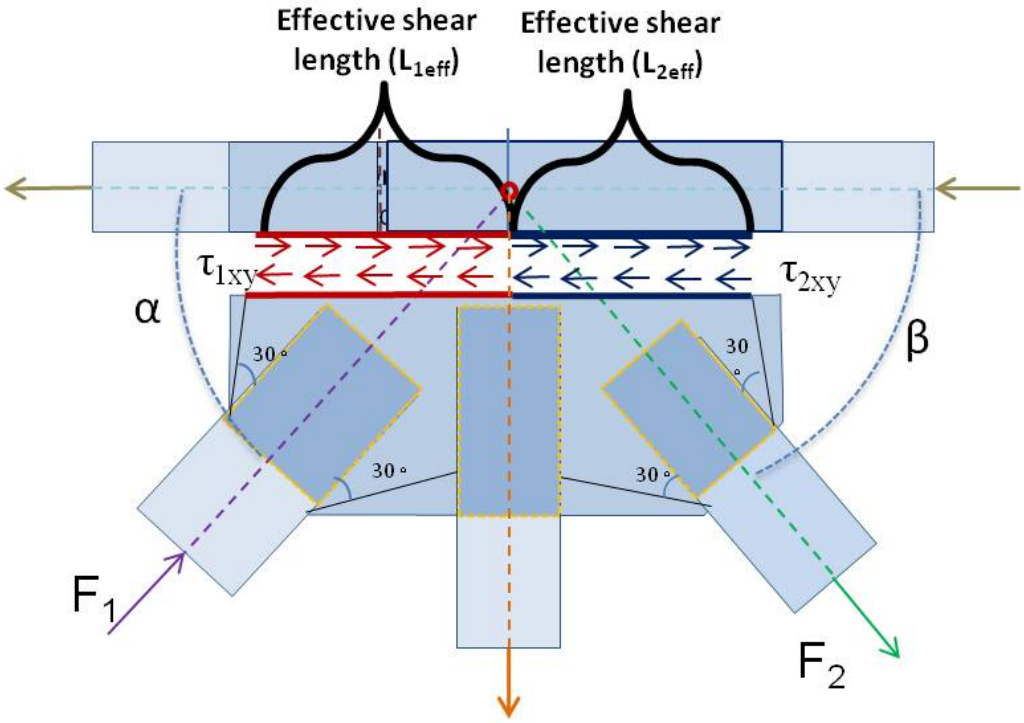

Figure 7.11: XY shear stress schematic shows that the shear stress are generated mainly by diagonal loads and is limited in the region on the rivet line between the 30 ° dispersion angle line and the line cross work point

7.6.3 Validation of the Effective Shear Length Method for the XY Shear Stress Distribution at the Horizontal Section

The shear stress distributions computed using Eq. 7.4 for the Type I, II, and III Loading Profiles are plotted in Figures 7.12 through 7.14 and compared with: (i) the Finite Element Analysis (FEA) results and (ii) the average shear stress computed considering the entire horizontal section and the sum of the horizontal components of the diagonal loads, which is suggested in the FHWA Guide. (iii) the 1.35 times average shear stress over entire horizontal section, which is also suggested in the FHWA Guide. In FHWA Guide, XY shear stress along horizontal section are considered in two methods 1) average shear stress along the

full length of the horizontal section if the gusset plate can provide enough stiffness after shear yielding and 2) reduction factor $\Omega = 0.74$ times average shear stress if the gusset plate can not provide enough stiffness after shear yielding. The second method considers parabolic stress distribution, analogized to shear stress at rectangular beam section and has the maximum stress equals 1.5 times average shear stress, but abruptly choose factor 1.35 for the maximum shear stress on the horizontal section to avoid overly conservative estimate.

Recall that the splice location did not significantly affect the shear stress on the horizontal section; therefore the FEA results shown in Figures 7.12 through 7.14 are the average shear stress distribution for all splice locations for each loading profiles. The results of statistics for R and R_{err} are listed in Table 7.11. Figures 7.15 and 7.16 plot the data in Table 7.11. It is worth to note that the correlation of coefficient is zero for all the Whitmore stress distribution because the Whitmore stress is a constant distribution and the variance and covariance of this distribution is zero. Correlation coefficient of Eq. 7.2 is meaningless in this condition.

Figures 7.15, and 7.16, and Table 7.11 show that consideration of separate uniform stress distributions resulting from the individual diagonal loads on each effective shear length better approximates the FEA shear stress distributions than using an average shear stress and 1.35 times average shear stress over the entire horizontal section. This is true whether the results for the maximum stress or overall stress distribution are considered. In most cases, all methods underestimate the peak value of the shear stress but using each diagonal's effective shear length results in smaller error. Further, using each diagonal's effective shear length also captures the impact of unequal diagonal loads, creating two stress plateaus rather than one average stress along the entire gusset. Both average shear stress and 1.35 times average stress under estimate shear stress in Type II Loading Profiles. This is highlighted when the Type II Loading Profiles are considered in Figure 7.13.

Finally, it is noted that using each diagonal's effective shear length results in larger errors for the Type III Loading Profiles, where the chord loads were increased, relative to other loading profiles. This is because the shear stress from chord loads is magnified when the

chord loads are large but their impact is neglected.

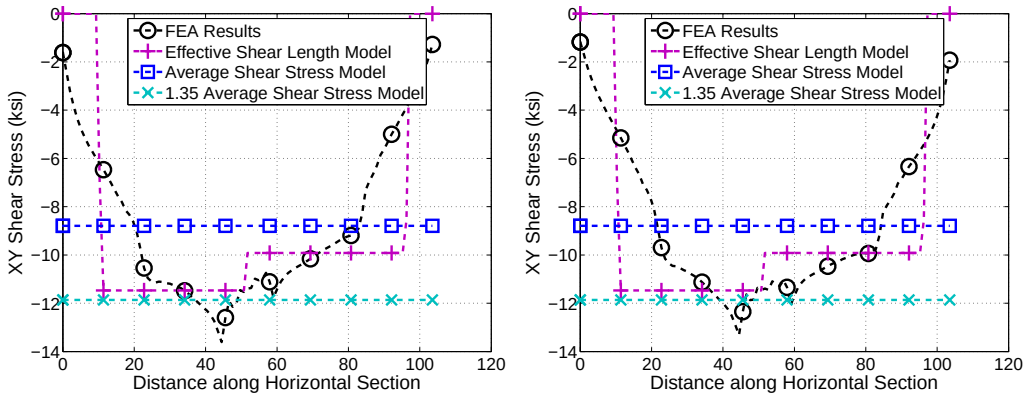

(a) Comparison of XY shear stress under Load 1

(b) Comparison of XY shear stress under Load 2

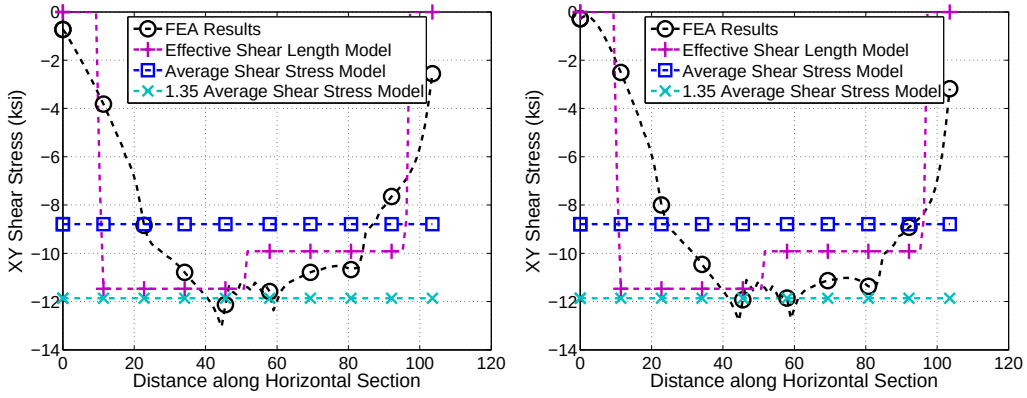

(c) Comparison of XY shear stress under Load 3

(d) Comparison of XY shear stress under Load 4

Figure 7.12: Comparison of XY shear stress distributions from the effective shear length model, the average shear stress model and the FEA results for the Type I Loading Profiles

Table 7.11: Statistics to evaluate error and correlation of the approximate shear stress distribution to the FEA results

	Shear Stress Distribution		Load 1	Load 2	Load 3	Load 4
Type I Loading Profiles	Effective Shear Length Model	R_{err}	-15.7%	-13.9%	-12.1%	-10.3%
		R	0.77	0.78	0.74	0.66
	Average Shear Stress Model	R_{err}	-35.4%	-34.0%	-32.6%	-31.3%
	1.35 Average Shear Stress Model	R_{err}	-12.81%	-10.90%	-9.03%	-7.20%
			Load 5	Load 6	Load 7	Load 8
Type II Loading Profiles	Effective Shear Length Model	R_{err}	4.5%	-16.1%	11.9%	14.2%
		R	0.89	0.78	0.91	0.92
	Average Shear Stress Model	R_{err}	-58.7%	-33.6%	-52.0%	-62.3%
	1.35 Average Shear Stress Model	R_{err}	-44.2%	-10.4%	-35.2%	-49.1%
			Load 9			
	Effective Shear Length Model	R_{err}	-15.05%			
		R	0.78			
	Average Shear Stress Model	R_{err}	-32.8%			
	1.35 Average Shear Stress Model	R_{err}	-9.3%			
			Load 10	Load 11	Load 12	Load 13
Type III Loading Profiles	Effective Shear Length Model	R_{err}	-8.7%	-9.8%	-11.8%	-13.7%
		R	0.78	0.80	0.79	0.74
	Average Shear Stress Model	R_{err}	-38.6%	-39.2%	-40.6%	-41.9%
	1.35 Average Shear Stress Model	R_{err}	-17.1%	-18.0%	-19.9%	-21.6%
			Load 14	Load 15	Load 16	
	Effective Shear Length Model	R_{err}	-15.6%	-17.5%	-20.1%	
		R	0.68	0.62	0.57	
	Average Shear Stress Model	R_{err}	-43.2%	-44.5%	-46.2%	
	1.35 Average Shear Stress Model	R_{err}	-23.3%	-25.1%	-27.4%	

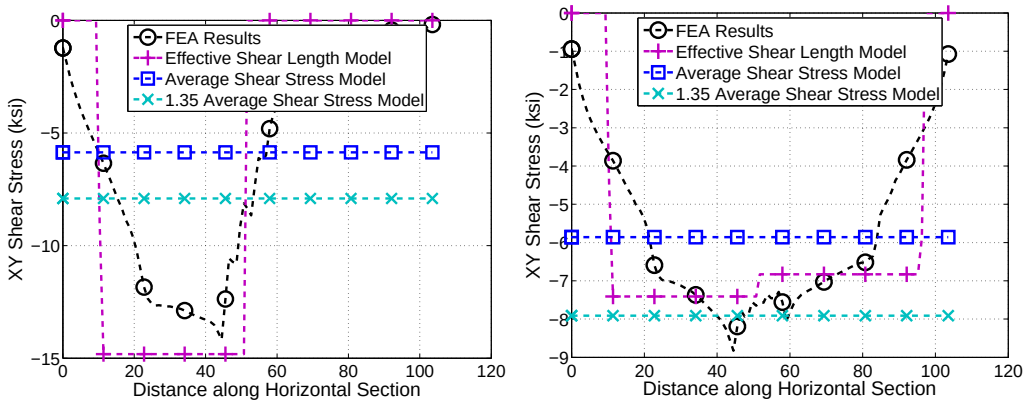

(a) Comparison of XY shear stress under Load 5

(b) Comparison of XY shear stress under Load 6

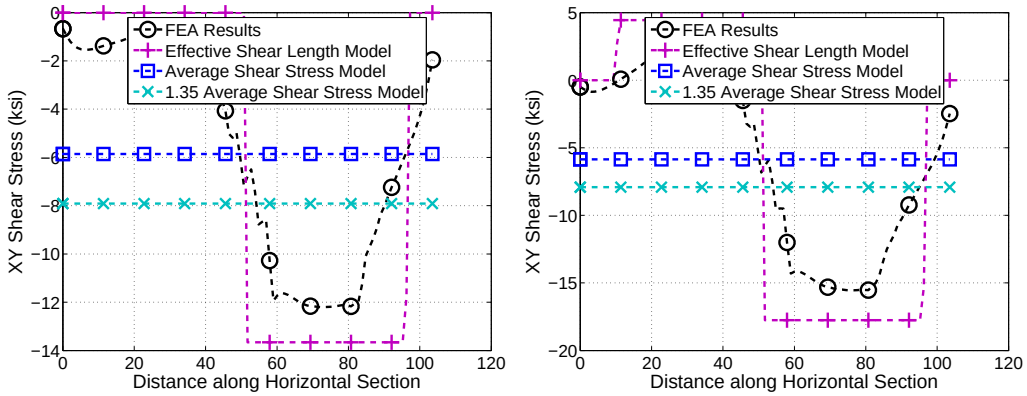

(c) Comparison of XY shear stress under Load 7

(d) Comparison of XY shear stress under Load 8

Figure 7.13: Comparison of XY shear stress distributions from the effective shear length model, the average shear stress model and the FEA results for the Type II Loading Profiles

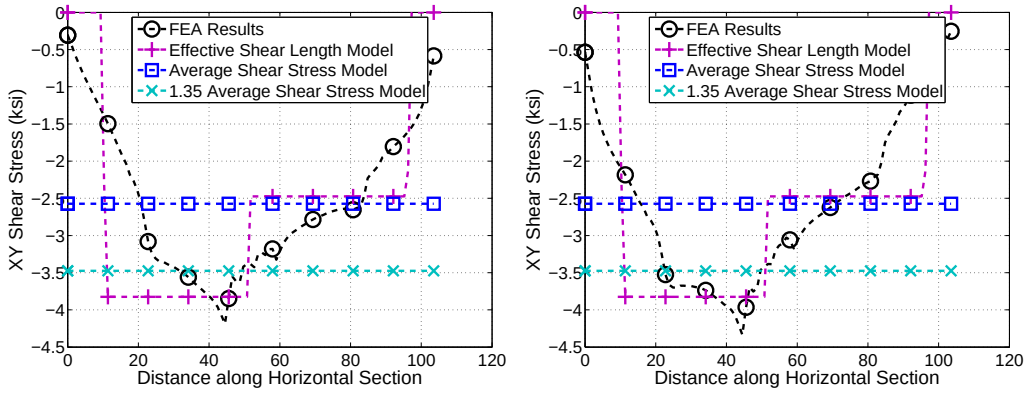

(a) Comparison of XY shear stress under Load 10

(b) Comparison of XY shear stress under Load 12

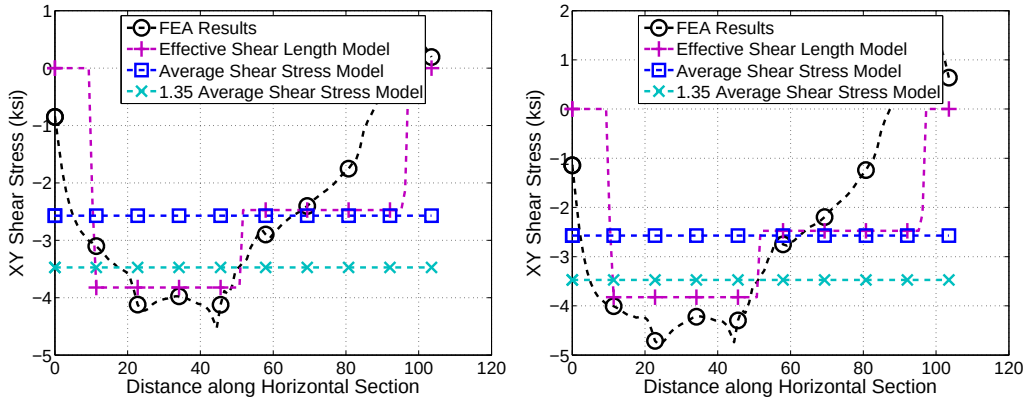

(c) Comparison of XY shear stress under Load 14

(d) Comparison of XY shear stress under Load 16

Figure 7.14: Comparison of XY shear stress distributions from the effective shear length model, the average shear stress model and the FEA results for the Type IIIing Load Profiles

7.7 XY Shear Stress Distribution at the Vertical Section

7.7.1 Observation of the XY Shear Stress Variation at the Vertical Section for the Type IV Loading Profiles

The XY shear stress distribution is examined at 1.5 (in) away from the outer vertical rivet line of the hanger connection. The XY shear stress distributions of the left vertical section

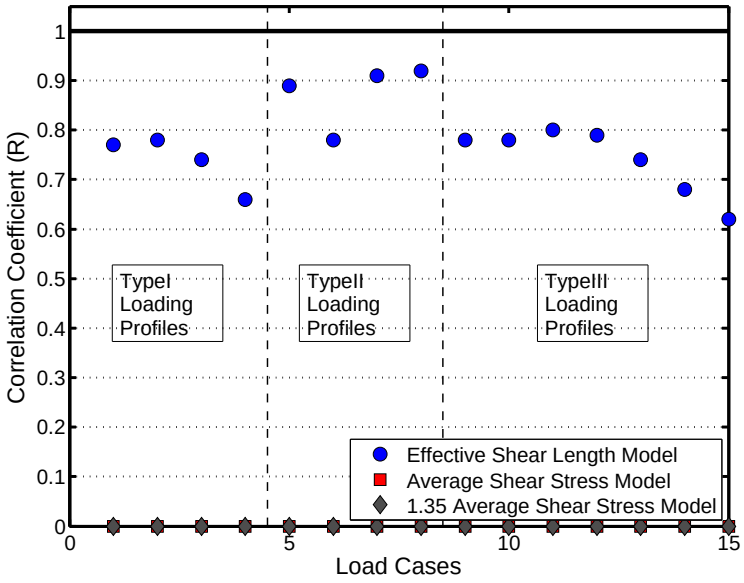

Figure 7.15: Correlation Coefficient, R, for the approximate stress distribution to the FEA results for the Type I, II, and III Loading Profiles

are plotted in Figure 7.17 and Figure 7.18 so that the impact of the right side member loads on the shear stress distribution of left side vertical section can be studied. In these figures the origin is set at the outer rivet line of the top chord and the X-axis is the vertical distance along the critical vertical section, extending to the end rivet row of the hanger. Note that, the vertical critical sections on the left and right side of the hanger are aligned with chord splice locations Cases SP5 and SP7.

Figure 7.17 shows that the shape of the shear stress distribution on the vertical critical section on the left side of the hanger changes as the diagonal loads on the right side of joint increases for all splice locations. When the right diagonal has zero load, Load 17 in Type IV Loading Profiles, the shear stress along the left side of the hanger is closer to an uniform distribution outside of the chord area and when the load in the right diagonal is increased the shape of the XY shear stress distributed become more linearly. While the shape of the stress distribution is influenced by the right side diagonal load, the location and magnitude of the peak XY shear stress on the left side of vertical section is not significantly

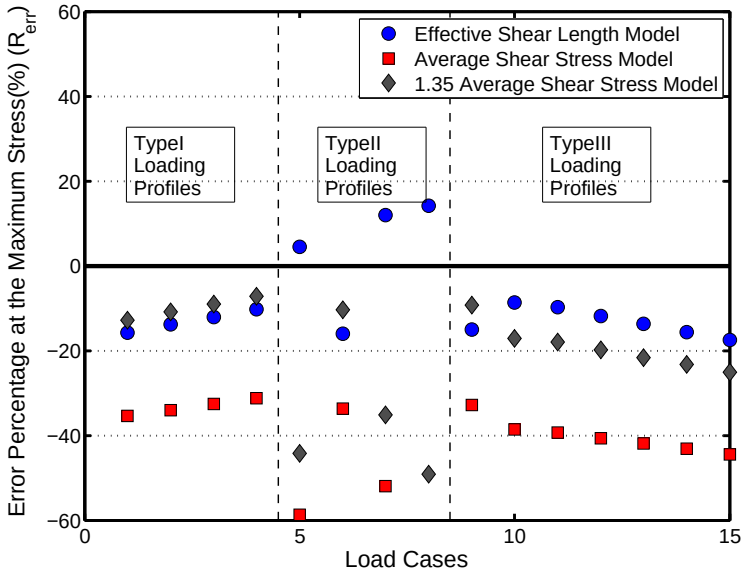

Figure 7.16: Percent Error, R_{err}, in the maximum shear stress between the approximate stress distributions and the FEA results for Type I, II, and III Loading Profiles

affected. The peak is close to the ends of the hanger on the left side diagonal for all splice locations in Type IV Loading Profiles. This observation reveals that the left-side diagonal load dominates the peak shear stress along the left side vertical critical section. In addition, the magnitude of the shear stress near the chord area is very low and can be neglected. The shear stress is found a little jump in the space between chord and hanger which shown between the $X \approx= 20$ to $X \approx= 25$. This stress jump is incurred due to the discontinuity of the geometry.

As expected, the splice location has no influence to the shear stress at the vertical section. Figure 7.18 shows that the stress distributions are almost overlapped for the results of different splice location except for SP5. SP5 is the case where the examined vertical section and chord splice are located along the same line section. This higher stress distribution at the chord splice is also observed at the vertical section on the right side of the hanger when the splice is at SP7. Tables 7.12 and 7.13 show the statistical data for the XY stress distribution on the left side of the hanger at the vertical section for the Type IV Loading

Profiles and splice locations respectively. As shown, when SP5 is neglected in Table 7.13, the R_{ij}^{min} is greater than 0.93, indicating little variation with splice location. Table 7.12 shows that for all splice locations, the distribution is slightly affected by the right side diagonal loads.

Table 7.12: C_v^{max} and R_{ij}^{min} for the loading parameter Type IV Loading Profiles over all considered splice locations

	SP1	SP2	SP3	SP4	SP5	SP6	SP7	SP8	SP9	SP10	SP11
C_v^{max}	0.092	0.094	0.097	0.096	0.094	0.086	0.084	0.086	0.088	0.089	0.089
R_{ij}^{min}	0.79	0.79	0.79	0.78	0.49	0.79	0.79	0.79	0.79	0.78	0.78

Table 7.13: C_v^{max} and R_{ij}^{min} for the splice location parameter over the Type IV Loading Profiles

	Load 17	Load 18	Load 19	Load 20	Load 21
C_v^{max}	0.013	0.014	0.007	0.008	0.010[1]
R_{ij}^{min}	0.97	0.93	0.88	0.85	0.82[2]

[1,2] SP5 and SP7 are neglected from both statistical calculations

7.7.2 Development of Approximating Method for the XY Shear Stress Distribution at the Vertical Section

It is clear that the diagonal on one side of the gusset plate gusset plate affects the shear stress distribution along the vertical section on the same side of the hanger. Similar to the XY shear stress on the horizontal section, a uniform distribution of the XY shear stress along the vertical section will be used to approximate the actual distribution. Section 7.7.1 studied the impact of the right side diagonal and hanger loads on the shear stress distribution at the vertical section on the left side of the hanger using Type IV Loading

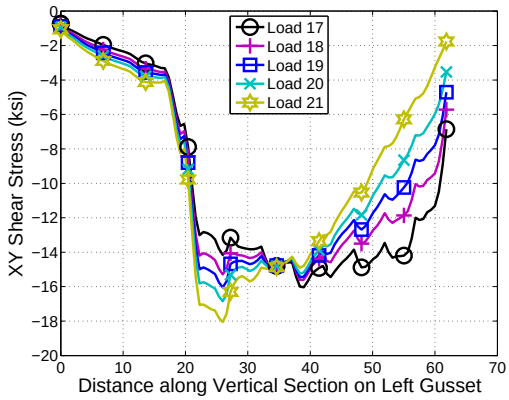

(a) Type IV loads with SP1: $C_v^{max} = 0.092$ and $R_{ij}^{min} = 0.79$

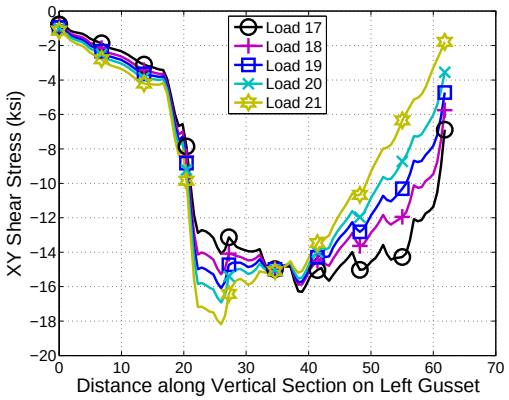

(b) Type IV loads with SP3: $C_v^{max} = 0.097$ and $R_{ij}^{min} = 0.79$

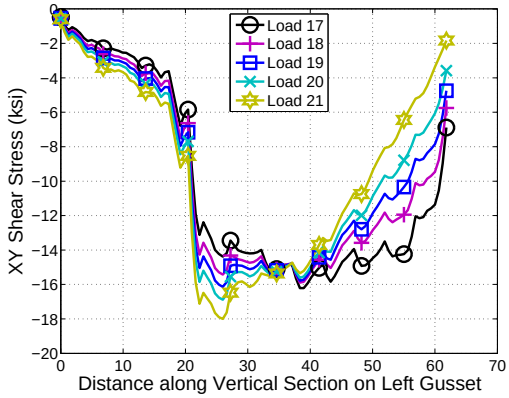

(c) Type IV loads with SP6: $C_v^{max} = 0.086$ and $R_{ij}^{min} = 0.79$

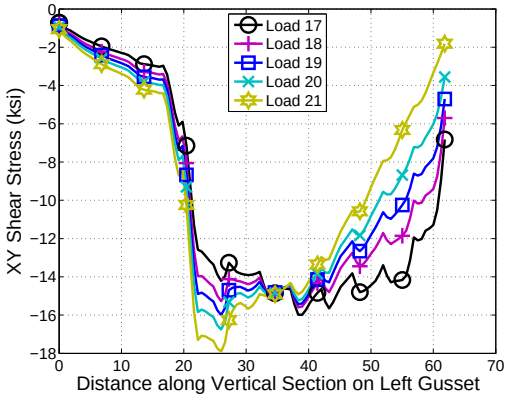

(d) Type IV loads with SP9: $C_v^{max} = 0.088$ and $R_{ij}^{min} = 0.79$

Figure 7.17: XY shear stress distributions along the vertical section to the left of the hanger when the five loads in the Type IV Loading Profiles apply to gusset plates with the splice locations at SP1, SP3 SP6, and SP9

Profiles. It was found that there was some interference from the opposite diagonal load and that is slightly changed the shape of the XY shear stress distribution from a uniform distribution to a slightly linear distribution. However, as shown in Figure 7.17, the shear stress on the left side of the hanger may still be approximated as uniform distribution over a particular length with adequate accuracy. Similar to the effective shear lengths for the

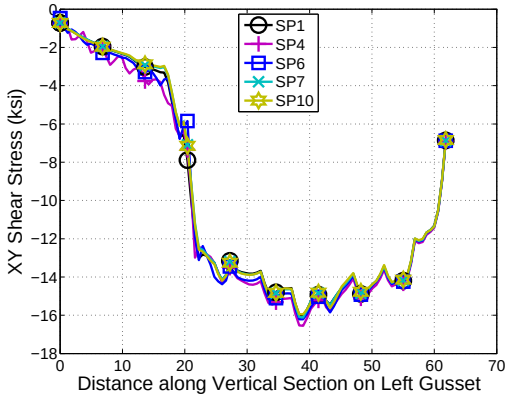

(a) Load 17 of Type IV Loading Profiles, $C_v^{max} = 0.013$ and $R_{ij}^{min} = 0.97$, for all splice locations

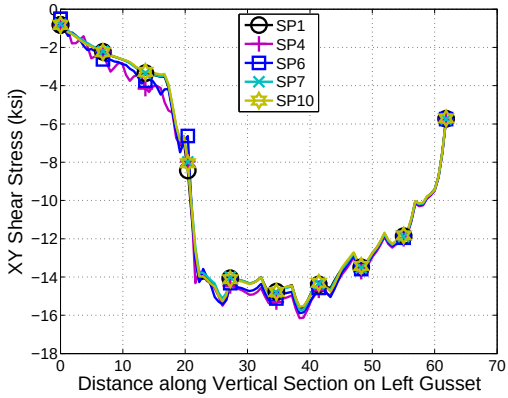

(b) Load 18 of Type IV Loading Profiles, $C_v^{max} = 0.014$ and $R_{ij}^{min} = 0.93$, for all splice locations

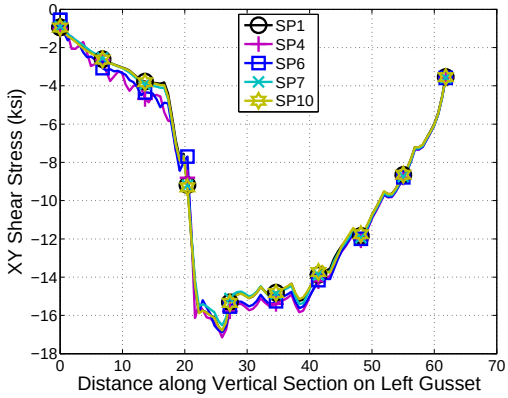

(c) Load 20 of Type IV Loading Profiles, $C_v^{max} = 0.008$ and $R_{ij}^{min} = 0.85$, for all splice locations

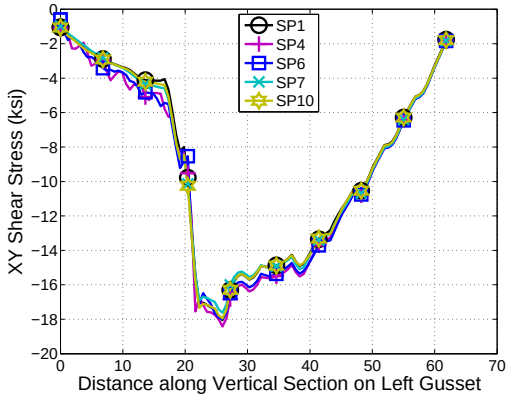

(d) Load 21 of Type IV Loading Profiles, $C_v^{max} = 0.010$ and $R_{ij}^{min} = 0.82$, for all splice locations

Figure 7.18: XY shear stress distributions along the vertical section to the left hanger for selected chord splice locations for each load in Type IV Loading Profiles

diagonals used to estimate the XY shear stress on the horizontal section, the effective shear length along the vertical section for a diagonal is defined as the length along the rivet line of the hanger bounded by the work point and the intersection of the 30° dispersion angle projection. The schematic of the effective shear length on the vertical section is shown in the Figure 7.19. The XY shear stress on the vertical shear effective section is estimated by

dividing the vertical component of the diagonal load by effective shear area which is the product of the thickness of the gusset plates and effective shear length.

7.7.3 Validation of Approximating Method for the XY Shear Stress Distribution at the Vertical Section

The EEA results used for comparison with the estimated shear stress on the vertical section are the mean values of all the splice locations for each Type IV Load Profiles since the splice locations have no influence on the XY shear stress on the vertical section (See Figure 7.18). The comparison of the estimated shear stress and the FEA results for the left and right side of the vertical critical sections are shown in Figures 7.20 and 7.21.

Figure 7.20 shows that even though the distributions are slightly affected by the increasing loads from the opposite diagonal, the uniform XY shear stress assumption still give good approximations for the maximum stress on the vertical section of the left side hanger. Table 7.14 shows the statistical results for the comparison and the R_{err} shows the error for Load 21 is around 17% for the left side vertical section, which is the maximum and is acceptable for engineering practice. Additionally, the correlation coefficients show low relation between the FEA results and approximated stress distributions when the load at left diagonal is small and the correlation coefficients increase when the diadonal load increases. However, the comparison of the shear stress distributions at the vertical critical section on the right side of the hanger seems away off the FEA results shown in Figure 7.21. This is because when the digoanal force is small and does not dominte the stress distributions on the one side, the influence from opposite diagonal force is more significant on the stress distribution for this side. Load 17 in the Type IV Loading Profiles has zero load in the right side diagonal, and therefore, the stress distribution on this side is shown influenced by other forces, however, the magnitude is small as shown in Figure 7.21. When the right side diagonal load is graduately increased in Loads 18 to 21 in the Type IV Loading Profiles, the distribution is closer to the FEA results and the error of the estimated maximum stress is also decreased.

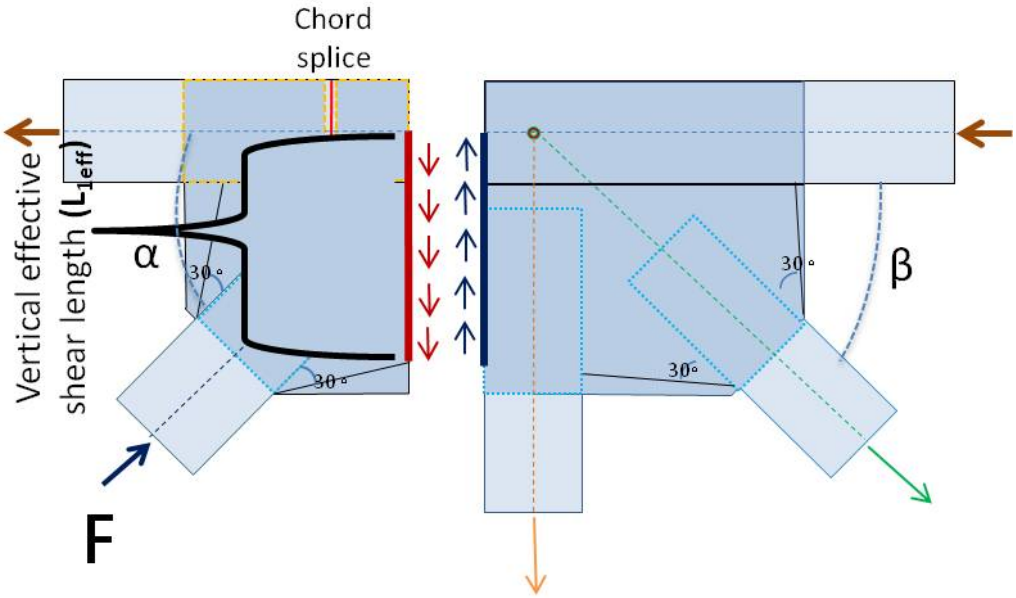

Figure 7.19: Schematic of uniform XY shear stress distribution model and effective shear length at the vertical section on the left side of the hanger

Table 7.14: Statistical results to evaluate error and correlation of the computed stress to the FEA results

			Load 17	Load 18	Load 19	Load 20	Load 21
Type IV Loading Profiles (On left side)	XY Uniform Shear Stress Model	R_{err}	-8.20%	-5.88%	-7.76%	-12.03%	-17.81%
		R	0.50	0.58	0.63	0.67	0.71
Type IV Loading Profiles (On right side)	XY Uniform Shear Stress Model	R_{err}	-100%	-49.50%	-37.89%	-31.22%	-25.23%
		R	0.0	0.49	0.57	0.62	0.64

7.8 X-direction Normal Stress Distribution at the Chord Splice

In the Chapter 6, the X-direction normal stress at the splice location was found to be the resultant of the combination of effects from axial chord force and the eccentric moment gen-

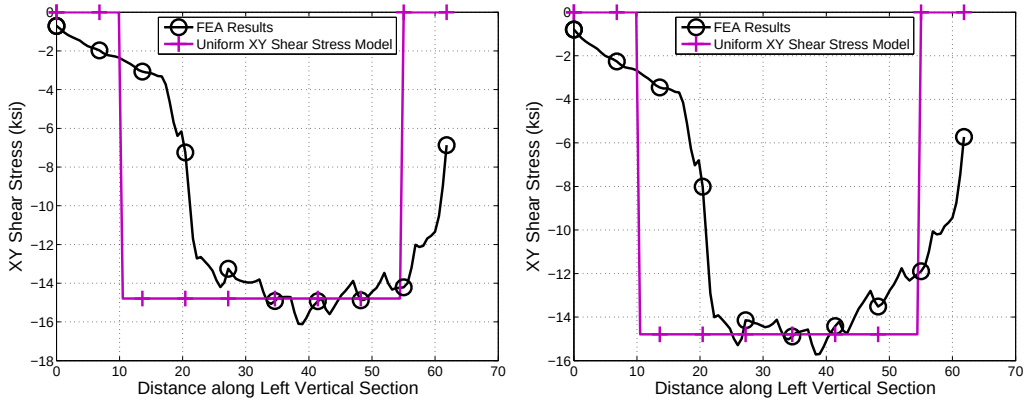

(a) XY shear stress on the vertical critical section for Load 17 averaged for all splice locations

(b) XY shear stress on the vertical critical section for Load 18 averaged for all splice locations

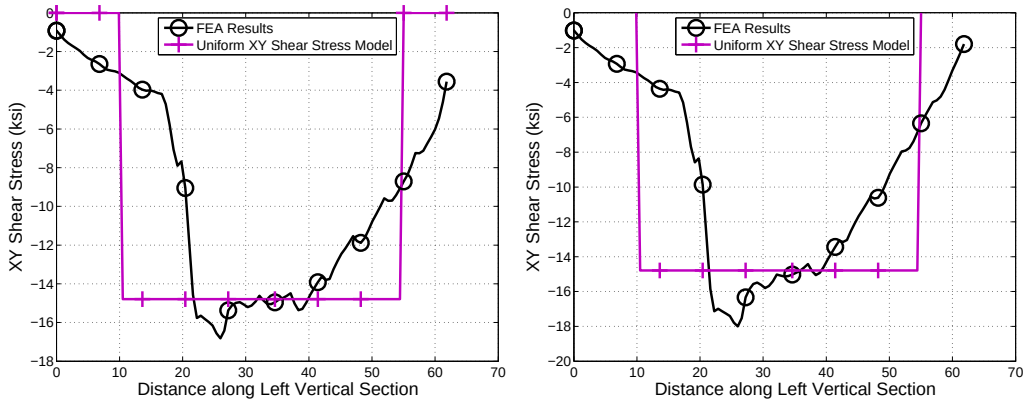

(c) XY shear stress on the vertical critical section for Load 20 averaged for all splice locations

(d) XY shear stress on the vertical critical section for Load 21 averaged for all splice locations

Figure 7.20: Comparison of uniform shear stress model and the FEA results for XY shear stress distributions on the left side vertical critical section for the Type IV Loading Profiles

erated by the asymmetric geometry of the splice. The proposed normal stress distribution for the chord splice was shown to adequately estimate the elastic stress along the chord splice when only chords were loaded and the X-direction normal stress at the chord splice was found to be unaffected by the splice location. However, once the loads from the diagonals and hanger are considered along with the chord loads, the X-direction normal stress distribution was significantly affected by the chord splice location as was shown in Figure

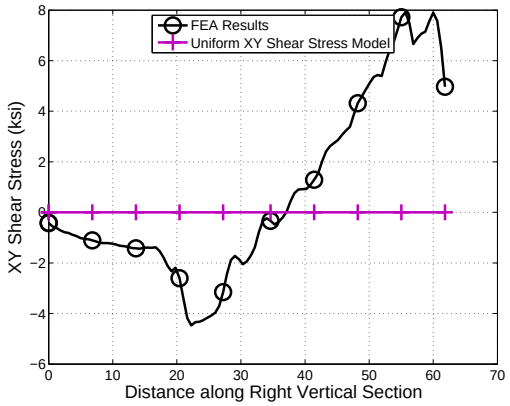

(a) XY shear stress on the vertical critical section for Load 17 averaged for all splice locations

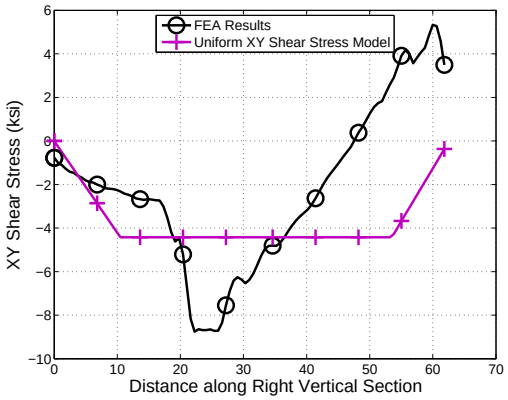

(b) XY shear stress on the vertical critical section for Load 18 averaged for all splice locations

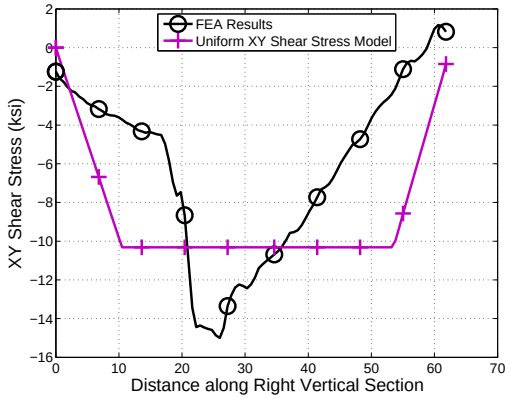

(c) XY shear stress on the vertical critical section for Load 20 averaged for all splice locations

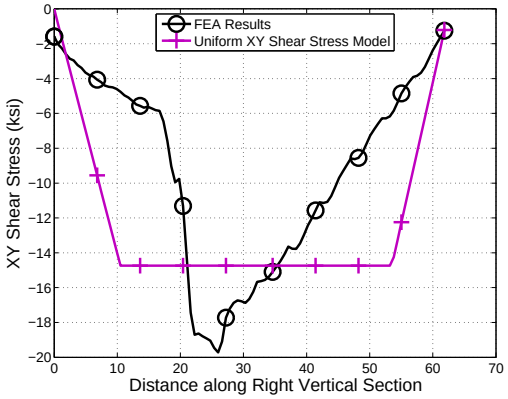

(d) XY shear stress on the vertical critical section for Load 21 averaged for all splice locations

Figure 7.21: Comparison of uniform shear stress model and the FEA results for XY shear stress distributions on the right side vertical critical section for the Type IV Loading Profiles

6.20. This section investigates the key parameters influencing the X-direction normal stress at the chord splice when all connected members are loaded. The stress at the chord splice is considered to be primarily affected by the chord and diagonal loads, thus the Type I and Type II Loading Profiles from the previous section are used again here.

7.8.1 Observations of the X-direction Normal Stress at the Chord Splice

7.8.1.1 Observation of the X-direction Normal Stress for the Type I Loading Profiles

The four Type I Loading Profiles were shown in Table 7.1 and were created by varying the chord loads while keeping the diagonal loads constant. The X-direction normal stress distributions at all splice locations for each load in Type I Loading Profiles loading are plotted in Figure 7.22. Sub-figures of Figure 7.22 show the the stress distribution for each loading profile. Observations regarding the stress distributions generated by the Type I Loading Profiles provide some basic insight as to how the member forces interact and affect the chord splice stress. These observations include:

1. Though the magnitude of the maximum normal stress changes with the loading profiles and the splice location, the shape of the stress distribution is very similar. The shape of this stress distribution has lower stress on the edge of the gusset plate, the origin of X-axis as shown in Figure 7.22, then the stress increases as the sampled point moves away the origin toward the first row of rivet line and the stress decreases as the sample point point moves further away the first row of rivet. This shape of the stress distribution implies the trapezoidal stress distribution model developed in Chapter 6 for stress at the chord splice is still effective for cases when all members are loaded.

2. The observation from Load Cases with zero load at chord member such as Load 1 and Load 3, found that the stress is near zero at splice locations such as SP1, SP2, SP10, and SP11 but the the stress is gradually increased and trapezoidal stress distributions are observed at the chord splices away the gusset plate edges. It implies that other member force will influence the stress at the chord splice but the influence is limited in the range from SP3 to SP9.

3. The stress distributions at outer splice locations such as SP1 and SP2 are similar while the stress distributions at splice locations from SP3 to SP6 varies linearly with splice location move inward to the work point as shown in Figure 7.22. Since the distance between each splice location is the same, the influence from another member's force

can be assumed having linear influence with the distance in a certain effective range. Recall in Section 7.6.2, the XY shear stress from the diagonal is uniformly distributed at an effective shear length and the shear force could generate linear influence to the chord splice based on force equilibrium at the section aligned with the splice location. Therefore, the assumption that the X-direction normal stress at chord splice is affected by diagonal load is made.

These observations lead to assumptions that a force coming from a diagonal will affect the stress at the chord splice and that effect is related to the splice location. This splice locations where the diagonal force affects the normal stress at the splice seems to be linear to its location and limited to a range between SP3 and SP9, which is corresponding to the interference zone on the horizontal section defined in Figure 5.3.

7.8.1.2 Observation of the X-direction Normal Stress of the Type II Loading Profiles

To further investigate the influence of the diagonal force on the X-direction normal stress at the chord splice, the Type II Loading Profiles shown in Table 7.2, which vary the diagonal loads but keep the chord loads constant, are used. As shown in Figures 7.23 and 7.24, the X-direction normal stresses at all splices with the variation of the Type II Loading Profiles reinforce the assumptions made in the previous section. The observations from Type II Loading Profiles include:

1. In Figures 7.23, the stress distributions appear to be the same at splice locations located on one side of the gusset plate when the diagonal force is zero in Load 5 and Load 7 while the stress distributions vary with the splice location on other side of gusset plate in which there is non-zero diagonal load. When the diagonal load is zero, the X-direction normal stress at the chord splice only affected by the chord load and therefore the splice location does not affect stress distribution as observed in Chapter 6. This observation further indicates that the diagonal force affects the stress at splices only on the same side of the gusset plate.

2. In Figure 7.24, X-direction normal stress distributions at the Case SP1 have very

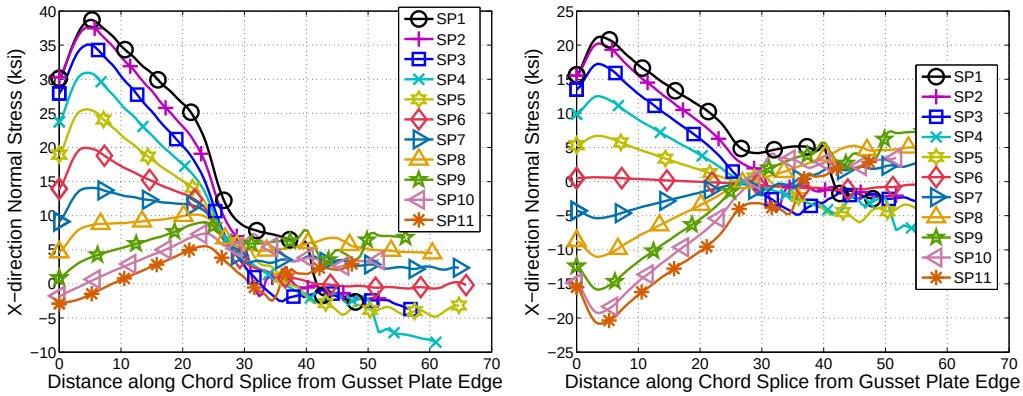

(a) Load 1 in Type I Loading Profiles is applied to gusset plate connection for all splice locations

(b) Load 2 in Type I Loading Profiles is applied to gusset plate connection for all splice locations

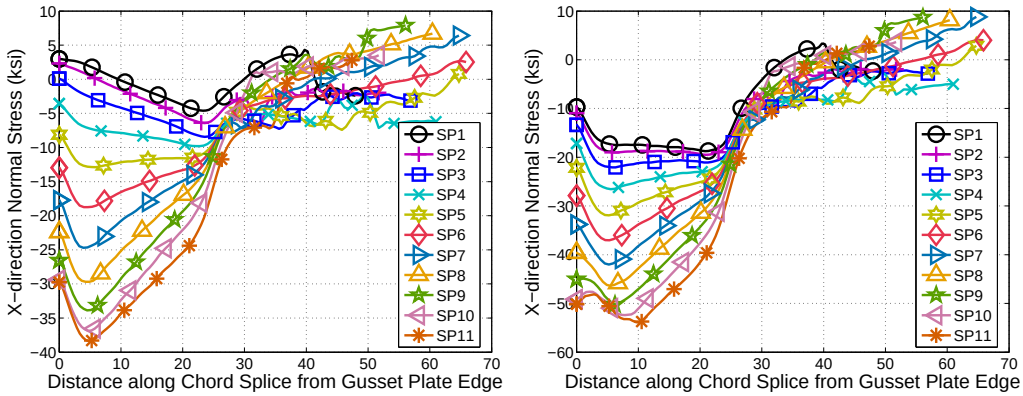

(c) Load 3 in Type I Loading Profiles is applied to gusset plate connection for all splice locations

(d) Load 4 in Type I Loading Profiles is applied to gusset plate connection for all splice locations

Figure 7.22: X-direction normal stresses at the chord splice for different Type I Loading Profiles and splice locations

similar stress distributions regardless of the loading profiles and the same is true for the Cases SP2, SP10, and SP11. This observation reinforces the conclusion in the previous section that the X-direction normal stress at the splices near the edges of gusset plates is only affected by the chord loads. Further observation shown in Figure 7.24 with Cases SP3, SP4, and SP5, X-direction normal stress distributions are affected proportionally by the magnitude of the diagonal loads. The maximum

stress is increased equally from Load 1 to Load 3 and is increased about the half increment from Load 3 to Load 4. The the ratio of the stress change is about the ratio of the load change in Member L9.

3. The diagonal load is found to increase or decrease the maximum X-direction normal stress at splices based on the direction of the chord and diagonal loads. In Figure 7.23, Load 8 is found increase the maximum stress at splice when the chord and diagonal loads both act in tension at the section aligned with the splice, such as in Cases SP3 to SP6. While for Load 6 the diagonal load acts in compression and the chord load acts in tension at the splice, thus the maximum stress is decreased with the variation of the splice location in Cases SP3 to SP6.

The X-direction normal stress at splices for Type I Loading Profiles and Type II Loading Profiles leads to some conclusions.

- The X-direction normal stress distribution at splices is determined by the chord load and affected by the diagonal load.
- The diagonal load only affect X-direction normal stress in a certain range in the gusset plate which is about from the splice location SP3 to the work point on one side of the gusset plate or from work point to the splice location SP9 on the other side of gusset plate. This region that diagonal load affects X-direction normal stress at splices corresponds to the region discussed in Chapter 5 when the TEP was derived. The schematic of the region was shown in Figure 5.3 and was denoted by *interference zone*.
- The influence of the diagonal load on the X-direction normal stress at splices is linear to the distance the splice located from the edge of the interference zone and proportional to the magnitude of the diagonal load. As the splice is located at the work point, the diagonal load has the maximum effect on the X-direction normal stress. In addition, the diagonal load may increase or decrease the maximum stress depending on the load direction of the chord and diagonal loads.

These observations clearly show that the net effect of the chord load and influence from the diagonal load shall be considered to approximate the X-direction normal stress at the chord

splice.

Finally, note that, the statistical data is not provided for the discussion of the X-direction normal stress discussion at splices with the variation of the Type I and Type II Loading Profiles since the stress variation is very significant, and the C_v^{max} is apparent large and the R_{ij}^{min} is apparent small. Besides, some near-zero stress distributions could cause problems with the results of C_v^{max} and R_{ij}^{min}.

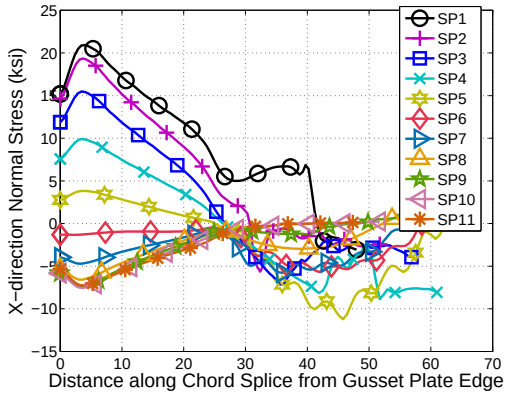

(a) X-direction normal stress distribution for all splice locations in Load 5 for Type II Loading Profiles

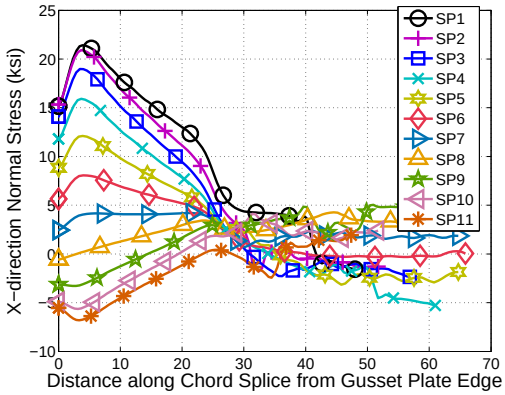

(b) X-direction normal stress distribution for all splice locations in Load 6 for Type II Loading Profiles

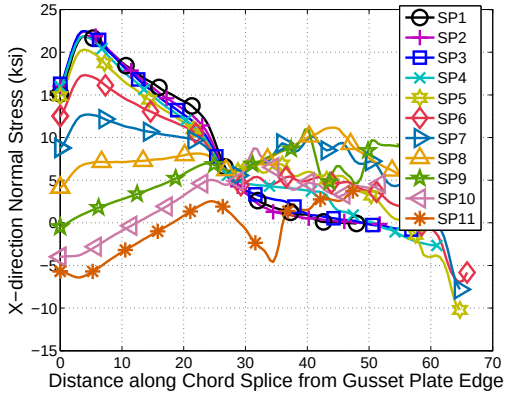

(c) X-direction normal stress distribution for all splice locations in Load 7 for Type II Loading Profiles

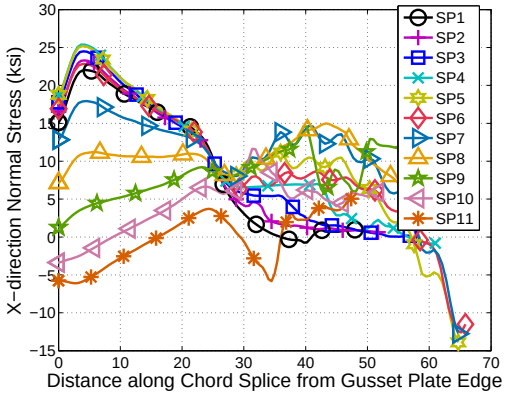

(d) X-direction normal stress distribution for all splice locations in Load 8 for Type II Loading Profiles

Figure 7.23: X-direction normal stress at all splice locations for Type II Loading Profiles

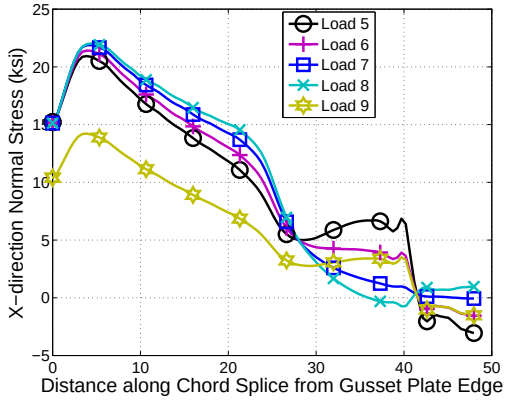

(a) X-direction normal stress distribution at Case SP1 for Type II Loading Profiles

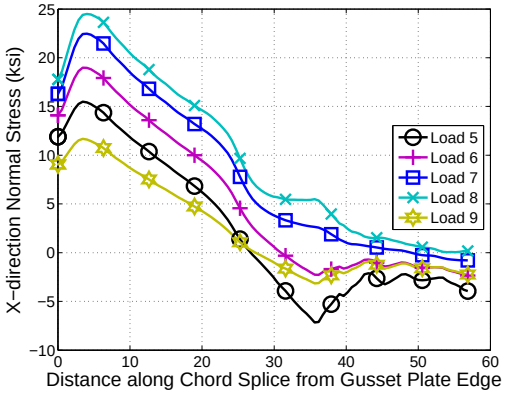

(b) X-direction normal stress distribution at Case SP3 for Type II Loading Profiles

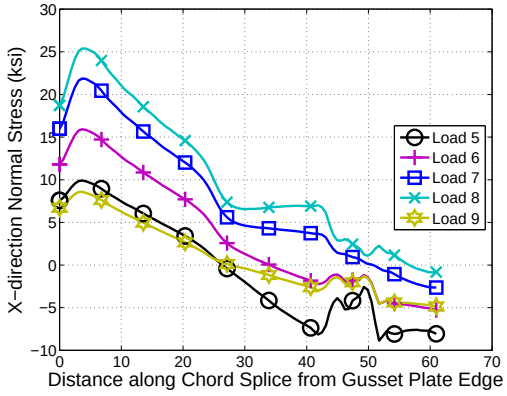

(c) X-direction normal stress distribution at Case SP4 for Type II Loading Profiles

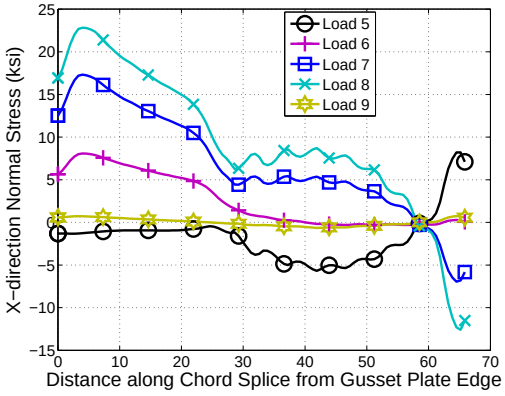

(d) X-direction normal stress distribution at Case SP5 for Type II Loading Profiles

Figure 7.24: X-direction normal stress for selected splice locations with variation of Type II Loading Profiles

7.8.2 Development of a Method for Approximating the X-direction Normal Stress Distribution at the Chord Splice

The Whitmore width approach currently used in practice to evaluate the stress at the chord splice was shown in Chapter 6 to be insufficient. Also in Chapter 6, a stress distribution model that considers the asymmetry of the configuration at the chord splice was developed

and shown to have good performance when only chord loads were considered to be acting on the joint. The study of the XY shear stress along the horizontal section provides a clue to understand how the diagonal load and the splice location affect the stress at the chord splice. The approximate XY shear stress along the horizontal section using the effective shear length for each diagonal, the chord loads, and the chord splice locations are shown schematically in Figure 7.25.

Figure 7.25 shows that the approximate XY shear stress is uniformly distributed along the effective length for each diagonal at the horizontal section. This stress then generates an accumulated shear force that varies linearly from zero at the outer edge of the effective shear length to the full value of the horizontal component of the diagonal force at the work point. Using this approximation and considering horizontal force equilibrium for a vertical cut of the gusset plate at the chord splice, the internal force at the chord splice can be taken as the net forces of the chord load and the accumulated shear force from the diagonal load. For example, if the chord splice is located half way along the diagonal's effective shear length, the net force at the splice would be the sum of the chord force and half of the horizontal component of the diagonal force. If the diagonal and chord forces are in the same direction, the net force at the splice is larger than the chord force and vice versa. Once the net force at the chord splice is determined, it is used in the trapezoidal stress distribution model, described in Chapter 6, to estimate the X-direction normal stress distribution at the chord splice for the gusset plate connection with all members loaded.

7.8.3 Validation of the Trapezoidal Stress Distribution Method for the X-direction Normal Stress at Chord Splice

The load cases in the Type I, II, and III Loading Profiles are used to verify that this method results in reasonable estimates of the stress at the chord splice. Figures 7.26 through 7.28 compare the stress distribution at the chord splice from FEA results with the approximated trapezoidal X-direction stress distribution using the net force at the splice for the three loading profiles. Each figure includes several sub-figures which are selected chord splice

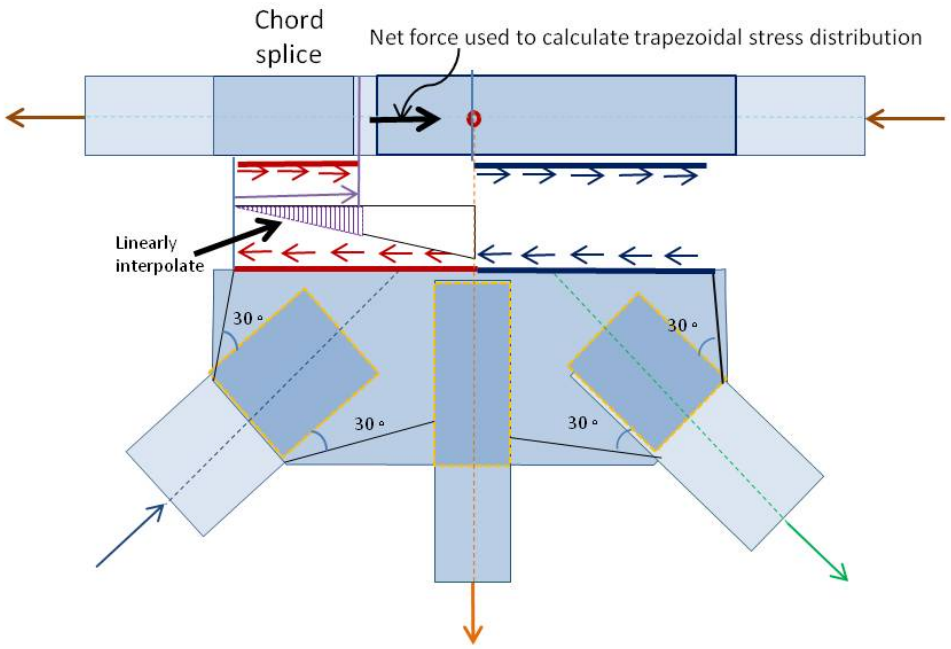

Figure 7.25: The net force at the splice is used to calculate stress at splice; the net force is the sum of the chord load and the interpolation of the horizontal force of the diagonal load

locations. The approximated trapezoidal stress distributions are represented by dashed lines and the FEA results are represented by solid lines. The R used to evaluate correlation between the FEA results and the estimated distribution are also given in the legend of each sub-figure and are computed for each load case at the loading profiles.

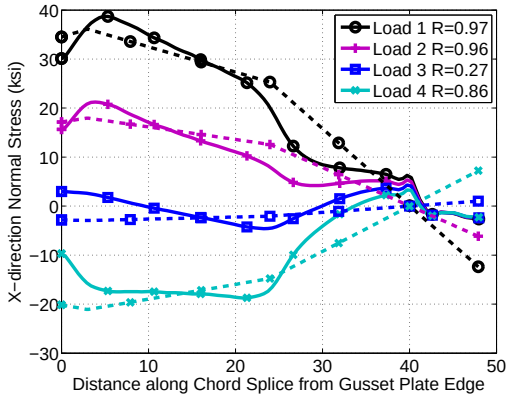

(a) X-direction normal stress comparison with SP1

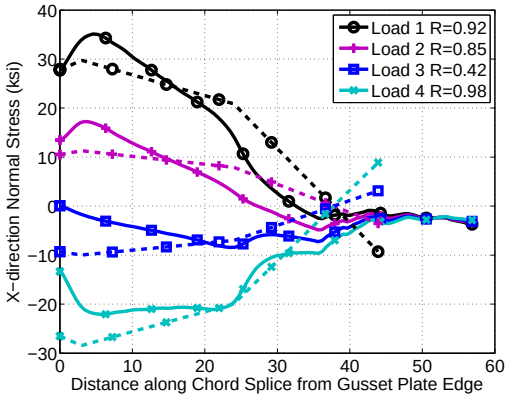

(b) X-direction normal stress comparison with SP3

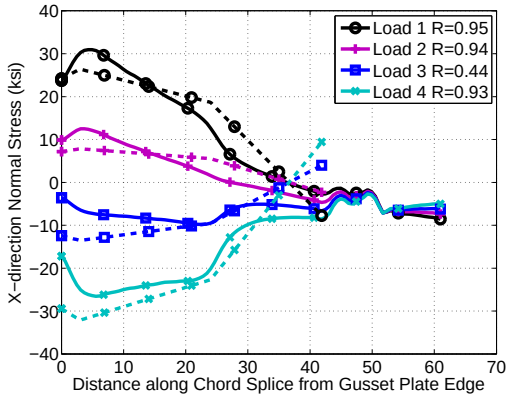

(c) X-direction normal stress comparison with SP4

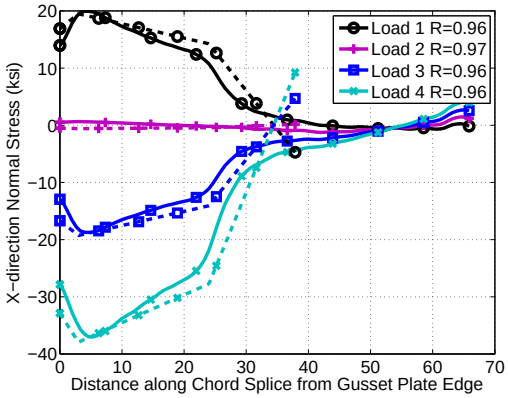

(d) X-direction normal stress comparison with SP6

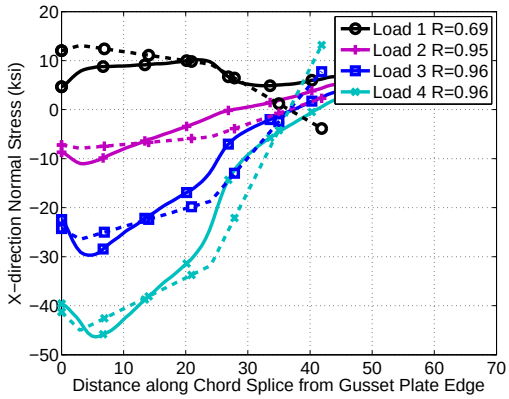

(e) X-direction normal stress comparison with SP8

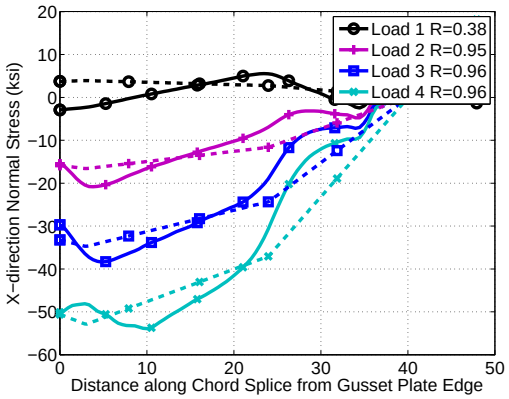

(f) X-direction normal stress comparison with SP11

Figure 7.26: X-direction normal stress at the splice locations for Type I Loading Profiles

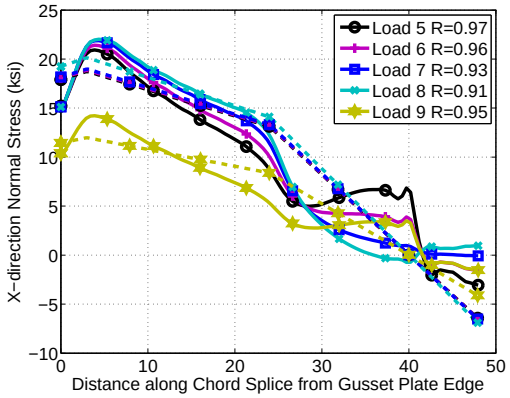

(a) X-direction normal stress comparison with SP1

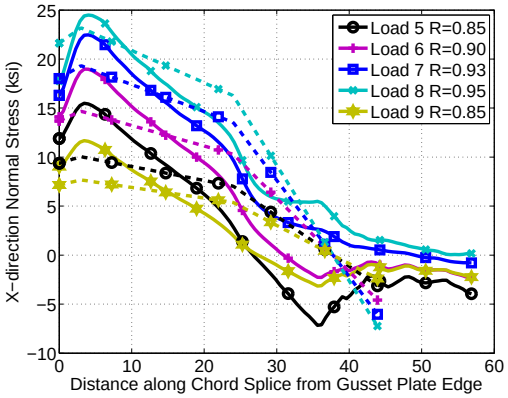

(b) X-direction normal stress comparison with SP3

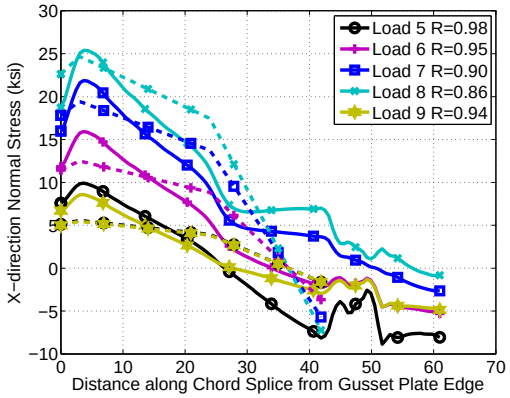

(c) X-direction normal stress comparison with SP4

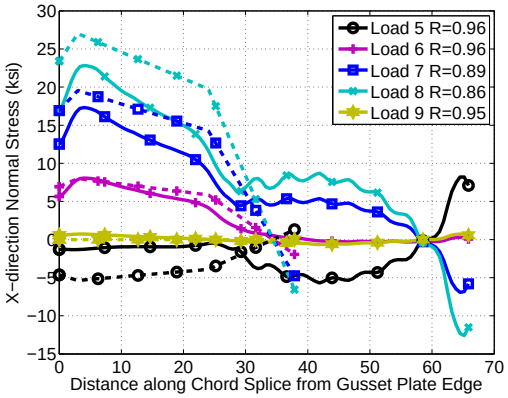

(d) X-direction normal stress comparison with SP6

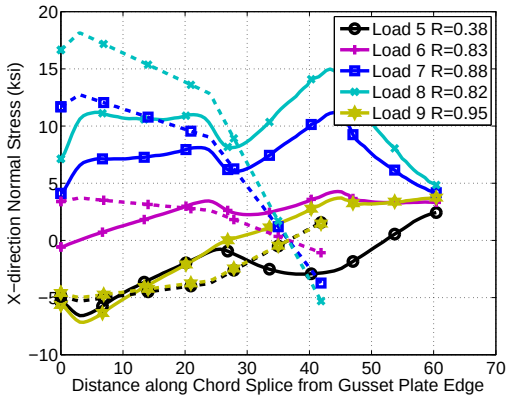

(e) X-direction normal stress comparison with SP8

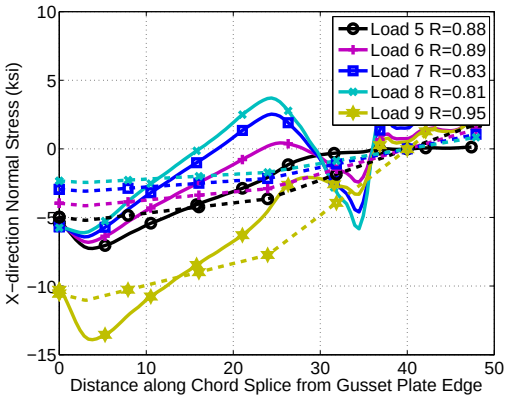

(f) X-direction normal stress comparison with SP11

Figure 7.27: X-direction normal stress at the splice locations for Type II Loading Profiles

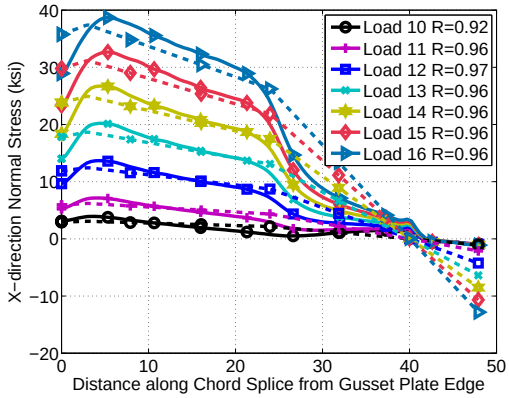

(a) X-direction normal stress comparison with SP1

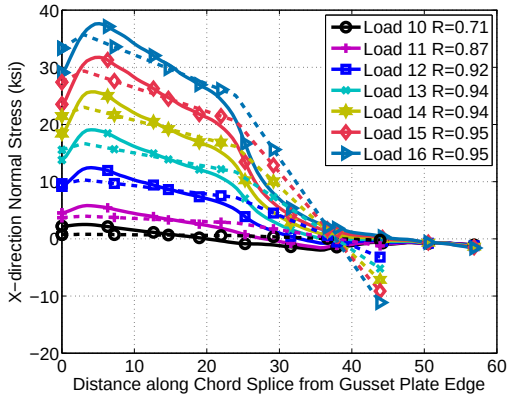

(b) X-direction normal stress comparison with SP3

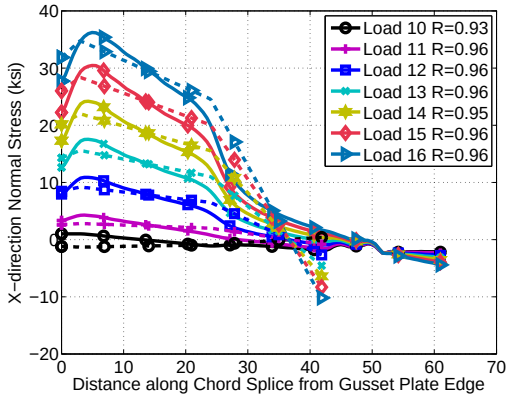

(c) X-direction normal stress comparison with SP4

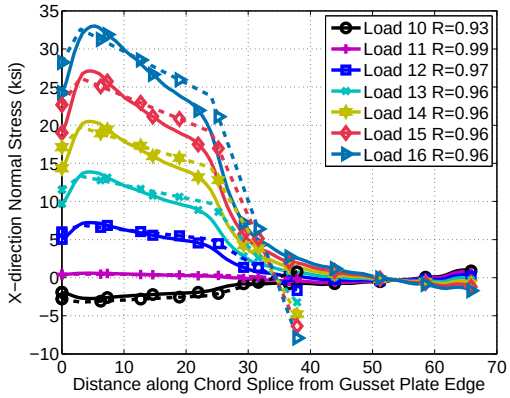

(d) X-direction normal stress comparison with SP6

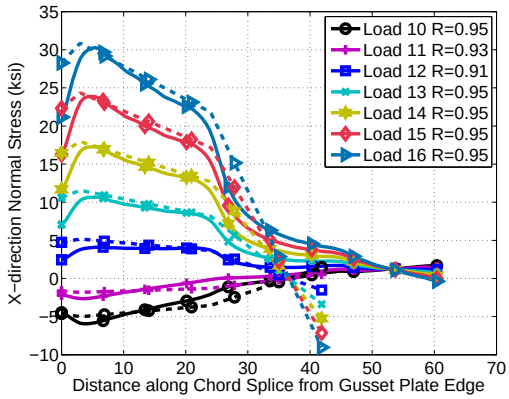

(e) X-direction normal stress comparison with SP8

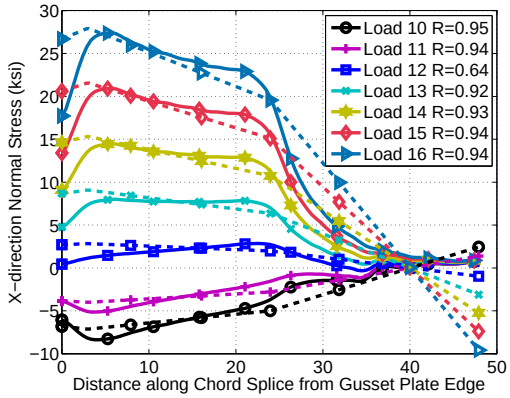

(f) X-direction normal stress comparison with SP11

Figure 7.28: X-direction normal stress at the splice locations for Type III Loading Profiles

For the Type I Loading Profiles, Figure 7.26, shows the computed stress distributions are close to the FEA results for most cases. This is also verified by correlation coefficient, R, which has values that are close to 1.0 when the net force at the splice is larger and dominating the stress distribution. However, when the net force is low and it generates the maximum stress less than 10 (ksi), the stress distributions might be affected by loads from member other than the chord and adjacent diagonal. In these cases the estimated distribution is less accurate and the R values are away from 1.0. Thus, when the maximum stress is smaller than 10 (ksi) in the distribution, the results of statistics will be neglected from the discussion.

The statistics R and R_{err} for each load case and splice location are listed in Table 7.15 for the Type I Loading Profiles. The average R is 0.93 and R_{err} is -4.93% for the Type I Loading Profiles. This indicates that the parameters considered in the approxiamtion of the stress distributions model at the chord splice are those that impact the distribution and that the estimate method is accurate for engineering practice.

Figure 7.27 shows the X-direction normal stress at the chord splice for Type II Loading Profiles, which have varying diagonal loads. Statistical results are given in Table 7.16. For these Loading Profiles, the average R is 0.81 and average R_{err} is -8.29% which indicates slightly poorer correlation between the FEA stress distribution and the approximated distribution than found for the Type I Loading Profiles. The worst correlations are observed for splice locations SP8 in Load 7 and Load 8 when the load in the right diagonal, L11, has high loads and results in a low net force at the chord splice. In these cases, the maximum stress on the gusset plate as a whole is not observed at the chord splice but instead occurs elsewhere along the horizontal section. The low net force at the splice results in larger relative influences on the stress at the splice from the other members that are not considered in the approximated stress distribution model for the chord splice. This influence will be further discussed in the next section when the moment eqilibrium is considered. However, in these cases the stress at the splice stress is low and the maximum gusset plate stress will occur elsewhere. This observation also demonstrates that the complexity of the stress interactions in gusset plates and that many minor factors that are neglected here would

need to be considered to fully estimate the stress distribution.

The results for the X-direction normal stress at the chord splice for the Type III Loading Profiles are shown in Figure 7.28 and the statistical results are listed in Table 7.17. The average R is 0.95 and average R_{err} is -3.53% over all the Type III loads. In general, the method of estimating the stress at the chord splice seems perform very well for all the TypeIII Loading Profiles.

Finally, the statistical results for all loading profiles and splice locations considered are plotted in the Figures 7.29 and 7.30. These two plots show the average correlation coefficient, R, equals to 0.92 and error percentage, R_{err}, is around -5.25%. Also shown are statistics for the stresses calculated using the Whitmore method with the worst case for chord load and connection length used and are shown in Tables 7.18, 7.19, and 7.20. The error percentages at the maximum X-direction normal stress along the splice location using the Whitmore's method for three type loading profiles are -21.7%, -40.16%, and -37.88% respectively, and the average error percentages for three loading profiles is -33.4%. The Whitmore's method is again verified inappropriate for stress estimate at chord splice for all members loaded. The correlation of coefficient is meaningless for all the Whitmore stress distribution because the Whitmore stress is a constant distribution and the variance and covariance of this distribution is zero. Correlation coefficient of Eq. 7.2 is meaningless in this condition. As shown, the proposed method is much better at predicting both the magnitude and distribution at the chord splice. Based on these results the developed method is recommended for evaluating the stress at the chord splices in gusset plate connection. A summary of the procedure is provided at the end of this chapter.

Table 7.15: Statistics to evaluate error and correlation of the approximated X-direction normal stress distributions to the FEA results for the Type I Loading Profiles

		Load 1		Load 2		Load 3		Load 4	
		R	R_{err}	R	R_{err}	R	R_{err}	R	R_{err}
	SP1	0.97	-6.77 %	0.96	-15.52 %	0.27[1]	36.09 %[1]	0.86	12.44%
	SP2	0.93	-12.65%	0.89	-27.65 %	0.09 [1]	2.16 %[1]	0.95	26.91%
	SP3	0.92	-15.34%	0.85	-34.70 %	0.42 [1]	24.19 %[1]	0.98	28.65 %
	SP4	0.95	-14.81%	0.94	-37.48 %	0.44 [1]	40.30 %[1]	0.93	20.83 %
Type I	SP5	0.97	-10.19%	0.96 [1]	-35.48 %[1]	0.84	32.88 %	0.93	12.12 %
Loading	SP6	0.96	-2.27 %	0.97[1]	196.9 %[1]	0.96	2.75 %	0.96	2.41 %
Profiles	SP7	0.92	15.28 %	0.93 [1]	-9.57 %[1]	0.96	-4.77 %	0.96	0.39 %
	SP8	0.69	29.55 %	0.95	-28.65 %	0.96	-11.04%	0.96	-3.01 %
	SP9	0.34 [1]	14.35 %[1]	0.89	-31.52 %	0.93	-13.53%	0.95	-4.87 %
	SP10	0.08 [1]	-3.84 % [1]	0.87	-28.60 %	0.92	-12.96%	0.94	-3.76 %
	SP11	0.38[1]	29.37 %[1]	0.95	-20.39%	0.96	-9.51 %	0.96	-2.01%
Average $R = 0.93$; Standard Deviation for $R = 0.05$									
Average $R_{err} = -4.93\%$; Standard Deviation for $R_{err} = 18.85\%$									

[1] is excluded from the average due to the low stress

Table 7.16: Statistics to evaluate error and correlation of the approximated X-direction normal stress distribution to the FEA results for the Type II Loading Profiles

		Load 5		Load 6		Load 7		Load 8		Load 9	
		R	R_{err}	R	R_{err}	R	R_{err}	R	R_{err}	R	R_{err}
	SP1	0.97	-10.54%	0.96	-11.94%	0.93	-13.29 %	0.91	-8.65%	0.95	-15.85 %
	SP2	0.90	-25.38%	0.92	-19.62%	0.93	-14.53%	0.93	-6.99 %	0.89	-27.63 %
	SP3	0.85	-35.22%	0.90	-22.73%	0.93	-14.11%	0.95	-5.38 %	0.85	-34.33 %
	SP4	0.98 [1]	-43.95%[1]	0.95	-21.65%	0.90	-11.32%	0.86	-2.97 %	0.94 [1]	-36.56 %[1]
Type II	SP5	1.00[1]	-168 %[1]	0.97	-15.18%	0.87	-3.89 %	0.79	3.80 %	0.96 [1]	-33.08 %[1]
Loading	SP6	0.96[1]	304.1%[1]	0.96 [1]	-0.86 %[1]	0.89	12.79%	0.86	18.28%	0.95 [1]	-100 %[1]
Profiles	SP7	0.71[1]	13.38 %[1]	0.79 [1]	39.59 %[1]	0.34	33.83%	0.21	32.10%	0.94 [1]	-11.44%[1]
	SP8	0.38 [1]	-19.18%[1]	0.83[1]	19.40 %[1]	-0.88[1]	58.22%[1]	0.82	61.93%	0.95 [1]	-30.05%[1]
	SP9	0.83 [1]	-28.56%[1]	0.71[1]	-148.8%[1]	-0.51[1]	32.47 %[1]	0.43 [1]	42.47%[1]	0.89	-32.48%
	SP10	0.86 [1]	-30.40%[1]	0.71 [1]	-62.39%[1]	-0.52[1]	-4.2 %[1]	0.45 [1]	11.80%[1]	0.87	-29.23%
	SP11	0.88 [1]	-28.33%[1]	0.89 [1]	-39.19%[1]	0.83 [1]	-51.92 %[1]	0.81 [1]	-59.92%[1]	0.95	-20.7 %
Average $R = 0.81$; Standard Deviation $R = 0.34$											
Average $R_{err} = -8.29\%$; Standard Deviation $R_{err} = 22.1\%$											

[1] is excluded from the average due to the low stress

Table 7.17: Statistics to evaluate error and correlation of the approximated X-direction normal stress distribution to the FEA results for the Type III Loading Profiles

		Load 10		Load 11		Load 12		Load 13	
		R	R_{err}	R	R_{err}	R	R_{err}	R	R_{err}
	SP1	0.92[1]	-21.81%[1]	0.96[1]	-13.59%[1]	0.97	-9.15%	0.96	-7.60%
	SP2	0.82[1]	-45.09 %[1]	0.90 [1]	-25.27%[1]	0.93	-14.96%	0.94	-11.54%
	SP3	0.71[1]	-68.89 %[1]	0.87 [1]	-31.82%[1]	0.92	-17.05%	0.94	-12.62%
	SP4	0.93[1]	-230 %[1]	-0.93[1]	-34.14%[1]	0.96	-15.62%	0.96	-11.18%
Type III	SP5	0.76[1]	74.47 %[1]	-0.76[1]	-32.20%[1]	0.98	-11.03%	0.97	-7.81 %
Loading	SP6	0.93[1]	17.56 %[1]	0.99 [1]	-19.90%[1]	0.97 [1]	-4.56 %[1]	0.96	-3.89 %
Profiles	SP7	0.94[1]	-3.32 %[1]	0.78 [1]	-5.22%[1]	0.95 [1]	7.23 %[1]	0.95	1.50 %
	SP8	0.95[1]	-15.68 %[1]	0.93 [1]	-31.30%[1]	0.91 [1]	25.84 %[1]	0.95	8.18 %
	SP9	0.92[1]	-20.05 %[1]	0.88 [1]	-34.24%[1]	0.89 [1]	20.45 %[1]	0.97[1]	13.69 %[1]
	SP10	0.91[1]	-19.77 %[1]	0.86 [1]	-30.96%[1]	0.87 [1]	11.85 %[1]	0.97[1]	16.12 %[1]
	SP11	0.95[1]	-14.91 %[1]	0.94 [1]	-22.29 %[1]	0.64 [1]	-0.58 %[1]	0.92[1]	13.29 %[1]

		Load 14		Load 15		Load 16	
	SP1	0.96	-6.80%	0.96	-4.62%	0.96	-3.44%
	SP2	0.94	-9.80 %	0.94	-6.87%	0.95	-4.92%
	SP3	0.94	-10.49%	0.95	-7.52%	0.95	-5.12%
	SP4	0.96	-9.19 %	0.95	-6.95%	0.96	-4.16%
Type III	SP5	0.97	-6.52 %	0.96	-4.94%	0.96	-2.46%
Loading	SP6	0.96	-3.64 %	0.96	-3.50%	0.96	-1.24%
Profiles	SP7	0.96	-0.18 %	0.96	-0.97%	0.96	0.62 %
	SP8	0.95	3.82 %	0.95	1.82 %	0.95	1.76 %
	SP9	0.97	6.76 %	0.97	3.72 %	0.96	2.46 %
	SP10	0.96	7.64 %	0.96	4.28 %	0.96	2.86 %
	SP11	0.93	5.79 %	0.94	2.90 %	0.94	1.83 %

Average $R = 0.95$; Standard Deviation $R = 0.01$

Average $R_{err} = -3.53\%$; Standard Deviation $R_{err} = 6.41\%$

[1] is excluded from the average due to the low stress

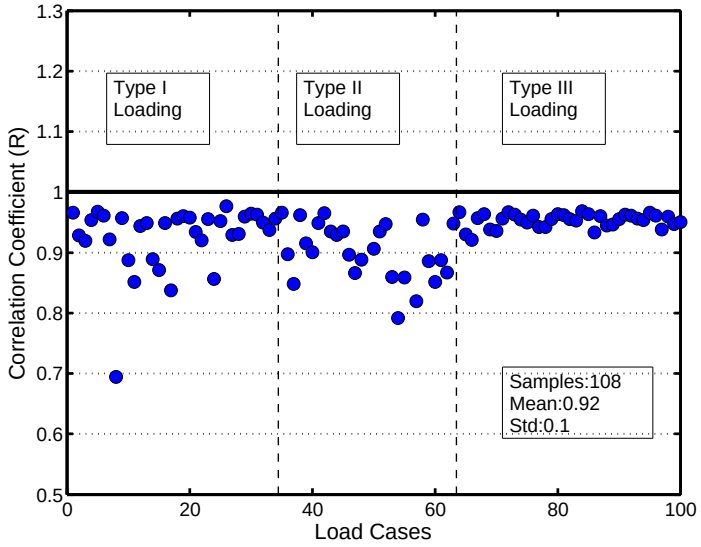

Figure 7.29: Statistics of the stress correlation coefficient R

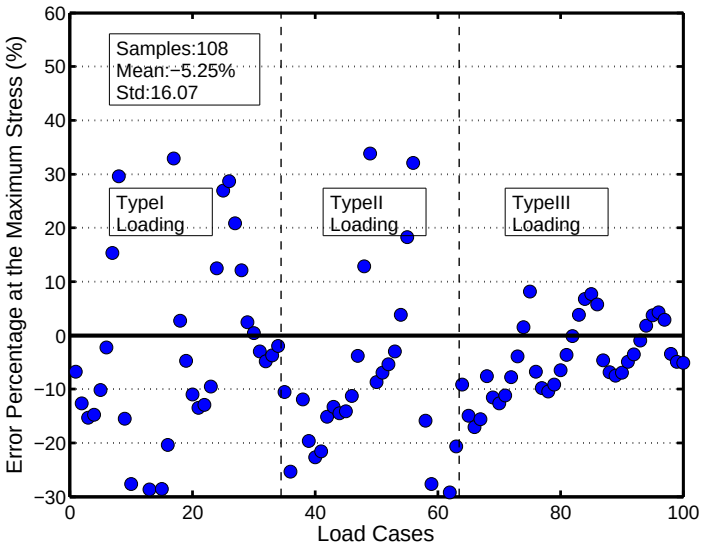

Figure 7.30: Statistics of the error percentage of the estimated stress to FEA results at the maximum stress R_{err}

Table 7.18: Statistics to evaluate error percentage and correlation coefficient of the Whitmore stress distributions at the chord splices to the FEA results for the Type I Loading Profiles

		Load 1		Load 2		Load 3		Load 4	
		R	R_{err}	R	R_{err}	R	R_{err}	R	R_{err}
	SP1	N.A.	-27.02%	N.A.	-33.52%	N.A.[1]	161.74%[1]	N.A.	-3.58%
	SP2	N.A.	-34.10%	N.A.	-38.59%	N.A.[1]	98.88%[1]	N.A.	-1.75%
	SP3	N.A.	-36.61%	N.A.	-35.57%	N.A.[1]	61.14%[1]	N.A.	-7.63%
	SP4	N.A.	-34.97%	N.A.	-19.61%	N.A.[1]	48.39%[1]	N.A.	-17.81%
Type I	SP5	N.A.	-28.24%	N.A.[1]	36.61%[1]	N.A.	21.21%	N.A.	-26.53%
Loading	SP6	N.A.	-15.29%	N.A.[1]	-1279.28%[1]	N.A.	-9.98%	N.A.	-31.63%
Profiles	SP7	N.A.	11.12%	N.A.[1]	70.38%[1]	N.A.	-25.64%	N.A.	-34.43%
	SP8	N.A.	43.08%	N.A.	-8.89%	N.A.	-32.24%	N.A.	-34.91%
	SP9	N.A.[1]	50.47%[1]	N.A.	-29.84%	N.A.	-34.34%	N.A.	-33.55%
	SP10	N.A.[1]	73.14% [1]	N.A.	-35.49%	N.A.	-32.53%	N.A.	-28.73%
	SP11	N.A.[1]	117.54%[1]	N.A.	-32.28%	N.A.	-26.43%	N.A.	-21.50%
Average $R_{err} = -21.7\%$; Standard Deviation $R_{err} = 18.33\%$									

[1] is excluded from the average due to the low stress

Table 7.19: Statistics to evaluate error and correlation coefficient of Whitmore stress distribution at the chord splices to the FEA results for the Type II Loading Profiles

		Load 5		Load 6		Load 7		Load 8		Load 9	
		R	R_{err}	R	R_{err}	R	R_{err}	R	R_{err}	R	R_{err}
	SP1	N.A.	-29.3%	N.A.	-31.01%	N.A.	-32.49%	N.A.	-32.93%	N.A.	-33.80%
	SP2	N.A.	-32.70%	N.A.	-37.71%	N.A.	-41.95%	N.A.	-44.11%	N.A.	-39.04%
	SP3	N.A.	-24.82%	N.A.	-38.67%	N.A.	-48.20%	N.A.	-52.47%	N.A.	-36.47%
	SP4	N.A.[1]	6.26%[1]	N.A.	-33.89%	N.A.	-51.88%	N.A.	-58.55%	N.A.[1]	-21.77%[1]
Type II	SP5	N.A.[1]	151.09%[1]	N.A.	-20.63%	N.A.	-52.67%	N.A.	-61.86%	N.A.[1]	28.33%[1]
Loading	SP6	N.A.[1]	-332.11%[1]	N.A.[1]	9.46%[1]	N.A.	-48.99%	N.A.	-61.30%	N.A.[1]	680.83%[1]
Profiles	SP7	N.A.[1]	-264.63%[1]	N.A.[1]	94.39%[1]	N.A.	-35.58%	N.A.	-54.39%	N.A.[1]	84.18%[1]
	SP8	N.A.[1]	-215.61%[1]	N.A.[1]	121.37%[1]	N.A.[1]	-6.17%[1]	N.A.	-32.01%	N.A.[1]	-6.45%[1]
	SP9	N.A.[1]	-196.07%[1]	N.A.[1]	-316.69%[1]	N.A.[1]	1.93%[1]	N.A.[1]	-22.78%[1]	N.A.	-29.19%
	SP10	N.A.[1]	-188.51%[1]	N.A.[1]	-218.44%[1]	N.A.[1]	32.85%[1]	N.A.[1]	0.69%[1]	N.A.	-35.34%
	SP11	N.A.[1]	-186.81%[1]	N.A.[1]	-192.50%[1]	N.A.[1]	-198.3%[1]	N.A.[1]	-203.2%[1]	N.A.	-32.33%
Average $R_{err} = -40.16\%$; Standard Deviation $R_{err} = 11\%$											

[1] is excluded from the average due to the low stress

Table 7.20: Statistics to evaluate error and correlation of Whitmore stress distribution at the chord splices to the FEA results for the Type III Loading Profiles

		Load 10		Load 11		Load 12		Load 13	
		R	R_{err}	R	R_{err}	R	R_{err}	R	R_{err}
	SP1	-N.A.[1]	-163.77%[1]	N.A.[1]	-32.04%[1]	N.A.	-28.91%	N.A.	-27.83%
	SP2	N.A.[1]	-175.19 %[1]	N.A.[1]	-37.05 %[1]	N.A.	-36.05%	N.A.	-35.78%
	SP3	N.A.[1]	-212.10 %[1]	N.A.[1]	-34.03%[1]	N.A.	-38.37%	N.A.	-39.75%
	SP4	N.A.[1]	171.04 %[1]	N.A.[1]	-18.83%[1]	N.A.	-36.40%	N.A.	-40.76%
Type III	SP5	N.A.[1]	115.65 %[1]	N.A.[1]	30.12%[1]	N.A.	-30.26%	N.A.	-39.65%
Loading	SP6	N.A.[1]	27.89 %[1]	N.A.[1]	394.02%[1]	N.A.[1]	-19.58%[1]	N.A.	-37.12%
Profiles	SP7	N.A.[1]	-14.18 %[1]	N.A.[1]	-337.21%[1]	N.A.[1]	-3.09 %[1]	N.A.	-33.78%
	SP8	N.A.[1]	-30.00 %[1]	N.A.[1]	-194.26 %[1]	N.A.[1]	22.00 %[1]	N.A.	-29.63%
	SP9	N.A.[1]	-35.86 %[1]	N.A.[1]	-31.13%[1]	N.A.[1]	28.54%[1]	N.A.[1]	-25.61%[1]
	SP10	N.A.[1]	-35.91 %[1]	N.A.[1]	-36.96%[1]	N.A.[1]	36.42%[1]	N.A.[1]	-22.71%[1]
	SP11	N.A.[1]	-30.18 %[1]	N.A.[1]	-33.70%[1]	N.A.[1]	45.69%[1]	N.A.[1]	-21.30 %[1]
		Load 14		Load 15		Load 16			
	SP1	N.A.	-27.26%	N.A.	-25.60%	N.A.	-24.72%		
	SP2	N.A.	-35.63%	N.A.	-34.21%	N.A.	-33.29%		
	SP3	N.A.	-40.40%	N.A.	-39.68%	N.A.	-38.96%		
	SP4	N.A.	-42.73%	N.A.	-43.15%	N.A.	-42.66%		
Type III	SP5	N.A.	-43.46%	N.A.	-45.01%	N.A.	-45.17%		
Loading	SP6	N.A.	-43.29%	N.A.	-46.44%	N.A.	-47.18%		
Profiles	SP7	N.A.	-42.83%	N.A.	-47.15%	N.A.	-48.85%		
	SP8	N.A.	-42.01%	N.A.	-47.57 %	N.A.	-50.40 %		
	SP9	N.A.	-41.47%	N.A.	-44.12 %	N.A.	-43.38 %		
	SP10	N.A.	-34.71%	N.A.	-34.63 %	N.A.	-34.32 %		
	SP11	N.A.	-22.89%	N.A.	-23.52 %	N.A.	-23.50 %		
Average $R_{err} = -37.88\%$; Standard Deviation $R_{err} = 7.43\%$									

[1] is excluded from the average due to the low stress

7.9 Y-direction Normal Stress Distribution at the Horizontal Section

7.9.1 Observations of the Y-direction Normal Stress at the Horizontal Section

The Y-direction normal stress at the horizontal critical section that is between the chord and hanger is considered in a more straightforward way since only the diagonal and hanger loads generate this stress. The chord loads are not expected to impact on the Y-direction normal stress significantly because they are generally orthogonal to it while the diagonal and hanger loads shall dominate the distribution. Although some concerns might be raised for the unbalanced moment generated by the chord load on the horizontal section, the unbalanced moment will be discussed later for the force and moment equilibrium on the horizontal section in this chapter. Considering this, it is expected that there would be little variation in the Y-direction normal stress distribution at the horizontal section of the Type I Loading Profiles where the chord loads are varied and the diagonal and hanger loads are constant. Conversely, large variation in the Y-direction normal stress distribution is expected for the Type II Loading Profiles where the diagonal and hanger loads are varied. This is verified by the comparison of the Y-direction normal stress distribution at selected splice locations for Type I and Type II Loading Profiles as shown in Figure 7.31. Figures 7.31(a) and 7.31(b) show the Y-direction normal stress distribution at the splice location SP3 and SP6 for the Type I Loading Profiles while Figures 7.31(c) and 7.31(d) show the distributions at the same selected splice locations for Type II Loading Profiles. Figure 7.31 also shows that only a small changes in stress is observed at the splice location due to the the discontinuity of the geometric configuration. The statistical data in Table 7.21 show the same trend, i.e. the splice location has little impact on the Y-direction normal stress distribution and the change in diagonal loads dominates the Y-direction normal stress distribution.

In the Type I Loading Profiles, which have near-equal and opposite diagonal loads, the Y-direction normal stress distribution is nearly a linear distribution as shown in Figures 7.31(a) and 7.31(b) if the region directly above the hanger is neglected because of the geometric discontinuity. This phenomenon might lead to the presumption that the Y-direction normal

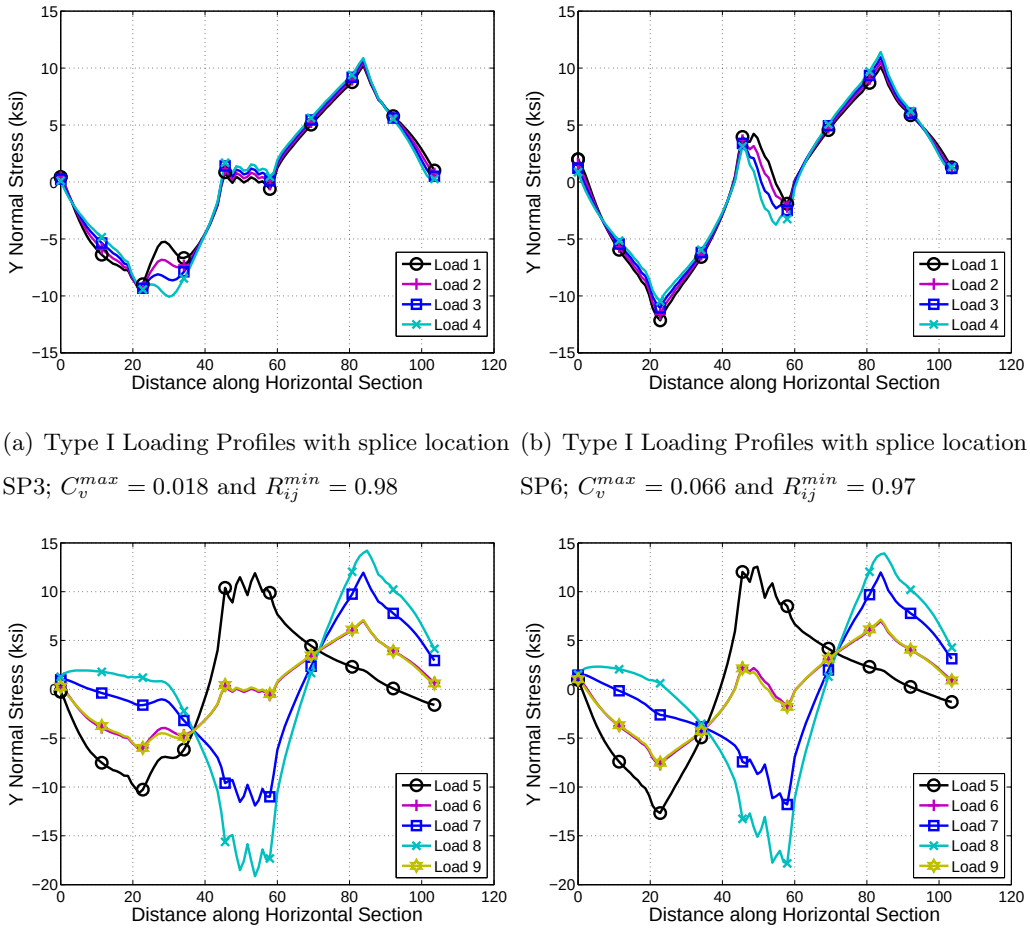

(a) Type I Loading Profiles with splice location SP3; $C_v^{max} = 0.018$ and $R_{ij}^{min} = 0.98$

(b) Type I Loading Profiles with splice location SP6; $C_v^{max} = 0.066$ and $R_{ij}^{min} = 0.97$

(c) Type II Loading Profiles with splice location SP3; $C_v^{max} = 0.56$ and $R_{ij}^{min} = 0.28$

(d) Type II Loading Profiles with splice location SP6; $C_v^{max} = 0.55$ and $R_{ij}^{min} = 0.20$

Figure 7.31: Stress distributions of Y-direction normal stress at the horizontal critical section for the Type I and Type II Loading Profiles with selected splice locations

stress distribution might be generated by bending moment on the horizontal section. This unbalanced moment is generated because the diagonal and hanger loads are not concurrent loads on the horizontal section and resulted in the application of beam theory for estimating the Y-direction normal stress on the horizontal section. However, the stress distributions from the Type II Loading Profiles shown in Figures 7.31(c) and 7.31(d) do not support that linear beam theory and the resulting linear stress distribution is insufficient to describe the

Y-direction normal stress at the horizontal section.

Figures 7.31(c) and 7.31(d) show when one diagonal has zero load, the peak stress area is moved to the middle of the horizontal section and the distribution is not linear at the section. Instead, for the Type I or Type II Loading Profiles, the Y-direction normal stress distribution shows peak stresses possible at three locations, the left diagonal corner projected vertically to the horizontal section, the hanger width projected vertically to the horizontal section, and the right diagonal corner projected vertically to the horizontal section. The peak stress close to the corner of the diagonal decays linearly from the corner toward both edges of the gusset plate while the stress around the hanger end shows a small plateau. As one of the diagonal loads approaches zero, the peak stress generated by that diagonal is diminished. This observation shows that the estimate of Y-direction normal stress distribution at the horizontal section may be better estimated by the load path for the connected elements acting pn the horizontal section and the equilibrium is enforce to determine the peak value of the distribution. This concept is similar to strut and tie model in reinforced concrete deep beam. The validation of this concept for the Y-direction normal stress on the gusset plate horizontal critical section will be discussed later in this chapter.

Tables 7.21 and 7.22 show the statistics for the observation of Y-direction normal stress at the horizontal section for Type I and II Loading Profiles. It verities the observation described above.

Table 7.21: C_v^{max} and R_{ij}^{min} for the Y-direction normal stress distribution at the horizontal critical section for the Type I and Type II Loading Profiles

		SP1	SP2	SP3	SP4	SP5	SP6	SP7	SP8	SP9	SP10	SP11
Type I Loading	C_v^{max}	0.006	0.169	0.018	0.049	0.058	0.066	0.061	0.053	0.045	0.038	0.031
Profiles	R_{ij}^{min}	0.98	0.98	0.98	0.97	0.97	0.97	0.97	0.97	0.96	0.96	0.96
Type II	C_v^{max}	0.56	0.56	0.56	0.55	0.56	0.55	0.56	0.52	0.48	0.5	0.59
Loading Profiles	R_{ij}^{min}	0.26	0.29	0.28	0.25	0.22	0.20	0.20	0.22	0.24	0.25	0.25

Table 7.22: C_v^{max} and R_{ij}^{min} for the splice location parameter over the Type I and Type II Loading Profiles

		Load 1	Load 2	Load 3	Load 4	
Type I Loading	C_v^{max}	0.12	0.08	0.05	0.07	
Profiles	R_{ij}^{min}	0.96	0.97	0.96	0.89	
		Load 5	Load 6	Load 7	Load 8	Load 9
Type II	C_v^{max}	0.07	0.10	0.07	0.05	0.08
Loading Profiles	R_{ij}^{min}	0.98	0.97	0.98	0.99	0.97

7.9.2 Development of the Approximating Method for the Y-direction Normal Stress Distribution at the Horizontal Critical Section

The observation presented in section 7.9.1 suggests that the Y-direction normal stress at the horizontal section may be better approximated by considering the load paths from the diagonals and hanger than by beam theory (where beam theory estimate a stress distribution based on elastic section properties of the horizontal section subjected to an axial load and moment). The proposed concept is represented schematically in Figure 7.32 and is denoted the load path model. The Y-direction normal stress on the horizontal section is taken as the sum of the normal stress generated separately by each diagonal and the hanger. The diagonal loads are assumed to generate a triangular stress distribution where the vertex of the triangle is located at where the corner of the diagonal, projected vertically, intersects to the horizontal section. The effective length along the horizontal section that is considered to be affected by the diagonal load is that bounded by the intersection of the 30° dispersion angle projected from each side of the diagonal. This is because the projection of the 30° dispersion angle from one side of the diagonal often expends off the gusset plate and complicates the calculation of the effective length. To simplify the calculation conservatively and satisfy the equilibrium of the perpendicular forces at the horizontal section, the effective length along the horizontal section for each diagonal is limited by the intersection of the of the dispersion angle from the other diagonal. Figure 7.32 shows that the effective section

for one diagonal is bounded by the intersection of its own dispersion angle and the other diagonal's dispersion angle with the horizontal section. The magnitude of stress at the peak of the triangle is determined by setting the vertical component of the diagonal load equal to the the integration of the triangular stress distribution. For the hanger, because it is normal to the horizontal and there is typically sufficient area on the horizontal section to develop the full dispersion area with 30° angles is used, the assumed stress distribution is a trapezoidal shape shown in Figure 7.32. The magnitude of the stress at the plateau is also computed by setting the hanger load equal to the integration of trapezoidal stress distribution over the area.

Once the Y-direction normal stresses along the horizontal section from each diagonal and the hanger are found, they are superimposed. Note that this approximation of the Y-direction normal stress on the horizontal section results in an unbalanced moment caused by the non-concurrent forces of each diagonal loads. This moment is typically small and is neglected. This is discussed further in Section 7.10.

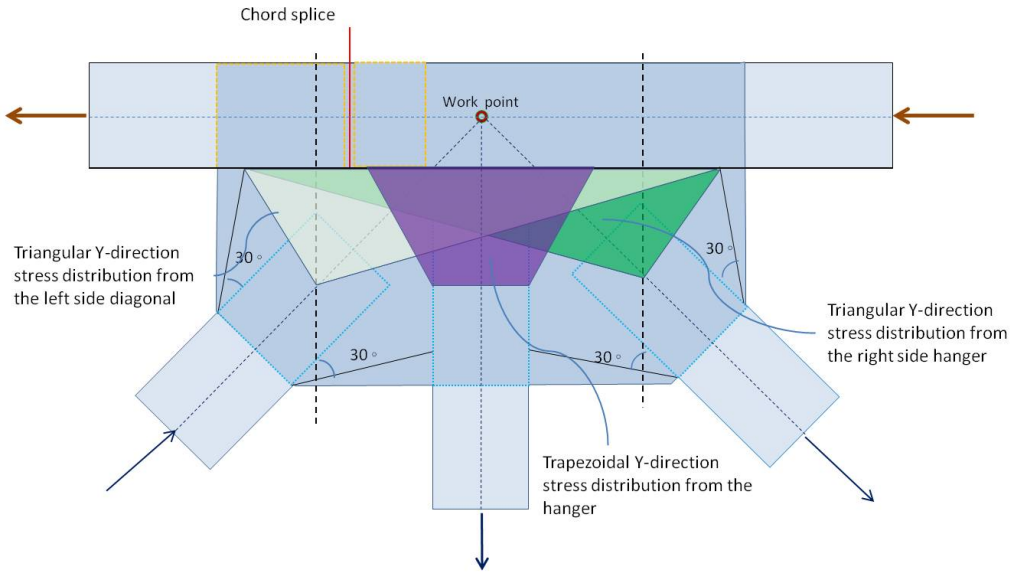

Figure 7.32: Schematic of the assumptions used to approximate the Y-direction normal stress on the horizontal section in the load path model

7.9.3 Validation of the Loading Path Method for the Y-direction Normal Stress at the Horizontal Section

The approximated Y-direction normal stress distributions using the proposed load path model at the horizontal section for the Type I, II, and III Loading Profiles are shown in Figures 7.33 through Figure 7.35 with the FEA results and the stress distribution found using beam theory. The smallest correlation factor, R, for the loading path approximated Y-direction normal stress is 0.92 while for the beam theory the smallest is 0.35. The statistics are listed in Table 7.23 and visualized in Figures 7.36 and 7.37 for the correlation coefficient of the stress distributions and the error percentage of the estimate at the maximum stress respectively. The loading path model is clearly shown to provide better estimates than beam theory for the Y-direction normal stress for both the overall stress distribution and the maximum stress.

For Type I Loading Profiles, the load path model provides a better estimate than beam theory; however, the difference is not very significant as shown in Figure 7.33. The stress distribution generated by beam theory also captures the trend of the distribution well for Type I Loading Profiles. However, for Type II Loading Profiles, beam theory is not able to estimate the stress distributions well and the load path model provides a much better result, as shown in Figure 7.34. For Type III loading profile again beam theory provides a decent approximate but the load path model is superior as shown in Figure 7.35.

The beam theory does not adequately estimate the Y-direction normal stress distribution at the horizontal section because the gusset plate is more like a deep beam. The loading path model method instead is based on considering the projected loading paths from the diagonal ands hanger to determine the possible stress distribution and then applies force equilibrium to compute the stress values. This is similar to the concept of strut-and-tie models which are often used in the design of reinforced concrete deep beams. The above comparisons verify that the loading path model for the Y-direction normal stress at the horizontal section provides a much better prediction than the conventional beam theory.

Table 7.23: Statistics to evaluate error and correlation of the computed stress to the FEA results

			Load 1	Load 2	Load 3	Load 4	
Type I Loading Profiles	Loading Path	R_{err}	9.23%	10.25%	12.08%	14.35%	
	Model	R	0.93	0.94	0.94	0.93	
	Beam Theory	R_{err}	-20%	-19.25%	-17.91%	-16.24%	
		R	0.80	0.80	0.80	0.81	
			Load 5	Load 6	Load 7	Load 8	Load 9
Type II Loading Profiles	Loading Path	R_{err}	44.76%	7.99%	23.44%	-19.81%	9.00%
	Model	R	0.92	0.94	0.92	0.92	0.94
	Beam Theory	R_{err}	-48.03%	-17.87%	-47.32%	-102.2%	-17.11%
		R	0.48	0.80	0.50	0.35	0.80
			Load 10	Load 11	Load 12	Load 13	
	Loading Path	R_{err}	17.41%	16.41%	14.46%	12.55%	
	Model	R	0.93	0.93	0.93	0.93	
	Beam Theory	R_{err}	-25.99%	-26.61%	-27.84%	-29.04%	
Type III Loading Profiles		R	0.77	0.77	0.77	0.77	
			Load 14	Load 15	Load 16		
	Loading Path	R_{err}	10.70%	9.45%	8.4%		
	Model	R	0.92	0.92	0.92		
	Beam Theory	R_{err}	-30.21%	-31.00%	-31.66%		
		R	0.77	0.77	0.77		

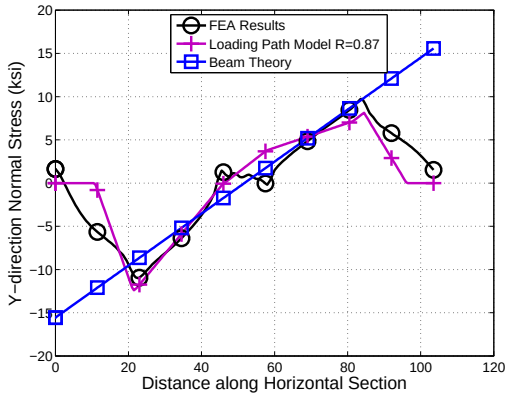

(a) Comparison of Y-direction normal stress distribution for Type I Loading Profiles Load 1

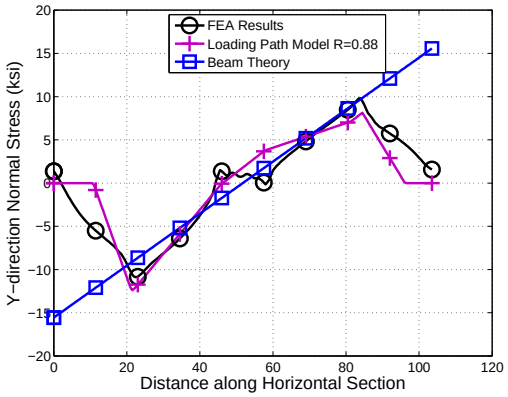

(b) Comparison of Y-direction normal stress distribution for Type I Loading Profiles Load 2

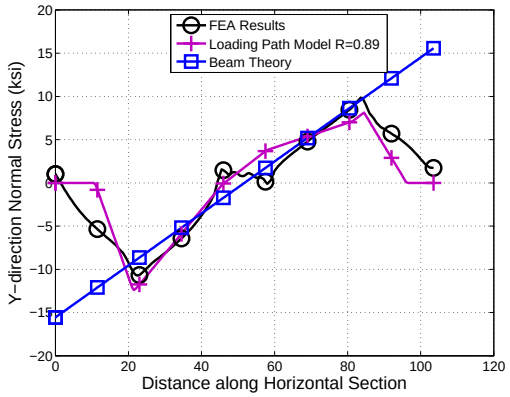

(c) Comparison of Y-direction normal stress distribution for Type I Loading Profiles Load 3

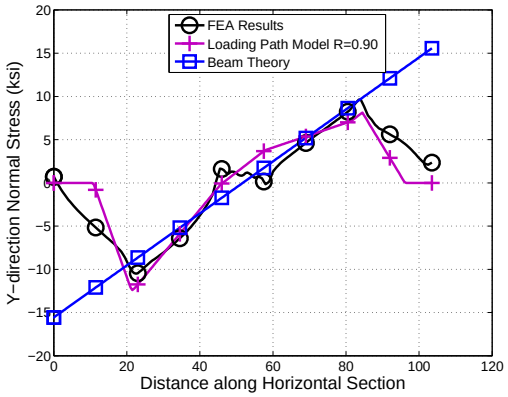

(d) Comparison of Y-direction normal stress distribution for Type I Loading Profiles Load 4

Figure 7.33: Y-direction normal stress distribution along the horizontal section from the load path model. beam theory, and FEA results for Type I Loading Profiles

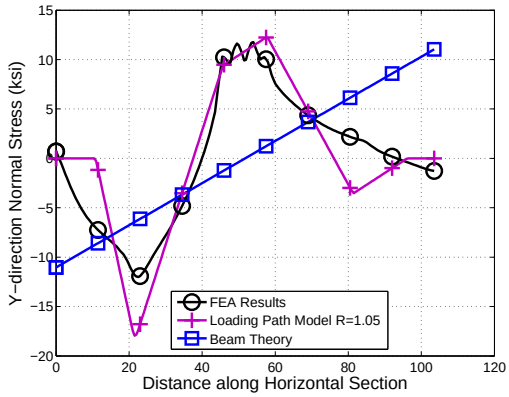

(a) Comparison of Y-direction normal stress distribution for Type II Loading Profiles Load 5

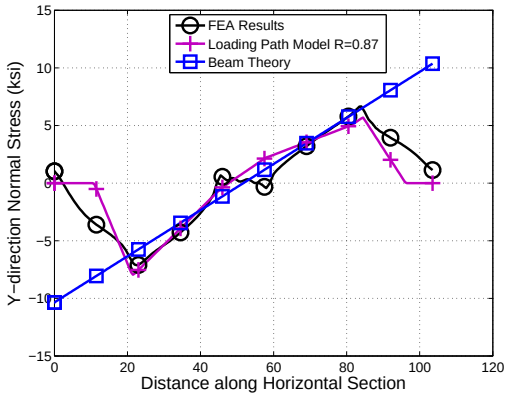

(b) Comparison of Y-direction normal stress distribution for Type II Loading Profiles Load 6

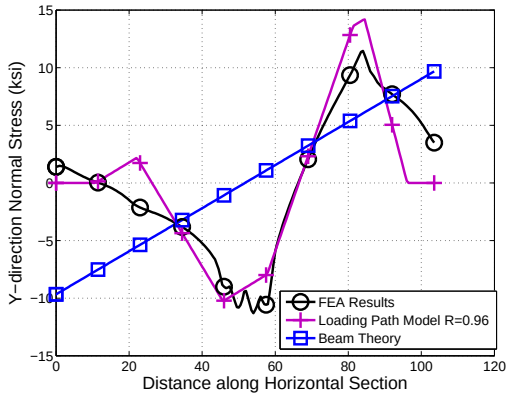

(c) Comparison of Y-direction normal stress distribution for Type II Loading Profiles Load 7

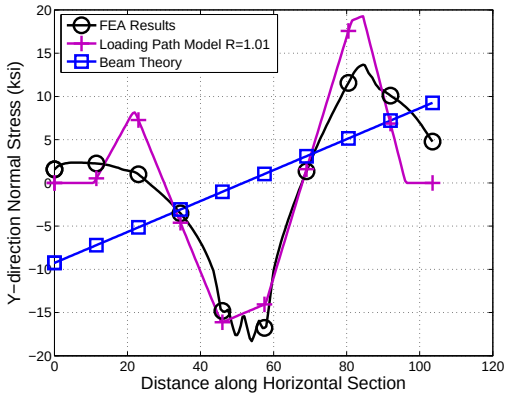

(d) Comparison of Y-direction normal stress distribution for Type II Loading Profiles Load 8

Figure 7.34: Y-direction normal stress distribution along the horizontal section from the load path model. beam theory, and FEA results for Type II Loading Profiles

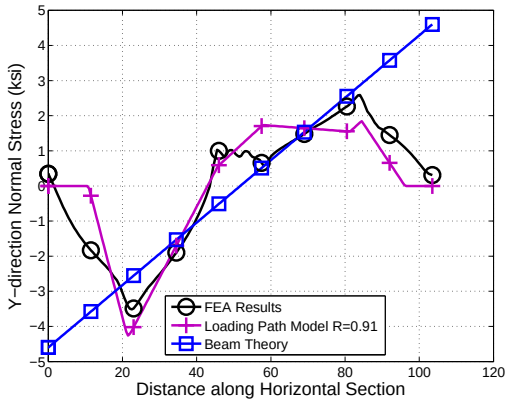

(a) Comparison of Y-direction normal stress distribution for Type III Loading Profiles Case 10

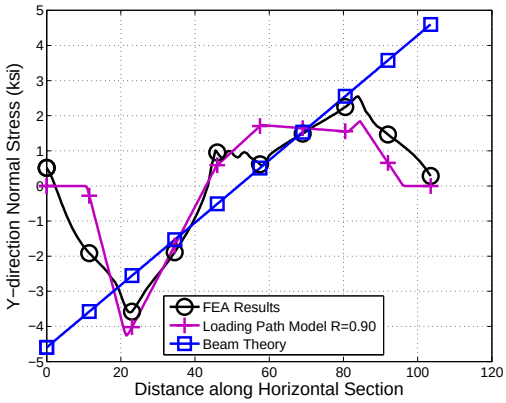

(b) Comparison of Y-direction normal stress distribution for Type III Loading Profiles Case 12

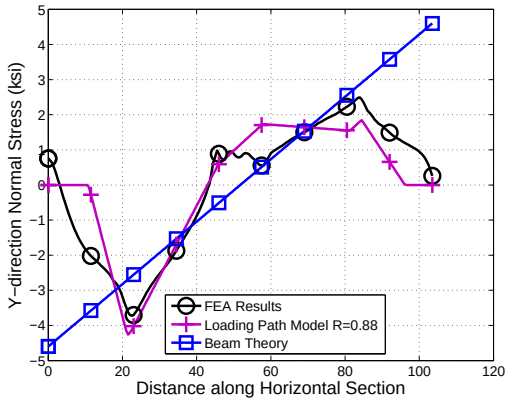

(c) Comparison of Y-direction normal stress distribution for Type III Loading Profiles Case 14

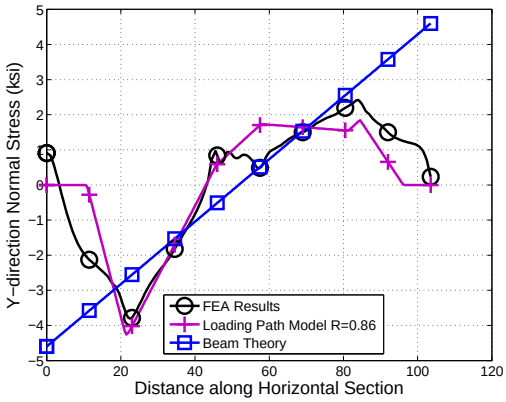

(d) Comparison of Y-direction normal stress distribution for Type III Loading Profiles Case 16

Figure 7.35: Y-direction normal stress distribution along the horizontal section from the load path model. beam theory, and FEA results for Type III Loading Profiles

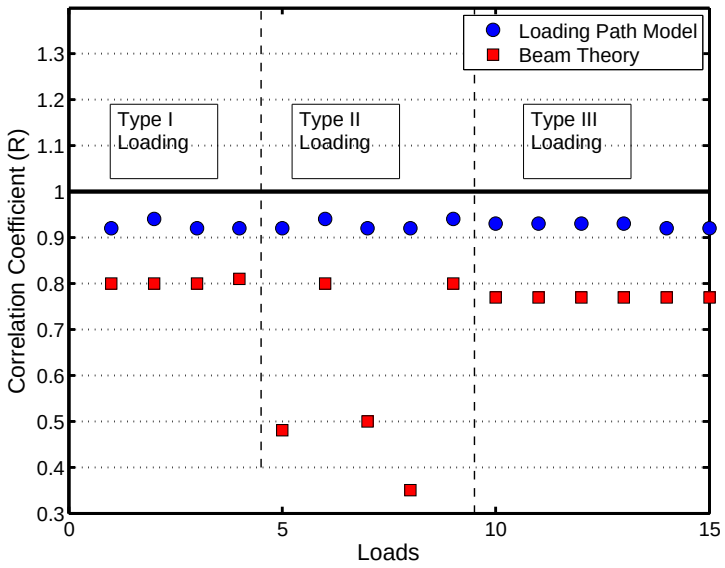

Figure 7.36: Statistics to evaluate the correlation of the computed Y-direction stress distribution on the horizontal section to the FEA results for Type I, II, and III Loading Profiles

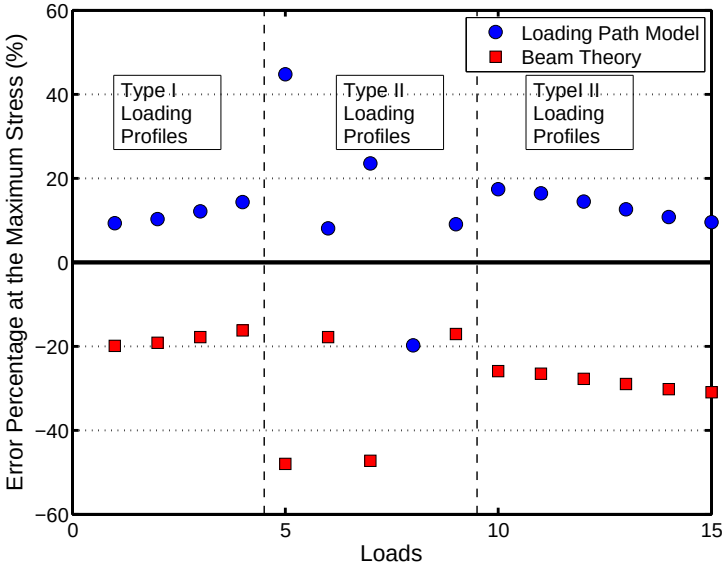

Figure 7.37: Statistics to evaluate the error percent of the computed Y-direction maximum stress on the horizontal section to the FEA results for Type I, II, III Loading Profiles

7.10 Equilibrium Consideration for the Approximate Stress Distributions at the Critical Section

7.10.1 Equilibrium at the Horizontal Section

The last step in examining the proposed approximate elastic stress distributions on the different critical sections is to examine if those distributions satisfy equilibrium with the external loads. Based on the lower bound theorem that if a stress distribution satisfies: 1) force equilibrium, 2) boundary conditions, and 3) it does not exceed the yield stress at any point, this stress distribution is regarded as the lower bound of plasticity, i.e., the upper bound of elasticity. The lower bound theorem is described and applied to analyze frame and plate limit state in Bruneau et al. [2011], Park and Gamble [1980], and Kaliszky [1989].

The stress distributions at the critical horizontal section includes the Y-direction normal stress and the XY shear stress as shown in Figure 7.38. The Equilibrium of horizontal forces are automatically satisfied because the stress distributions are derived from the individual external loads acting on the horizontal section. The question is if the proposed Y-direction normal stress distributions satisfy moment equilibrium since the vertical components of the two diagonal loads are not acting at the same point at the horizontal section. Figure 7.32 shows the assumed triangular Y-direction normal stress distributions from both diagonals would provide resultant forces that act through the centroids of the triangles, which is close to the locations where the diagonal load is assumed to act on the horizontal section. Therefore, even though moment equilibrium is not directly imposed to establish the proposed approximate stress distributions, the unbalanced moment is small. For example, in Type I Loading Profiles, the moment generated by the loading path mode is 10653 (kips-in) while the unbalanced moment generated from the moment equilibrium of vertical components of the diagonal forces on the horizontal section is 10240 (kips-in). The error percentage of the moment between two models is about 4%. If this 4% unbalanced moment acting on the horizontal section as acting on a beam section, the Y-direction nocmal stress for this unbalanced moment will have higher stress at the edges of the horizontal section and barely no influence on the stress in the middle area of the section. The impact of unbalanced

moement on the Y-direction normal stress at the horizontal section is negligible. This can also be verified in load cases with heavy load on one side of the diagonal and light load on the other diagonal. Load 5 and 7 in Type II Loading Profiles show the error percentage of the unbalanced moment for is 1.2% Load 5 and 6.5% for Load 7. The error of the unbalanced moment in both cases are negligible. The proposed stress distribution model could be modified to provide moment equilibrium by slightly adjusting the effective length to make the centroid of each triangular stress distribution from the diagonal load coincide with where the diagonal's centerline intersects the horizontal section. However, the difference in the overall distribution would be small and the moment varies if the horizontal section is moved vertically even as small amount. Considering the small magnitude of the unbalanced moment, it will be neglected.

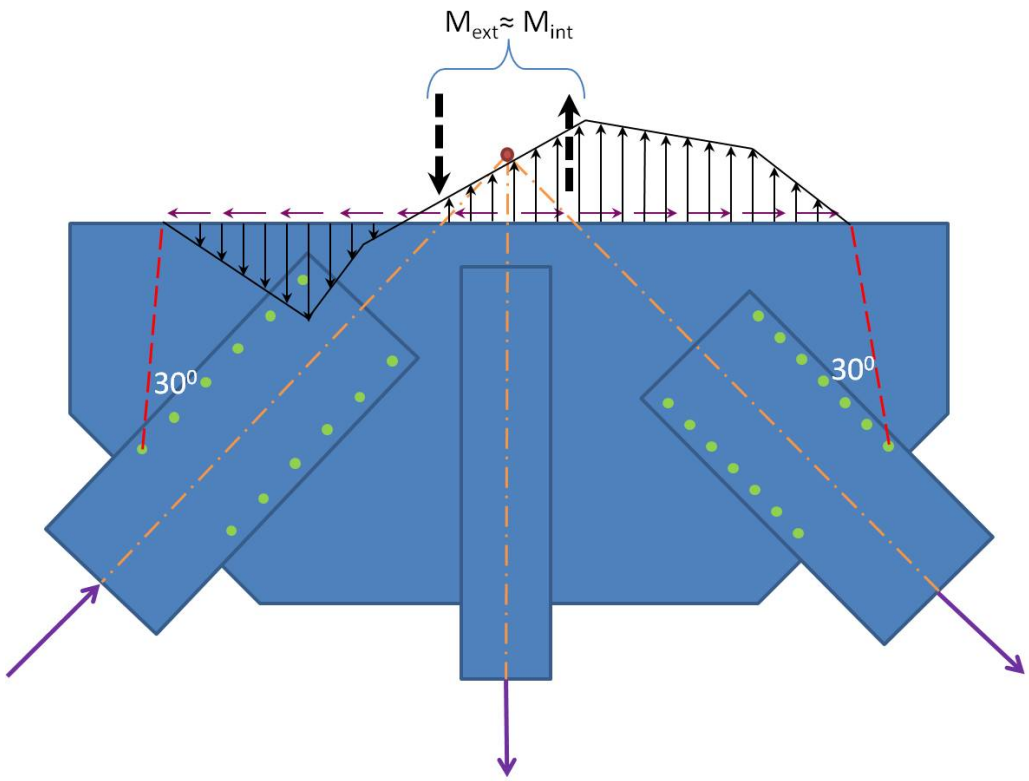

Figure 7.38: Equilibrium of the external forces and the resulting forces from proposed stress distributions on the horizontal section

7.10.2 Equilibrium at the Vertical Section

The stress distributions at the vertical critical sections are also examined for equilibrium requirement. For example, considering the vertical section passing the chord splice and along one side of the hanger as shown in Figure 7.39, there are two stress distributions presented on this vertical section, the X-direction normal stress distribution at the chord splice which is the superposition of the trapezoidal stress distribution from the chord load and the stresses from the moment due to the eccentricity between the chord centerline and the centroid of the trapezoidal stress distribution, and XY shear stress which assumed uniformly distributed on the vertical effective shear section. Any vertical section passing through a chord rather than at a splice is more complicated because it involves the consideration of how much chord load from fasteners has been passed to the gusset.

Therefore, first, we consider equilibrium at the vertical section passing through work point. Since the X-direction normal stresses at the chord splice are themselves derived from equilibrium about the chord centerline and the chord and diagonal forces both acting at work point, the summation of external moment in Figure 7.39 is equal to zero. Similarly, the summation of the vertical and horizontal forces is also equal to zero, i.e. the X-direction normal stress calculated using net force between the chord load and the horizontal component of the diagonal load, the effective shear stress calculated using the vertical component of the diagonal load. This equilibrium of the assumed stress distribution helps maintain it accuracy when chord splice is at work point or when the diagonal load is small and splice location is near the work point which the additional external moment at the vertical section is small. However, when the chord splice is further from the work point, i.e. within the interference zone, there is an additional external moment which is due to the eccentricity between the locations where the chord force and diagonal force act on the vertical section. This additional external moment is difficult to estimate because not all load of the diagonal may be developed, i.e. if the vertical section actually passes through the diagonal, and the effective area that the partial loads from the diagonal acting on the vertical section is not clear. The incurred additional moment on the vertical section might be small but it may still have some influence on the X-direction normal distribution at the chord splices.

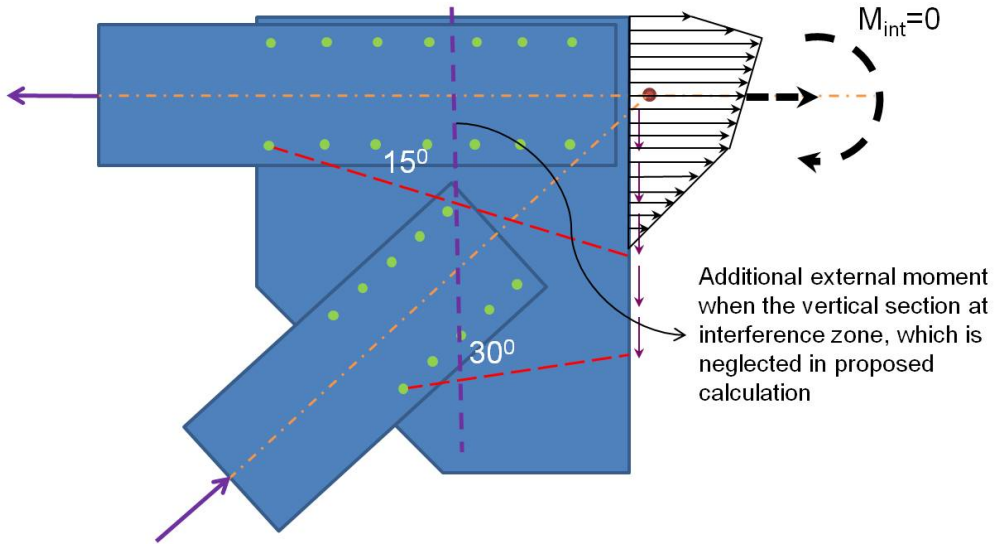

Figure 7.39: Equilibrium of the external forces and the resulting forces from proposed stress distributions on the vertical section

The impact of this moment can be seen in Figures 7.27(b), 7.27(c), 7.27(e) where the proposed stress distribution does not match the FEA results as well when the chord splice is away from work point within the interference zone and the diagonal load is large as shown in Load 5, Load 6, and Load 8. This unbalance moment may cause the approximate normal stress distribution over or under estimate of the stress distributions. The complexity of the X-normal stress at the vertical section is resulted from two different unbalanced moments acting on the vertical section, the primary unbalanced moment comes from the asymmetric geometry which is considered when the trapezoidal X-normal stress distribution at chord splice is developed, and the secondary unbalanced moment is generated due to the non-concurrent forces of the chord and diagonal forces on the vertical section which is generally considered small and can be neglected.

The influence of the secondary unbalanced moment is discussed in detail by observing Loads 5 and 6 in splice locations SP3 and SP4 as shown in 7.27(b) and 7.27(c). In these cases, the net force, which is a summation of the chord load and the horizontal component of the diagonal load, is in tension and the primary and secondary balanced moment both increase

tensile stress at the edge on the chord splice so that the neglect of secondary unbalanced moment generate under-estimates the results. On the contrast, in the splice location case SP8 for Loads 6, 7, and 8 as shown in 7.27(e), the net force is in tension, the primary unbalanced moment causes the edge of the gusset plate in tension, and the secondary unbalanced moment otherwise causes the edge of the gusset plate in compression, so that the neglect of the secondary unbalanced moment results in a over-estimated approximated stress distribution.

If considering a proper additional moment is added to the vertical section to satisfy moment equilibrium where the chord splice located, the estimation of the X-direction normal stress distribution can be improved. Figure 7.40 compare normal stress distributions for splice location SP7, SP8, and SP9 with the Load 6, Load 7 and Load 8 from Type II Loading Profiles with the results from an additional moment with an proper assigned magnitude added to the existing stress distribution. The additional moment direction shall correspond to the secondary unbalanced moment acting on the considered vertical section and the magnitude is arbitrary assigned to generate stress distributions with good match to the FEA results. Figure 7.40 shows the the stress distribution with a proper secondary unbalanced moment superimposed to the existing stress distribution can improve the approximation of the X-normal stress model. The method of calculating the secondary unbalanced moment is not proposed at this moment. The magnitude of the secondary unbalanced moment is difficult to estimate because 1:) partial load shall be considered shedding to the vertical section where the vertical section does not pass through the work point, and 2) the effective section resisting the secondary unbalanced moment might be different from the 15° dispersion angle effective section developed for the chord splice.

Overall, though the secondary moment generated by an eccentricity between the diagonal and chord loads at the vertical section when it is away from the work point may affect the accuracy of the proposed stress distribution model, the error of the estimated maximum stress at the chord splice is tolerable for an approximated model. Since the secondary moment at the vertical section is significant only when there is high diagonal load, this high diagonal load will also be observed generating high XY shear stresses at the horizontal or

vertical sections. The neglect of the secondary moment does not affect the procedure to find the maximum stress on the gusset plates. In the next sections, the calculation examples for several practical gusset plate joints will show the applicability of the proposed stress distributions on the critical sections.

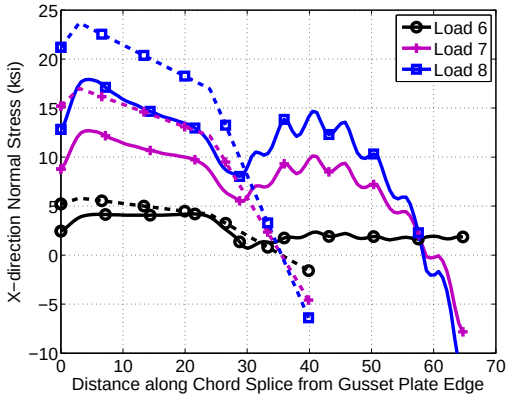

(a) Stress distribution comparison for splice location SP7

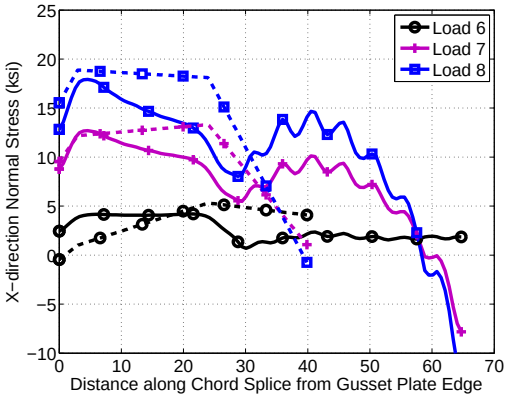

(b) Stress distribution with additional moment comparison for splice location SP7

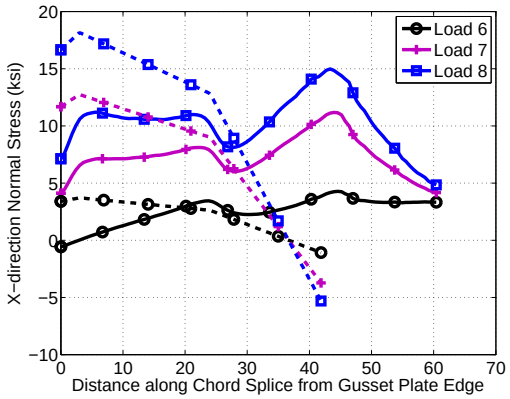

(c) Stress distribution comparison for splice location SP8

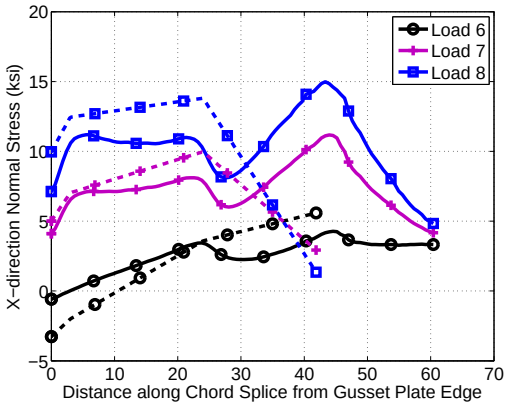

(d) Stress distribution with additional moment comparison for splice location SP8

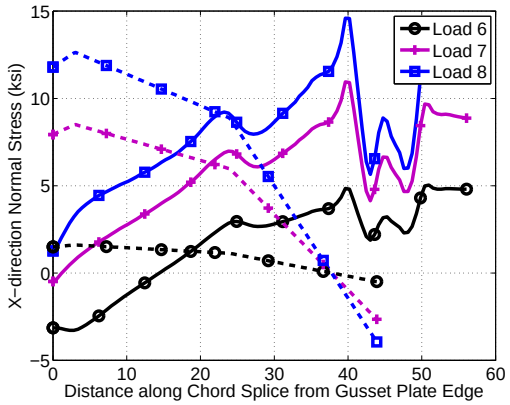

(e) Stress distribution comparison for splice location SP9

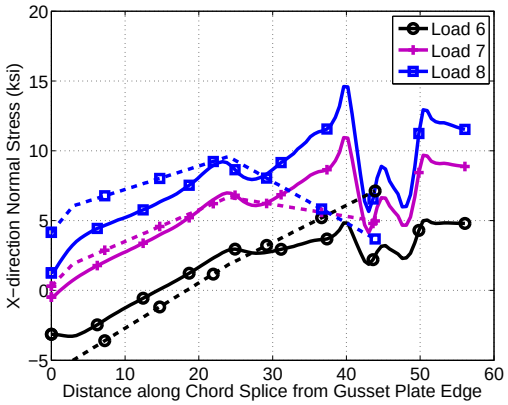

(f) Stress distribution with additional moment comparison for splice location SP9

Figure 7.40: Comparison of the X-direction approximated stress distribution with the FEA results and additional external moment added to the X-direction approximated stress distribution with the FEA results

7.11 Summary of Stress Components at Critical Sections and Superimposition of Stresses at Critical Locations

In this chapter, stress distributions for the normal and shear stress components at the critical sections were found through the observation of the FEA results and application of statistical tools. Then the approximate stress distributions corresponding to these stress distributions at the critical sections were proposed and verified with the FEA results using statistics. The proposed approximate stress distributions were found agree with the FEA results well and also satisfy equilibrium on the critical sections. These stress distributions at the critical sections and the methods to estimate the approximate stress distributions are summarized as follows:

- The XY shear stress distribution along the critical horizontal section was found to be uniformly distributed within an effective shear length. The effective shear length on one-side of the gusset plate is the horizontal critical section bound by a line with 30° dispersion angle from the first outer fastener of the same-side diagonal and a vertical line passing through the work point as shown in Figure 7.11. The XY shear stress distribution should be estimated independently for each side of the effective shear length using each diagonal load. The chord load was found to have slight effect to the XY shear stress distribution and is neglected in the estimation. The XY shear stress distribution can be discontinuous along the horizontal section when the approximate shear stresses are very different from each side so that the XY shear stress at the discontinuity can be considered using the average shear stress from both sides.

- The X-direction normal stress distribution at the chord splices was found to be combination of an axial trapezoidal normal stress distribution and a bending normal stress distribution due to the eccentricity of the chord geometry. The net force considered on this section is a sum of the chord load and a partial of the horizontal component from the diagonal load, which is proportional to the splice location. The horizontal component of the diagonal load has full influence when the splice is aligned with the work point and has no impact when the splice is located outside of interference zone.

This is shown in Figure 7.25. The effective length for the X-direction normal stress at the chord splice is a length along the chord splice and is bound by the gusset plate edge and a line with 15° dispersion angle from the first outer fastener of the chord as shown in Figure 6.9.

- The Y-direction normal stress distribution along the critical horizontal section is approximated by the loading path method. The diagonal loads are found generate triangular stress distributions where the vertex aligned with the diagonal corner projected to the critical horizontal section. The hanger load is found that generates a trapezoidal stress distribution, which is symmetric to the center line of the hanger, on the critical horizontal section. The effective length of the Y-direction normal stress on the critical horizontal section is the overlap lengths projected on the horizontal section by lines with 30° dispersion angle from the first outer fastener of the each side diagonal. Therefore, the Y-direction normal stress distribution on the critical horizontal section is the superimposition of each Y-direction normal stress distribution. The vertex of each Y-direction normal stress can be calculated by making the integral of the stress distribution along the effective section equal to the Y component of diagonal or hanger loads. This is shown in Figure 7.32

- The XY shear stress distribution along the critical vertical section on either side of the hanger is approximated by the uniformly distributed shear stress along the vertical effective shear length. The XY shear stress on the vertical section is generated by the vertical component of one-side diagonal load. The vertical effective shear length is bound by the line of 30° dispersion angle from the diagonal intersected with the vertical section and the line passing the work point horizontally as shown in Figure 7.19. The XY shear stress distribution shape is found affected by the load from another diagonal but the maximum shear stress on the section has very little variation in spite of the load from another diagonal.

7.12 Estimating Maximum Stress at Key Gusset Plate Locations

The approximate stress distributions along critical sections developed in the previous section make the evaluation of the total elastic stress states at certain points on gusset plates possible. If the normal and shear stress components at certain points are known, the equivalent Von Mises stress can be calculated. Peak values of stress components are often observed on the horizontal and vertical sections as followings: 1) the X-direction normal stress at the chord splice has a peak close to the gusset plate edge, 2) X-direction normal stress at the chord splice has a peak value close to inner edge of chord members, 3) the XY shear stress along the horizontal section can have a plateau over a long length, 4) the XY shear stress along the vertical sections at either side of the hanger can have a plateau over a long length, and 5) the Y-direction normal stress can have peaks at projected diagonal and hanger corners on the horizontal section. Therefore, for a Warren-type gusset plate joint, there might be eight locations where the potential peak stresses may occur along the critical sections and for Pratt-type joints there may be five such locations. The maximum equivalent Von Mises stress can be found by examining these potential high stress locations.

Von Mises stress is used as equivalent stress in this section. Eq. 7.5 shows the calculation of equivalent Von Mises stress for plane stress. The σ_x, σ_y, σ_{xy} in the equation are the approximate stress using the developed methods in previous sections to estimate the component stress distribution at those points. The locations of each point is illustrated in Figure 7.41 and the detail of these points from 1 to 8 are described as follows:

- Point 1 is located at the chord splice close to the edge of gusset plates and only X-direction normal stress is considered. The approximate stress distribution along the chord splice is used to estimate the X-direction stress component at this point. The peak stress value at the first kink from the gusset plate edge along the chord stress distribution is considered for this point.

- Point 2 is located at the chord splice near or cross the critical horizontal section so that several stress components are considered. The X-direction normal stress from chord loads, the Y-direction normal stress from the diagonal and hanger loads, and

the XY shear stress from the diagonal loads are the stress components to be combined at this point. The peak of the approximate X-direction normal stress distribution at the second kink from the gusset plate edge on the chord splice is considered for X-direction normal stress at this point. The Y-direction normal stress component at this point is the superimposed Y-direction normal stress calculated from the hanger and the diagonal loads at this point. The XY shear stress component at this point is calculated using effective shear length method for uniform XY shear stress on each side of the horizontal section. When Point 2 is aligned vertically with the work point, the XY shear stress distribution along the horizontal section may be discontinuous because of different loads at each diagonal. The higher XY shear stress or the average shear stress from both sides are considered. The former one may generate overly-conservative estimate while the latter shows better estimate at this location. The average shear stress is suggested for the estimate XY shear stress at point 2 for this case. In the calculation examples in the next section, the stress value using the higher XY shear stress and average XY shear stress for stress combination are marked for comparison.

- Points 3 and 4 are located on the horizontal section where the diagonal corner projected on the horizontal section so that the Y-direction normal stress and the XY shear stress are considered for this points. The XY shear stress is calculated from one side of diagonal load using the effective shear length while the Y-direction normal stress is found from the superimposed Y-normal stress distribution generated by the diagonal and hanger loads at this piint.

- Points 5 and 6 are located at the intersection of the vertical section beside the hanger and the horizontal section. Therefore, the higher XY shear stress component calculated between using the horizontal effective shear length and vertical effective shear length of one-side of the gusset is considered. The Y-direction normal stress at this point is generated from the superimposed approximate Y-normal stress distribution from the diagonal and hanger loads at these points. If the chord splice is aligned with this section, the X-direction normal stress component need to be considered such as

Point 2.

- Points 7 and 8 are principal stress at the end of the diagonal calculated using Whitmore method. The equivalent Von Mises stress is equal to the Whitmore's stress at these points.

$$\sigma_v = \sqrt{\frac{(\sigma_x - \sigma_y)^2 + \sigma_x^2 + \sigma_y^2}{2} + 3\sigma_{xy}^2} \tag{7.5}$$

By calculating equivalent Von Mises stress for all these points, the maximum equivalent stress and its location is expected to be acquired from those results. The next section describes the implementation of this method on Joints U10, L2, U3, and L1 and compares the results with the FEA results.

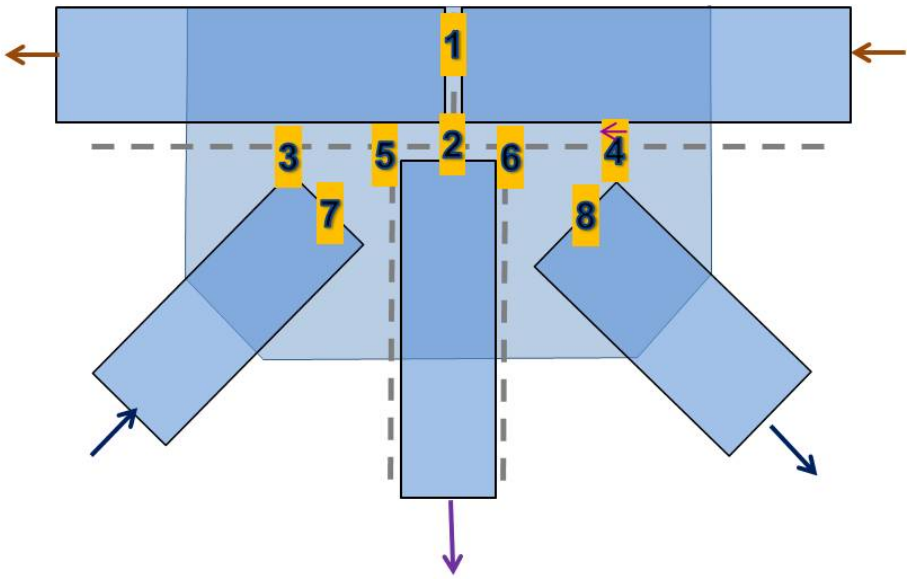

Figure 7.41: Eight locations and stress states have possible maximum equivalent stresses including Whitmore stress at diagonal ends

7.13 Application to Example Bridge Joints

7.13.1 Joint U10

Joint U10 described in detail in Chapter 4 is a Warren type connection with chamfered diagonal members and a chord splice is located at the work point. The chord splice consists of 3/8" thick flange and 1/2" thick web splice plates. Because of the chamfer on the diagonals, the interference zone is quite a small area and the interaction of the stress components is expected to be significant in the connection's gusset plates. The geometry of the joint and the effective length for the XY shear stress on the critical sections are shown in Figure 7.42(a). The loading profile and the FEA results is shown with Von Mises stress contours in Figure 7.42(b). The detailed hand-calculation procedure for each stress distribution is not shown here. In lieu of showing the calculation procedure, Matlab was used to generate each stress plot of distribution on the critical sections and these are shown with the FEA results in Figure 7.43. The locations and the magnitudes of the peak stress for the individual stress distributions can be read from the plots and calculate Von Mises stress for potential high stress points. The stress components for the potential high stress points in Figure 7.43 are tabulated with the calculated Von Mises stress and FEA results in Table 7.13.1.

Figure 7.43 shows the proposed methods for estimating stress distributions on critical sections are consistent with the FEA results for Joint U10. Von Mises stress calculated in Table 7.13.1 is shown have the maximum value at point 5 which agrees with the FEA results shown in Figure 7.42(b). In addition to adequately estimating the maximum stress in the gusset plates, the Von Mises stress at other potential high stress locations is also shown to be adequately estimated by the proposed distributions when compared to the FEA results. Overall, the example implementation Joint U10 shows that the computed stresses based on the proposed methods have good agreement with the FEA results for both the individual stress distributions and also for the combination of the stresses using the Von Mises equation.

Table 7.24: Peak stress at critical points in Figure 7.42(b) for Joint U10

Locations	σ_X	σ_Y	τ_{XY}	Von Mises	FE Analysis
1	8.3	0.0	0.00	8.3	10-15
2	6.9	3.9	-23.0	40.3	40-45
3	0.0	-19.7	-23.0	44.4	40-45
4	0.0	14.1	-19.8	37.1	35-40
5	0.0	-2.0	-26.9	46.6	45-50
6	0.0	9.7	-20.3	36.5	35-40
Whitmore 7	N.A.	N.A.	N.A.	-26.1	35-40
Whitmore 8	N.A.	N.A.	N.A.	20.7	35-40
	Splice	Left Diagonal	Hanger	Right Diagonal	Shear Stress(Ω = 1.0)
FHWA Guide[1]	14.5	-26.1	5.9	20.7	18.2
TEP [2]	25.1	-45.2	10.2	35.9	N.A.

[1] FHWA Guide considering Whitmore stress at the end of member

[2] Triage Evaluation Procedure (TEP) using Whitmore stress times square root 3.0

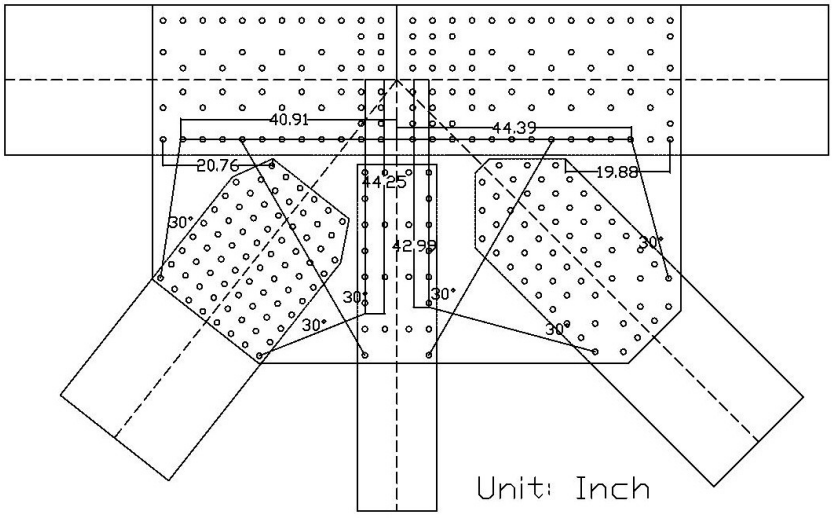

(a) Illustration of effective lengths for proposed stress distributions on critical sections

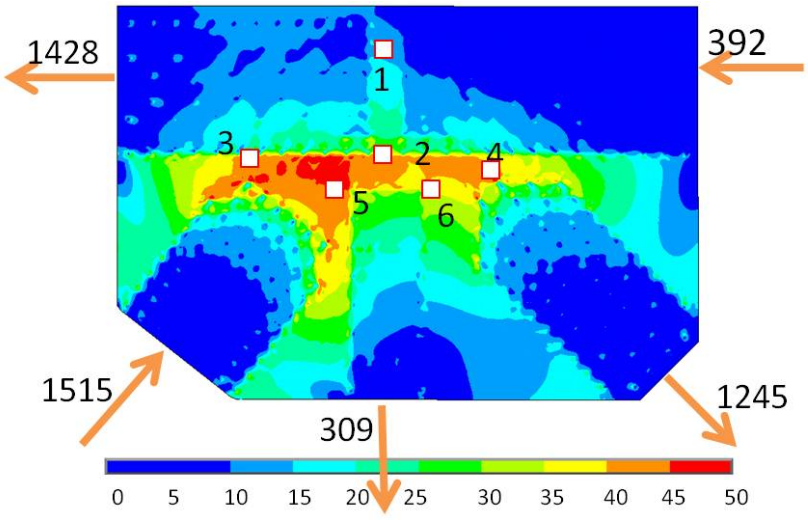

(b) Von Mises stress contours for Joint U10 and identification of possible high stress locations

Figure 7.42: Schematic of effective lengths for stress component on the critical section and the FEA results for the Von Mises stress contours for Joint U10

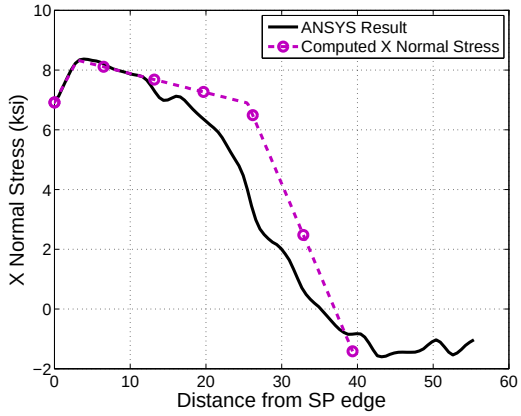

(a) X-direction normal stress at the chord splice

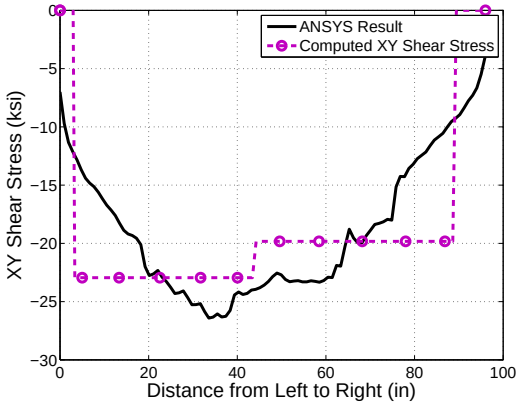

(b) XY shear stress at the horizontal section

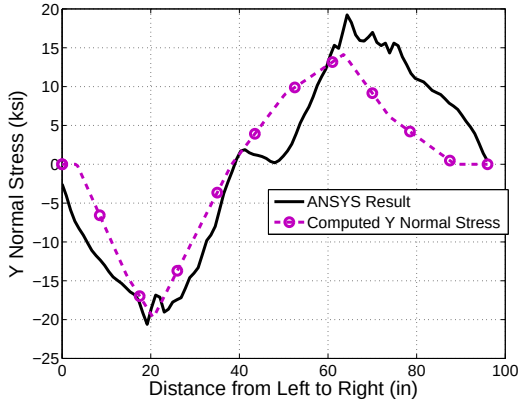

(c) Y normal stress at the horizontal section

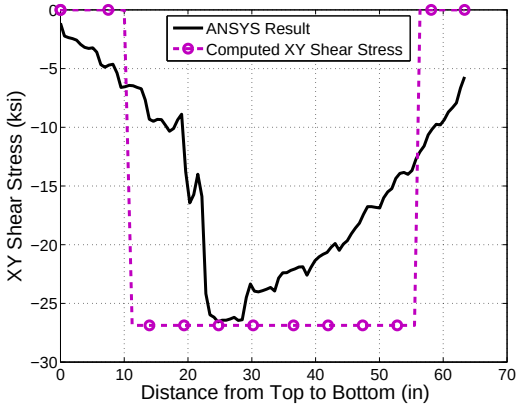

(d) XY shear stress at the left vertical section

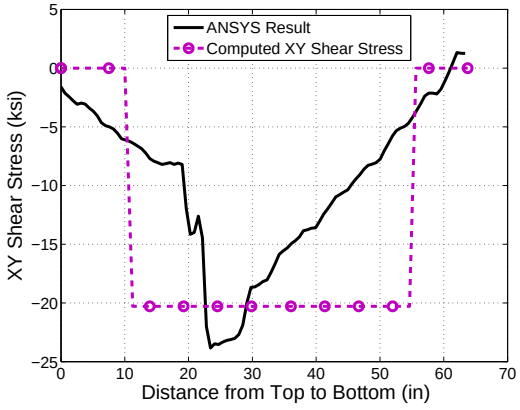

(e) XY shear stress at the right vertical section

Figure 7.43: Individual stress distributions on critical sections and comparison with the FEA results for Joint U10

7.13.2 Joint L2

Joint L2, described in detail in Chapter 4, is a Warren type gusset plate with non-chamfered diagonal members and the chord splice is located away from the work point and within the interference zone. The chord splice consists of only 3/8" thick flange splice plates and the gusset plates. Because of the non-chamfered diagonal members, the interference zone is relative spacious in Joint L2 as noted in Chapter 4. Joint L2 is a joint where it was observed that the stress at the chord splice might cause some larger stresses in the interference zone. The geometry and the effective lengths for computing the XY shear stress on the critical sections are shown in Figure 7.44(a). The loading profile and the FEA results is shown with Von Mises stress contours are shown in Figure 7.44(b). Each stress distribution on each critical sections is plotted along with the FEA results in Figure 7.45. The locations and the magnitudes of the peak stress for individual stress distribution can be read from each plot and used to calculate Von Mises stress at potential high stress points. The stress components at potential high stress points in Figure 7.44 are tabulated along with the calculated Von Mises stress at each location and FEA results in Table 7.13.2.

The estimated Von Mises stress is found to have a maximum value at Point 2 of Figure 7.44 and the value is very close to the FEA results. At other locations of high stress, the estimated Von Mises stresses match with the FEA results except at Points 3 and 4. A further look shows that computed Von Mises stress at Point 3 is over estimated while it is under estimated at Point 4. The over-estimation at Point 3 is because of the relatively large interference zone due to the non-chamfered diagonals which results in an over estimation of the Y-direction normal stress distributions in Figure 7.45(c). The under-estimated Von Mises stress at Point 4 is due to an under-estimation of the XY shear stress on the left of the hanger as shown in Figure 7.45(b). The under-estimattion of the XY shear stress on the left chord of horizontal section is caused by the assumption that the effect from chord loads on the XY shear stress can be neglected. Recall that the chord load only slightly influence the XY shear stress at the horizontal section. The left chord load of Joint L2 is found to have a load that is over seven times the horizontal component of the diagonal load resulting in a larger influence of the chord load on the XY shear stress and a under-estimation of the XY

shear stress from the approximate method. Although neglecting the shear stress from chord loads causes an under-estimation at of the Von Mises stress at Point 4, it does not affect the estimate of the maximum Von Mises stress on the gusset plates because the large chord load will simultaneously result in high stress at the chord splice, which is well estimated by the proposed trapezoidal stress distribution at the chord splice. The computed stress distribution at the chord splice is shown to be consistent with the FEA results even though the splice location is away from the work point and within interference zone for Joint L2. Overall, approximation of the proposed method for Joint L2 shows that the estimated Von Mises stress has good agreement with the FEA results in the estimate of the elastic stresses on gusset plates.

Table 7.25: Peak stress at critical points in Figure 7.44(b) for Joint L2

Locations	σ_X	σ_Y	τ_{XY}	Von Mises	FE Analysis
1	27.2	0.0	0.0	27.2	25-30
2	24.7	5.5	10.8	29.3	30-35
3	0.0	9.4	10.8	20.9	10-15
4	0.0	-5.3	5.9	11.5	15-20
5	0.0	-4.2	6.3	11.7	10-15
6	0.0	1.0	10.8	18.8	20-25
Whitmore 7	N.A.	N.A.	N.A.	8.6	5-10
Whitmore 8	N.A.	N.A.	N.A.	14.1	20-25
	Splice	Left Diagonal	Hanger	Right Diagonal	Shear Stress(Ω = 1.0)
FHWA Guide[1]	17.01	-8.6	3.4	14.0	6.4
TEP [2]	29.5	-14.9	5.9	24.2	N.A.

[1] FHWA Guide considering Whitmore stress at the end of member

[2] Triage Evaluation Procedure (TEP) useing Whitmore stress times square root 3.0

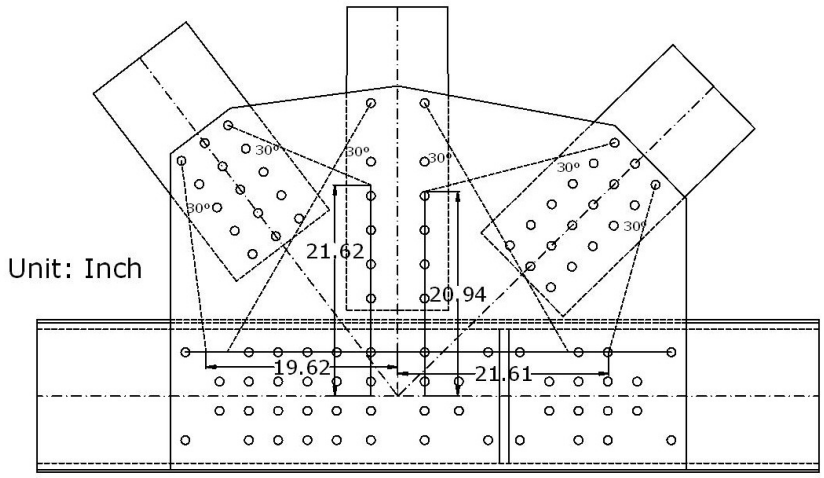

(a) Illustration of effective lengths for proposed stress distributions on critical sections

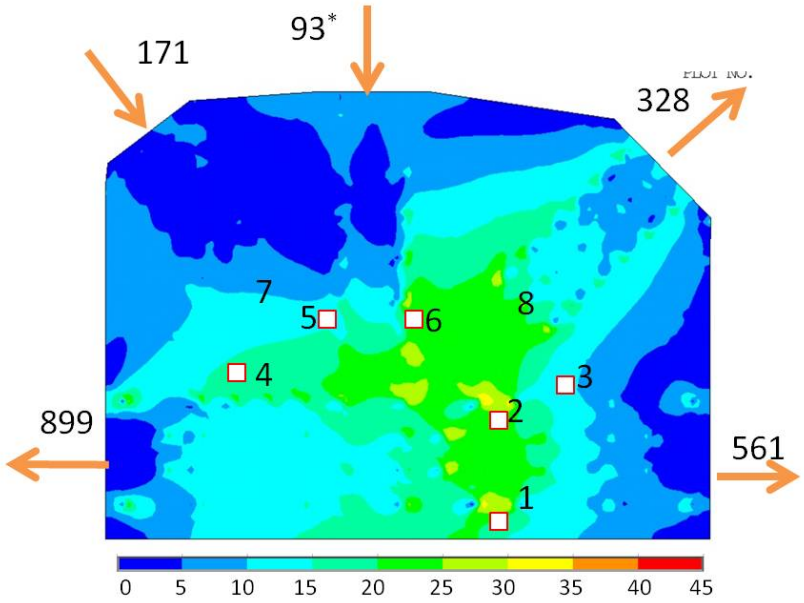

(b) Von Mises stress contours for Joint L2 and possible high stress locations

Figure 7.44: Schematic of effective lengths for stress component on the critical section and the FEA results for the Von Mises stress contours for Joint L2

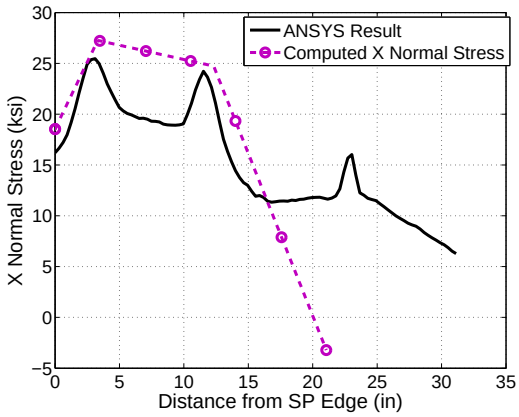

(a) X-direction normal stress at the chord splice

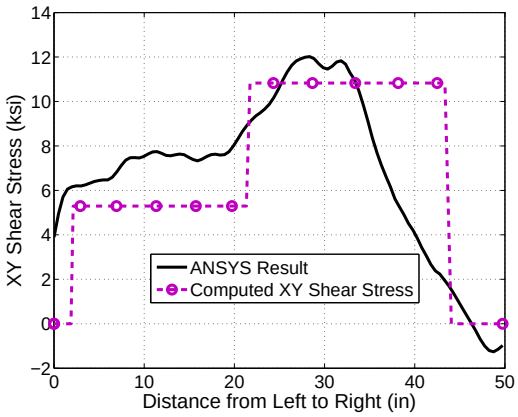

(b) XY shear stress at the horizontal section

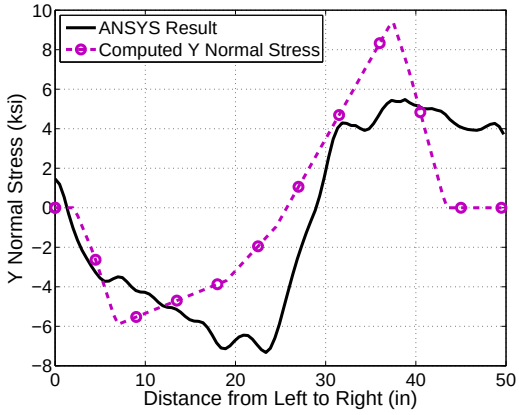

(c) Y-direction normal stress at the horizontal section

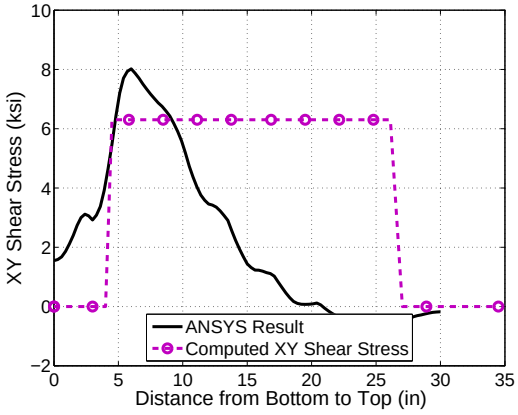

(d) XY shear stress at the left vertical section

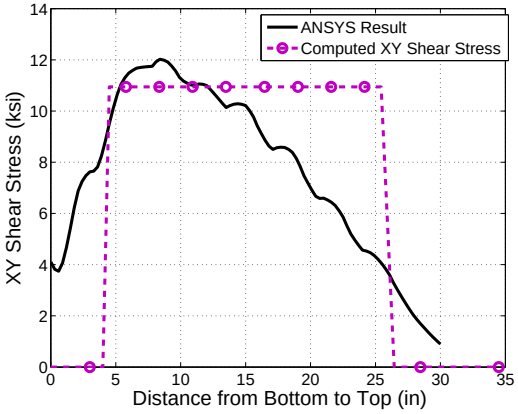

(e) XY shear stress at the right vertical section

Figure 7.45: Individual stress distributions on critical sections and comparison with the FEA results for Joint L2

7.13.3 Joint L1

Joint L1, described in detail in Chapter 4, is a Warren type gusset plate with one chamfered diagonal member on the left, a non-chamfered diagonal member on the right and the chord splice located at the work point. The chord splice consists of only 3/8" thick flange splice plates and the gusset plates. The geometry and the effective lengths for the XY shear stress distributions on the critical sections are shown in Figure 7.46(a). The loading profile and the FEA results are shown with Von Mises stress contours in Figure 7.46(b). Each stress distribution on the critical section is plotted with the FEA results individually in Figure 7.47. The stress components for the potential high stress points in Figure 7.46 are tabulated along with the calculated Von Mises stresses and FEA results in Table 7.13.3 .

The estimated Von Mises stress at Points 2, 3 and 5 appear to be the highest which is consistent with the high stress area identified in the FEA results in Figure 7.46(b). Point 2 has the maximum stress computed from the approximate method while the maximum Von Mises stress from the FEA results is near Point 5. The over-estimation of the Von Mises stress at Point 2 is due to the discontinuous approximate XY shear stress at the work point as shown in Figure 9.2(a). Since the splice is located at the work point in this case, Point 2 is at the discontinuity in the approximate shear stress distribution on the horizontal section. In these cases it is logical to use the average of the XY shear stress from the left and right sides to estimate the Von Mises stress at Point 2. Doing so results in an estimate of 29.0 ksi for the Von Mises stress which more closely matched the FEA results. In addition, the XY shear stress on the right side of the horizontal section is lower than the FEA results as shown Figure 9.2(a) because the chord load on right is over four times the horizontal component of the load at the right diagonal. It is worth noting that the zero-load in the left chord does not influence the adequacy of the proposed stress distributions and that the Whitmore stress at the end of the left diagonal seems to be much lower than the stress there from FEA results.

Table 7.26: Peak stress at critical points in Figure 7.46(b) for Joint L1

Locations	σ_X	σ_Y	τ_{XY}	Von Mises	FE Analysis
1	16.7	0.0	0.0	16.7	15-18
2	15.4	-7.7	-18.2	37.5 (29.0[1])	27-30
3	0.0	14.2	-18.2	34.6	27-30
4	0.0	-1.4	-5.7	10.0	15-18
5	0.0	-6.6	-18.3	32.4	30-33
6	0.0	-8.8	-5.7	12.0	15-18
Whitmore 7	N.A.	N.A.	N.A.	21.6	30-33
Whitmore 8	N.A.	N.A.	N.A.	8.1	9-12
	Splice	Left Diagonal	Hanger	Right Diagonal	Shear Stress(Ω = 1.0)
FHWA Guide[1]	10.1	21.6	-11.9	-8.1	9.9
TEP [2]	17.5	37.4	20.6	14.0	N.A.

[1] Using the average shear stress calculated from both diagonal loads instead of using the larger one

[2] FHWA Guide considering Whitmore stress at the end of member

[3] Triage Evaluation Procedure (TEP) using Whitmore stress times square root 3.0

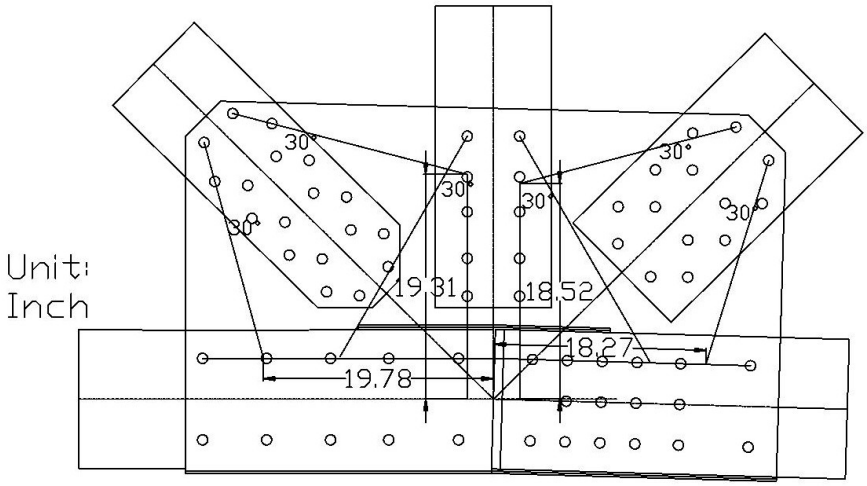

(a) Illustration of effective sections for proposed stress distributions on critical sections

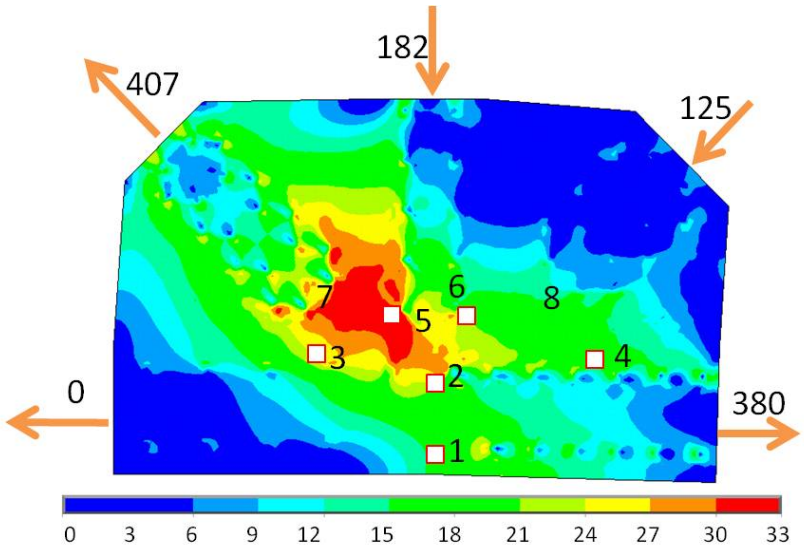

(b) Von Mises stress contour of joint L1 and possible high stress locations

Figure 7.46: Schematic of effective lengths for stress component on the critical section and the FEA results for the Von Mises stress contours for Joint L1

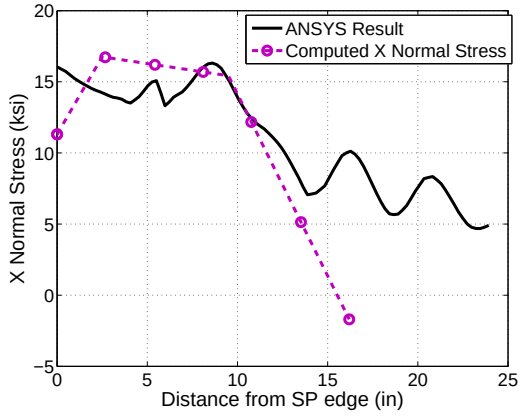

(a) X-direction normal stress at the chord splice

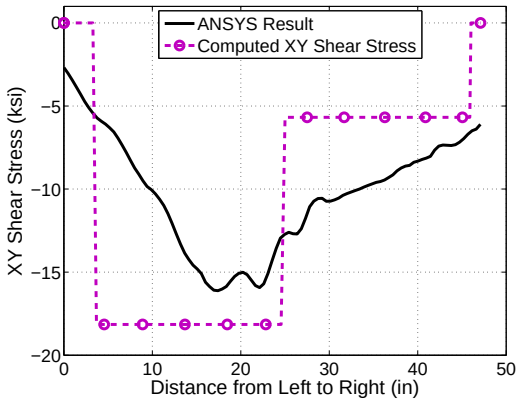

(b) XY shear stress at the horizontal section

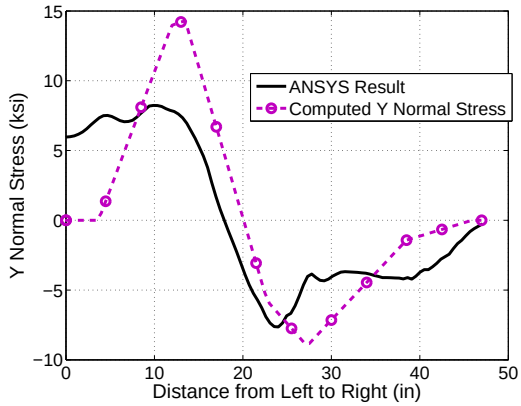

(c) Y-direction normal stress at the horizontal section

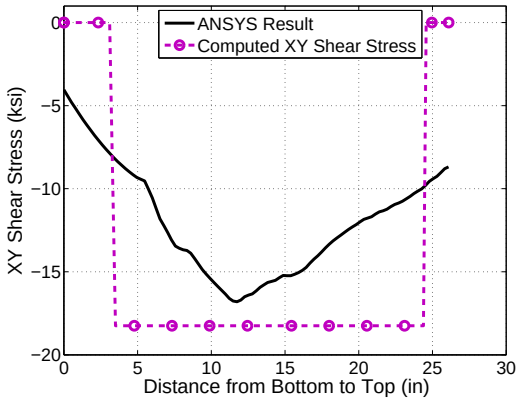

(d) XY shear stress at the left vertical section

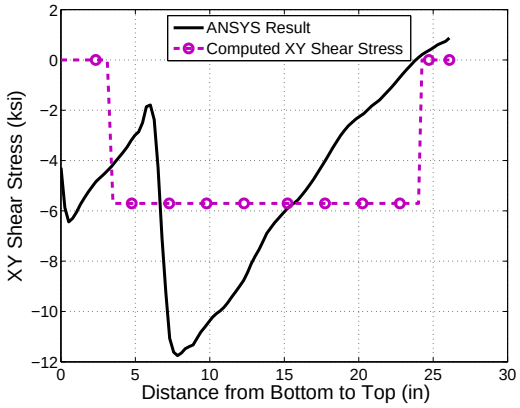

(e) XY shear stress at the right vertical section

Figure 7.47: Individual stress distributions on critical sections and comparison with the FEA results for Joint L1

7.13.4 Joint U3

Joint U3 is a Pratt type gusset plate with one non-chamfered diagonal member and a chord splice located outside the interference zone. The chord splice consists of only 3/8" thick flange splice bars and double 5/16" web splice plates. The geometry and the effective lengths for estimating the XY shear stress distributions on the critical sections are shown in Figure 7.48(a). The loading profile and the FEA results are shown with Von Mises stress contours in Figure 7.48(b). Each stress distribution on each critical sections is plotted with the FEA results individually in Figure 7.49. The stress components for the potential high stress locations in Figure 7.48 are tabulated along with the calculated Von Mises stress and FEA results in Table 7.13.4.

All estimated Von Mises stresses at the potential high stress locations show good agreement with the FEA results and the maximum Von Mises stress is observed at the chord splice. The computed stress distribution at the chord splice agrees well with the FEA results because the stress at the chord splice is solely determined by the chord load and is not affected by the diagonal load as shown in Figure 7.49(a). Joint U3 is an example where the triage evaluation procedure which slightly under-estimates the maximum stress at this joint and can be improved by using the approximate stress distribution and combination rules developed in this chapter.

Table 7.27: Peak stress at critical points in Figure 7.46(b) for Joint U3

Locations	σ_X	σ_Y	τ_{XY}	Von Mises	FE Analysis
1	20.9	0.0	0.0	20.9	18-21
2	17.7	0.0	0.0	17.7	15-18
3	0.0	6.4	5.5	11.4	9-12
4	0.0	-1.2	6.0	10.5	12-15
Whitmore 5	N.A.	N.A.	N.A.	6.6	9-12
	Splice		Left Diagonal	Shear Stress($\Omega = 1.0$)	
FHWA Guide[1]	12.14		6.6	N.A	
TEP [2]	21 [3]	11.4			

[1] FHWA Guide considering Whitmore stress at the end of member

[2] Triage Evaluation Procedure (TEP) using Whitmore stress times square root 3.0

[3] Outside of the interference zone and the result shall be neglected

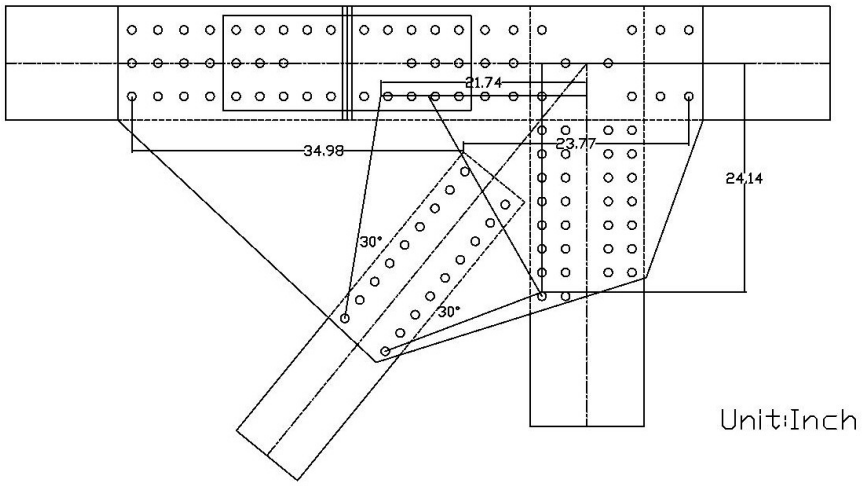

(a) Illustration of effective sections for proposed stress distributions on critical sections

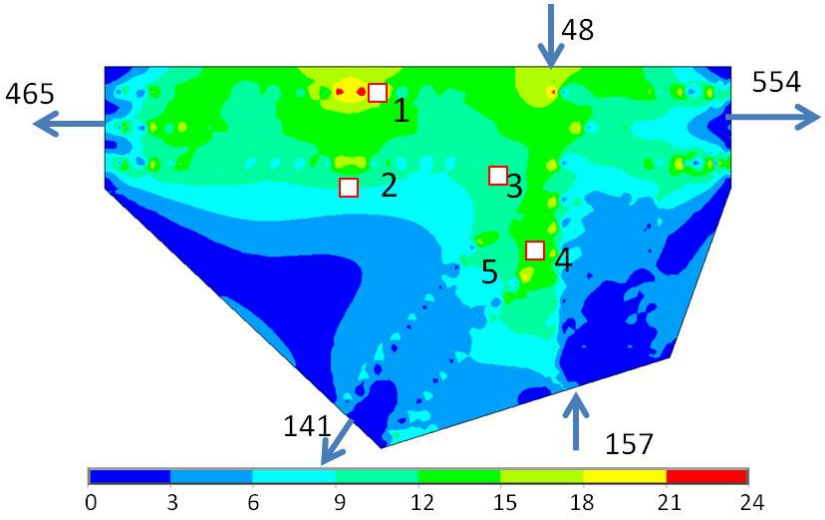

(b) Von Mises stress contour of joint U3 and possible high stress locations

Figure 7.48: Schematic of effective lengths for stress component on the critical section and the FEA results for the Von Mises stress contours for Joint U3

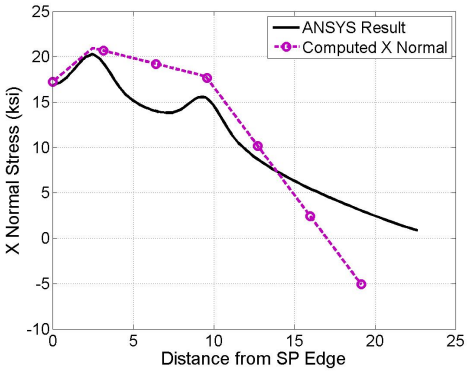

(a) X-direction normal stress at the chord splice

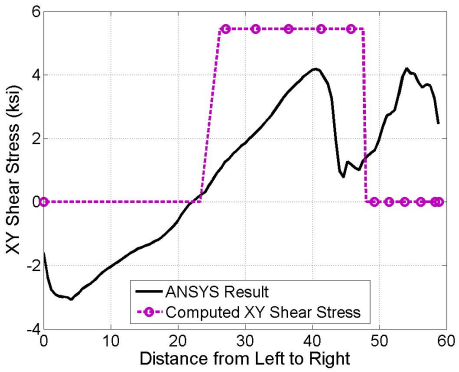

(b) XY shear stress at the horizontal section

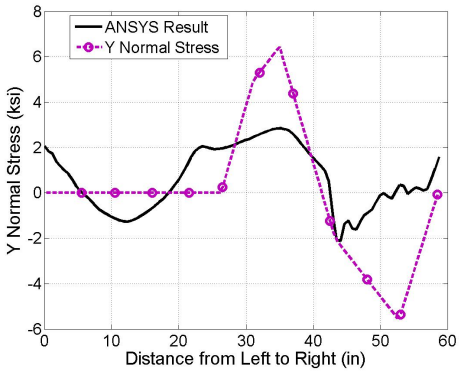

(c) Y-direction normal stress at the horizontal section

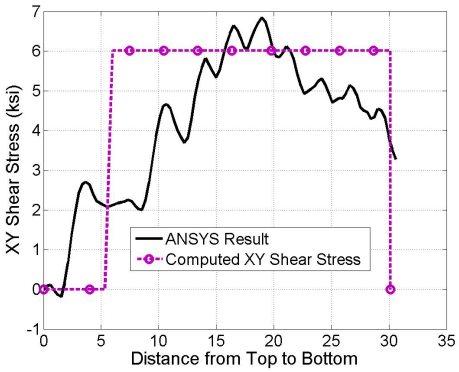

(d) XY shear stress at the left vertical section

Figure 7.49: Individual stress distributions on critical sections and comparison with the FEA results for Joint U3

Chapter 8

RIVETED CONNECTIONS

8.1 Introduction

Olson [2010] found that rivet shear resistance often governs joint capacity when determining the load rating for existing steel truss bridges. The shear resistance of a group of rivets is governed by two considerations: 1) the single rivet shear strength and 2) any group effects that impact the distribution of forces between rivets. Olson [2010] studied historical rivet test data and showed that the suggested rivet shear strengths used by AASHTO [2010] was overly conservative. From the study, Olson [2010] tabulated the results of historical rivet shear strength tests in Chapter 2 Table 2.1. It was found that the nominal shear strength given by AASHTO [2010] was close to the effective rivet yield (ERY) strength in the literature and Olson [2010] issued a recommendation to increase the suggested single rivet shear strength. Recommended rivet strengths were subsequently increased in a interim revision to the AASHTO [2011]. In addition, the total shear strengths of rivets in a joint, requires additional shear strength reduction from the sum of individual shear strength to account for a group effect that is a function of connection length. The combination of lower rivet strengths and the connection length factor resulted in connection shear resistance controlling the strength of several gusset plate connections investigated by Olson [2010]. However, experiments by Jost [2012] showed that long connections do not display the unbuttoning failure mode and do not have capacity less than the sum of the individual rivet strength if they are loaded more uniformly rather than only at their end. This indicates the mechanism of the force transfer and the interaction between fasteners and connected elements require further study. Here an analytical study of fasteners interacting with connected elements at different load levels is performed to further investigate the long connection effect in riveted joints.

This chapter described the experiments conducted on older rivets from previously in service truss bridges to investigate shear strength deterioration relative to rivet strengths reported in the literature. Furthermore, a rivet spring model was developed and verified using riveted connection tests conducted by Jost [2012]. This model was used to simulate long riveted connection tests conducted by Dlugosz [1962] and study the variation in force for each rivet along the connection length at different load steps. The load steps are small to enable observations of the correlation of the rivet force and connection element strain variation over the entire response. In addition, a geometric parameter, A_n/A_s, which was found to affect long connection behavior by Dlugosz [1962] and Fisher et al. [1963] was also studied. Finally, a modified design equation for rivet shear strength was proposed to eliminate what is found to be an overly conservative approach to accounting for connection length in AASHTO [2010]. Modification of the strength equations may help to avoid unnecessary replacement or reinforcement of rivets in older connections.

8.2 Shear Strength of Vintage Single Rivets

Rivet tensile and shear strengths were important issues when rivets were initially used in industry a century ago. Many studies examined factors that affect rivet tensile and shear strengths including rivet materials, rivet grip length, heat temperature, riveting tool, single/double shear strength, and driven/undriven rivets. (AREMA [1905], Talbot and Moore [1911],Wilson and Thomas [1938], and Wilson et al. [1942]). However, very few studies investigated those properties for vintage rivets which may have been in service in steel structures and steel truss bridges for decades. D'Aniello et al. [2011] fabricated test specimens from vintage rivets and plates and re-examined those factors that might affect rivet tensile and shear strength. The material he used for fabrication was stored in the warehouse of Italian Railway Network Agency for over fifty years. D'Aniello et al. [2011] concluded that most rivet tests showed that they were stronger than nominal values specified in standard [EN : 1993]. However, these tests were conducted on the vintage material stored in warehouse not on rivets in service for decades.

A donation of salvaged bridge components and individual rivets removed from the Wash-

ington State Department of Transportation bridge provided a good opportunity to study the rivet shear strength and joint shear resistance for bridges which were in service for decades. Two different tests were conducted on these salvaged rivets and connections, single rivet shear strength tests of vintage rivets and long connection tests. The single rivet shear strength tests are documented in this chapter and the long connection tests are documented in a Master Thesis by Saura M. Jost in Jost [2012].

8.2.1 Rivets for Single Rivet Shear Strength Test

In the single rivet shear strength tests, the rivets were from steel truss bridges which were built in 1948 and dismantled in 2010 and were made with ASTM 141-39 rivet steel. In the long connection tests performed by Jost [2012], the connections were from steel truss bridges built in 1932 and the rivets were made with ASTM 141-32T rivet steel. They both have the same nominal tensile strength between 52ksi and 62ksi. The rivets used in the single rivet shear strength tests have different levels of corrosion since they are from different parts of the bridge. It is interesting and useful to establish the correlation between the shear strength and the degree of corrosion. The rivets were categorized into three different levels of corrosion and carefully photographed, measured and recorded. The three categories are: 1) Group A had extensive visible corrosion 2) Group B had a medium amount of rust, and 3) Group C had very little rust. None of the rusts had significant loss of area due to corrosion. Each group has two sets of rivets and each set has four actual rivets. The categorized rivets are shown in Figure 8.1 and were labeled as RXY-Z, where X indicates the rivet group, Y indicates the rivet set and Z indicates the rivet number in the set. The diameter of these rivets were measured at several points to determine an average diameter and area. Because these rivets might be loaded in shear for many years and cycles of loading, some deformation of the rivet shafts were observed. The rivet grip was not a perfect cylinder and the rivet diameter was also not uniform along the grip. The rivet diameter at the shear planes applied during testing, which were located at 0.5 (in) and 1.0 (in) from the rivet head, were measured and recorded. A total of five measurements around the circumference at each shear plane were made, which is equivalent to measure the diameter about every

72° degrees around the circumference. The data is documented in Appendix A Tables A.1, A.2, and A.3. The average diameters of Groups A, B and C were 0.9294 in., 0.9276 in., and 0.9359 in. respectively, and the grip length were between 3 in. to 5 in.. The average diameter for the three groups showed no significant difference even though they had different corrosion levels. The average diameter was smaller than the 15/16 in. hole diameter the rivet were used in and indicates the riveting procedure may not fully fill the rivet hole or there may be lost area due to corrosion. This may be because these were longer grip rivets (Kulak et al. [1987]). The nominal diameter of the rivets was assumed to be 7/8 in. based on the 15/16 in. hole diameter. Nominal stresses computed using the nominal diameter are used to compare rivet shear strengths obtained here with those in the literature, which are typically reported as nominal values.

8.2.2 Single Rivet Shear Strength Test Setups

The setup for the single rivet shear strength tests consisted of three parallel rectangular plates with a 1 in. diameter hole in each to place the rivet through so they could be tested in double shear. The setup is shown in Figure 8.2. The plates were made from ASTM A514 high strength steel with a minimum yield stress of 100 ksi. High strength steel was used for the plates to minimize local yielding around the bearing area so the apparatus could be used repeatedly. The rivet were each placed through the three plates and a washer was tack welded to the extension of the rivet without a head to prevent the plates from moving apart during the tests. The three plates that applied the shear to the rives were placed on a bottom horizontal plate with welded rails to stabilize the three standing vertical plates. Figure 8.2(a) shows a dimensioned drawing of the setup and photos of the assembled setup and instruments are shown in Figure 8.2(b).

The tests were conducted by applying a vertical force to the middle of the three vertical plates using a 300 kip capacity Universal Testing Machine (UTM). Instrumentation for the tests included four duncan potentiometers and one laser extensometer. Two duncan potentiometers, P1 and P3, measured the displacement between the top and bottom UTM

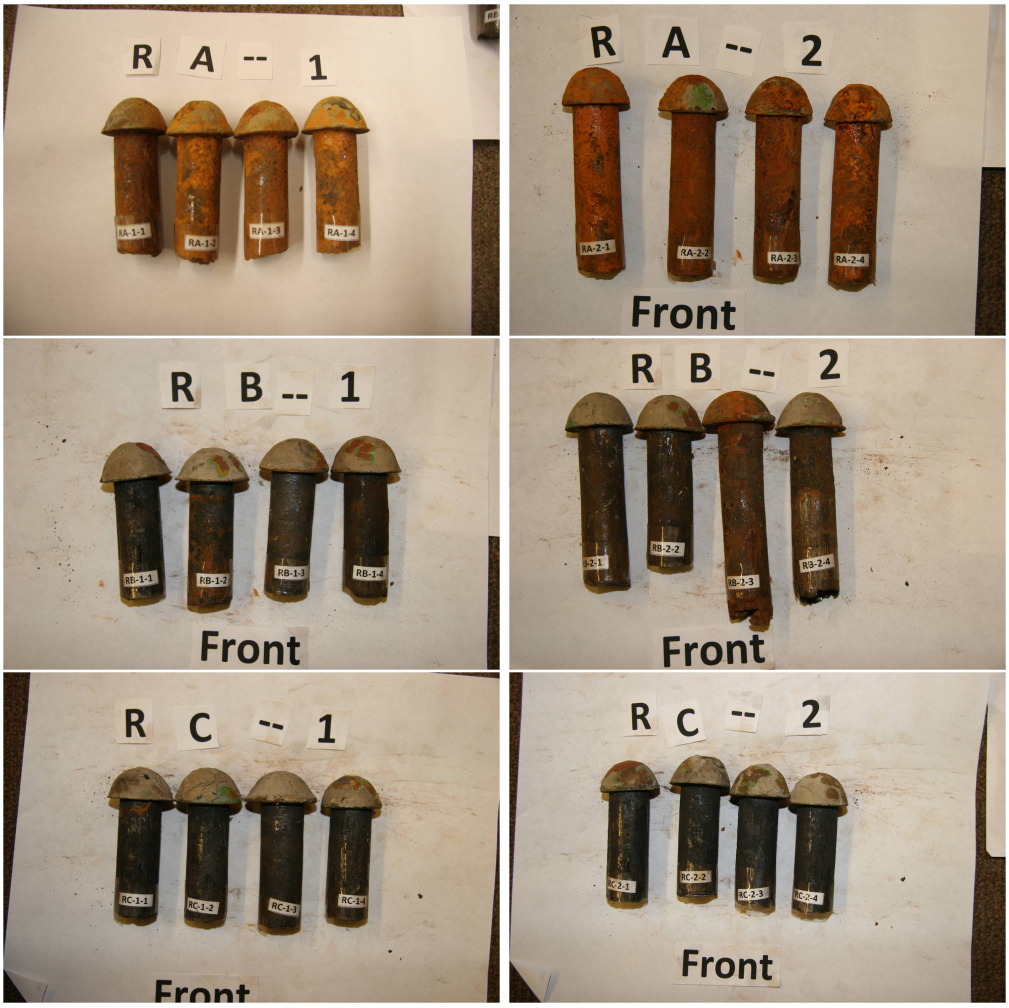

Figure 8.1: Different corrosion levels for the three groups of rivets

platforms, and were fastened to the both outer vertical plates of the setup. The other two duncan potentiometers, P2 and P4, measured the rivet shear displacement, and were fastened to the movable central vertical plate and deployed on both the front and back sides. The center of the test setup coincided with the center of the UTM's loading platform to ensure uniform compressive loads. The duncan potentiometers were also deployed symmetrically to account for any the possible rotation due to uneven deformation. An additional laser extensometer was used to validate the measured data from the duncan potentiometers.

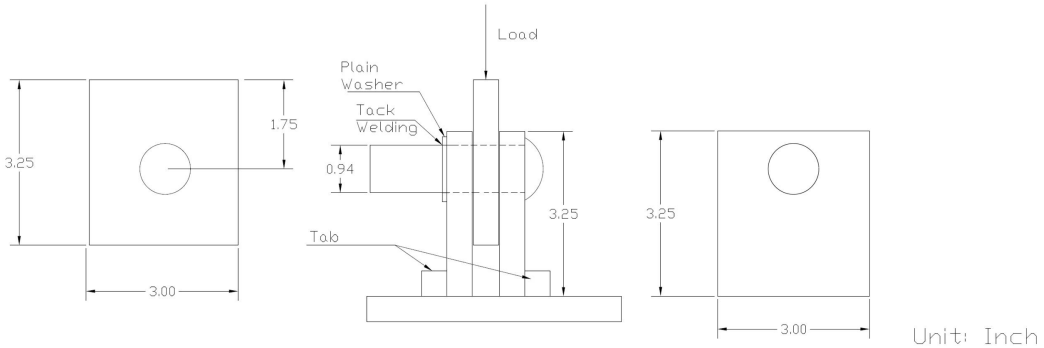

(a) Test setup with dimensions

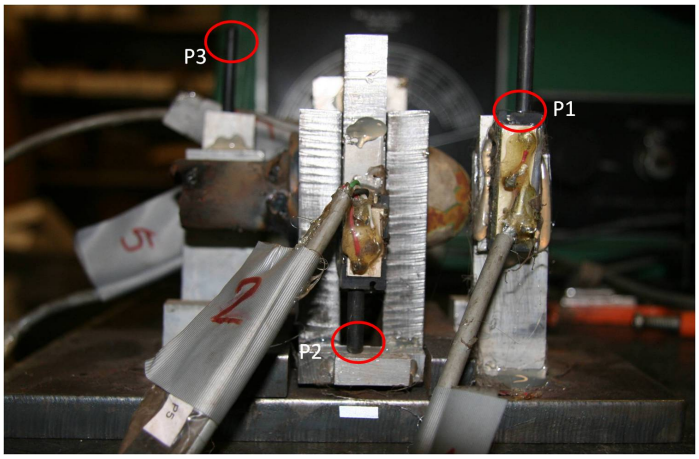

(b) Side view photo of the instrumentation and test setup

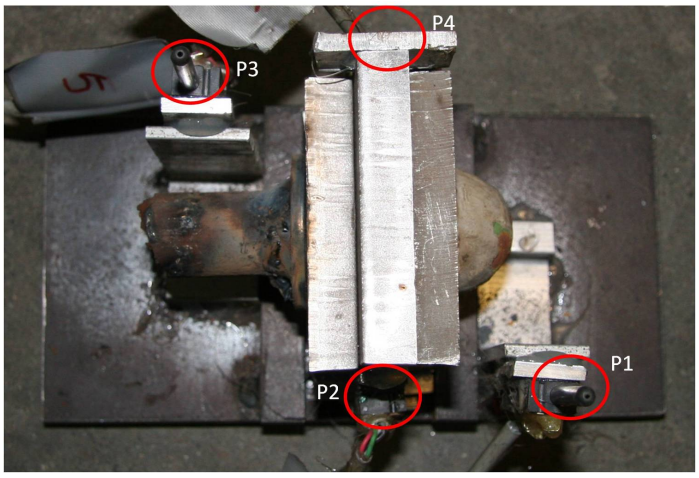

(c) Top view photo of the instrumentation and test setup

Figure 8.2: Test setup for single rivet shear strength tests

8.2.3 Rivet Shear Force versus Deformation Curves

The rivets were loaded in double shear in the test apparatus until failure. The shear force-deformation plot for each rivet is shown in Appendix A Figures A.1 through A.6. For most rivets, except RB1-1, RB1-4, and RB2-3, the shear force-deformation curve measured by four duncan potentiometers and the laser extensometer were very close and the average of the deformation data from the five different measurements was taken as the representative shear force-deformation curve for the rivet. The rivet shear force-deformation curve for each group was also found by averaging the individual rivet curve in that group.

Figure 8.3 shows the rivet shear force-deformation curve for each group along with the single rivet shear tests conducted by Dlugosz [1962] at Lehigh University. Dlugosz [1962] conducted double shear tests on 7/8 in. A141 single rivet using a jig which was very similar to the test apparatus used here. However, in Dlugosz's tests the rivets were installed using standard procedures so there existed a initial clamping force in the rivet grip that generated friction between connected plates. This explains the difference in the initial stiffness as the specimens tested here were in bearing from the beginning. The ultimate shear force was about 63.6 kips and the maximum rivet shear stress was 55.3 ksi in Dlugosz [1962]'s test. Figure 8.3 shows that the vintage rivets tested here had slightly less ultimate strength but more deformation before failure. The ultimate shear force for Groups A, B,and C were 60.83 kips, 61.71 kips, and 62.51 kips, which corresponded to nominal ultimate shear stress of 50.58 ksi, 51.31 ksi, and 51.98 ksi respectively. This shows that the visible corrosion did affect the ultimate shear strength but the impact was very small. When these results and those from Dlugosz [1962] are compared to other results from the literature where rivet strength is determined from connection tests, the rivet shear strength is lower in these tests than the average from literature, which showed the average shear strength is around 60 ksi for A141 rivets when only short connections were considered (Table 2.1[1]). This may be because these two sets of tests were conducted in double shear and for undriven tests which may cause 10% to 25% difference, as described by Wilson et al. [1942].

[1]carbon steel rivet, ASTM A141 rivet and ASTM A502 Grade I rivet were considered having similar property when the average shear strength were taken form literature

In summary, tests on previously in service rivets shows that though the shear strength of rivet is impacted by corrosion but for the levels of corrosion seen here that impact is negligibly small. In addition, even though the rivets were tested in double shear, undriven rivet, and somewhat corroded, the rivet shear strengths are twice the value that of the strength given by AASHTO [2010] and are still larger than the revised values in the AASHTO [2011]. This conclusion reinforces the findings by Olson [2010] that suggested the rivet shear strengths used in joint evaluation were overly conservative.

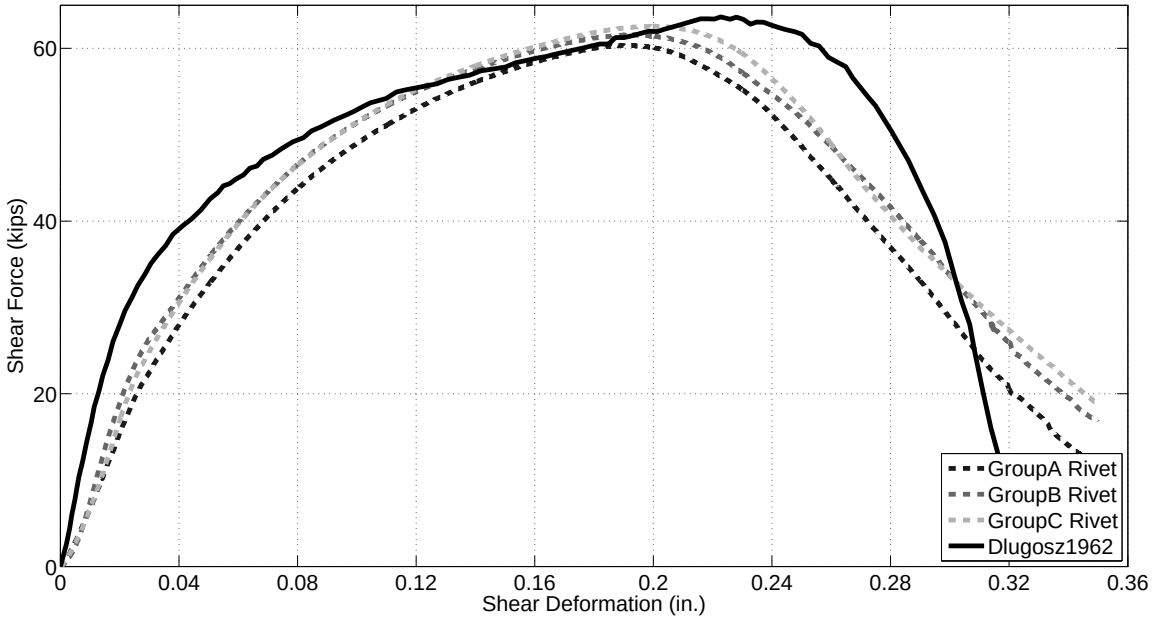

Figure 8.3: Shear force-deformation curve of ASTM 141 single rivet test

8.3 The Effect of Connection Length on Connection Strength

The rest of this chapter investigates the effect the connection length on the connection's shear strength, which is denoted by the long connection effect hereafter. The long connection effect was demonstrated in riveted and bolted butt splice connection tests at Lehigh University in the 1960's and 1970's. The fasteners in the butt joints where connected elements were loaded at their end and the fasteners transfer tensile or compressive loads

between connected elements through shear, were found to have failure initiating at the end row of the fasteners of the connection. The strength of the connection was found to be less than the sum of the fastener shear strength for long connections. This failure mode, which begins with fracture of the outer fasteners and continues with fracture towards the middle of the connection, is called unbuttoning and it is a premature failure in the sense that it occurs prior to developing the full strength of all fasteners. A theoretical solution was developed by Fisher [1964] to calculate the shear forces resisted by the individual rows of fasteners in the connections at connected element yield and fastener failure. They concluded that the fastener strength in long connections should be reduced for butt splice type connections to account for the long connection effect. The current AASHTO [2010] requires joint fastener strength to be reduced based on factor calculated by $1 - \frac{0.25L}{50}$ where L is the connection length between the first row and the last row of rivets of a connection.

8.3.1 Development of Modeling Methodology for Riveted Connection Using Tests by Jost [2012]

Jost [2012] also tested long connections but her connected elements were loaded with shear forces. The tests found the long connection effect was insignificant when joints were loaded in shear. Jost [2012]'s tests provided not only a different perspective to consider the shear resistance strength of fasteners in a long connection but also provided riveted joint test data that can be used for calibration of analytical models. In this section, the development of a rivet modeling methodology is described. Two rivet modeling methodologies are considered for modeling Jost [2012]'s test, and the results are compared with test results to select a rivet model for further FEA analyses. The results are used to study the long connection effect in end loaded butt joints in a later section.

The test specimens fabricated by Jost [2012] used long riveted sections of the guardrail from two decommissioned Washington State steel truss bridges as shown in Figure 8.4. These two steel truss bridges were in service on State Highway No. 12 from 1931 to 2010 in Washington State. The sections of the guardrail from these two steel truss bridges were

fabricated to proper lengths and sections in order to study the long connection effect when connected elements are loaded in shear. The guardrail section consisted of one C6x8.2 channel and two 3x4x$\frac{5}{16}$ angles which are riveted by $\frac{5}{8}$ in. rivets in a 4 in. spacing. The original geometry of the guardrail made it difficult for direct testing. The guardrail cross section was unsymmetric and loading that geometry would have generated a moment and the channel and angle yielded or buckled before the rivets develop their full capacity for long connection. Therefore, the guardrail section was cut in half along the middle of the channel web and fastened with high strength bolts inside on HSS section and also to a plate to eliminate the unsymmetric geometry. The angle and channel were reinforced to increase their axial load capacity to prevent yielding and buckling. The assembled specimen is illustrated in Figure 8.5(a) and a cross section is shown in Figure 8.5(b). The middle plate and the HSS box were connected to the channels and angles using A490 high strength bolts. The A490 bolts had higher capacity than the rivets such that the connected rivets would control the specimen capacity. The assembly was placed in a Universal Testing Machine (UTM) and the middle plate was pushed through the HSS to shear the rivets. The load was applied to the top of the middle plate, and passed as shear force into the channel web, then as shear force in the rivets connecting the channel flange and the angle's long leg. Jost conducted five connection tests that include connection lengths with 2, 4, 7, 11, and 17 rivets in a row. and the tests showed that the average rivet shear strength at connection failure in all five specimens was about 62.1 ksi (Jost [2012]). The unbuttoning failure mode was not observed in these long connection tests.

In addition to testing long connections in shear, Jost [2012] also provided shear force-deformation test results for 5/8 in. driven rivets in single shear from the shortest connections. The shortest specimen, which included two rivets in a row and a total of four rivets, provided two load-deformation curves from two duncan potentiometers which are shown in the Figure 8.6, and the average rivet curve from these plots is also shown Figure 8.6. This shear force-deformation behavior includes the deformation of the rivet and bearing deformation of the plates. This shear force-deformation curve is used as the basis for a uni-directional nonlinear spring element simulating individual rivet behavior in the analytical

simulations, discussed in the next section.

Figure 8.4: Section of guardrail consisting of one channel and two angles

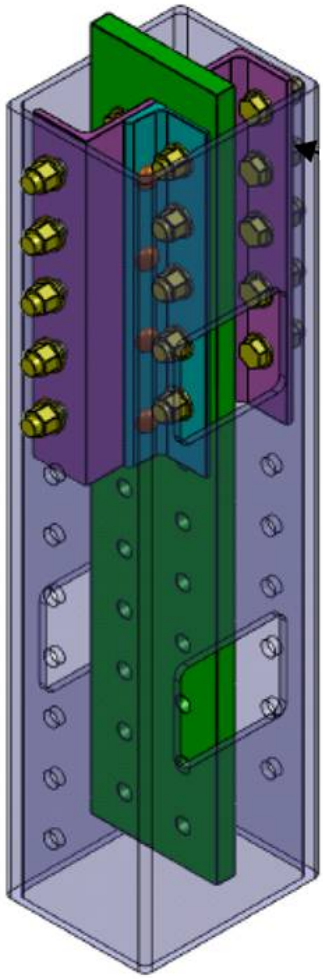

(a) Illustration of specimen assembly

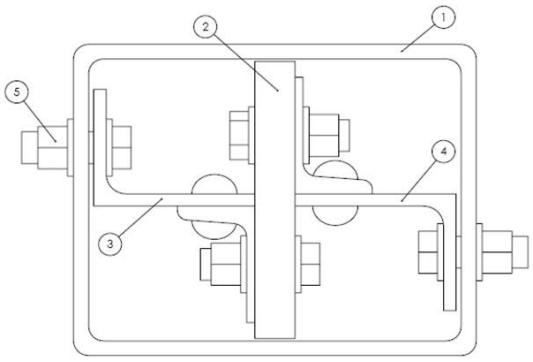

Part No.	Name	Material	Grade [ksi]
1	HSS 10 x 8 x 3/8"	A500	46
2	PL 7 1/8 x 1"	A572	50
3	West Guardrail	A7	36*
4	East Guardrail	A7	36*
5	¾" Bolts	A490	

*Nominal strength, C6x8.2 and L4x3x5 were tested separately for tensile strength

(b) Cross section of assembled specimen

Figure 8.5: General test setup used by Jost [2012]

8.3.2 Modeling of Riveted Connections

In previous FE analyses rivets were modeled as rigid links between adjacent nodes in the gusset plate and truss members. However, for the investigation of the long connection effect, the behavior of the rivets, and the local deformation of member and gusset plates around the rivets was simulated in more detail. Rivets can be modeled in FEA in very complex ways,

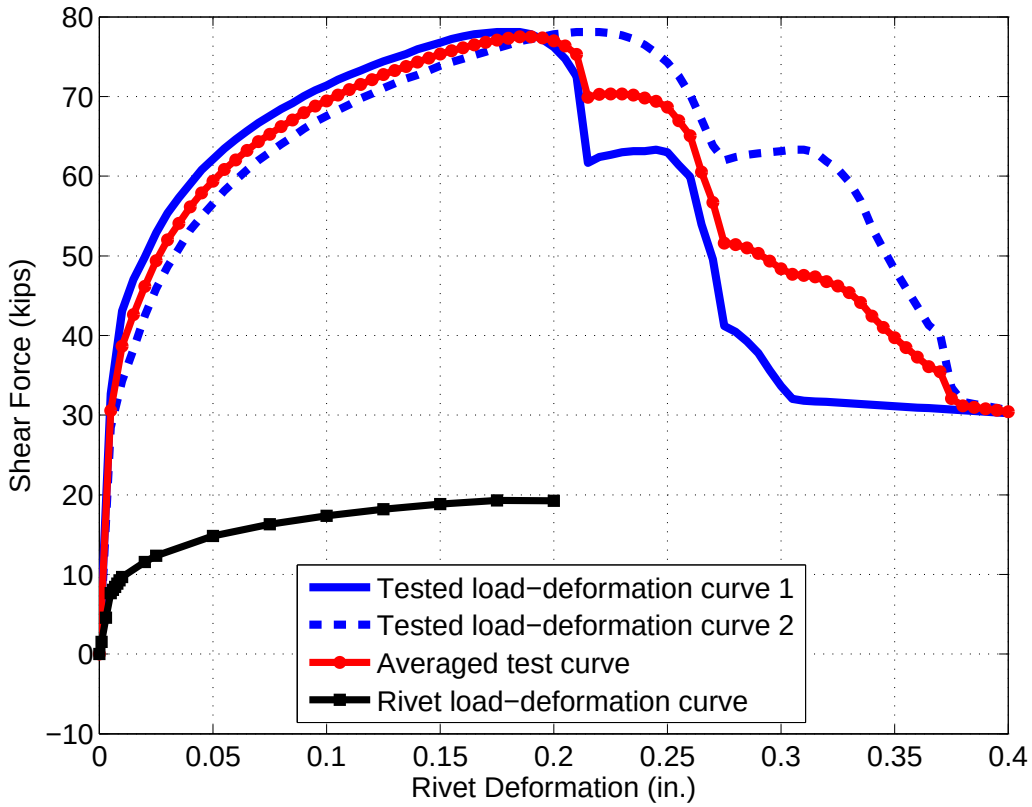

Figure 8.6: Rivet spring model property was produced from the shortest of the connection tests conducted by Jost [2012]

including using solid elements and considering friction, pretension of rivet grip, contact surface behavior, and ...etc. Modeling rivets and connected elements in this way is time-consuming, mesh sensitive, and does not provide direct insight into the shear forces as stresses must be integrated over the rivet area. An alternative method to model rivets is to use a nonlinear spring element that is assigned the shear force-deformation relationships including the rivet and local plate bearing deformations. The ANSYS Element COMBIN39 was used to model these combined rivet and local plate bearing behaviors and was calibrated using the long connection tests conducted by Jost [2012].

There are two modeling methods used to consider how the rivet spring is connected to the plates in the FEA. In the first method, the rivet spring are connected to the plates directly at

the nodes where the rivet is located without modeling the rivet holes. This is similar to the method used for analysis of gusset plate joints where rivets were modeled as rigid links. In the second method, the plate material at the rivet is removed to model the void of the rivet hole. Half of the circumference of the rivet hole in each plate is assumed to resist the bearing loads in the direction of loading of each plate. The nodes along this half circumference of the rivet hole in the plate are connected to a node at the center of the rivet hole using a multi-point-constraint (MPC), essentially a rigid beam element in ANSYS. Therefore, the half circumference at each plate in the direction of bearing forms a rigid surface on the bearing area. Two nonlinear spring elements representing the rivet deformation in orthogonal directions perpendicular to the rivet grip, i.e. the in-plane directions, were connected to the nodes at rivet hole centers of the two connected plates. These two nonlinear spring provide shear resistance in the longitudinal and transverse direction of the modeled connections. Another nonlinear spring was deployed in the rivet grip direction, i.e. the out-of-plane direction, with a tensile elastic stiffness property to prevent opening between two connected plates. This modeling methodology is shown in the Figure 8.7. The first method is clearly simpler and convenient but it must provide adequate accuracy. The second method may provide better results since it included the hole deformation. Three test specimens from Jost [2012] were modeled using both methods and their performance is assessed via comparison with test results.

Three tests by Jost [2012] were simulated to observe the performance of the two different modeling methods for specimens with 2, 7 and 17 rows of rivets. The channels, angles, middle plates and HSS section, were modeled with ANSYS Elelment SHELL181. An illustration of the 7 riveted connection FEA model is shown in Figure 8.8. The channels and angles were made from A7 steel with a nominal 36 ksi yield stress, the middle plates were made from A572 steel with a nominal 50 ksi yield stress, and the HSS section was made of A500 with a nominal 46 ksi yield stress. The nominal yield stress were used in the analysis. Elastic modulus and Poisson's ratio for steel component were 29000 ksi and 0.33 respectively. Surface contact element pairs, CONTA174 and TARGE170, were applied to the potential surface contact pairs in the model. These contact surface pairs include

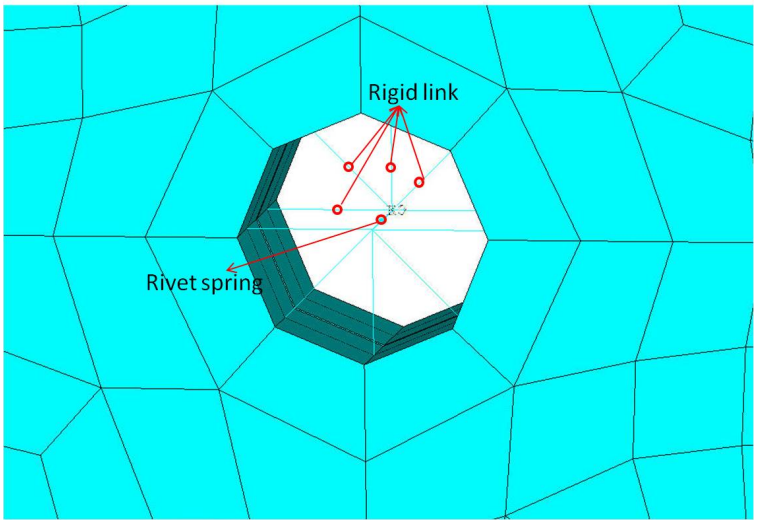

Figure 8.7: Illustration of the rivet modeling method that includes the rivet hole

the channel-to-middle plate interface, the channel-to-angle interface, and the angle-to-HSS interface. Point-to-surface was applied to the interface between the middle plate and the HSS section. Contact modeling in this simulation is critical since the designed specimen had some torsional twist. The applied surface pair contacts and point-to-surface contact prevent the model from twisting and helps the algorithm converge. In addition, several points along the edge of the middle plate were fixed in its out-of-plane degree of freedom to further prevent the middle plate from twisting. In the test, a sliding friction on stainless interface prevented this twisting. The top of the middle plate was constrained to be a rigid surface and a concentrated load was applied to the center of the rigid surface to assure uniform load through plate end. The A490 high strength bolts connecting the test specimen between the angle and the HSS section and the channels and the middle plate were modeled as individual rigid links. This is reasonable since no slip was observed at the bolts during testing. The boundary condition at the bottom of the HSS section was fixed in three translational degrees of freedom for all nodes on the boundary.

Figures 8.9(a), 8.9(b), and 8.9(c) show the comparisons of overall load-displacement curves for the FEA results using the two modeling methods and the test results. The test load-

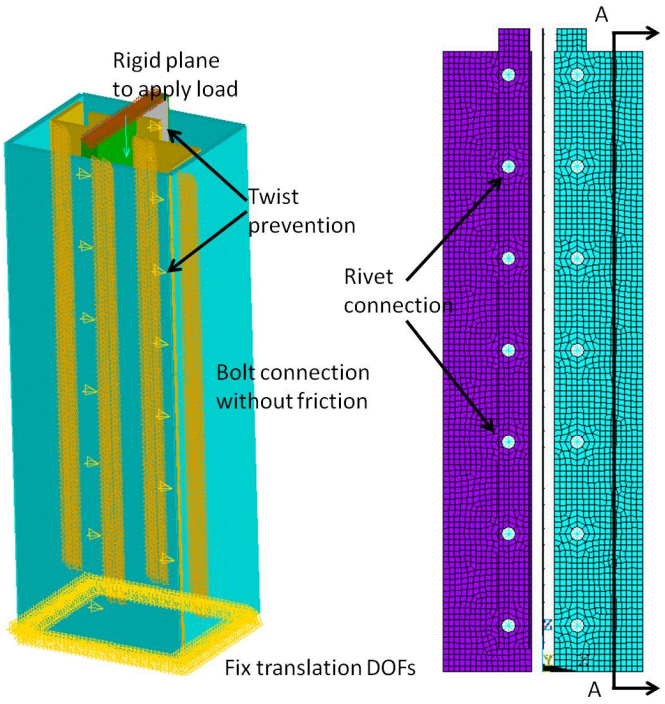

Figure 8.8: Analytical model of the 7 rivet row connection length specimen tests tested by Jost [2012]

displacement curves used for comparison were revised by removing the rivet slip from the original raw data because slip was not simulated in the analytical model. It is difficult to know the initial tensile stress in the driven rivets and the initial gap between the rivet shank and the edge of rivet hole which is necessary for modeling slip. The FEA results for the models that consider the rivet holes show good agreement for the load-displacement curves when compared with all three test results while the FEA results for the models that do not simulate rivet holes show good agreement in the linear range of behavior but have lower stiffness that thee experiments after yielding of the rivets and connected elements.

The difference in stiffness between the rivet modeling methods is due to the rigid elements that prevent the bearing surface from deformation in the the models where holes are cut out. The models without the holes essentially double count the bearing deformations, leading

to an underestimate of the stiffness, especially as local yielding occurs around the rivets. Based on these comparisons and discussion, the modeling method including the rivet hole and associated rigid links as shown in Figure 8.7 will be used all remaining simulations in this chapter to investigate long connection effect. As mentioned in previous section, the shear force-deformation property used for the nonlinear spring element resulted from the test results and it includes the deformation of both the rivet in shear and connected plates in bearing.

Finally, it is interesting to verify Kay [2011]'s claim that the modeling methods for the fasteners does not significantly affect the stress on the connected elements except locally at the holes. The compressive principal stress and Von Mises stress along the section A-A, which was located along one of the connected angle legs in the test specimen as shown in Figure 8.8, were plotted for two different rivet modeling methods for the 7 rivet row connection test at the specimen fail load. Figure 8.10 verifies that both modeling methods have similar stress distributions along the section A-A. The compressive principal stress distribution from the simulation without modeling the rivet holes is somewhat more jagged than that from the simulation where the holes are modeled. This is because the nonlinear spring element connects only to a single node at each rivet location resulting in higher stress concentrations at the rivets and while the model with the rivet holes distributes the load to several nodes around the rigid surface of half of the rivet hole which mitigates the stress concentration. Again, the modeling method where the holes are considered is selected for the rest of the analyses discussed in this chapter.

8.3.3 Simulation of the Dlugosz [1962]'s Riveted Butt Joint Tests

Most of the butt joints tested at at Lehigh University in the 1960's and 1970's were bolted connections. Dlugosz [1962] conducted tests on three riveted butt joints for three different lengths to compare the behavior between riveted and bolted joints. Bolts and rivets behave differently because rivets materials have lower strength but more ductility than bolt material. The ductility of the rivets can provide more ability to redistribute loads between the

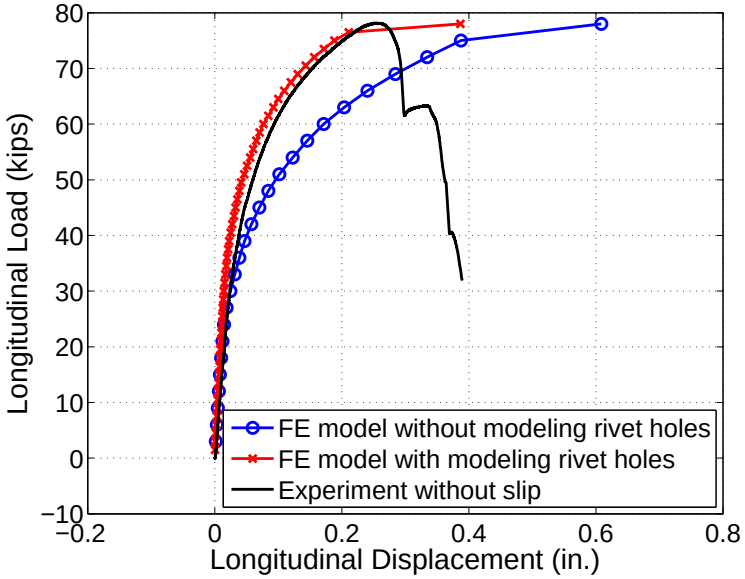

(a) Validation of the FEA results with the test results for the 2 rivet row from Jost [2012]

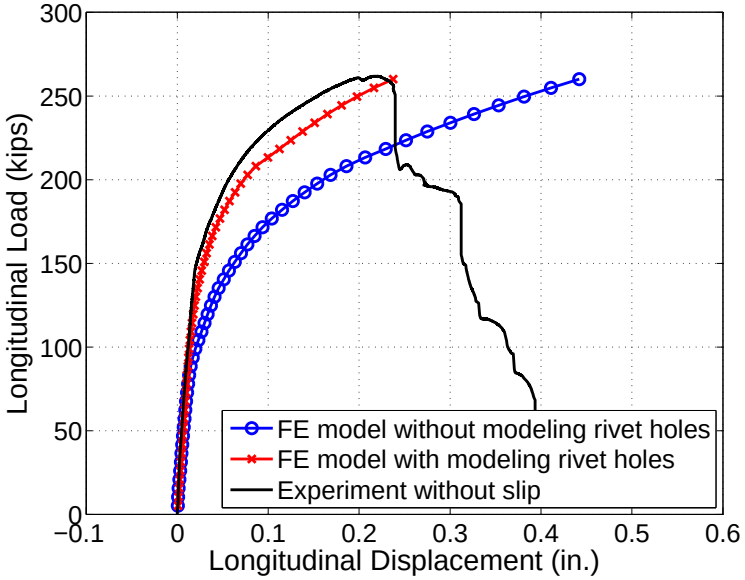

(b) Validation of the FEA results with the test results for the 7 rivet row from Jost [2012]

Figure 8.9: Validation of the FEA results with the test results

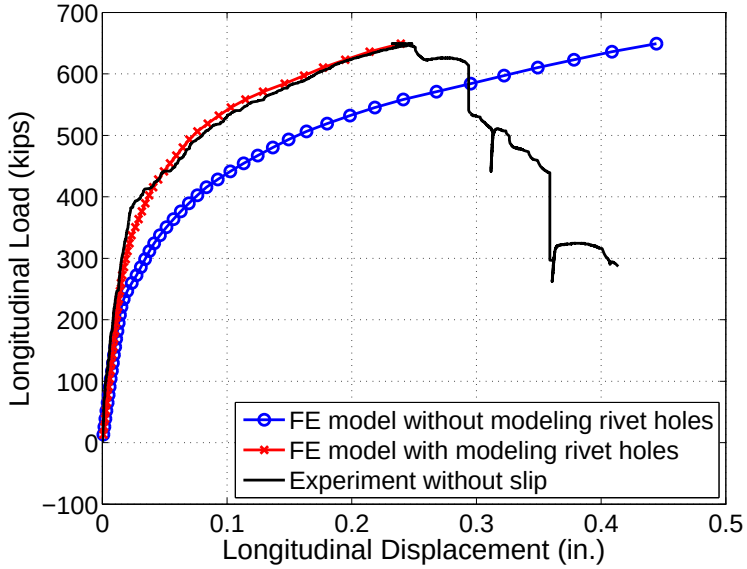

(c) Validation of the FEA results with the test results for the 17 rivet row from Jost [2012]

Figure 8.9: Validation of the FEA results with the test results

rivets in a riveted joint so that riveted joints may not be as significantly impacted by the long connection effect. To investigate this, Dlugosz [1962] modified the test specimens used for bolted joints by Bendigo and Rumpf [1960] to comply with a balanced design, where the ratio of allowable connected member load, $T \times A_n$, to allowable rivet shear resistance, $S \times A_s$, was near 1.0. Connected element tension strength, T, and rivet shear strength, S, are allowable stress, A_n is net area for the connected elements, and A_s is shear area for the rivets. The test specimens achieved balance design by adjusting the ratio of the rivet shear area, A_s to the connected plate net area, A_n to be about $1 : 0.76$ for riveted connection as shown in Figure 8.12. Dlugosz [1962] conducted joint tests on three different connection lengths, 21 in., 31.5 in., and 42 in., which had 7, 10, and 13 rivet rows along the connection lengths. Figures 8.11 and 8.12 illustrate basic information of the specimen geometry and test results for the riveted connection tests by Dlugosz [1962]. However, the figure from Dlugosz [1962] contains an error. The values given in the original table for t are actually for 2t. The thickness of each lap plate was 1 in. This has been verified by examining their

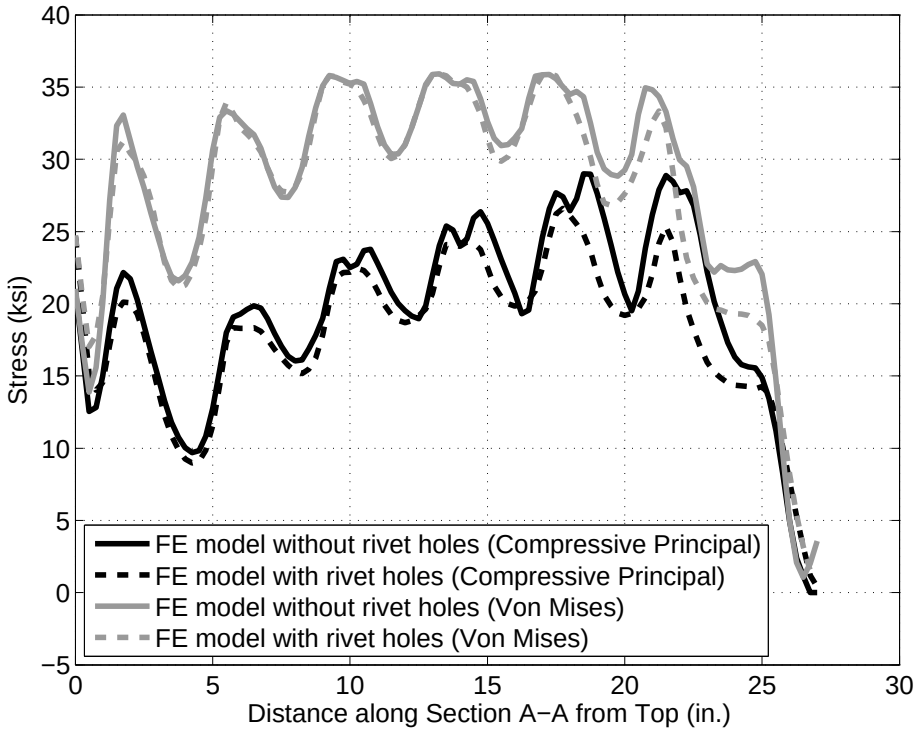

Figure 8.10: Compressive principal stress and Von Mise stress along section A-A section using the two different rivet model methods considered for the 7 rivet row model at the load when the rivet failure

results and their calculations of joint properties such as the gross area and net area of the specimens which is shown in Figures 8.11 and 8.12. Dlugosz [1962] found that although load re-distribution was observed in the riveted joints and the deformation in the riveted joints was larger than in bolted joints, the long connection effect still resulted in an unbuttoning failure mode at a load less than the sum of the rivet strength. The unbuttoning factor, which was defined as the ratio of the average rivet shear stress at the joint failure to the ultimate rivet stress from single rivet shear tests, of three specimens gradually decreased when the connected length increased. The unbuttoning factor for these three connection lengths from Dlugosz [1962] were 0.84, 0.75, and 0.74.

The FE modeling method where the rivet hole is modeled is used to simulate Dlugosz

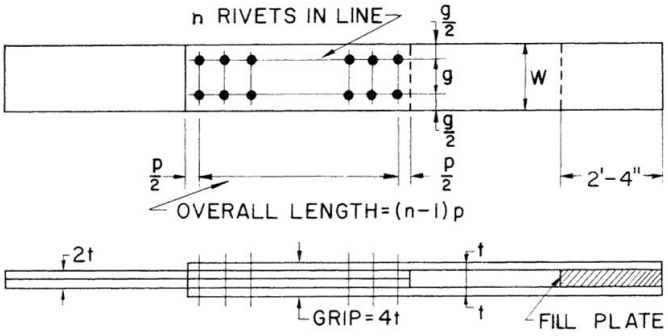

MARK	n	t	WIDTH IN.	GAGE IN.	g/d_h	$A_{riv.\ nom.}$ SQ. IN.	A_{net} SQ. IN.	T/S
DR71	7	2"	8.48	4.24	4.52	16.83	13.21	1:0.78
DR101	10	2"	11.12	5.56	5.94	24.04	18.49	1:0.77
DR131	13	2"	13.78	6.89	7.35	31.25	23.81	1:0.76

FIG. 1 DIMENSIONS OF JOINTS, DR SERIES

Figure 8.11: Dimensions and properties of long riveted joint tests conducted by Dlugosz [1962]

[1962]'s three test specimens and re-examine the variation of the load distribution to the rivet along the connection length in different loading stages. The analytical model includes A7 main and lap plates with a 37.5 ksi yield stress and A141 7/8" rivets modeled using uniaxial nonlinear springs with the rivet shear force versus deformation behavior taken from single rivet tests reported by Dlugosz [1962]. The rivet shear properties observed from the single rivet tests were a 13 kips yield force and 31.5 kips ultimate strength per single shear face. The specimen unbuttoning fail load reported from the tests were used as the maximum load in the simulations.

8.3.4 Variation of Rivet Force Distributions During Different Load Stages

In order to observe the variation of the rivet force distributions during a loading process, the loads taken by each rivet along the connection length were plotted in small loading

ITEM	UNITS	DR 71	DR 101	DR 131
PATTERN			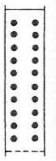	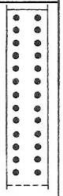
ALL holes drilled $\frac{15}{16}$"				
ALL pitches $3\frac{1}{2}$"				
Gage = $\frac{1}{2}$"				
RIVETS				
No. in line		7	10	13
No. of $\frac{7}{8}$" A141 rivets		14	20	26
Nom. shear area	sq. in.	16.83	24.04	31.25
PLATES				
Nom. width	in.	8.48	11.12	13.78
Nom. thickness	in.	2	2	2
Nom. gross area	sq. in.	16.96	22.24	27.56
Nom. net area	sq. in.	13.21	18.49	23.81
Actual net area	sq. in.	13.18	18.47	23.73
% Deviation in net area	%	-0.21	-0.11	-0.34
T/S RATIO (A_S/A_N)				
Nominal		1:0.78	1:0.77	1:0.76
Actual		1:0.78	1:0.77	1:0.76
WORKING LOAD (T=20,000 S=15,000)	kips	252	361	469
SLIP LOAD (First Major)		444	518	830
Nom. rivet shear	ksi	26.4	21.6	26.6
Nom. tension, net section	ksi	33.6	28.0	34.9
TYPE OF FAILURE		rivet	rivet	rivet
Load at failure	kips	738	942	1216
Nom. rivet shear	ksi	43.9	39.2	38.9
Nom. tens.-net section	ksi	55.9	51.0	51.0
Act. tens.-net section	ksi	56.0	51.0	51.2
UNBUTTONING FACTOR				
U		0.836	0.747	0.741

Figure 8.12: Long joint test results from Dlugosz [1962]

increments up to ultimate load, i.e. the load at the failure of the specimen reported in Dlugosz [1962]. The FEA results for three tests are shown in Figures 8.13(a), 8.13(b), and 8.13(c) as rivet force versus rivet row. Fifty loading increments are considered and are represented by the fifty near horizontal lines in the plots. Several important loading stages are marked and separated by the different degrees of gray color in the plots. Each stage include several force distributions resulted from the load increments. Rivet elastic limit is marked as white, plate net section elastic limit is marked as light gray, plate gross section elastic limit is marked as gray, and all component yield is marked as darker gray. The limits

of rivet, net section and gross section yielding are calculated using the reported material property and specimen geometry. Figure 8.14 shows the percentage of the difference between the maximum rivet shear force and the average rivet shear force to the average rivet shear force for each load increment. The maximum rivet force occurs in the outer rivets of the connection.

In the beginning of the load increments, both rivets and plates are elastic, the end rivets take higher force than the average force in the rivets. The value of the ratio depends on the connection length. The longer the connection length, the higher portion of load taken by the end rivets. This is consistent with the theoretical elastic solution studied by Batho [1916] and Hrennikoff [1941] among others. However, this region is not a concern for the connection lengths examined here since rivet is made by ductile material, the rivet yielding occurs when the load continues increasing. As the rivets start yielding, loads are redistributed toward the rivets in the middle of the connection and the percentage of the rivet force difference goes down for all different connection length. The forces taken by the rivets along the connection become more even. Rivet yielding is regarded as important stage that mitigate uneven rivet force distribution along the connection length. When the plate net section yields, the percentage of the rivet force difference continues decrease and the least value of the percentage of the rivet force difference is found between the net section yielding and gross section yielding as shown in Figure 8.14. In Figure 8.13 a near even horizontal line is also observed between the load stages of plate net section and gross section yielding. Plate yielding over the gross section is regarded as another critical stage that aggravate higher forces taken by the end row of rivet.

When the load approaches to yield the gross section, the end rivets begin to take larger loads than the rivets in the middle do and the percentage of the rivet force difference increases with the increase of the load and connection length. This is because yielding of the connected plates is not uniform, the end portion of the connected plates yields first, decreases the tensile stiffness of the end portion of the connected plates, and generates more deformation than the middle portion of the connected plates. The increasing non uniformity of the rivet loads finally causes the unbuttoning failure that begins with the outer rivets.

Two important observations need to be addressed: 1) the outer rivets still take higher forces even in the load stage between net section yielding and gross section yielding where the most even force distribution is observed after rivets yield 2) In these three specimens, the sum of rivet shear resistance has higher capacity than the yield capacity of the connected plates. This is defined as "Weak Plate" condition. Table 8.1 shows the calculated loads for different load stages for each specimen and listed the unbuttoning factor calculated from the analytical study. The unbuttoning factor is defined as the ratio of the average shear force to the rivet shear strength when joint fails in shear for experiments. For analytical study here, the unbuttoning factor is defined as the ratio of the average shear force to the maximum force at outer rivet for each load stage. It is found that the unbuttoning factor for the analytical study is larger than the experimental results at the connection failure. This is because the interpretation of the rivet load-deformation curve by digitizing it from Dlugosz [1962]'s document may not precisely reflect the real test result. This result also indicates the determination of the unbuttoning factor is significantly affected by the rivet shear load deformation behavior. However, the trend of the joint behavior is similar. When the connection increases, the unbuttoning factor decreases at the joint failure and the largest unbuttoning factor are all observed between net section yielding and gross section yielding for three specimens.

In Fisher [1964]'s study, which used a combination of experimental and analytical methods, the same phenomenon was observed in bolted connections and the end bolts started to take much larger loads at the onset yielding of the gross section and the joints survived for a certain period after the yielding of the gross section. An illustration from Fisher [1964]'s study is shown in Figure 8.15. The white bar indicates that the gross section is elastic while the shaded bars indicate gross section yielding. Obviously, the loads taken by rivets along the connection length are much more uneven at the point when the joints fails after significant gross section yielding than they are before the gross section yields. This observation again implies that yielding of the connected elements is critical to aggravate the unbuttoning failure mode in long connections. The uneven load distribution is caused by the plate stiffness decreasing quickly after the gross section yields. The end portions of the connected

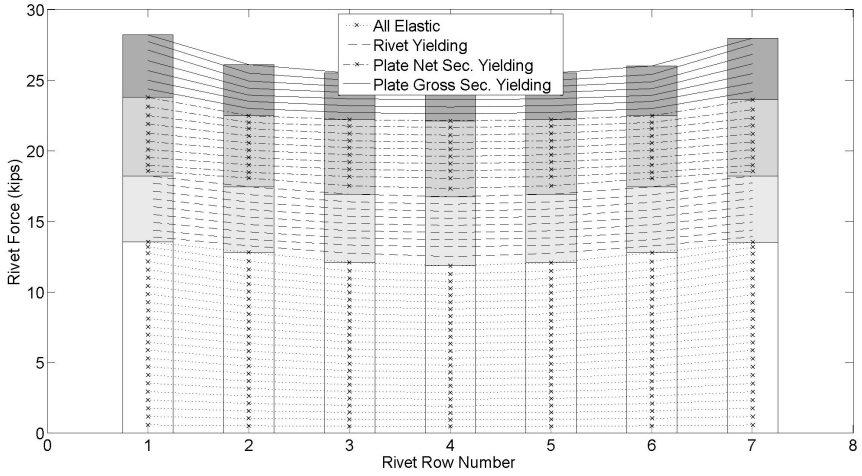

(a) Progressive rivet force distribution for the 7 rivet row specimen from Dlugosz [1962]

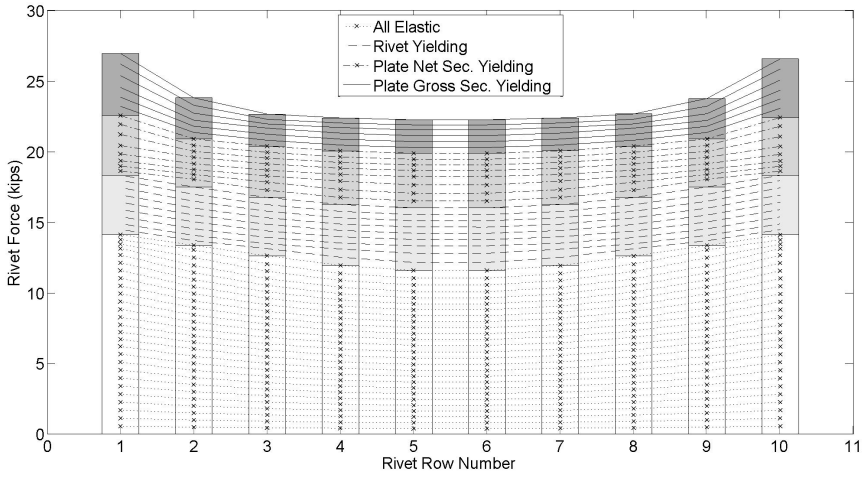

(b) Progressive rivet force distribution for the 10 rivet row specimen from Dlugosz [1962]

Figure 8.13: Rivet force distribution for three length specimens

plate, which have the highest gross section stress deform more than the plate section at the middle of the joint. This larger deformation at the end of the connected plate makes the end row rivets deform more than the rivets in the middle of the joint. Consequently, the end row rivets end up with larger force and fail first, initiating the unbuttoning failure.

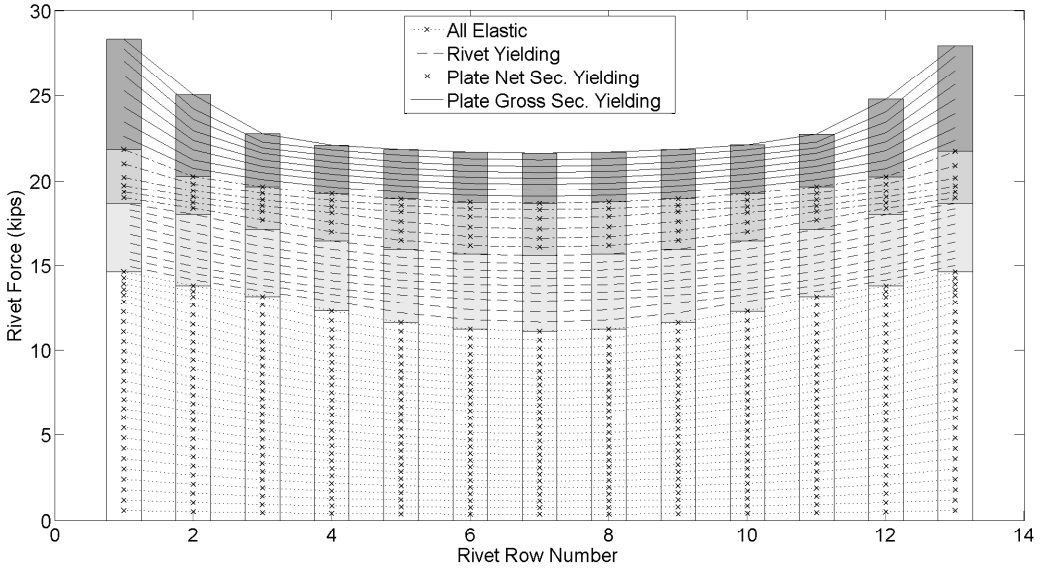

(c) Progressive rivet force distribution for the 13 rivet row specimen from Dlugosz [1962]

Figure 8.13: Rivet force distribution in tapered specimens

Again, all these experiments and analytical studies of the unbuttoning failure mode are for "Weak Plate" conditions where the plate yield capacity is less than the sum of rivet shear resistance.

8.3.5 Strong Plate Condition

There is almost no discussion in the literature for connections with strong connected plates in literature. "Strong Plate" condition is considered to be a connection that plate yield capacity is larger than sum of the rivet shear strength. To study the effect of "Strong Plates" to the force distribution in riveted connections, the tested specimens used by Dlugosz [1962] were modified by increasing area at one end to have the connected plate yield capacity equals to the load at the connection failure in experiments, which was the maximum load used in the analyses described above. The other end of the specimen was kept the same dimension as in the previous study so the load taken by both end rivets can be compared

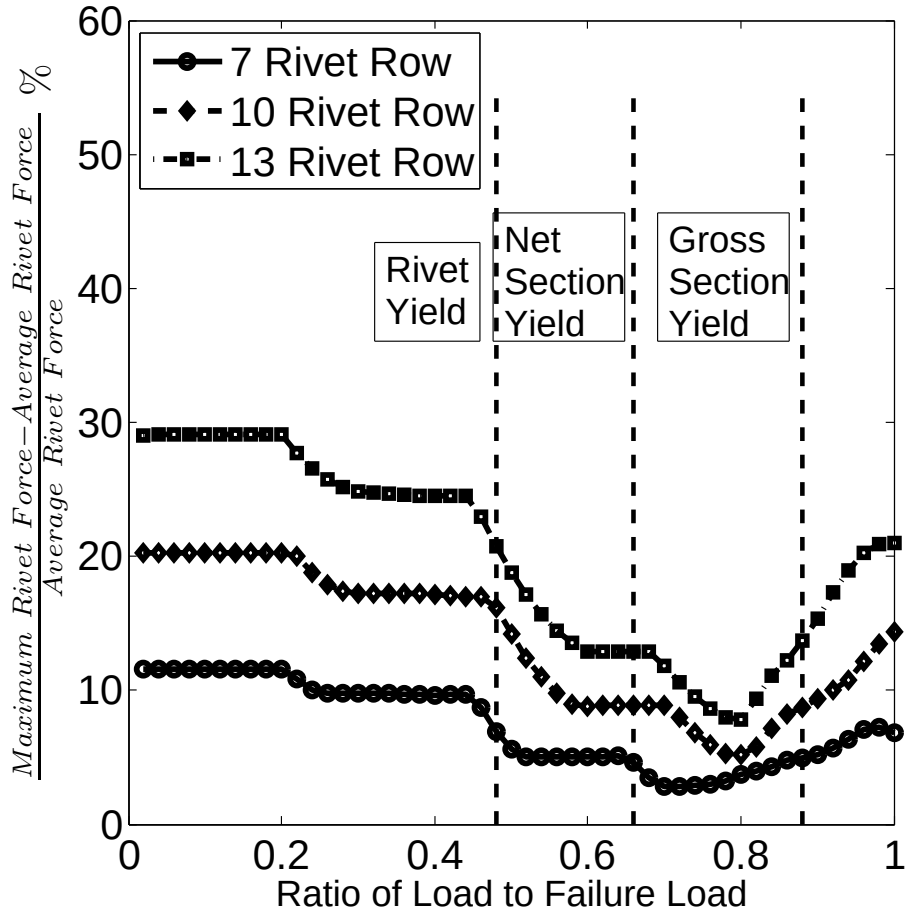

Figure 8.14: The smallest the percentage of the rivet force difference between rivet end force and rivet average force in the connection are observed during the load increments between the net section yielding and the gross section yielding

under the same loading condition. As shown in Figure 8.16, the narrow width W_1 is equal to the width corresponding to the specimens tested by Dlugosz [1962] and the wide width W_2 generated plate yield capacity equal to the failure load. Figure 8.16 demonstrates specimen with 7 rivet rows.

Figures 8.17(a), 8.17(b), and 8.17(c) show the rivet force distribution along the connection length in small load increments. The rivets at the end of plate without the enlarged area

Table 8.1: Load and unbuttoning factor in several important load stages

Specimens	Item	Rivet Yield	Net Section Yield	Gross Section Yield	Rivet Failure
7 Rivet Row (21 in.)	Load	364 kips	495 kips	636 kips	738 kips
	Unbuttoning factor[1]	0.96	0.97	0.96	0.94
10 Rivet Row (31.5 in.)	Load	520 kips	693 kips	834 kips	942 kips
	Unbuttoning factor[1]	0.92	0.95	0.93	0.87
13 Rivet Row (42 in.)	Load	677 kips	893 kips	1034 kips	1216 kips
	Unbuttoning factor[1]	0.89	0.92	0.91	0.83

[1] Unbuttoning factor $\frac{AverageRivetForce}{MaximumRivetForce}$

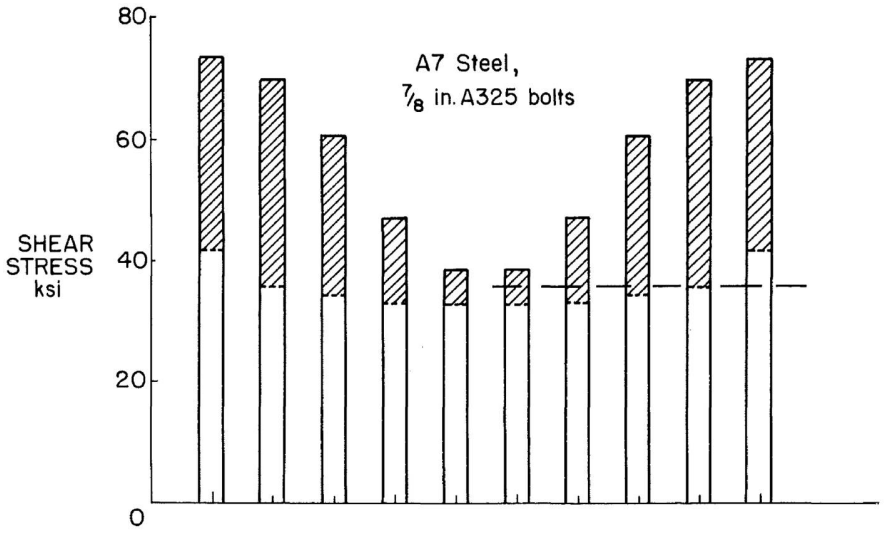

Figure 8.15: Fisher [1964]'s also showed that uneven loads taken by rivets aggravated after gross section yielded. The shadow area indicates gross section has yielded.

have much higher loads than the rivets on the other end with enlarged area at the maximum load. This effect increases with increasing connection length. The force taken by the end

rivets with the enlarged area is near to the force taken by the middle rivets. The calculated unbuttoning factor using the maximum rivet force at the enlarged area side are 0.98, 0.96, and 0.95 for three specimens from short to long connection lengths. This verifies that yielding of the connected element is a critical factor to aggravate the uneven load distribution and the unbuttoning failure mode. This means that for joints that have a fastener shear strength that is less than the gross section yield strength of the connected elements, i.e. "Strong Plate" condition, the fastener capacity need not be dramatically reduced for the long connection effect. A small reduction factor 0.9 can be considered for the reliability.

This observation also agrees with the study of the influence of the ratio of net area of the connected element, A_n, to shear area of the fasteners, A_s, on the long connection effect from the literature Fisher and Struik [1974]. They found that increasing A_n/A_s will decrease the likehood of the unbuttoning failure mode. As the factor of A_n/A_s approaches infinity, there was no unbuttoning observed in the joints. This finding is important when considering the shear resistance capacity of a joint using the current AASHTO requirement AASHTO [2011], especially like a diagonal member connected to gusset plates in a truss bridge connection where the Whitmore method is used to calculate the gusset plate yield capacity and has an enlarge area of the connected member and provide higher yield capacity. A discussion of current requirement and examples will be illustrated in the next section.

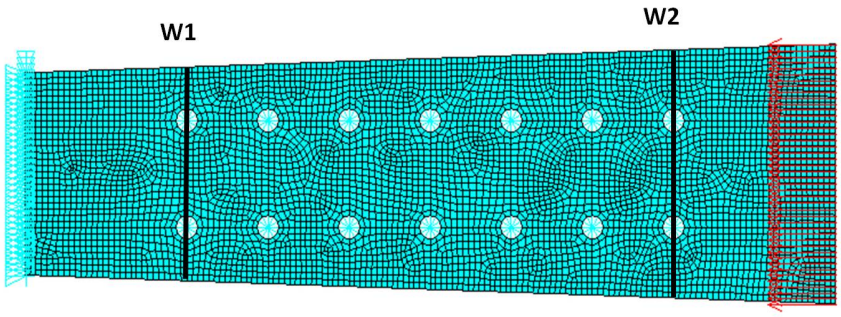

Figure 8.16: Geometry of tapered analytical specimen to study the effect of stiffness of connected element to the long connection effect

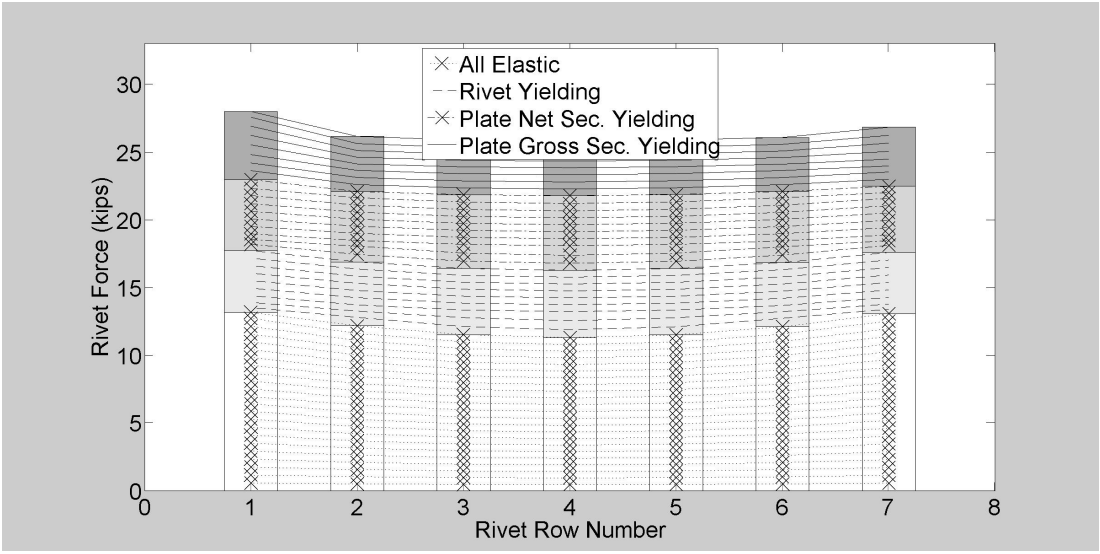

(a) Rivet force distribution along the connection length in small load increments for tapered 7 rive row specimens

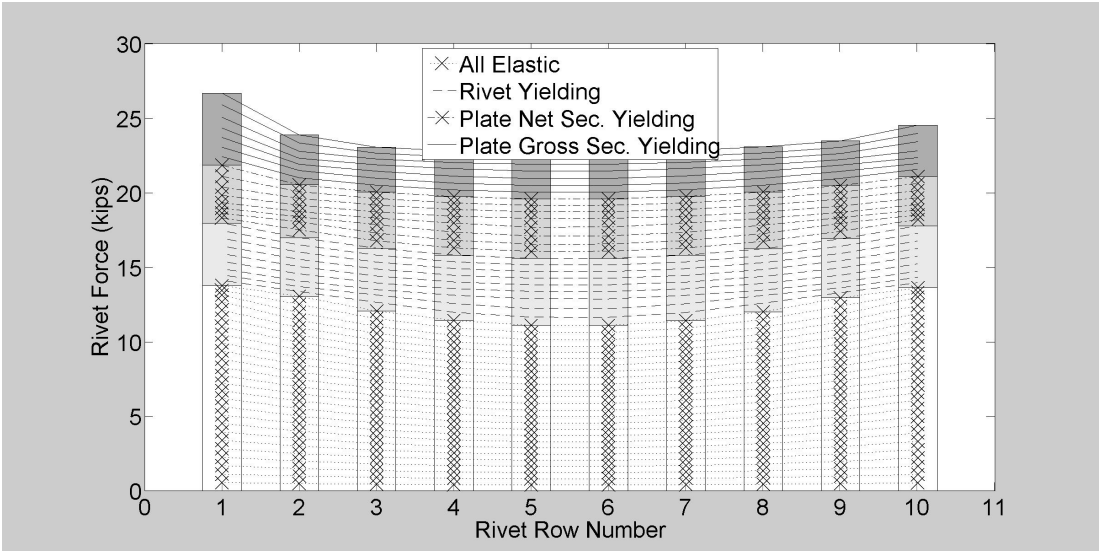

(b) Rivet force distribution along the connection length in small load increments for tapered 10 rive row specimens

Figure 8.17: Rivet force distribution in tapered specimens

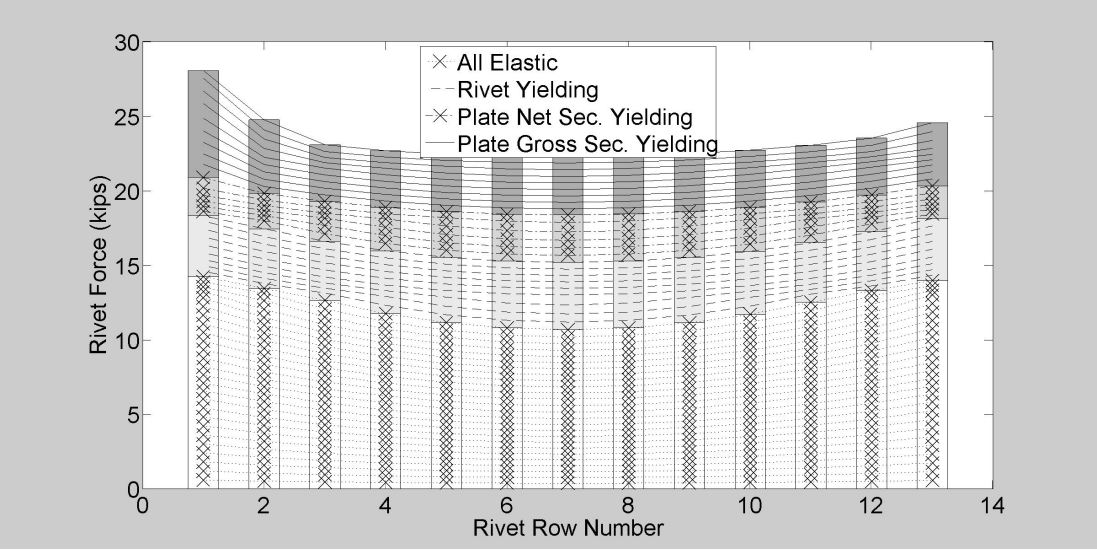

(c) Rivet force distribution along the connection length in small load increments for tapered 13 rive row specimens

Figure 8.17: Rivet force distribution in tapered specimens

8.3.6 Experimental Results for Strong Plate and Weak Plate conditions

Experimental results from literature also support that the joints with "Strong Plate" and "Weak Plate" perform different behaviors. The series joints tests conducted at Lehigh University by numerous researchers were considered as "Weak Plate" condition where the connected plate yield capacity is less than the sum of the rivet shear strength. Table 8.2 listed the tests that failed in fasteners for the series joint studies and also provides a reference for each. The connected lengths, the load at rivet failure, the load at plate gross section yielding and the joints failure modes are presented in this Table. It is found that the unbuttoning failure is observed when the connected length exceeds 20 in.. Further, in these joints that had fastener failure in unbuttoning mode, the plates always yielded before the rivet failure. This supports that the notion that yielding of plates aggravate the unbuttoning failure of joints again.

In contrast to the study for "Weak Plate" condition, the study for joints in "Strong Plate"

conditions is very rare. By examining the tests conducted by Davis et al. [1940], one of his tests shows "Weak Plate" condition. Table 8.3 shows the joint failure in Davis et al. [1940]'s tests. The unbuttoning failure is observed in many joints which have connected lengths over 20 in and "Weak Plate" condition except the joints indicated by darker shading. Further observation found that in these joints, plate gross section yield capacity is larger than the ultimate loads and the joints failed without unbuttoning mode. These specimens were denoted as ASM12, ANM12, ANM24, and ANM36. The first letter of the specimen indicates the test series, the second letter of the specimen indicates material of connected plates, where N is nickel steel and S is silicon steel, and the third letter of the specimen indicates material of rivets where M is manganese steel. By using proper ultimate shear strength of manganese rivet, the unbuttoning factors for these three specimen are 0.9, 0.93, 0.96, and 0.94.

In other words, when these joint tests failed in fasteners, the plates were in an elastic state and all the rivets were sheared altogether without the unbuttoning failure mode even though the joints had long connected length. By calculation, it is found that in these cases, the loads at joint failure are above 90% of the sum of rivet shear resistance. This result is consistent with the analytical study of the enlarged area specimen in previous section, where the 0.9 reduction factor is considered. This means that for joints that have a fastener shear strength that is less than the gross section yield strength of the connected elements, the fastener capacity need not be dramatically reduced for the long connection effect.

8.3.7 Discussion of Reduction Factor for Connected Length

Fisher et al. [1963] used the unbuttoning factor to indicate the joint shear resistance to the sum of the fastener shear strength. This unbuttoning factor was used as a reduction factor considering the connection length effect for a joint shear resistance in current code (AASHTO [2011]). The unbuttoning factor for the tests conducted by Dlugosz [1962], the reduction factor of the AASHTO code, the unbuttoning factor for the enlarged specimens and tests conducted by Davis et al. [1940] are shown in Figure 8.18. The reduction factor

of the AASHTO code is calculated by $1 - \frac{0.25L}{50}$ and uses factor 0.75 when the connected length over than 50 in.. Apparently, the current code is not enough to describe two different conditions "Weak Plate" and "Strong Plate". The current code is not conservative for the specimen with "Weak Plate" such as results from Dlugosz [1962] and is overly-conservative for the specimen with "Strong Plate" such as results from Davis et al. [1940] and enlarged specimen studied analytically.

Therefore, it is recommended for "Weak Plate" condition, since the plate yield governs the capacity of the joint, no reduction factor is required. For the "Strong Plate" condition, a 0.9 reduction factor can be applied to reduce the joint shear resistance.

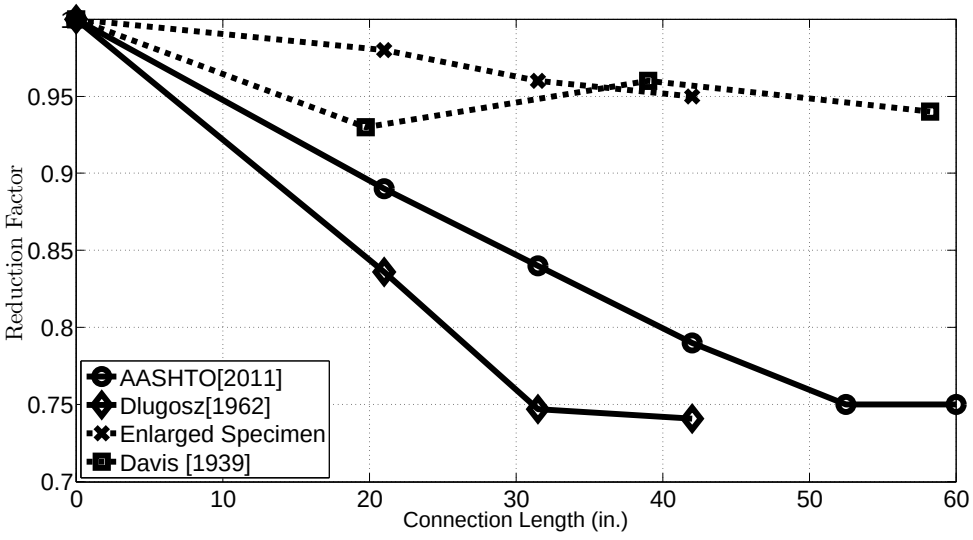

Figure 8.18: Reduction factor from code, test results and analytical study

8.4 Comparison with Current Design Code Requirements

The treatment of the long connection effect in current design and evaluation codes was described in this section. A conservative reduction factor, 0.9 for the long connection effect considering yielding limit of the connected members is applied to the joint shear resistance and the code requirements are compared with that. *The Manual for Bridge Evaluation*

2011 Interim Revisions Section 6A.6.12.5 AASHTO [2011] is used for the discussion.

For AASHTO [2011], shear resistance for a ASTM 141 rivet is:

$$R_n = \varphi_s F_u R_1 R_2 R_3 m A_r \tag{8.1a}$$

where φ_s is resistance factor for rivet in shear, taken as 0.8, R_1 ratio of shear/tensile strength, taken as 0.67, $\varphi_s F_u R_1$ for A141 rivet is taken 32 ksi, R_2 is a adjustment equation of the reduction factor for connection length less than 50 in., take as $1 - \frac{0.25L}{50}$, m is number of fraying surface, R_3 is reduction factor for undeveloped filler plate, taken as 1.0 when no filler plate presents, and Ar is rivet area for the undriven nominal diameter. When connection length is over than 50 in., a constant reduction factor 0.75 is used
Thus for A A141 rivet, a single plane factored shear resistance will be

$$R_n = 32(1 - \frac{0.25L}{50})A_r \tag{8.1b}$$

$$R_n = 24A_r \; when \; L \geq 50in. \tag{8.1c}$$

Assume a gusset plate connection on a steel truss bridge connects an diagonal member with connected length 52.5 in. The diagonal is made of built-up box shape with material of 36 ksi yield stress and a gross cross sectional area is 60 in.^{2}. The gusset plates are made steel with a 36 ksi yield stress and are 1/2 in. thick. The built-up box is connected to the gusset plates using 5/8 in. rivets with 3.5 in. spacing in the long and short connection directions. The rivet pattern is rectangular and includes 16 rivets in the long direction and 6 rivets in the short direction. The capacity of the joint can be calculated by the following:

The factored yield capacity of the built-up box is

$P_r = \varphi_y A_g F_y$

$P_r = 0.95 A_g F_y = 0.95 \times 36 \times 60 = 2025$ kips

The factored yield capacity of the gusset plate using Whitmore width is

$P_r = \varphi_y A_w F_y$

$P_r = 0.95 A_w F_y = 0.95 \times (3.5 \times 15 \times \tan 30^\circ \times 2 + 17.5) \times (2 \times \frac{1}{2}) \times 36 = 2671$ kips

The factored net section fracture resistance of gusset plate of the built-up box is

$P_r = \varphi_u P_{nu} = 0.8 F_u A_n U$

$P_r = 0.8 \times 58 \times (3.5 \times 15 \times \tan 30^\circ \times 2 + 17.5 - (\frac{5}{8} + \frac{1}{8}) \times 6) \times (2 \times \frac{1}{2}) \times 1 = 3416$ kips

The joint shear resistance using Eq. 8.1c for considered shear planes will be:

$R_n = 24 A_r N_s$

$R_n = 24 \times (0.306) \times (6 \times 16 \times 2) = 1410$ kips

By the regulation, the rivet shear resistance will govern the joint capacity and the capacity is 1410 kips. However, if the gross section yielding of the connected member is considered, the rivet shear resistance would not be reduced dramatically by 0.75 and a conservative 0.9 factor can be applied to the original capacity. The joint capacity would be

$R_n = 0.9 \times 32 A_r N_s$

$R_n = 0.9 \times 32 \times (0.306) \times (6 \times 16 \times 2) = 1692$ kips

Although the joint shear resistance still gonverns the joint capacity, the capacity is raised about 20%.

8.5 Summary

In this chapter, the evaluation equations for joint fastener shear resistance have been reviewed considering the shear strength of fasteners and the long connection effect. The tests on previously in service older rivets demonstrated that the rivet shear strength had insignificant deterioration after decades of service. The visible corrosion at the levels documented was found to only slightly affect the shear strength. Considering that the riveting procedure, and the difference between rivet strength in single versus double shear might increase rivet shear strength, the shear strength suggested in current regulations is reasonably conservative.

The joint fastener shear resistance is determined by four factors, fastener strength, fastener ductility, connection length, and yielding of connected member. The long connection effect is currently considered by AASHTO in the evaluation of fastener shear resistance regardless

of whether the joint is short or long. Literature review showed that the long connection effect may be observed even when the joint is in the range of 20-30 in. long. However, the current code only consider the first three factor in evaluating joint fastener shear resistance, neglecting the impact of stress in the connected member, i.e. yielding of connected member. In this study, it was found that the long connection effect was insignificantly when the connected element is elastic but the rivet is yielded and after the connected element yields over the gross section, it causes exaggerated deformation of the yielded rivets at the end of the joint and their early failure. The joint shear resistance for "Weak Plate" and "Strong Plate" conditions, indicating the different stress states in the connected member, shall be clearly separated.

A reduction factor, 0.9, for fastener shear resistance in "Strong Plate" condition is proposed to provide a more accurate assessment of the fastener shear resistance in a joint. For the joint shear resistance calculated larger than yield capacity of connected member, "Weak Plate" condition, the joint capacity is governed by the connected element yield capacity and no further reduction is required for the joint shear resistance.

Table 8.2: Joints that failed by rivet shearing from the series tests at Lehigh University

Reference	Joint type	Specimen no.	Length (in)	Rivet fail (kips)	Plate yield (kips) [1]	Fail mode
Foreman and Rumpf [1958]	Compact joint, A7 plates and A 325 Bolts	B3	10.5	1750	1188	all bolted sheared
		B5	14	1680	1188	unbuttoned
		B6	7	1550	1188	unbuttoned
		BR2	14 [2]	1300	1188	shear of rivets
Bendigo and Rumpf [1960]	Compact and long joint with A7 plates and A 325 Bolts	D71	21	1126	734	all bolts shear
		D81	24.5	1286	822	unbuttoned
		D91	28	1358	909	unbuttoned
		D101	31.5	1506	997	unbuttoned
		D701	21	1213	776	unbuttoned
		D801	24.5	1313	854	unbuttoned
		D901	28	1497	978	unbuttoned
		D1001	31.5	1667	1102	unbuttoned
		B3	10.5	1750	1188	all bolts sheared
		B5	14	1680	1188	unbuttoned
		B6	7	1550	1188	unbuttoned
		A3	10.5	1820	1188	all bolts sheared
		G1	7	1798	1188	all bolts sheared
Hansen and Rumpf [1960]	Long joint A7 plates and A 325 Bolts	D10	31.5	1544	1115	unbuttoned
		D13A	42	1988	1382	unbuttoned
		D13	42	1854	1382	unbuttoned
		D16	52.5	2085	1640	unbuttoned
Dlugosz [1962]	Long joint A7 plates and A 141 Rivets	DR71	21	738	560	unbuttoned
		DR101	31.5	942	734	unbuttoned
		DR131	52.5	1216	909	unbuttoned
Fisher et al. [1963]	A440 plates fastened with A325 Bolts	E41b	10.5	754	554	all bolts sheared
		E41c	10.5	770	570	all bolts sheared
		E41e	10.5	782	618	all bolts sheared
		E41f	10.5	727	575	all bolts sheared
		E41g	10.5	767	577	all bolts sheared
		E41	10.5	728	579	all bolts sheared
		E71	21	1188	884	unbuttoned
		E101	31.5	1610	1193	unbuttoned
		E131	42	2125	1655	unbuttoned
		E161	52.5	2545	1968	unbuttoned
		E46	10.5	2180	1749	all bolts sheared
		E74	21	2410	1760	unbuttoned
		E741	21	2250	1776	unbuttoned
Sterling and Fisher [1965]	Long joint A440 plates and A 325 Bolts	E721	21	1070	739	unbuttoned
		E722	21	1270	1033	unbuttoned
		E163	52.5	2180	1651	unbuttoned
		E164	52.5	2785	2308	unbuttoned
Sterling and Fisher [1965]	Long joint A440 plates and A490 Bolts	K42a	10.5	980	667	all bolts sheared
		K42b	10.5	980	689	all bolts sheared
		K42c	10.5	996	705	all bolts sheared
		K42d	10.5	1004	730	all bolts sheared
		K131	42	1425	1039	unbuttoned
		K132	42	1312	1036	unbuttoned
		K133	42	1660	1454	unbuttoned
		K191	63	1794	1436	unbuttoned

[1] 33 ksi is used for A7 yielding stress and 43 ksi is used for A440 yielding stress

[2] Bolts were replaced by A141 rivets

Table 8.3: Joints that failed by rivet shearing from the series tests by Davis et al. [1940]

Specimen no.	Joint Type	Length (in)	Rivet fail (kips)	Plate yield (kips)	Ratio of ultimate/plate-yield load	Fail Mode[1]
ACC18 [2]	Lap type splice	28.5	787	650.844	1.21	y
ACC36		56.5 [3]	1446	1252.852	1.15	y
ACC54		84.5	2120	1929.812	1.10	y
ASC18		23.5	775	708.564	1.09	n
ASC36		46.5	1525	1337.248	1.14	y
ASC54		69.5	2166	1994.475	1.09	y
ACM12		19.75	715	641.124	1.12	n
ACM24		39	1460	1255.428	1.16	y
ACM36		58.5	2017	1894.604	1.06	y
ASM12		19.75	682	696.681	0.98 [4]	n
ASM24		39	1470	1317.437	1.12	n
ASM36		58.25	2054	1989.699	1.03	y
ANM12		19.75	704	735.84	0.96	n
ANM24		39	1464	1505.16	0.97	n
ANM36		58.25	2140	2164.215	0.99	n
BCC20a		19	975	731.718	1.33	n
BCC20b		26.5	1013	756.387	1.34	y
BCC20c		34	988	762.228	1.30	y
CCC7		10	358	330.004	1.08	y
DCC7		8	623	496.111	1.26	n
FSCB	Butt and shingle type splice	63.25	1850	1435.2	1.29	y
FSCD		63.5	1799	1415.367	1.27	y
FSCC		84.25	2660	2215.29	1.20	y
FSCE		87.75	2688	2135.56	1.26	y
FSCF		66.5	2652	2117.165	1.25	y

[1] y: unbuttoning fail mode; n:all rivet sheared

[2] ACC, first letter indicates test series, second letter is the initial of the plate steel (carbon, silicon, or nickel), and the third letter indicates the initial of the rivet steel (carbon or manganese).

[3] When connections become longer ($\geq 20in$), unbuttoned phenomenon are almost observed except the cases marked by red background color

[4] When rivets failed and plates are not yielded, no unbutton phenomenon observed

Chapter 9

DISCUSSION OF GUSSET PLATE LOAD RATING: TRIAGE EVALUATION PROCEDURE, REFINED EVALUATION PROCEDURE, AND RIVET CONNECTION STRENGTH

The Triage Evaluation Procedure (TEP) and the Refined Evaluation Procedure (REP) are used to evaluate gusset safety sequentially as a two step evaluation procedure. The TEP is derived using conservative assumptions of gusset plate geometry and loading profiles to estimate the onset yielding of gusset plate and may underestimate gusset plate initial yield capacity. The application of the TEP under bridge load rating evaluation frame resulted in three out of thirty five joints had a rating factor smaller than 1.0 in Service II load limit state as shown by Olson [2010]. These results indicated that these three joints may have some yielding in the gusset plates under this load limit. However, the FEA results of these joints under this load limit showed no yielding area observed in these gusset plates. Therefore, the REP is applied to re-examine the maximum stress in these gusset plates as a second step (after the TEP) as it removes many of the conservative assumptions used in the TEP.

More joints had rating factors smaller than 1.0 because the rivet shear resistance was indicated to be insufficient in the load rating procedure using the recommended rivet shear strength and reduction factor for the joint connection length effect in AASHTO [2007] (Olson [2010]) . However, these joints had been in service for decades and the investigation by Olson [2010] showed that the recommended rivet shear strength is too conservative to precisely reflect the real joint shear resistance. The recently published "The Manual for Bridge Evaluation 2011 Interim Revisions" (AASHTO [2011]) has increased the recommended rivet shear strength and revised the reduction factor for joint connection length. This revision of rivet shear resistance has removed much of the overly-conservative evaluation in the load

rating procedure for the joint shear resistance in the evaluation of Washington Bridges by Olson [2010]. Though the increased rivet shear strength seems to have resolved the most urgent issue in the gusset plate load rating procedure, the confused mix of conservative rivet shear strength and underestimating the joint connection length effect in the current code as discussed in Chapter 8 may still result in overly-conservative evaluation when the riveted joint has long connection length. An example of overly-conservative estimate of shear resistance for a riveted joint was discussed at the end of Chapter 8.

9.1 Application of the TEP and REP for Joint L9 Gusset Plate

Three joints indicated by Olson [2010] that have rating factor less than 1.0 in service II load limit state are BR 101-217 Joint L3 which was specified mill-to-bear at chord splice, BR 101-217 Joint U2 which has chord splice away from the interference zone in the gusset plates, and BR 31-36 Joint L9 which has equal and opposite diagonal loads and shows conservative estimate in the interference zone. The previous two joints are related to the location of chord splice. For Joint L3, the "mill-to-bear" for two compressive chord at the chord splice can be neglected from the check procedure since the force is directly transfered from one chord to another. For Joint U2, the REP has been verified as being able to estimate stress at the chord splice accurately in Section 7.13, which used Joint U3 as an example. Joint L9, however, which has the geometric configuration and load distribution close to the TEP assumptions, which is the worst case scenario of stress interaction in the interference zone, shows a conservative estimate in the load rating evaluation. To avoid complex finite element analysis or reinforcement of the joint, the REP can be applied to re-examine the stress status in Joint L9 to determine the safety of this joint. The procedure of the TEP and the REP applied to Joint L9 are demonstrated in this section.

The Rating Factor (RF) less than 1.0 indicates that the Joint L9 gusset plate may be yielding. The REP is used to calculate the Von Mises stress in the Joint L9 gusset plates and to identify the magnitude and the location of the maximum stress. The procedure is presented here.

The AASHTO MBE-LRFR load rating equation has been shown as Eq. 4.1 in Chapter 4 was again given in Eq. 9.1. The Service II load limit is considered for the application. The dead load and live load for the Service II limit load in Joint L9 were cited from Olson [2010] and listed in Table 9.1. The factored load in Table 9.1 is calculated using Eq 9.1 assuming that RF is equal to 1.0 when Service II limit load are applied so the factored load would be $1.0 \times DL + 1.3 \times LL \times (1 + 0.33)$. The capacity $\phi_c\phi_s\phi R_n$ using the TEP is considered as $0.95 \times 0.9 \times 1.0 \times \frac{33}{\sqrt{3}}$, where the 33 is yield stress of the gusset plates. Since $\gamma_{DC} = \gamma_{DW} = 1$, the dead load effect is calculated by the dead load divided by the Whitmore section. The live load effect is calculated by $1.3 \times 1.33 \times$ Whitmore stress. The area of the Whitmore section for each connected member in the gusset plate were listed in Table 9.1. The Rating Factors (RFs) evaluated using Eq. 9.1 for the TEP and the FHWA are both listed in Table 9.1. The FHWA considers the capacity of gross section yielding, and net section rapture using Whitmore section, and shear resistance along the horizontal section.

$$RF_{AASHTO\_LRFR} = \frac{\phi_c\phi_s\phi R_n - \gamma_D DC - \gamma_{DW} DW}{\gamma_{LL}(LL + IM)} \tag{9.1}$$

where $\phi_c = 0.95$, $\phi_s = 0.9$, $\phi = 1.0$, $R_n = \frac{F_y \times \text{Whitmore Area}}{\sqrt{3}}$, $\gamma_{LL} = 1.3$, $\gamma_{DC} = 1.0$, $\gamma_{DW} = 1.0$, DC is the component dead load effect, DW is the wearing surface dead load effect, LL is live load effect and IM is the dynamic impact allowance which can be represented as 0.33 times live load effect.

It was found that the chord member (L8) provides the smallest RF less than 1.0, indicating the onset of yield might be observed here. To verify the stresses on the gusset plate, the REP is applied to find the maximum stress and its location. The REP calculates each stress distribution along the horizontal and vertical critical sections in the Joint L9 gusset plates as described in Chapter 7 and the FEA results for each stress distribution are shown in Figure 9.2. The combined Von Mises stresses for each high stress point are calculated and shown in Table 9.1 with the comparison of the stress range from the FEA. The Von Mises contour as shown in Figure 9.1 shows nowhere in the gusset plate is the stress over the yield stress, which is 33 ksi in Joint L9 gusset plates. The result of the REP shows that the maximum

stress in the gusset plate is about 24 ksi at Point 2 or 5 which is consistent with the FEA results. The comparison of the results from the REP and the FEA results indicates that the REP predicts the magnitude and location of the maximum stress precisely and removes the overly-conservative estimate from the TEP.

However, the REP is difficult to apply within the load rating equation because the load rating equation assumes that the dead load effect and live load effect can be superimposed to gain a total effect, which is not true for the Von Mises stress in the gusset plates. The dead load effect and live load effect from each member acting on the gusset plate are different and the Von Mises stress is not a linear combination of the stress, i.e. the Von Mises stress calculated from dead load plus the Von Mises stress calculated from live load does not equal the Von Mises stress calculated by applying the dead load plus live load. Therefore, the ratio of capacity to demanding is considered and listed in the last column of Table 9.1. The capacity is the yield stress of the gusset plate and the demand is the stress at the high stress point. The results show that under the Service II limit load, the worst case still has capacity higher than demand.

Table 9.1: Triage Evaluation Procedure for Joint L9

	Dead Load (kips)	Live Load (kips)	Factored Load (kips)	Whitmore area ($in.^2$)	TEP Rating Factor (RF)	FHWA RF
L9-L8	-309.17	-134.91	-543.4	30.1	0.78	0.95 controlled
L9-U8	248.2	103.56	421.5	33.7	1.68	by horizontal
L9-U9	-47.67	-16.78	-74.4	32.3	16.51	shear capacity
L9-U10	-235.49	-106.54	-423.2	32.1	1.56	
L9-L10	0	0	0	25.2	N.A.	

Table 9.2: Peak stress at critical points in Figure 9.1

Locations	σ_X	σ_Y	τ_{XY}	Von Mises	FE Analysis	Capacity/Demand
1	-18.7	0.0	0.0	18.7	15-18	1.7
2	-14.4	-5.6	-12.1	24.4	24-27	1.35
3	0.0	10.0	-9.4	19.1	21-24	1.72
4	0.0	-8.5	-12.1	22.6	18-21	1.46
5	0.0	0.5	-13.9	24.1	24-27	1.37
6	0.0	-3.1	-11.1	19.5	21-24	1.69
Whitmore 7	N.A.	N.A.	N.A.	12.5	15-18	2.64
Whitmore 8	N.A.	N.A.	N.A.	13.2	21-24	2.5

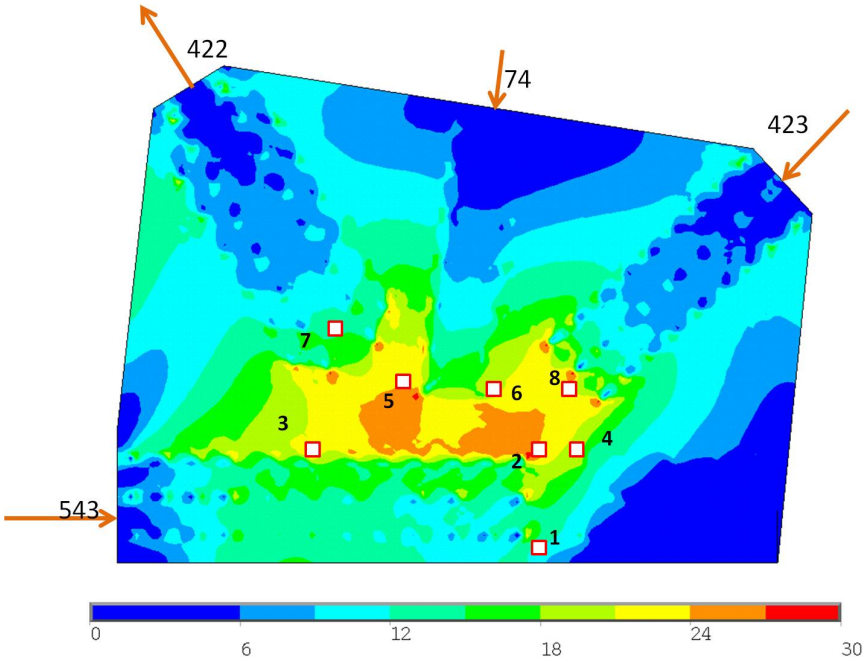

Figure 9.1: Von Mises stress contour of joint L9 and possible high stress locations

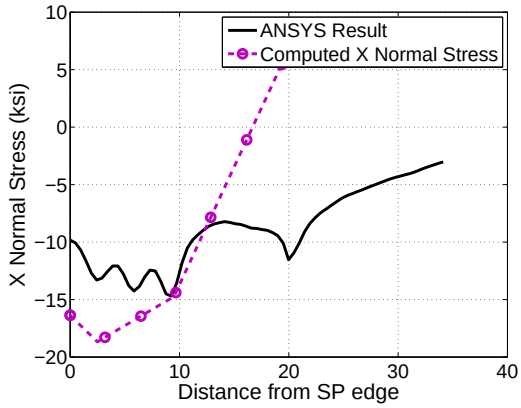

(a) X-direction normal stress at the chord splice

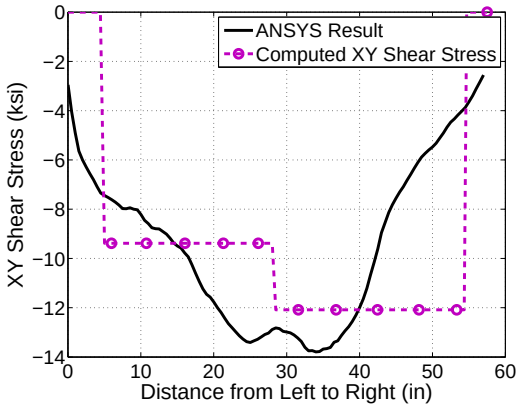

(b) XY shear stress at the horizontal section

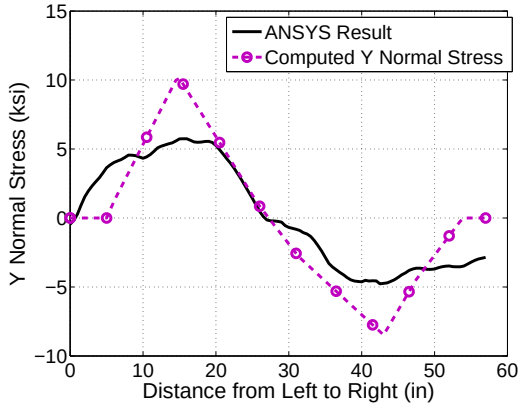

(c) Y-direction normal stress at the horizontal section

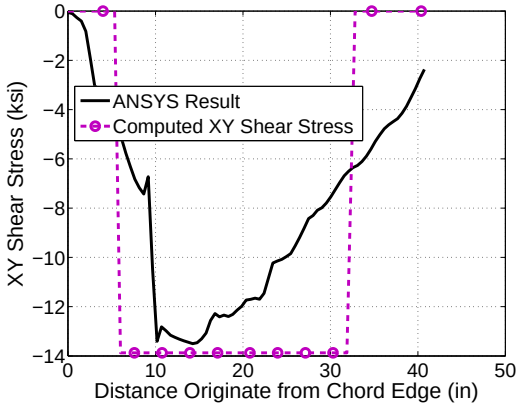

(d) XY shear stress at the left vertical section

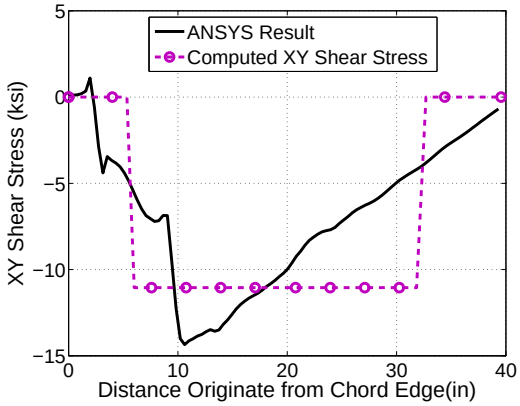

(e) XY shear stress at the right vertical section

Figure 9.2: Individual stress distributions on critical sections and comparison with the FEA results

Chapter 10

SUMMARY, CONCLUSIONS, AND RECOMMENDATION FOR FURTHER RESEARCH

10.1 Summary

This dissertation described an analytical investigation of the behavior of steel truss bridge gusset plate connections aimed at improving our understanding, developing a more rapid procedure for identifying potentially insufficient gusset plates in existing structures and assessing the adequacy of current evaluation procedures. First, a robust method for modeling gusset plate connection subassemblages using finite elements was developed and subsequently used to develop detailed models of several connection geometries. This method models gusset plates and connected members with shell elements and extends connected members to the next gusset plate joint with beam elements. The interface of the shell elements and the beam element for each truss member is formed by constraining edge nodes of the shell element to the end node of the beam element. The axial loads from connected members are applied to the node of the extended member and other degrees of freedom of this node are restrained. The rivets are constrained such that all degrees of freedom of the coincident nodes at the gusset plates and connected members are equal. A mesh refinement study showed the 0.5 in. edge length is sufficient to produce accurate stress distributions along the critical sections in gusset plates. Either a floor beam load is placed on the gusset plate attachments or linear buckling analysis is conducted to generate slight imperfections for the gussets to initiate buckling. This modeling method was found to provide good results when compared with experiments and simulations by others and reduces modeling time relative to modeling with solid elements.

Finite element models were then developed for several joints from bridges in Washington State and they were used to study gusset plate stress distribution. Specifically, the onset of

yielding in gusset plates caused by the interaction of stresses generated by various connected truss members was studied for several joint geometries. A procedure for rapidly assessing whether gusset plates are yielding, denoted the Triage Evaluation Procedure (TEP), was developed and was shown to be conservative relative to the current evaluation procedures and also can use envelope truss member loads rather than point-in-time loads which eliminates the need to check many different load cases for each joint. The TEP was found be overly conservative in some cases where the chord splice was positioned outside the interference zone, an area enclosed by the ends of the diagonals, prompting a more detailed investigation of the stress distribution along critical sections of the gusset plate.

The FE models were then used to examine the elastic stress distributions at critical sections of the gusset plate and how those are influenced by variations in gusset plate geometry and truss member load distributions. From these observations, a more detailed procedure, meant to be employed on joints that failed the TEP, to estimate the magnitude and location of the maximum stress in truss bridge gusset plates was developed. When compared to analytical results, the Refined Evaluation Procedure (REP) was found to be quite accurate in predicting the maximum stress and its location for a range of gusset plate geometries and load distributions providing a more refined method for evaluating gusset plate yielding for joints that fail the TEP.

Finally, the behavior of long riveted connections was studied to evaluate current methods of reducing the strength of such connections based on their length. To do this, an analytical model including fastener nonlinear behavior and rivet holes was developed and validated against experimental results conducted from Jost (2011). Individual rivet behavior was simulated using data from experimental results for single rivet tests described in this document. The calibrated models were used to study the behavior of joints with different connection lengths and develop recommendations for modifications to the current approach for accounting for the effect of length on connection strength.

Overall, the research described in this dissertation has contributed the following: 1) a method for analyzing gusset plate connection subassemblages using finite elements, 2) the Triage Evaluation Procedure to rapidly assess yielding in the interference zone of gusset

plate connections, 3) the identification of the normal and shear stress components generated by the particular connected member forces at critical gusset plate sections and the development of approximate stress distribution models at these sections, 4) the Refined Evaluation Procedure to calculate the maximum equivalent stress in a gusset plate and identify its location, 5) experimental results for single rivets with moderate corrosion levels loaded in single shear that were used to generate a fastener nonlinear behavior model, and 6) a recommendation for revisions to the current approach to reduce connection shear strength based on connection length.

10.2 Conclusions

The following conclusions and recommendations are drawn from the studies described in this dissertation. They are organized into subheadings that represent the major areas of research findings.

10.2.1 Gusset Plate Subassembly Modeling Methodology

The finite element modeling method to simulate gusset plate joint subassemblages that includes proper treatment of boundary conditions was verified to produce reasonable results for internal gusset plate stresses a small distance away from the rivets and was found to be applicable for studying gusset plate behavior. Analysis results compared well with experimental results from the literature and analysis results by others.

10.2.2 The Triage Evaluation Procedure for Predicting the Onset of Gusset Plate Yielding

The Triage Evaluation Procedure (TEP) was developed to rapidly identify the gusset plate at risk. The TEP considers the worst-case scenario for interaction of the stresses in the interference zone and can be applied to the enveloped forces of a joint without calculating concurrent loads for a gusset plate joint which is difficult due to moving live load considerations in bridges. The TEP was verified to conservatively predict the onset of gusset plate

yielding and work within the context of current bridge load rating procedures to assess the safety of gusset plate connections. It was found that for some gusset plate geometries, the TEP may be overly conservative when the initial yielding is not in the interference zone.

10.2.3 The Refined Evaluation Procedure for Gusset Plate Stress Estimate

The Refined Evaluation Procedure (REP) uses approximate stress distributions along critical sections of the gusset plate and then combines them to approximate and locate the maximum gusset plate stress. The following conclusions include the approximate stress distributions at those critical sections which were based observations of gusset plate stresses from many analyses considering truss member loading variations and different chord splice locations. They were compared with FEA results for many different gusset plate configurations and found to agree well.

10.2.3.1 The Approximation of the Normal Stress Distribution at the Chord Splice

A trapezoidal stress distribution that includes the consideration of axial force and bending moment was developed to estimate the elastic stress distribution at the chord splice. The Whitmore method was found to drastically under-predict the maximum stresses at chord splices because of the asymmetry of such connections. Two important traits of the trapezoidal stress distribution model relative to the Whitmore method are: 1) a 15° dispersion angle over the connection length is proposed to replace the 30° dispersion angle from Whitmore to calculate the effective section at the chord splice, and 2) the net force, which considers the chord force and a portion of the force from the adjacent truss diagonal is used to estimate the stress at the chord splice. The portion of the diagonal force used depends on the location of the splice inside the interference zone. When the splice is at the work point of the joint the entire diagonal load is used and when it is outside the interference zone none of the diagonal load is used. Linear interpolation is used for splice locations inside the interference zone.

The trapezoidal stress distribution model was found to perform consistently well when

additional web and flange splice plates are present at the chord splice and was verified to perform well for variations in gusset plate geometry including different ratios of connected length to connected width of the chord and different gusset plate thicknesses. Modeling the flexibility of the fasteners was also included in the analytical models and the proposed distribution was still found to reasonably represent the results.

10.2.3.2 Approximation of the Stress Distribution at the Horizontal Section

The stress distributions at the critical horizontal section that were investigated include the shear stress and Y-direction normal stress.

- The shear stress at the horizontal section was found to be uniformly distributed over lengths shorter the than entire gusset plate, denoted the effective shear lengths, and was mainly governed by the diagonal forces. The uniform shear stress over the effective shear length was found to be reasonably approximated by using the horizontal component of the diagonal force divided by the effective shear length times the gusset plate thickness. The effective shear length was defined as a length on the critical horizontal section bounded by the Whitmore 30° dispersion angle from the diagonal and a vertical section through the work point of the joint. Therefore, the shear stresses at the critical horizontal section can be calculated independently from using each diagonal force and its effective shear length. This effective shear length method was found to have better agreement with the FEA results than the uniform distribution used in the current FHWA Guide or parabolic shear stress distribution that would result from an analysis considering the gusset plate in bending.

- The Y-direction normal stress distribution on the horizontal critical section was approximated by a load path model which considers triangular normal stress distributions from the diagonals and a trapezoidal stress distribution from the hanger. The approximate Y-normal stress distribution was found to provide a better estimate than using beam theory to estimate normal stresses at the horizontal critical section.

- The proposed shear and normal stress distributions at the horizontal section were

found to satisfy force equilibrium. Moment equilibrium was found to be satisfied in most cases with errors not exceeding 5% in any case discussed in this dissertation.

10.2.3.3 Approximation of the Shear Stress Distribution at the Vertical Section

Similar to the horizontal section, an effective shear length for the critical vertical section was proposed as the length along the critical vertical section confined by a horizontal line at the work point and the Whitmore 30° dispersion angle from the diagonal. A uniform shear stress distribution along the effective shear length was assumed to be generated by the vertical component of the diagonal force. Force and moment equilibrium was found to be satisfied for the critical vertical section passing through the work point. When the chord splice and critical vertical section is away from the work point, moment equilibrium was not satisfied but the increased stress due to the unbalanced moment was found to be negligible.

10.2.3.4 The Refined Evaluation Procedure to Calculate the Maximum Equivalent Stress

The maximum equivalent stress is identified by comparing the Von Mises stress at several potential high stress locations. The potential high stress points are at points along the critical sections so the equivalent Von Mises stress at these points can be calculated using the proposed approximated stress distributions along these sections. These potential high stress points include points at 1) the chord splice, 2) the intersection of the chord splice and horizontal section, 3) the intersection of the horizontal and vertical section 4) the intersection of the projection of the diagonal's corner and the horizontal section, and 5) the end of the diagonal where the stress is calculated using Whitmore's method. The effectiveness of this procedure to identify the magnitude and location of the maximum stress was verified by comparison with FEA analysis results for several actual gusset plate connections from bridges.

10.2.4 Vintage Rivet Strength and Riveted Connection Finite Element Model

The shear strength of vintage rivets tested in double shear showed that the moderate levels of rivet corrosion only slightly decreased the shear strength compared to results from similar tests on original rivets in the literature. The results suggest that the rivet shear strength used in the current AASHTO (AASHTO [2011]) is conservative despite a recent increase in those values. A rivet analytical model was developed by using uniaxial nonlinear springs to simulate the rivet shear and plate bearing, and also to simulate the void of the rivet holes. The model was verified to have good agreement with the results of joint tests conducted by Jost [2012]. The stress distributions in the connected elements a small distance away from the rivet was found to be similar and to provide sufficient accuracy regardless of the flexibility of the rivet model.

10.2.5 The Effect of Connection Length in Riveted Joints

The effect of connection length was studied using the analytical model and verified by comparison with experimental results from the literature. The analytical study showed that the relative rivet forces in different rivet rows in long connections vary at different load stages. The ductility of the rivets provides load redistribution after rivet yielding initiates. A nearly uniform rivet force distribution is found between the stages of connected member net section yielding and gross section yielding, as the rivets are deforming inelastically. After gross section yielding of the connected elements, the end row of rivets resist a much larger proportion of the load. Connection length was found to amplify the loads in the outer rivets during this final stage of loading. It was found that the shear resistance of the rivets in a joint should be reduced linearly with increasing connection length but only if the connected elements are yielding in the gross section. If the connected elements are not yielding in the gross section, a uniform reduction factor of 0.9 is suggested for the condition that the shear resistance of the rivets is less than the connected member yield capacity, the “Strong Plate” condition, and no reduction is required if the shear resistance of the rivets is larger than the connected member yield capacity, the “Weak Plate” condition, since the joint capacity

will be governed by the connected member. The proposed reduction factor is verified by the analytical results and experiments in the literature.

10.3 Recommendations for Further Research

This study has resulted in a practical and accurate analytical modeling method for gusset plate connections with flexible fasteners in steel truss bridges. The evaluation procedures to rapidly assess the gusset plate safety, estimate the maximum Von Mises stress and identify its location, predict the yield capacity at the chord splice and more accurately consider shear resistance of the fasteners at the connection have also been developed. The analytical modeling method and the evaluation procedures can be advanced further by:

- Inclusion of the line search algorithm in the solution of procedure for the analytical model to enable the prediction of gusset plate buckling. Using Newton-Raphson algorithm with line search is shown to be able to predict gusset plate buckling in the Appendix. More experimental studies are needed to verify the robustness of the analytical buckling study. With the insight of the stress distributions in the gusset plate connection and the buckling capacity predicted by the analytical model, an evaluation procedure for gusset plate buckling capacity can be developed that considers the impact of the gusset plate stress state on buckling.

- Inclusion of a fracture model in the finite element models to analytically predict fracture initiated at the rivet holes. The method of modeling rivets with flexible springs and simulating the rivet holes can be advanced with the consideration of fracture criterion to predict the fracture behavior of the connected elements in regions of high plastic strain. Experiments may be needed to verify the analytical model with the fracture criterion. The evaluation procedure for block shear capacity can be developed from the analytical results using this model. Of particular concern is the block shear capacity of the tension chord connections where the tensile stress is not uniformly distributed among the end row of the rivet holes and a reduction factor on the block shear strength might be needed.

Appendix A

RIVET EXPERIMENTAL DATA

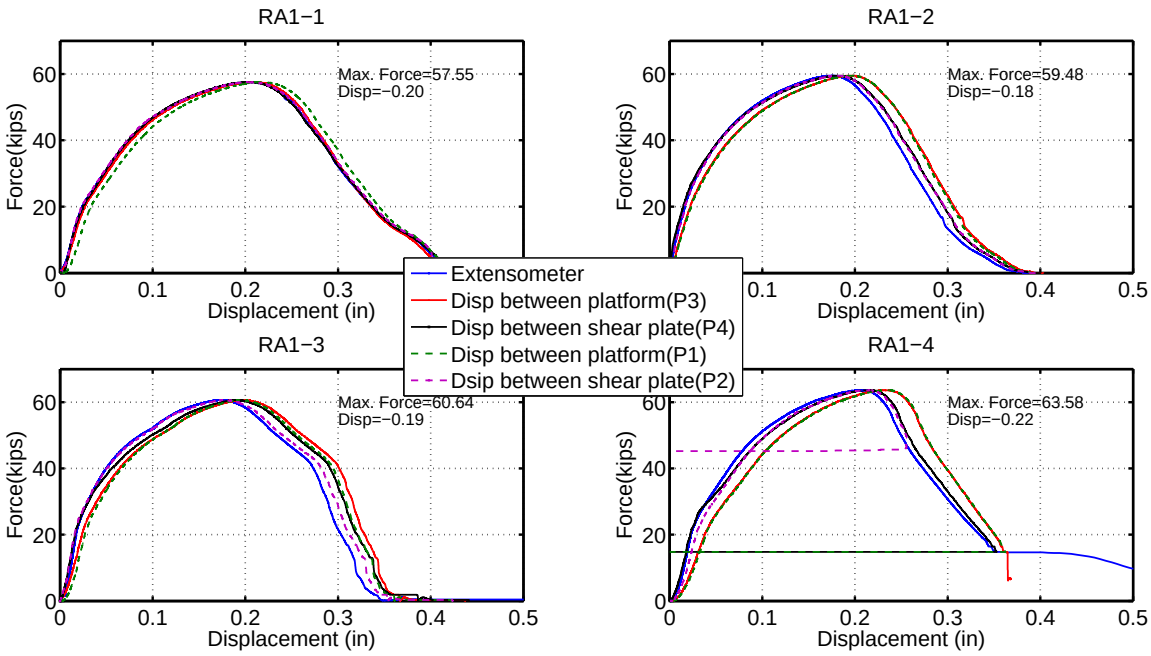

Figure A.1: Load and shear deformation curves for rivet group RA1

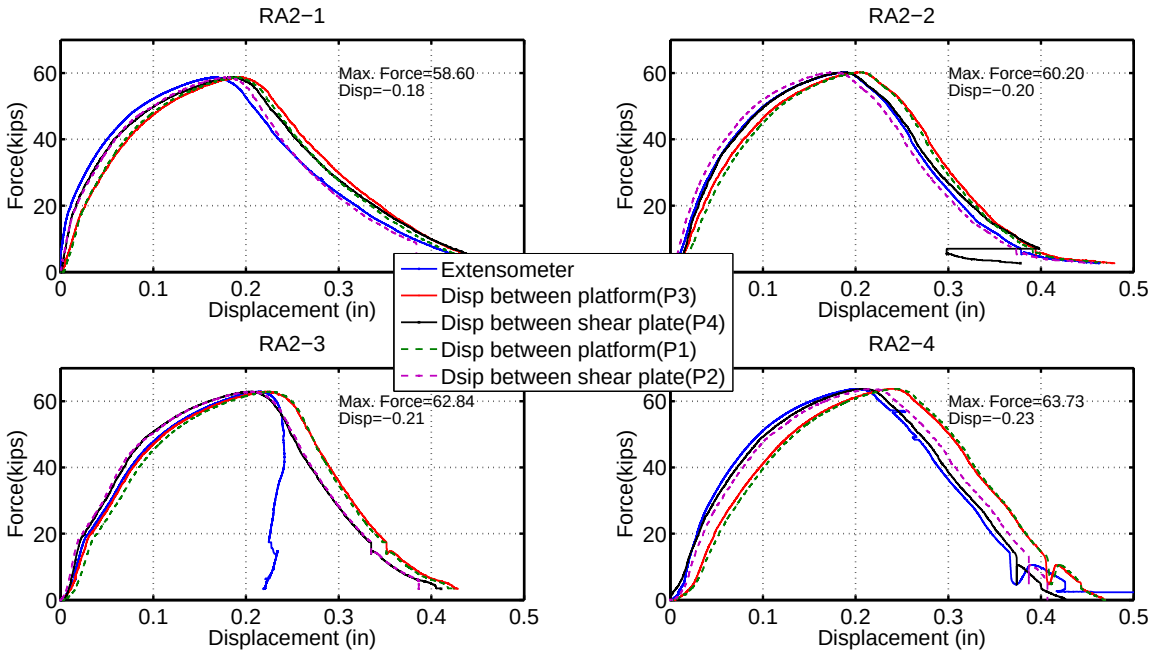

Figure A.2: Load and shear deformation curves for rivet group RA2

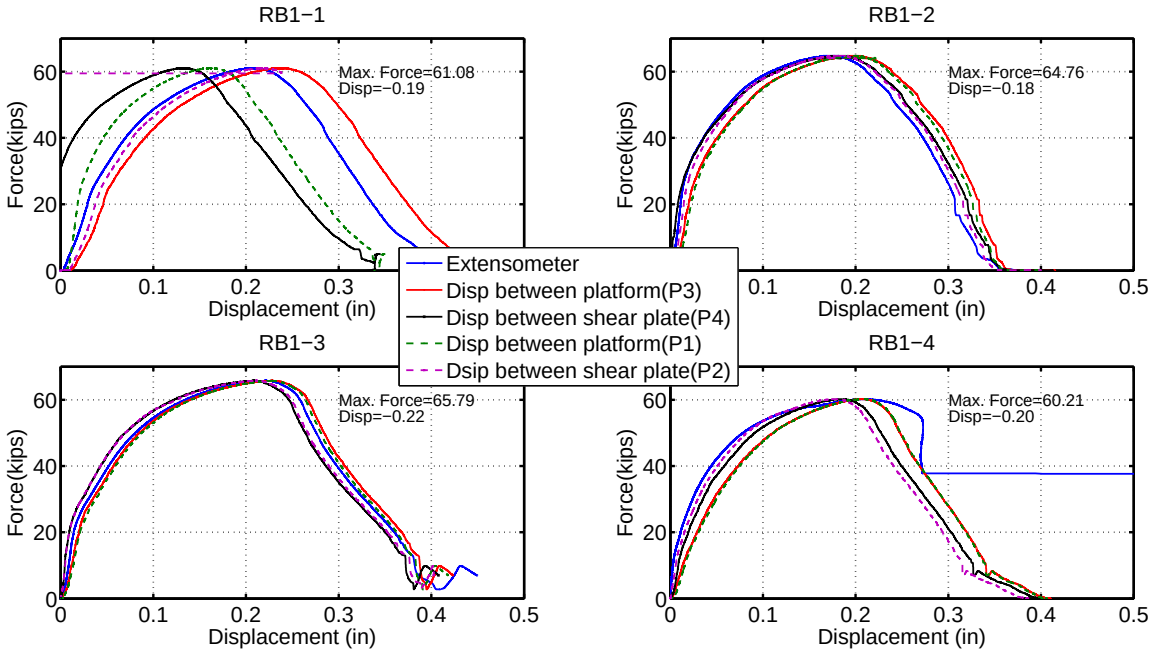

Figure A.3: Load and shear deformation curves for rivet group RB1

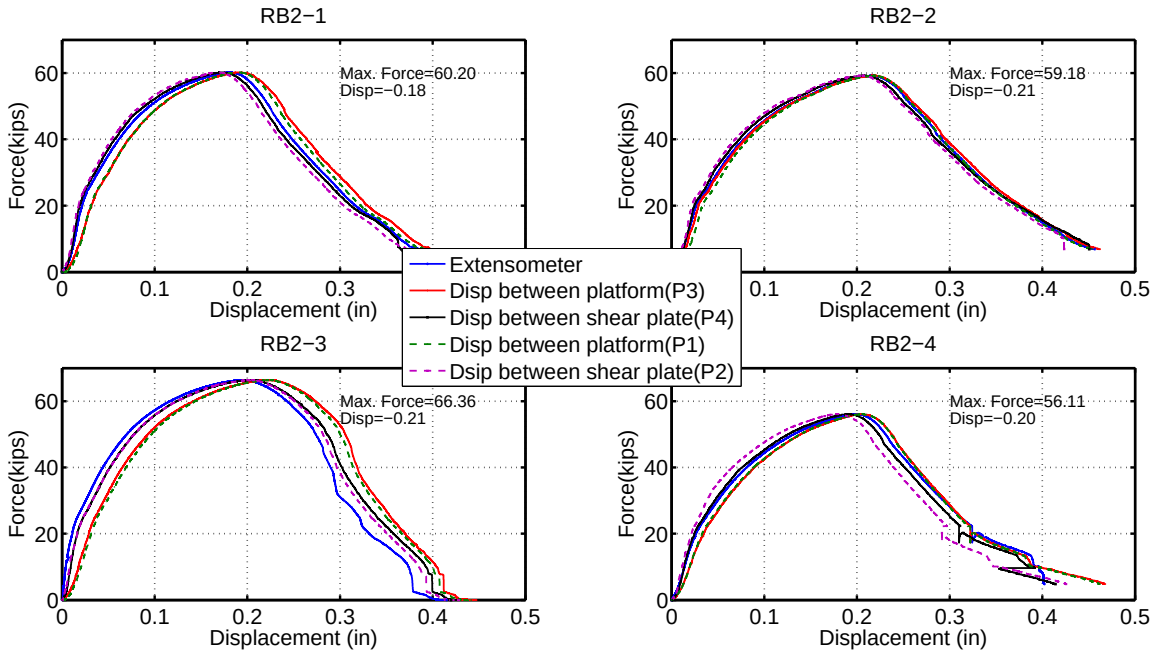

Figure A.4: Load and shear deformation curves for rivet group RB2

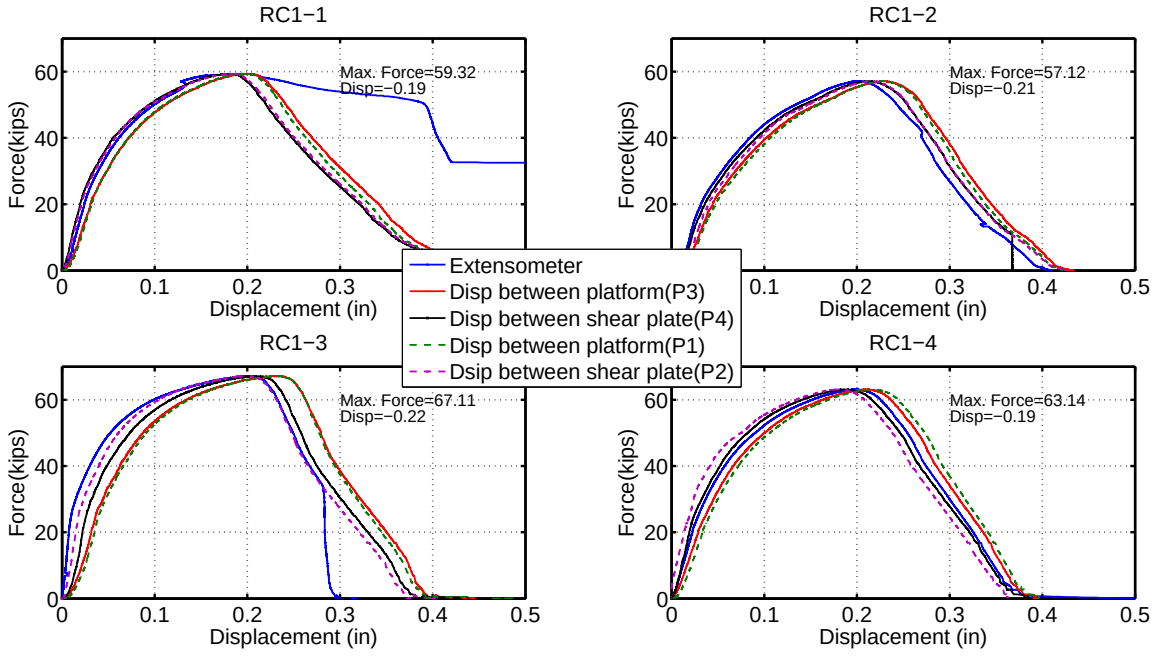

Figure A.5: Load and shear deformation curves for rivet group RC1

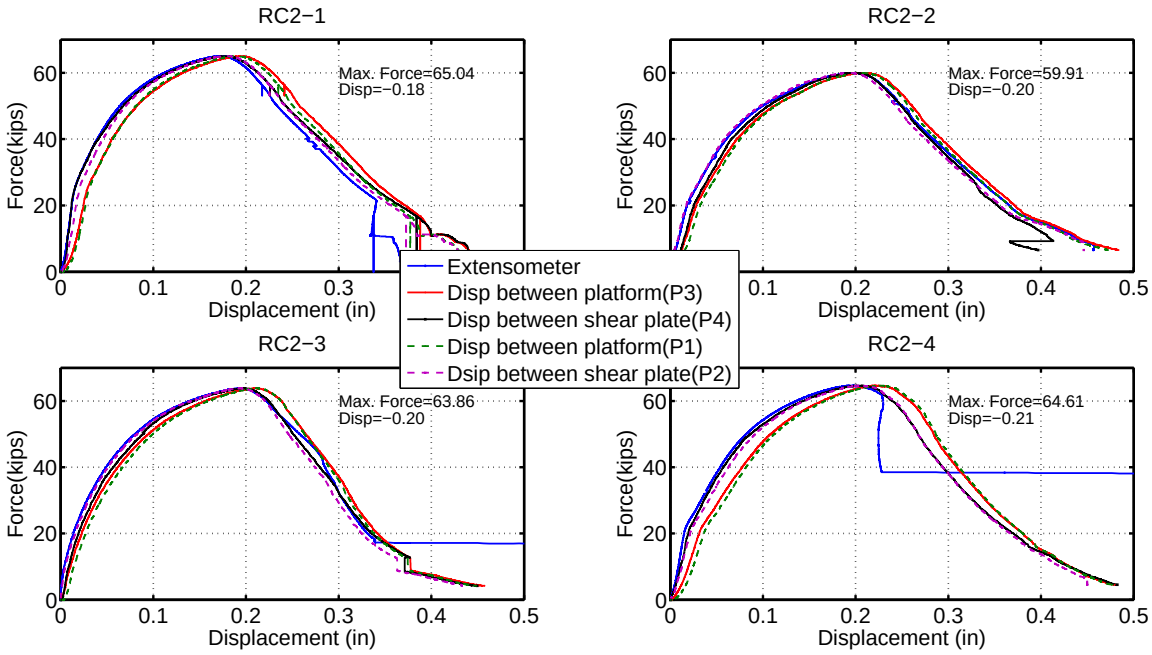

Figure A.6: Load and shear deformation curves for rivet group RC2

Table A.1: Rivet Properties for group RA

	RA1-1					RA1-2				
Grip Length	2.47					2.4				
Avg. Diameter	0.9249					0.9232				
head plane	0.936	0.924	0.91	0.925	0.922	0.927	0.916	0.919	0.945	0.91
tail plane	0.93	0.928	0.925	0.927	0.922	0.928	0.915	0.93	0.931	0.911
	RA1-3					RA1-4				
Grip Length	2.41					2.5				
Avg. Diameter	0.9182					0.9239				
head plane	0.917	0.91	0.944	0.9	0.922	0.919	0.93	0.947	0.925	0.917
tail plane	0.917	0.905	0.937	0.904	0.926	0.91	0.927	0.923	0.928	0.913
	RA2-1					RA2-2				
Grip Length	3.17					3.22				
Avg. Diameter	0.9267					0.9219				
head plane	0.93	0.944	0.905	0.921	0.905	0.913	0.93	0.915	0.935	0.911
tail plane	0.93	0.95	0.93	0.937	0.915	0.913	0.937	0.915	0.912	0.938
	RA2-3					RA2-4				
Grip Length	3.20					3.16				
Avg. Diameter	0.928					0.9264				
head plane	0.95	0.92	0.926	0.917	0.919	0.92	0.912	0.94	0.911	0.926
tail plane	0.945	0.928	0.93	0.92	0.925	0.928	0.921	0.946	0.92	0.94
	RA3-1					RA3-2				
Grip Length	3.18					3.18				
Avg. Diameter	0.9276					0.9394				
head plane	0.931	0.93	0.92	0.931	0.923	0.944	0.954	0.951	0.945	0.948
tail plane	0.93	0.932	0.92	0.93	0.929	0.92	0.935	0.932	0.94	0.925
	RA3-3					RA3-4				
Grip Length	3.23					3.16				
Avg. Diameter	0.9636					0.9288				
head plane	0.975	0.972	0.978	0.967	0.967	0.939	0.921	0.922	0.917	0.923
tail plane	0.958	0.954	0.962	0.954	0.949	0.94	0.921	0.935	0.937	0.933

Table A.2: Rivet Properties for group RB

	RB1-1					RB1-2				
Grip Length	2.27					2.38				
Avg. Diameter	0.9336					0.936				
head plane	0.932	0.928	0.94	0.925	0.939	0.934	0.938	0.94	0.94	0.941
tail plane	0.936	0.931	0.941	0.929	0.935	0.932	0.931	0.93	0.938	0.936
	RB1-3					RB1-4				
Grip Length	2.365					2.365				
Avg. Diameter	0.9327					0.9303				
head plane	0.94	0.938	0.936	0.929	0.932	0.938	0.94	0.905	0.91	0.937
tail plane	0.929	0.928	0.933	0.934	0.928	0.935	0.938	0.935	0.937	0.928
	RB2-1					RB2-2				
Grip Length	3.182					2.785				
Avg. Diameter	0.9214					0.9414				
head plane	0.945	0.912	0.942	0.909	0.91	0.942	0.942	0.95	0.935	0.926
tail plane	0.941	0.912	0.921	0.903	0.919	0.945	0.944	0.942	0.95	0.938
	RB2-3					RB2-4				
Grip Length	3.75					3.142				
Avg. Diameter	0.9292					0.9072				
head plane	0.926	0.935	0.931	0.942	0.945	0.88	0.918	0.875	0.932	0.89
tail plane	0.93	0.93	0.922	0.92	0.911	0.9	0.921	0.903	0.933	0.92
	RB3-1					RB3-2				
Grip Length	3.04					2.91				
Avg. Diameter	0.9339					0.9284				
head plane	0.933	0.935	0.934	0.922	0.935	0.937	0.929	0.934	0.927	0.93
tail plane	0.936	0.939	0.937	0.939	0.929	0.935	0.916	0.934	0.919	0.923
	RB3-3					RB3-4				
Grip Length	3.08					3.14				
Avg. Diameter	0.9176					0.9198				
head plane	0.909	0.922	0.915	0.919	0.91	0.919	0.918	0.919	0.922	0.932
tail plane	0.921	0.92	0.92	0.917	0.923	0.904	0.92	0.902	0.932	0.93

Table A.3: Rivet Properties for group RC

	RC1-1					RC1-2				
Grip Length	2.47					2.25				
Avg. Diameter	0.9308					0.9151				
head plane	0.925	0.917	0.93	0.914	0.95	0.915	0.93	0.908	0.925	0.911
tail plane	0.933	0.936	0.938	0.933	0.932	0.91	0.912	0.909	0.913	0.918
	RC1-3					RC1-4				
Grip Length	2.67					2.355				
Avg. Diameter	0.9603					0.9367				
head plane	0.958	0.97	0.955	0.963	0.963	0.93	0.94	0.927	0.93	0.946
tail plane	0.955	0.953	0.959	0.962	0.965	0.941	0.945	0.941	0.932	0.935
	RC2-1					RC2-2				
Grip Length	2.365					2.42				
Avg. Diameter	0.9345					0.9187				
head plane	0.939	0.93	0.94	0.926	0.934	0.92	0.902	0.9	0.92	0.91
tail plane	0.941	0.936	0.936	0.925	0.938	0.93	0.922	0.922	0.923	0.938
	RC2-3					RC2-4				
Grip Length	2.24					2.33				
Avg. Diameter	0.9345					0.934				
head plane	0.925	0.945	0.926	0.934	0.941	0.93	0.951	0.928	0.937	0.911
tail plane	0.927	0.946	0.925	0.945	0.931	0.938	0.941	0.927	0.945	0.932
	RC3-1					RC3-2				
Grip Length	2.3					2.34				
Avg. Diameter	0.9419					0.9425				
head plane	0.94	0.932	0.934	0.938	0.936	0.936	0.934	0.945	0.939	0.952
tail plane	0.954	0.945	0.948	0.945	0.947	0.949	0.942	0.948	0.94	0.94
	RC3-3					RC3-4				
Grip Length	2.7					2.46				
Avg. Diameter	0.9377					0.9443				
head plane	0.931	0.938	0.93	0.938	0.942	0.939	0.951	0.94	0.937	0.937
tail plane	0.935	0.94	0.943	0.935	0.945	0.948	0.948	0.947	0.955	0.941

Appendix B

YIELDING CAPACITY AT THE CHORD SPLICE

In this appendix, gross section yielding at the chord splice will be discussed. The gross section yielding is considered as a gusset plate limit by examining the yield capacity at all the connected member end in the gusset plates using effective section method for the current code (AASHTO [2011]). The Whitmore method are used in the current provision to calculate the effective section and yield capacity. However, the application of the Whitmore method at the chord splice was verified inappropriate in estimating elastic stress as described in Chapter 6. Instead, the effective length using the 15° dispersion angle proposed in Chapter 6 was verified better estimating the elastic stress distributions at the chord splice. In addition, the stress at chord splice is an interaction results from axial force and bending moment where the considered axial force is the net force between the chord load and the partial of the horizontal component of the diagonal load. Therefore, in this appendix, the yield capacity using this effective section at chord splice and considering the equation of the interaction between axial and flexural force will be discussed.

For the tensile or compressive yield capacities at the chord splice, the contours of X-direction stress and equivalent plastic strain from the FEA are used to identify the yielding. The proposed yield capacity using the effective length section and the interaction equation of axial and bending forces at the chord splice is calculated as the demand used in the FE analysis. The X-direction stress contours are used to verify the degree of gusset plate yielding under that demands and the equivalent plastic strain contours are used to verify that the gusset plate is still away from the material fracture. Thus, when the demands in the gusset plates analytical model is equal to the proposed yield capacity at the chord splice, the FEA results is expected to have serious yielding but not over the strain limit. An number of 3% plastic strain is conservatively considered as the limit of material fracture.

B.1 Yielding Capacity at Gusset Plate Chord Splices

At the chord splices, only the yield capacity is considered because the unsupported length between the end rows of opposite chord is often small and allows fully yielding to be developed without failure in elastic buckling. In the previous study, a trapezoidal model of stress distribution using 15° dispersion angle is considered for the elastic stress at the chord splice. In the yield limit state, the effective section is considered achieving yielding stress uniformly in lieu of elastic trapezoidal stress distribution. Tensile or compressive capacity P_c considers that the gross section yields at the effective section in a uniform stress and bending capacity M_p considers plastic moment for the effective gross section, too. The interaction diagram for combined axial and flexural forces at yield limit state is used to estimate the yield capacity at the chord splice. This equation is shown in AISC [2011] H.1 and used in Eq. B.1a.

By substituting the tensile or compressive yielding, P_c, the plastic moment, M_p, and the bending moment from the eccentricity, $M_r = P_r \times e$ into Eq B.1a, the yield capacity of the effective gross section at the chord splice can be rewritten as the a reduction factor times the tensile gross section yield capacity as shown in Eq. B.1e. The load demand at chord splice shall be less than the P_r described in Eq B.1a. The load demand at the chord splice is the net force between the chord load and the horizontal component of the diagonal loads when the chord splice is located at the work point. As the chord splice is not located the at work point, a linearly influence from the horizontal component of the diagonal load at the chord splice shall be considered as described in Chapter 7.

$$\frac{P_r}{P_c} + \frac{8}{9}\frac{M_r}{M_p} \leq 1 \tag{B.1a}$$

substitute P_c, M_r, and M_p into Eq B.1a

$$\frac{P_r}{P_c} + \frac{8}{9}\frac{P_r e}{F_y \frac{1}{4} 2tW_{eff}^2} \leq 1 \tag{B.1b}$$

$$\frac{P_r}{P_c} + \frac{8}{9}\frac{P_r e}{P_c \frac{1}{4} W_{eff}} \leq 1 \tag{B.1c}$$

$$\frac{P_r}{P_c}(1 + \frac{8}{9}\frac{4e}{W_{eff}}) \leq 1 \tag{B.1d}$$

$$P_r \leq P_c(\frac{9W_{eff}}{9W_{eff} + 32e}) \tag{B.1e}$$

where e is the eccentricity indicating center of effective section to the line of external chord force; M_r is moment incurred by the eccentricity $P_r \times e$; P_r is gross yielding capacity considering the geometric eccentricity; P_c is the tensile or compressive yield capacity of effective section; M_p is plastic moment of effective gross section ; W_{eff} is the effective section width at the chord splice from the edge of the chord splice to the intersect of the 15° dispersion angle line.

To evaluate the effect of Eq. B.1e with diverse of geometry and loading distributions, the gusset plate joints with different aspect ratio L/W of the connected length and width at chord are used. The parameters of eight joints including gross section yield capacity P_c, reduction factor, and capacity P_r is tabulated in Table B.1. The validation considers two different loading condition, the first loading condition only applies P_r to the chord members and keeps zero load at the diagonals and hanger. The capacity calculated using the Whitmore's 30° dispersion angle for the eight joints are compared with the proposed yield capacity at the chord splice.

The second loading condition applies P_r as the net fores of the chord and horizontal component forces at chord splice with full load at diagonals and hanger. In eight joints, the first four joints used one loading distribution in which the left diagonal load (L9) is in compression and the second four joints uses another loading distribution in which the left diagonal load (L9) is in tensile but both loading distributions have the same net force at the chord splice. The loading for each member for two loading distributions in eight joints are listed in Table B.2.

Table B.1: Geometric parameters and yield demand applied to gusset plate joints for Eq. B.1 verification

L/W	w	l	d	W_{eff}	e	$\frac{9W_{eff}}{9W_{eff}+32e}$	P_c (kips)	P_r (kips)	Whitmore (Kips)	Ratio
1.8	22.5	41.25	3	36.55	2.14	0.83	1882.47	1558.54	2539.76	1.63
2.2	22.5	48.75	3	38.56	2.80	0.79	1985.97	1578.70	2762.76	1.75
2.5	22.5	56.25	3	40.57	3.46	0.77	2089.47	1603.40	2985.76	1.86
2.8	22.5	63.75	3	42.58	4.12	0.74	2192.96	1631.60	3208.76	1.97
3.2	22.5	71.25	3	44.59	4.78	0.72	2296.46	1662.57	3431.77	2.06
3.5	22.5	78.75	3	46.60	5.44	0.71	2399.95	1695.74	3654.77	2.16
3.8	22.5	86.25	3	48.61	6.10	0.69	2503.45	1730.72	3877.77	2.24
4.2	22.5	93.75	3	50.62	6.77	0.68	2606.94	1767.18	4100.77	2.32

The stress contours generated by the FEA results in the first loading condition are shown in Figure C.1. As shown, under the load demand, which equals to the gross section yield capacity, a significant yield area is generated at the chord splice but the equivalent plastic strains are still low, indicating the chord splice yielded seriously but is still away to the fracture limit. In all eight joints, the yield area and equivalent plastic strain show a similar pattern and magnitude levels under the gross section yield capacity. However, as same procedure using the Whitmore's 30° dispersion angle to calculate the effective section and the yield demand at the chord splice, the yield area is much larger. The plastic strains are also inconsistent. The stress contours using the Whitmore's method to estimate yield capacity are shown in Figure B.1. The other four gusset plates using the Whitmore's method to estimate yield capacity show the solutions do not converge, indicating the equivalent plastic strain exceeded 15% and causing the FEA terminated before the converge solution achieved. Using Whitmore method to calculate yield capacity at the chord splice does not demonstrate conservative and consistent results.

The stress and strain contours for loading condition with full loads are shown in Figure B.2.

Table B.2: Varying member loads when the demand of chord load equals to defined yield capacity

L/W	P_r (kips)	U9(kips)	L9(kips) [1]	L10(kips)	L11(kips) [2]	U10(kips)	Whitmore Stress(ksi) [3]
1.8	1558.54	2488.15	-1500	400	1099.14	781.33	50.45
2.2	1578.70	2508.31	-1500	400	1099.14	801.49	46.76
2.5	1603.40	2533.01	-1500	400	1099.14	826.19	43.69
2.8	1631.60	2561.21	-1500	400	1099.14	854.39	41.11
3.2	1662.57	1352.70	500	100	-696.36	2154.97	32.34
3.5	1695.74	1385.87	500	100	-696.36	2188.15	30.83
3.8	1730.72	1420.85	500	100	-696.36	2223.13	29.52
4.2	1767.18	1457.31	500	100	-696.36	2259.59	28.38

[1] 51.7029° diagonal to horizontal line

[2] 45° diagonal to horizontal line

[3] Stress at defined limit state using 30° Whitmore section

In all eight joints, all demands, the net force, at chord splice are kept the same but two different loading distributions at diagonals and hanger are considered. All eight joints show significant yield area at chord splice and low equivalent plastic strain, demonstrating the robustness of the Eq. B.1e when the influences from diagonals and hanger are considered. The patterns of yield stress and plastic strain are slight different though the demands at chord are the same for two different loading conditions. The loading conditions slightly slightly affect the yield area at the chord splice. The difference is negligible and does not affect the evaluation of the yield capacity at the chord splice.

The last column in Table B.2 shows the larger value of the Whitmore's stress using two connected chord loads. As the aspect ratio of chord connection L/W becomes larger, indicating larger gusset plate connection, the estimated stress by the Whitmore's methods is

much lower than the yielding stress. With the longer connection length, the Whitmore's stress becomes lower. Again, it is verified that the Whitmore's method is inappropriate at the chord splice for both elastic range and yield limit.

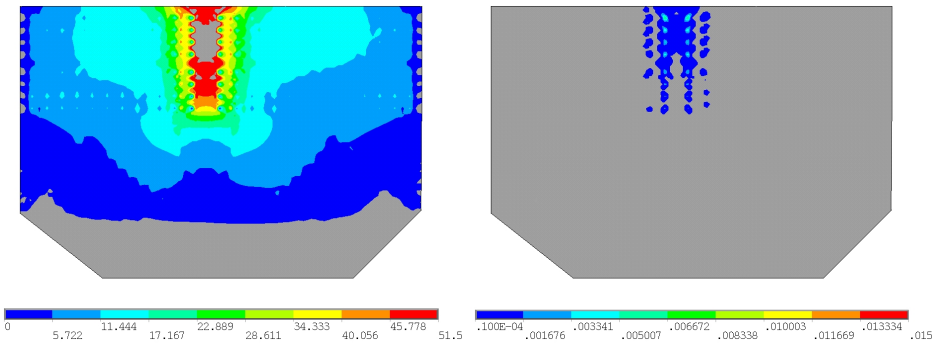

(a) Normal stress contour for L/W=1.8 (b) Equivalent plastic strain L/W=1.8

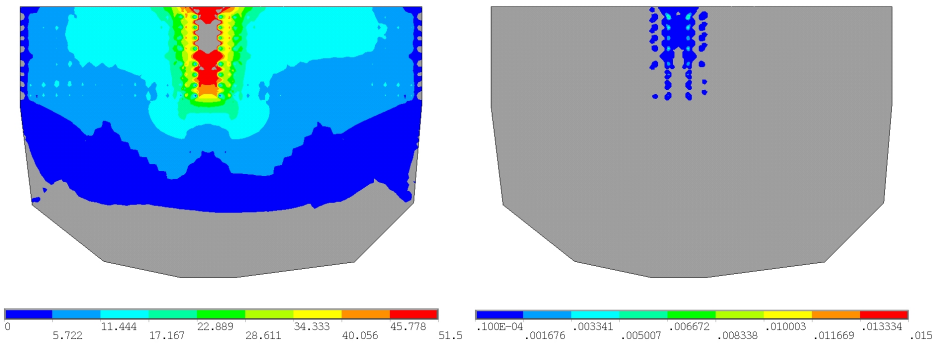

(c) Normal stress contour L/W=2.2 (d) Equivalent plastic strain L/W=2.2

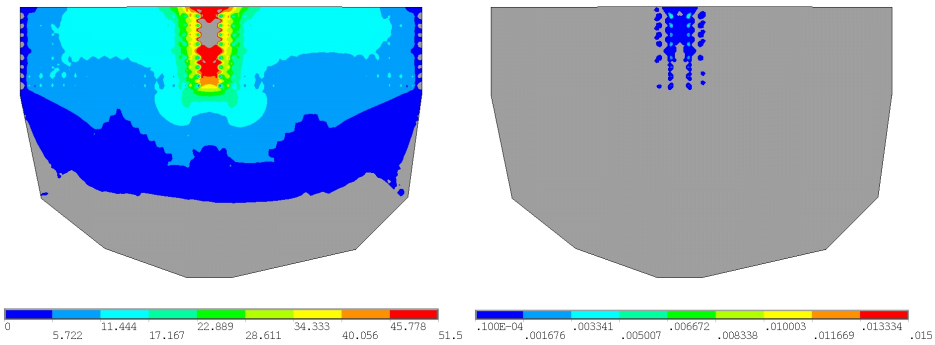

(e) Normal stress contour L/W=2.5 (f) Equivalent plastic strain L/W=2.5

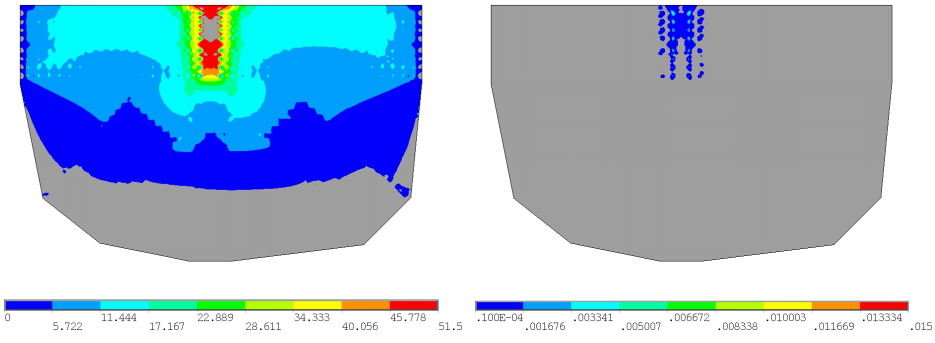

(g) Normal stress contour for L/W=2.8 (h) Equivalent plastic strain L/W=2.8

Figure B.1: Normal stress and equivalent strain of gusset plate chord splice under calculated limit state load

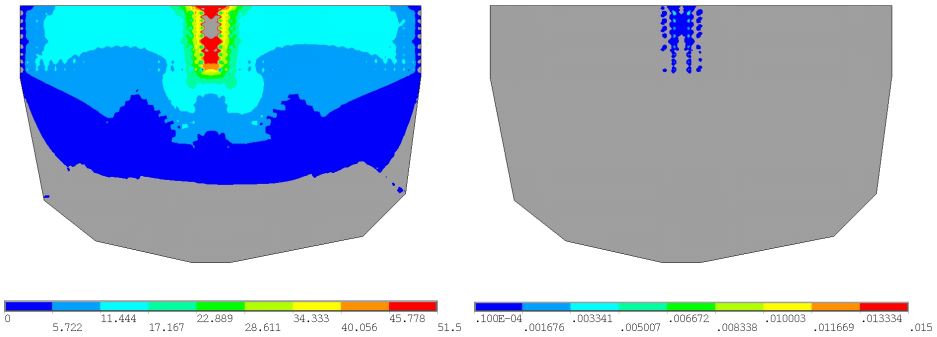

(i) Normal stress contour for L/W=3.2 (j) Equivalent plastic strain L/W=3.2

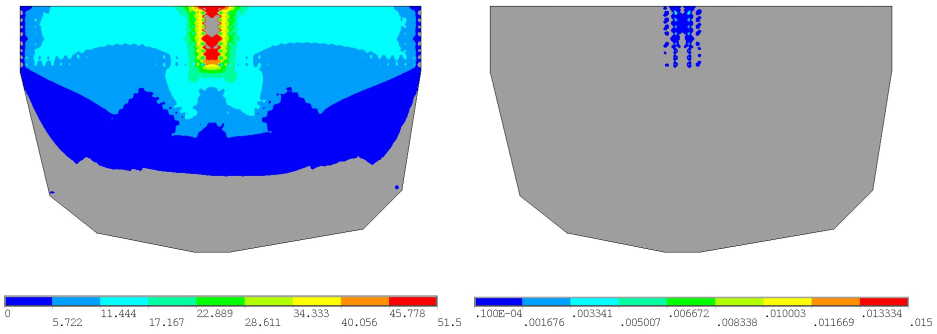

(k) Normal stress contour for L/W=3.5 (l) Equivalent plastic strain L/W=3.5

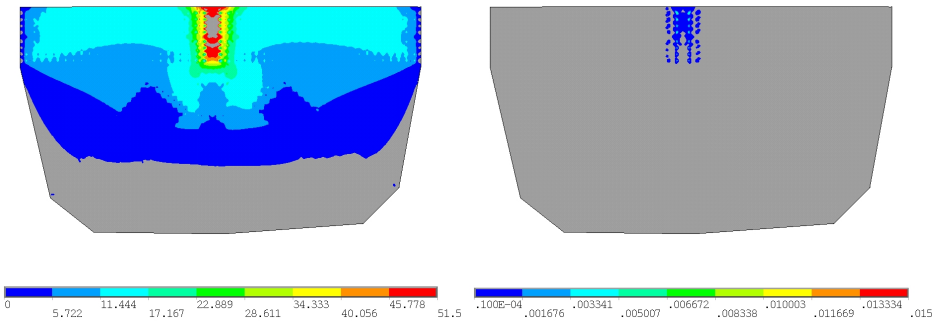

(m) Normal stress contour for L/W=3.8 (n) Equivalent plastic strain L/W=3.8

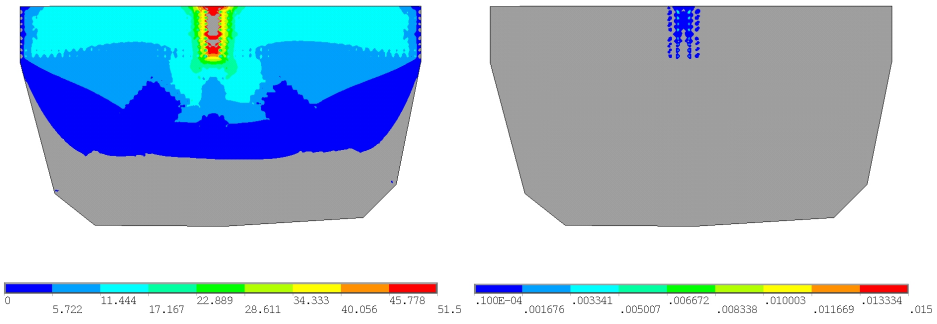

(o) Normal stress contour for L/W=4.2 (p) Equivalent plastic strain L/W=4.2

Figure B.1: Normal stress and equivalent strain of gusset plate chord splice under calculated limit state load

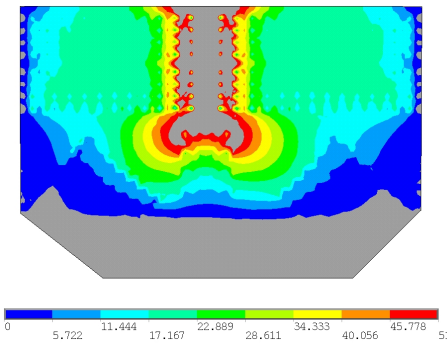

(q) Normal stress contour for L/W=1.8

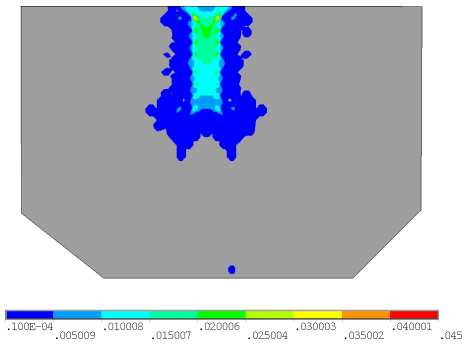

(r) Equivalent plastic strain L/W=1.8

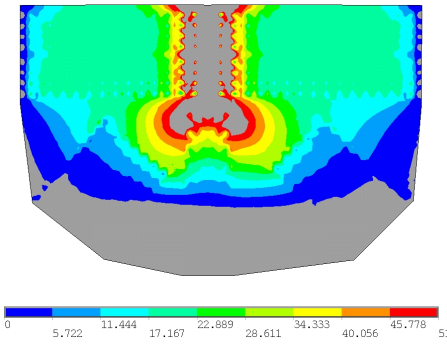

(s) Normal stress contour L/W=2.2

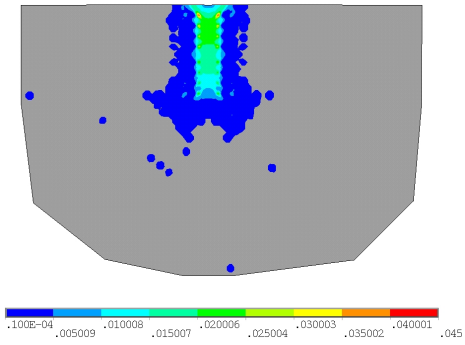

(t) Equivalent plastic strain L/W=2.2

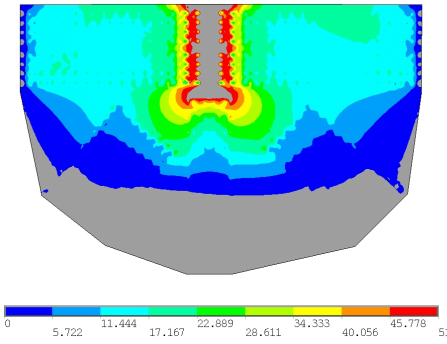

(u) Normal stress contour L/W=2.5

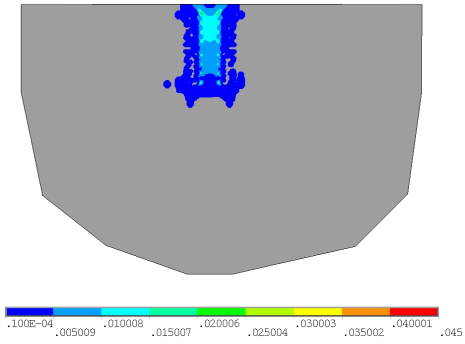

(v) Equivalent plastic strain L/W=2.5

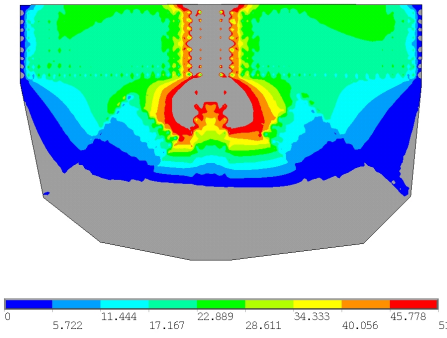

(w) Normal stress contour L/W=2.8

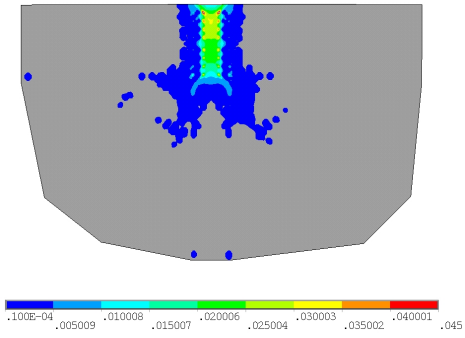

(x) Equivalent plastic strain L/W=2.8

Figure B.1: Normal stress and equivalent strain of gusset plate chord splice under limit state load using Whitmore's method

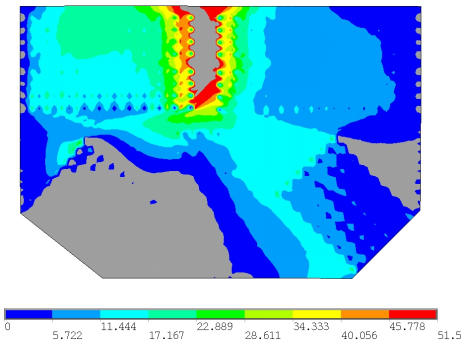

(a) Von Mise contour for L/W=1.8

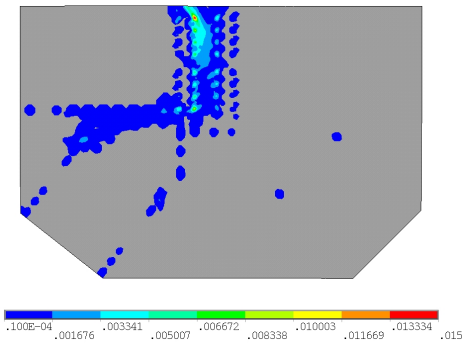

(b) Equivalent plastic strain L/W=1.8

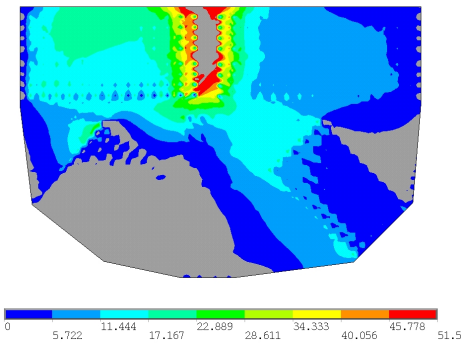

(c) Von Mise contour L/W=2.2

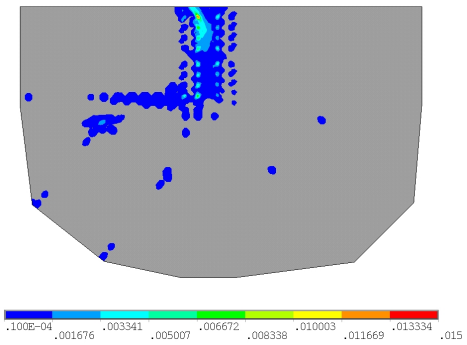

(d) Equivalent plastic strain L/W=2.2

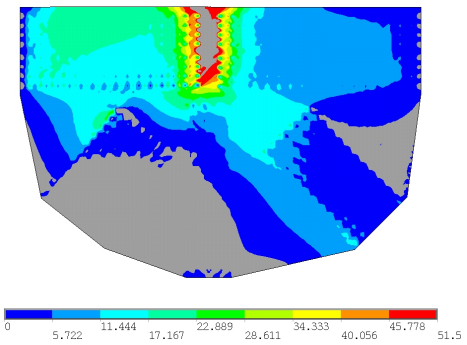

(e) Von Mise contour L/W=2.5

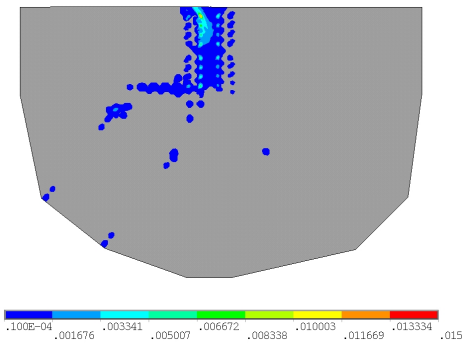

(f) Equivalent plastic strain L/W=2.5

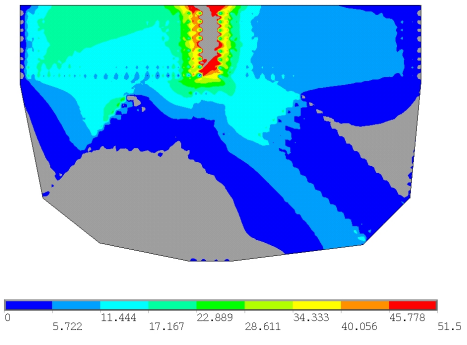

(g) Von Mise contour for L/W=2.8

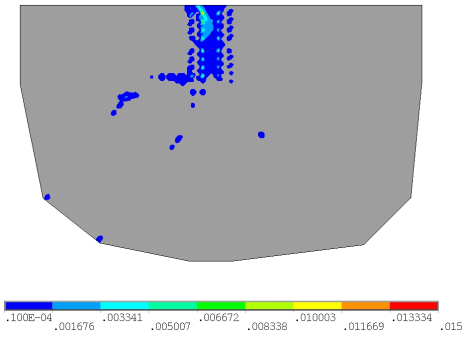

(h) Equivalent plastic strain L/W=2.8

Figure B.2: X-direction normal stress and equivalent strain of gusset plate chord splice under limit state load with diagonal and hanger loads

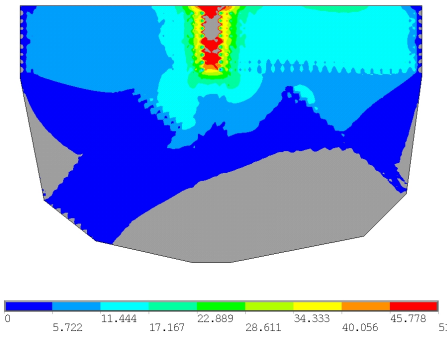

(i) Von Mise contour for L/W=3.2

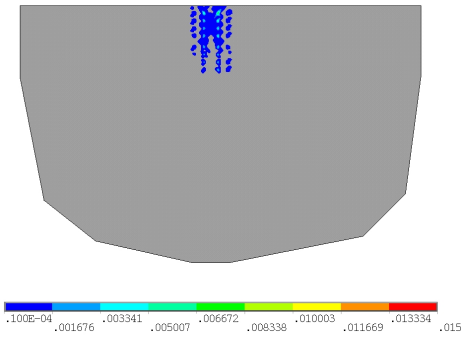

(j) Equivalent plastic strain L/W=3.2

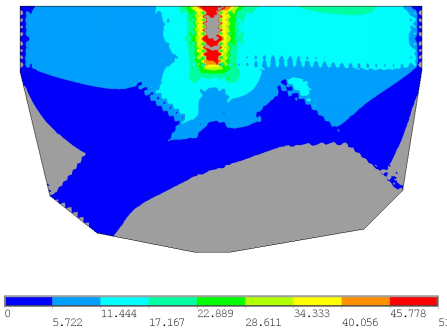

(k) Von Mise contour for L/W=3.5

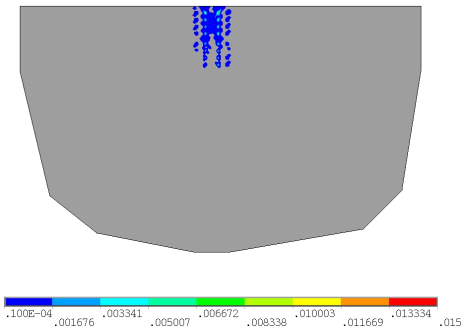

(l) Equivalent plastic strain L/W=3.5

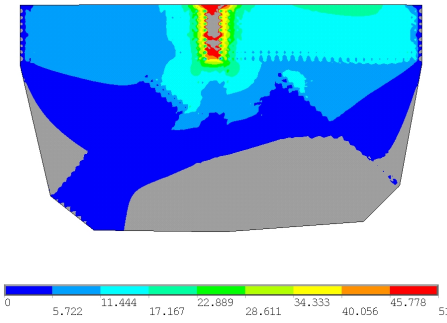

(m) Von Mise contour for L/W=3.8

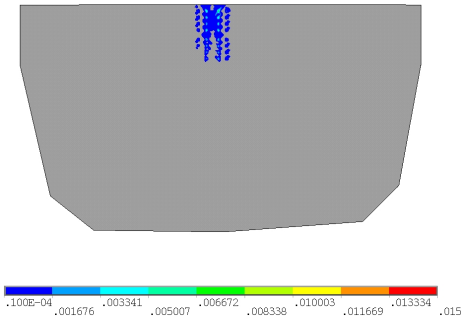

(n) Equivalent plastic strain L/W=3.8

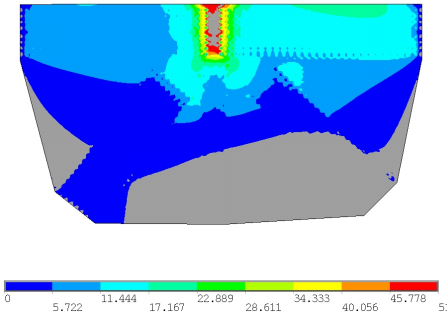

(o) Von Mise contour for L/W=4.2

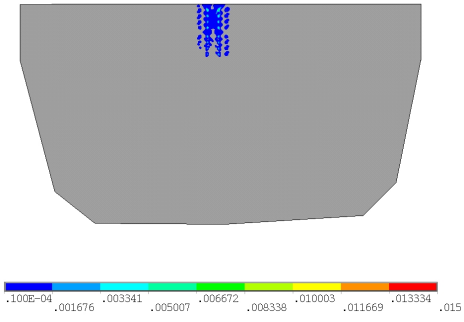

(p) Equivalent plastic strain L/W=4.2

Figure B.2: X-direction normal stress and equivalent strain of gusset plate chord splice under limit state load with diagonal and hanger loads

Appendix C

SHEAR RESISTANCE ALONG CRITICAL SECTION

Shear resistance capacity of gusset plate in current regulations considers shear yielding at horizontal gross section. An reduction factor, Ω, is used if plates are not stiff enough to achieve fully yielding and fails in shear buckling. However, there is no clear definition for sufficient stiffness to choose Ω but depends on engineer's judge. Besides, using whole gross section calculating its shear capacity might be improper because elastic shear stress at critical sections is verified mainly determined by the load from one-side diagonal and the shear stress exaggerates only if the chord load on the same side of gusset plate has much larger load than the diagonal load. The diagonal load from another side has does not affect the shear stress at the other sides. Therefore, the shear capacity provided by one side of gusset plates section might not be help to resist shear demand from another sides. The method specified in current regulations to estimate shear resistance capacity might be under over estimating gusset plate shear capacity at the horizontal section.

The elastic shear stress at critical section is calculated by using the horizontal or the vertical component of diagonal load divided by effective shear sections which are a length of critical section intersected by Whitmore's 30 $\circ$ dispersion angle from first row of outside fastener of diagonal and a virtual line passing work point perpendicular to the section. This method was demonstrated good consistence with the FEA results for estimating shear stress along the horizontal and vertical section. To validate the effective shear length method also validates in inelastic range, the shear capacity calculated by using this method is considered as diagonal load demand and apply the corresponding loads on gusset plate joints. Eq. C.1 shows the calculation of the diagonal load to generate shear yielding at the horizontal critical section.

$$\frac{F_{diagonal} \times cos\theta}{2tW_{eff}} \leq \frac{F_y}{\sqrt{3}} \tag{C.1a}$$

$$F_{diagonal} \leq \frac{2F_y \times W_{eff}t}{\sqrt{3} \times cos\theta} \tag{C.1b}$$

By using Eq. C.1b, a load distribution which generate shear yielding at one side of horizontal critical section and keep another side elastic can be designed. The FEA results of XY shear stress and equivalent plastic strain are used to validate the shear resistance limit of gusset plates. Furthermore, a 25% increase of this loading distribution was applied to the joints to observe if the horizontal section provided by gusset plate on other side will contribute to the shear resistance capacity. To mitigate the possible interference from chord loads, the total horizontal shear force is evenly taken by two chord member to keep loading distribution equilibrium.

The XY shear stress contours at calculated shear yielding limit and 1.25 times of it are shown in Figure D.3(b) and C.1(b). The shear yielding stress is taken as $51.5/\sqrt{3} = 29.73$ ksi which is shown gray color in the stress contour. In Figure D.3(b), there is one small patch is observed yielded along horizontal critical section while a bigger yielding patch is found close to the critical vertical section. A further check found that the shear capacity at the vertical section is smaller then the shear capacity at the horizontal section. Therefore, the loading distribution that designed to initially shear yield the horizontal section actually yields the vertical section earlier than the horizontal section. The mistake of designed loading distribution otherwise emphasize the advantage of effective shear length method to consider the shear resistance capacity. In addition, the shear yielding area seems very small in the XY shear stress contour and is over conservative to estimate shear yielding limit. However, the equivalent stress (Von Mises stress) considers not only XY shear stress but normal stress. With the higher shear stress at the critical section, the higher the normal stress will be expected. The equivalent plastic strain contour shows at the calculated shear yielding limit, a significant area at the left half of gusset plates yields, though the magnitude of plastic strain is small. The plastic strain is less than 0.1% in load of shear yielding limit

and is not over 0.3% even in the 25% increased loads of shear yielding limit. The equivalent plastic strain contours are shown in Figure C.1(c) and C.1(d). This small plastic strain guarantees that the effective shear section method is capibable to estimate the shear yielding limit at critical sections but is conservative enough to avoid steeel material fracture. This validates that the effective shear section method is a reliable and conservative method to calculate shear resistance capacity of gusset plates at critical section.

Finally, the XY shear stress is observed over shear yielding criterion mostly in the left half of gusset plate while the right half of gusset plate is not yielded in shear. Even though in the 25% increased loads, the yielded area only observed on the left side of gusset plates, but no yielding is observed on the right side of the gusset plate, indicating the right side of gusset plate does not provide additional shear capacity. The shear stress calculated by the effective shear length method for horizontal and vertical cirtical sections at the right side of the usset plate shows the estimated shear stress does not exccced the shear yielding criterion in these loading consitions. The results shows that the full critical section is not used to resist shear force indicating that using the full critical section to calculate shear resistance capacity in currrent regulation is improper.

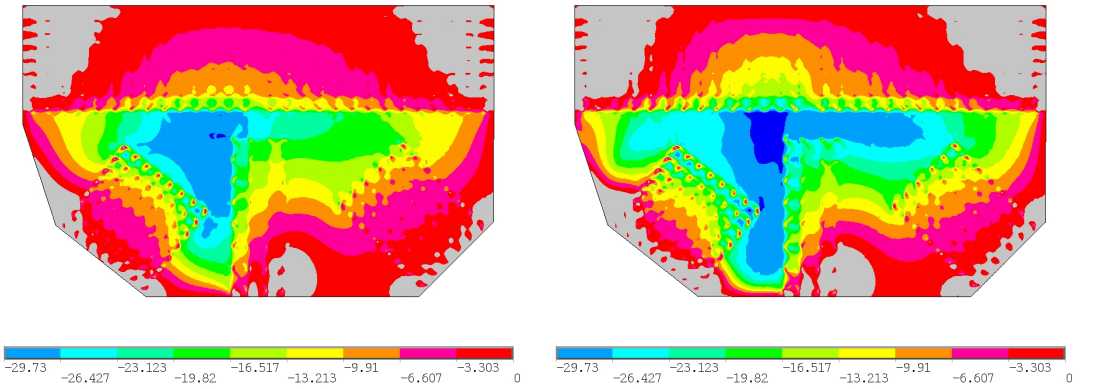

(a) XY shear stress@ horizontal shear resistance limit

(b) XY shear stress@ 1.25 times of horizontal shear resistance limit

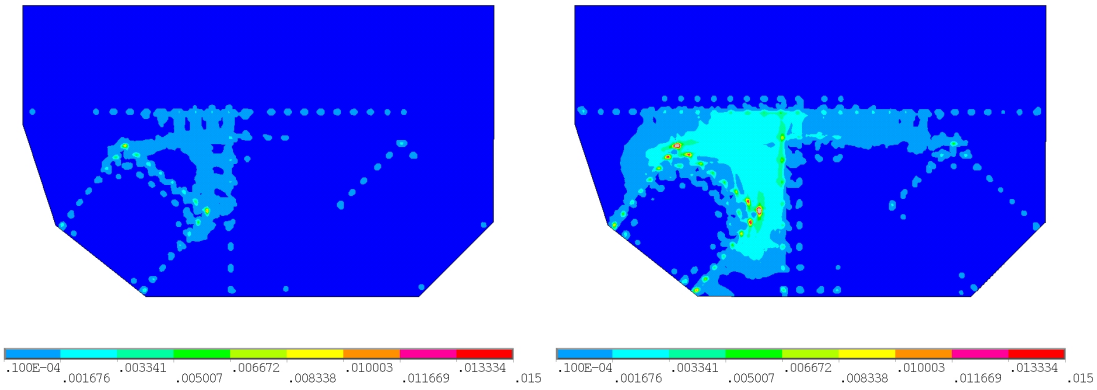

(c) Equivalent plastic strain@ horizontal shear resistance limit

(d) Equivalent plastic strain@ 1.25 times of horizontal shear resistance limit

Figure C.1: Shear stress and equivalent strain contour at shear resistance limit state

C.0.1 Shear resistance in other joints with different geometries

The effective shear section method for shear resistance limit shows conservative and consistent with the FEA results in the gusset plates with geometry similar to the joint U10. Joint U10 is a large gusset plate connection with relative short distance from the end of diagonal to the adjacent rivet lines. The distance from the diagonal end to the adjacent rivet line and various geometries might affect the accuracy of effective shear section method. To examine

the application of effective shear section method to various geometries of gusset plates, joint L2 which has relative long distance from the diagonal end to the adjacent rivet lines and joint U3 which is a Pratt type joint are loaded with the calculated shear resistance capacity.

Joint L2 has similar shear yielding capacities for both diagonals in vertical and horizontal critical sections. The calculated diagonal load demand using Eq. C.1b for the joint L2 is to be $F^{left}_{diagonal} \leq 840$ kips for shear yielding limit at left horizontal section, $F^{left}_{diagonal} \leq 706$ kips for shear yielding limit at left vertical section, $F^{right}_{diagonal} \leq 786$ kips for shear yielding limit at right horizontal section, and $F^{right}_{diagonal} \leq 778$ kips for shear yielding at right horizontal section. A connected member loading distribution using $F^{left}_{diagonal} = 706$ and $F^{right}_{diagonal} = 786$ will be assumed to generate shear yielding at the left vertical section and the right vertical and horizontal sections for joint L2. Figure C.1(e) and C.1(g) show that the shear stress is about 5% to 10% lower than the shear yielding criterion in both left and right cirtical sections but the equivalent plastic strains show a large area is in the inelastic range.

The consistent observation is shown in joint U3, too. The $F_{diagonal} \leq 447$ kips for shear yielding limit at the horizontal section, $F_{diagonal} \leq 404$ kips for shear yielding limit at vertical section and a loading distribution using $F_{diagonal} = 404$ will be assumed to generate shear yielding at the vertical section. Figure C.1(f) and C.1(h) show a patch area around the vertical section is close to the shear yielding criterion and some area is yielded and in the plastic range at the vertical section.

The conservative estimations of the shear yielding limit are observed in the application of this method. It is about 5% to 10% over conservative in estimating shear yielding capacity but a considerable area has exceeded the Von Mises yielding criterion due to corresponding normal stress at critical sections. From the global point of view, the over conservative in the shear yielding may be mitigated in considering the equivalent stress and still keep the overall estimation conservative.

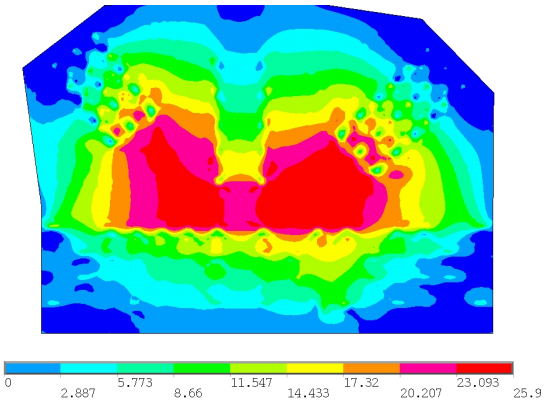

(e) XY shear stress@ vertical shear resistance limit of Cle Elm birdge joint L2

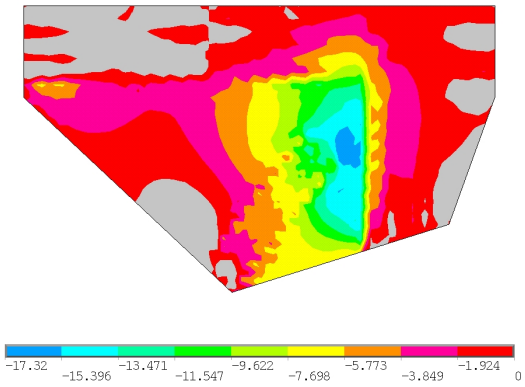

(f) XY shear stress@ vertical shear resistance limit of Hor River bridge joint U3

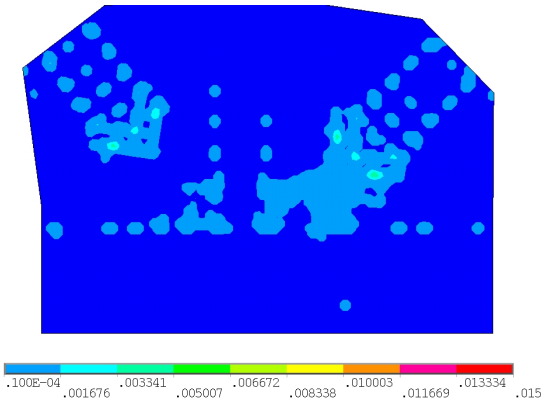

(g) Equivalent plastic strain@ vertical shear resistance limit of Cle Elm bridge joint L2

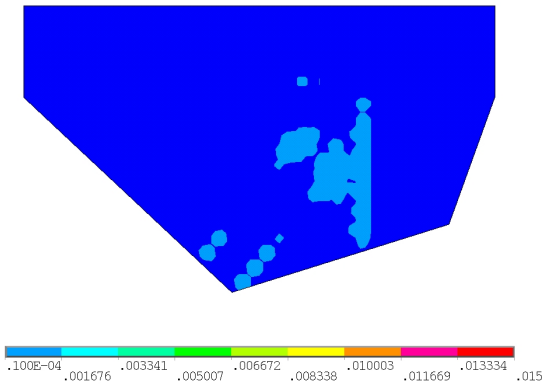

(h) Equivalent plastic strain@ vertical shear resistance limit limit of Hor River bridge joint U3

Figure C.1: Shear stress and equivalent strain contour at shear resistance limit state

Appendix D

GUSSET PLATE BUCKLING CAPACITY

Simulating gusset plate buckling numerically and determining buckling load from the numerical analysis are important to study gusset plate buckling behaviors. However, these two procedures are not easy to implement numerically. General finite element method does not converge to the solution when a sudden large deformation or structural soften occurs and often terminates the FEA solving process. It is not valid to determine the buckling load using the load as the FEA is unable to converge and terminate the procedure because the termination of the analysis may be caused by other factors, such as local stress concentration. Besides the instability of the conventional FEA when the buckling occurrence, the load-deflection curve in practice doest not show significant bifurcation behavior. It is difficult to determine the buckling load by just using one method. This is because the stable post buckling behavior of plates shows inherent difficult in defining the buckling load for plates with imperfections (Singer et al. [1985]). Many techniques has been developed to determine the buckling load in practice but none of them are precisely predicting buckling load, P_{cr} (Singer et al. [1985]). In this appendix, the simulations of gusset plate buckling using finite element method will be described and the method used to determine analytical buckling load is also discussed. The methods will then be applied to discuss gusset plate buckling capacity under the influence of the gusset plate stress states.

D.0.2 Simulation of Gusset Plate Buckling Behavior in the Finite Element Analysis

The conventional finite element method using the Newton-Raphson algorithm for path-dependent nonlinear problems has difficulty in solution converge when a sudden large deformation occurs with zero or negative slope. The residual of the Newton-Raphson method

after several iterations in one step will still not achieve the targeted tolerance because the zero or negative slope may result in snap-through solution or larger residual with the positive the displacement or load increment. Considering the reasons of this algorithm failure, there are two ways to improve the solution converge. The first method is to avoid calculating the residual in the iterations of each time step so that the FEA is not terminated at the bifurcation region. The second method uses special skill to overcome the bifurcation region.

The first method is called "Explicit Dynamics method" (Simulia [2008]) which considers a static problem as a dynamic problem. Instead of using the Newton-Raphson algorithm, central difference algorithm is used in the dynamic problem to solve the solution at "t+1" step without calculating residual. The criterion of the solution converge for central difference algorithm depends the size of each time step. As long as the time step is smaller than $\Delta t \leq min\left(L_e\sqrt{\frac{\rho}{\lambda+2\mu}}\right)$, where ρ is material density, $\lambda and \mu$ are material constant, central difference algorithm ensure the solution converged to the exact solution. Therefore, the explicit dynamics method avoid the non-converge solution in the conventional finite element static analysis and is appropriate for buckling and post-buckling analysis.

The second method is the application of line search technique along with the Newton-Raphson method to overcome the converge when the solution path has zero or negative slope in a time step. The Newton-Raphson requires that load or displacement residual decreases to less than the tolerance in a default full time step but the default time step may be too big to acquire the converged solution. Line search technique scales the solution vector in the default time step from 0.05 to 1.0, i.e. scale of time step, and thereby to gain less residual when the current slope is near-zero or negative. The solution vector with line search can be written as $u_{i+1} = u_i + s\Delta u_i$, where s is a scale factor between 0.05 and 1.0., so that a smaller solution vector is used to calculate residual to achieve the targeted tolerance. Line search with the Newton-Raphson method is particular suitable for buckling and post-buckling analysis.

In this dissertation, finite element package, ABAQUS, is used to implement the explicit dynamics algorithm for the gusset plate buckling analysis and ANSYS, is used to implement the Newton-Raphson algorithm with line search technique. Element type and modeling

methodology used in ANSYS is the same as described in Chapter 3 but uses line search technique with nonlinear large deformation analysis. The finite element model information used in ANSYS are exported for the build of the finite element models in ABAQUS. These information include all the node coordinate, element connectivity of each element, material properties, and boundary conditions. Therefore, the finite element model in ABAQUS is identical with the one used in ANSYS. The corresponding element types in ABAQUS are used for the explicit dynamics analysis. The shell element used in ABAQUS is S4R which is a four node quadrilateral element with six degrees of freedom at each node. S4R is formulated with reduced integration, large strain and hourglass control. The beam element is three dimensional linear interpolation Timoshenko beam. In addition, the mass density and damping ratio are required to input in the system property.

The explicit dynamic analysis is intrinsically modeling a quasi-static problem using dynamic equations so that the essential dynamic behavior is observed in the structural behavior. Figure D.1 shows the load-deflection curve for a node located in the potential buckling area. Small and high frequency vibrations are observed in the load-deflection curves when the load-deflection curve is observed closely. To mitigate the substantial vibration from the dynamic analysis, pre-process for analysis and post-data-process is necessary. Before conducting analysis, linear bulk viscosity, which is used to damp high frequency because of the small element length and mitigate hourglass effect in dynamic analysis, and mass scaling factor, which is used to stabilize the analysis at the initial load step as load applied to the system have to be setup properly. However, the inertial force and the damping force incurred by system mass and damping shall be examined to be small enough to not affect the internal forces generated by the system stiffness in each time step. In addition, a cosine or sine ramped load curve can be used instead of linear ramped load curve. The sine or cosine load curve substantially mitigates the vibration in the initial load step because the linear ramped load in the initial step generates dynamic behavior such as a impulse load applied on the system and generate high amplitude and frequency vibration.

In spite of the pre-process analysis for the explicit dynamic analysis, the resulting load-deflection curves still have a very small vibration in the load-deflection curve as shown in

Figure D.1. Fast Fourier Transform (FFT) is used to filter the high frequency vibration and the low-frequency characteristics of the load-deflection curve is shown in red-dashed line. Because of the tiny time step required in the explicit dynamic analysis, thousands of data points consist of the load-deflection curve. To more accurately sample the load-deflection curve and determine the buckling load, a monotonic increasing interpolation function is applied to the load-deflection curve to acquire the sample data points and are shown in black circles in Figure D.1. The black circle shows a smooth and accurate sampled load-deflection curve which will be used for determining the buckling load in the gusset plate connection. The method to estimate buckling load using a load-deflection curve will be discussed in the next section.

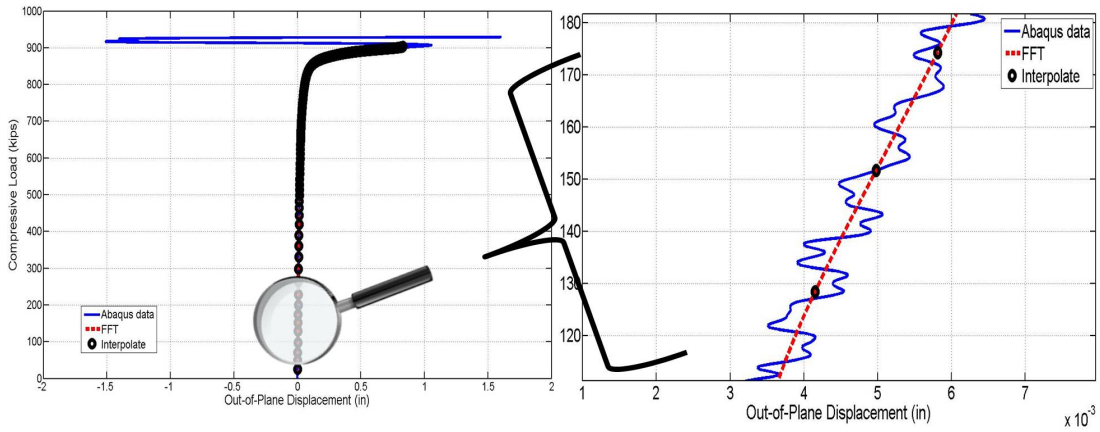

Figure D.1: The FE explicit dynamic analysis for gusset plate buckling behavior along with FFT results and monotonic increasing interpolate function for the load-deflection curve

The buckling loads predicted using explicit dynamic method with ABAQUS and using the Newton-Raphson algorithm and line search with ANSYS are verified by two gusset plate buckling failures for verification. The first case is from the gusset plate connection experiment conducted by Ocel et al. [2012] and the other case is the failure of Joint U10 in the I-35W bridge. The failure load of Joint U10 was estimated by Ocel and Wright [2008] with the consideration of the load stage on the I-35W bridge after the additional construction load were applied. The estimated failure load that failed Joint U10 is assumed

between 2291 kips to 2388 kips. Gusset plate GP307SS3 was observed failed in the buckling during the experiment conducted by Ocel et al. [2012]. It had a failure load of 716 kips in the compressive diagonal. The results are tabulated in Table D.1

Table D.1: Comparison of estimated buckling load between numerical analysis and gusset plate failure

Gusset Plate	Estimate Failure Load [1]	Explicit Dynamics Method	Newton-Raphon with Line Search
Joint U10	2291-2388	2249 (2770)[2]	2205 (2579)[2]
GP307SS3	716	719	670

[1] unit: kips

[2] Predicted buckling load at the end of the compressive diagonal

Table D.1 shows both estimates of the explicit dynamics method and the Newton-Raphson with line search agree with the experimental and practical failure cases. The maximum error percentage is about 6%, which is accurate in failure prediction. Three out of four cases under estimate the failure load which shows conservative estimate. This is because: 1) The predicted buckling load is not failure load. Gusset plate connection does not fail immediately after the buckling occurs though the margin from the buckling to the failure may be small. 2) The earlier predicted failure may be due to the the analytical modeling method which does not simulate the comcompressive stiffness provided by connected members. There were no contact elements modeled between gusset plates and member plates so that the gusset plates buckle and penetrate the coinnected members ealier which will be prevented in practice.

Overall, both analytical buckling estimate by these two methods agree with the results from the experimental and practical failure. The explicit dynamics method requires more work in pre-analysis and post-data process while the Newton-Raphson with line search is simpler in the implementation. Therefore, the Newton-Raphson with line search using ANSYS software package will be used for gusset plate buckling discussion.

D.0.3 Determination of Buckling Load from Load-Deflection Curve

Theoretically, buckling is defined as a bifurcation behavior of a member or system which originally deflects in the direction of applied load and then suddenly deflects in a different direction. In practice, buckling is defined a sudden large displacement increment when a small load increment is applied. In the gusset plate buckling study, the out-of-plane displacement was plotted versus the compressive diagonal load and the buckling load is determined from the load-deflection curve. A typical plate buckling plot shown in Figure D.4and indicated by Singer et al. [1985] that it is difficult to determine the buckling load precisely since the bifurcation phenomenon is affected by the post-buckling behavior and boundary conditions.

To improve the accuracy and consistence in estimating the buckling load from the load-deflection curve, two steps are takes in this study. The first step is selecting proper nodes from the FE model to represent plate buckling behavior. It was found that not all nodes in the buckling area show monotonic and smooth load-deflection curves. The nodes located in the buckling region for Joint U10 and GP307SS3 are plotted by blue circles in Figure D.3 and the nodes underlined by the red solid circles show the nodes that generate proper load-deflection curves. Most nodes on the compressive edge of Joint U10 can present proper buckling curve while only part of the nodes in the end of compressive diagonal area have proper load-deflection curves. These nodes are located in a certain width at the end area of the compressive diagonal. The nodes near the vertex of the triangle area were found exhibit out-of-plane displacement reversal rather than significant buckling bifurcation. This may because the constraints in the boundary of the triangular area.

The second step is to average the load-deflection curve represented by these nodes to magnify the bifurcation of buckling behavior on the load-deflection curve. Figure D.4(a) shows the example of each load-deflection curve for the nodes selected from the buckling area in GP307SS3 and the estimated buckling load is colored by the red line along the load-deflection curve while Figure D.4(b) shows the average of these load-deflection curve from Figure D.4(a). Figure D.4(a) shows the each load-deflection curve has different stiffness

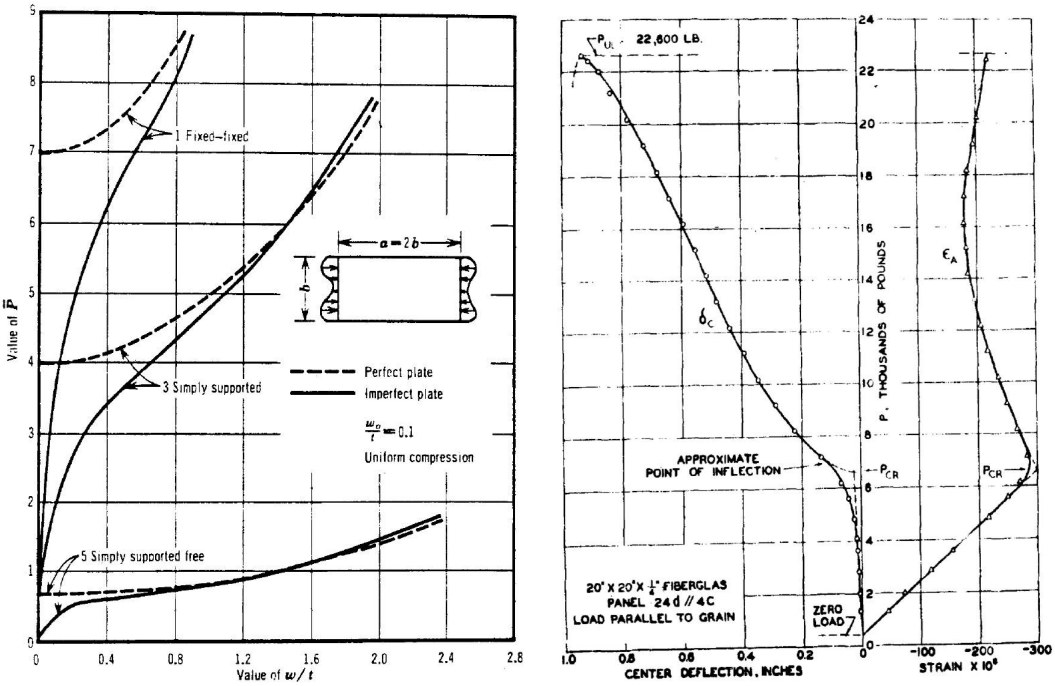

(a) Plate post-buckling behavior affected by the boundary conditions (Rhodes and Harvey [1977])

(b) Difficulty in determining plate buckling load (Hoff et al. [1948])

Figure D.2: Singer et al. [1985] indicated that precisely predicting buckling load from experimental data is difficult because of the increasing strength in the post-buckling behavior of plates

before and after bifurcation occurs and shows a range of the buckling loads. However, the average of the load-deflection curve shows a reasonable buckling load-deflection curve and a good estimate of the buckling load as shown in the red line. The average load-deflection curve will be used for determining the buckling load. As the load-deflection is more accurately representing the overall buckling behavior of the compressive region, the buckling load can be determined by looking at the sharp stiffness changes along the load-deflection curve. A general method that the point where the slope on the load-deflection curve decreases to 15% of the initial slope is considered as the structural buckling. Using this method, the buckling load for Joint U10 and GP307SS3 were determined and show good agreement with the experimental and practical failure cases in Table D.1.

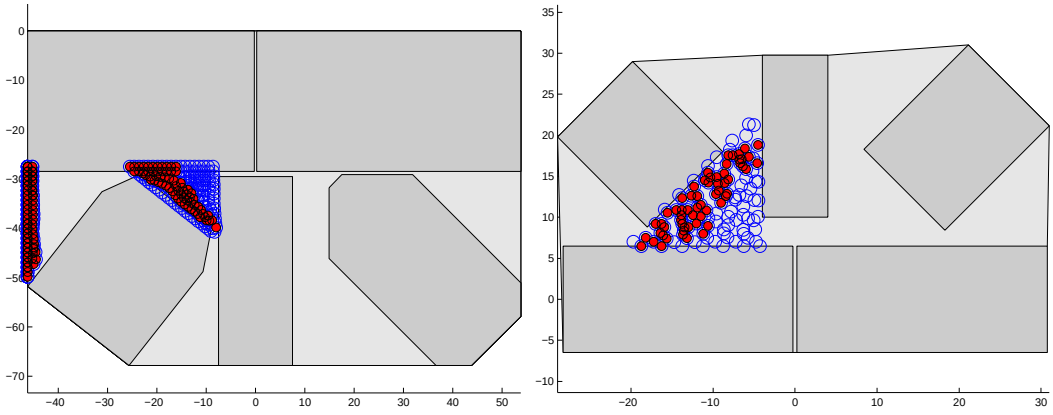

(a) Joint U10 (b) Joint GP307SS3

Figure D.3: Nodes shows clear buckling modes

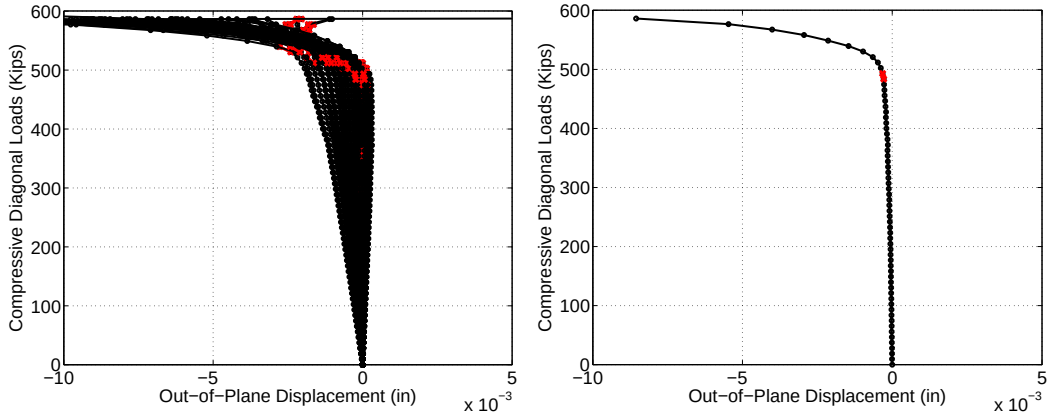

(a) Load deflection curve for each node in the buckling area (b) Load deflection curve for the average of the

Figure D.4: Comparison of the buckling load prediction using each load deflection curve and average load deflection curve

Finally, it worthy notes that the buckling load for Joint U10 estimated from two load-deflection curves are different. Buckling load estimated at the compressive edge is smaller than the buckling load estimated at the end region of the compressive diagonal. For Joint U10, the The compressive edge was found that had significant out-of-plane displacement

prior to the joint failure (Ocel and Wright [2008]) and the slenderness ratio is larger than the maximum requirement of the compact section which is $\frac{l}{t} \geq 2.06\sqrt{\frac{E}{F_y}}$ (AASHTO [2008]. The failure load estimated by Ocel and Wright [2008] is close to the predicted buckling load at the compressive edge by the FEA while the buckling load at the end region of the compressive diagonal is larger than the failure load. The buckling at the compressive edge may need more studies.

Appendix E

BLOCK SHEAR AT CONNECTED CHORD MEMBER

For the conventional block shear check at chord connection, the tensile and shear stress along the connected periphery are shown not to be determined by the chord loads solely. If the chord connection is in tension, the tensile stress at the end of gusset plates is the net force of chord and diagonal loads and the shear stress is mainly determined by the diagonal load. Therefore, it is reasonably to neglect block shear check of gusset plates at chord members. The chord splice yielding and horizontal shear yielding shall provide sufficient capacity to ensure the gusset plate safety. Assume the chord splice yielding limit and horizontal shear yielding limit are both achieved at the same time, the stress contours are shown in Figure E.1. A significant yielding is observed along the chord connection periphery and the maximum equivalent plastic strain is about 2% which may be regarded close to material fracture. The stress component X normal stress and XY shear stress show yieldinged contours at the chord splice and the horizontal section. The gray color indicates the stress over the maximum contour colot legend while dark blue indicates the stress under the minimum contour color legend.

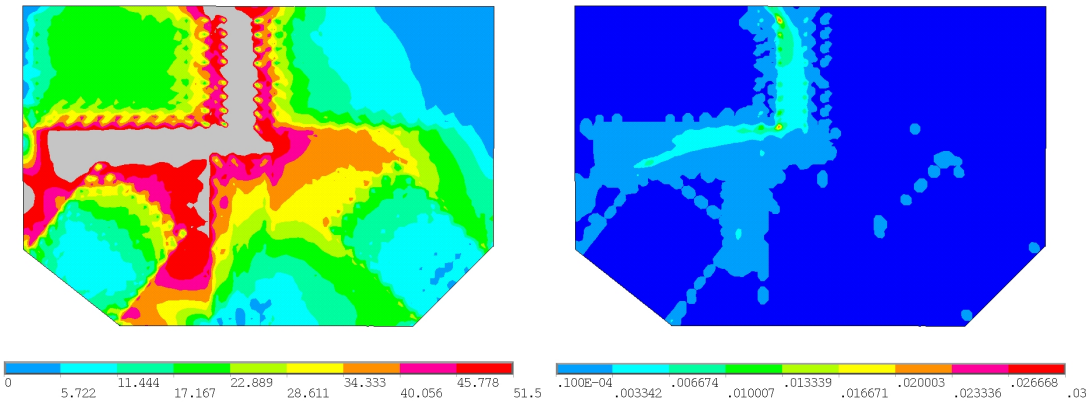

(a) Von Mises stress at limit of chord splice yielding and horizontal shear yielding

(b) Equivalent plastic strain at limit of chord splice yielding and horizontal shear yielding

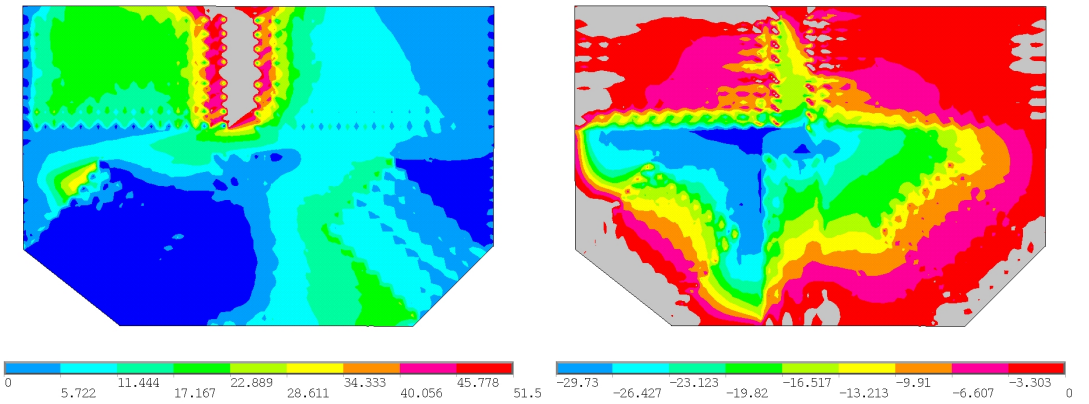

(c) X normal stress as chord splice yielding

(d) XY shear stress as horizontal shear yielding

Figure E.1: Chord splice yielding and horizontal shear yielding in lieu of block shear in chord connection

BIBLIOGRAPHY

1. AASHTO. *Standard Specification for Highway Bridge*. American Association of State Highway and Transportation Officials, 2th edition, 1935.

2. AASHTO. *Standard Specification for Highway Bridge*. American Association of State Highway and Transportation Officials, 5th edition, 1949.

3. AASHTO. *Standard Specification for Highway Bridge*. American Association of State Highway and Transportation Officials, 8th edition, 1961.

4. AASHTO. *Standard Specification for Highway Bridge*. American Association of State Highway and Transportation Officials, 12th edition, 1977.

5. AASHTO. *Guide Specification for Strength Evaluation of Existing Steel and Concrete Bridges*. American Association of State Highway and Transportation Officials, 1989.

6. AASHTO. *AASHTO LRFD Bridge Design Specifications*. American Association of State Highway and Transportation Officials, 4th edition, 2007.

7. AASHTO. *The Manual for Bridge Evaluation*. American Association of State Highway and Transportation Officials, 1st edition, 2008.

8. AASHTO. *AASHTO LRFD Bridge Design Specifications*. American Association of State Highway and Transportation Officials, 5th edition, 2010.

9. AASHTO. *The Manual for Bridge Evaluation*. American Association of State Highway and Transportation Officials, 2nd edition, 2010.

10. AASHTO. *The Manual for Bridge Evaluation 2011 Interim Revisions*. American Association of State Highway and Transportation Officials, 2nd edition, 2011.

11. AASHTO. *AASHTO LRFD Bridge Design Specifications*. American Association of State Highway and Transportation Officials, 6th edition, 2012.

12. AISC. *Steel Construction Manual*, 2002.

13. AISC. *Steel Construction Manual*, 2005.

14. AISC. *Steel Construction Manual*, 2011.

15. Inc ANSYS. *ANSYS Academic Research*, 11 edition, 2008.

16. AREMA. Tests of riveted joints. In *Proceedings of the Sixth Annual Convention of the American Railway Engineering and Maintenance of Way Association*, volume 6. Iron and Steel Structures, Report of Committee, 1905.

17. C. Batho. The effect of end connections on the distribution of stress in certain tension members. *Journal of the Franklin Inst.*, 180(2), 1915.

18. C. Batho. The partition of the load in riveted joints. *Journal of the Franklin Inst.*, 182 (5), 1916.

19. A Robert Bendigo and John L. Rumpf. Static tension tests of long bolted joints. Technical Report 271.8, Fritz Engineering Laboratory Report, 1960.

20. W. Jeffrey Berman, Bo-Shiuan Wang, W. Aaron Olson, W. Charles Roeder, and E. Dawn Lehman. Rapid assessment of gusset plate safety in steel truss bridges. *Journal of Bridge Engineering*, 16(2):221–231, 2012.

21. R. Bjorhovde and S.K. Chakrabarti. Test of full-size gusset plate connections. *Journal of Structural Engineering*, 111(3):667–684, March 1985.

22. R.L. Brockenbrough. Design guide 15:. AISC Rehabilitation and Retrofit Guide, 2002.

23. V.L. Brown. *Stability of Gusseted Connections in Steel Structures*. PhD thesis, University of Dlaware, 1988.

24. Michel Bruneau, Chia-Ming Uang, and Rafael Sabelli. *Ductile Design of Steel Structures*. McGraw-Hill, 1 edition, 2011.

25. S.K. Chakrabarti and R.M. Richard. Inelastic buckling of gusset plates. *Structural Engineering Reviewing*, 2:13–29, March 1990.

26. J.J.R. Cheng, M.C.H. Yam, and S.Z. Hu. Elastic buckling strength of gusset plate connections. *Journal of Structural Engineering*, 120(2):538–559, February 1994.

27. J.J.R. Cheng, G.Y. Grondin, and M.C.H. Yam. Design and behavior of gusset plate connections. In *Fourth International Workshop on Connections in Steel Structures, Roanoke, Virginia, USA*, pages 307–317, 2000.

28. E. Jr. Chesson and W. H. Munse. Behavior of riveted truss-type connections. *ASCE Transactions*, 123:1087–1128, 1958.

29. E. Jr. Chesson and W. H. Munse. Riveted and bolted joints: Truss-type tensile connections. *Journal of Structural Division*, 89:67–106, Feb 1963.

30. M. D'Aniello, F. Portioli, , L. Fiorino, and R. Landolfo. Experimental investigation on shear behavior of riveted connections in steel structures. *Engineering Structures*, 33: 516–531, 2011.

31. Raymond E. Davis, Glenn B. Woodruff, and Harmer E Davis. Tension tests of large riveted joints. 105(1):1193–1245, 1940.

32. W. Stanley Dlugosz. Static tension tests of long riveted joints. Master's thesis, Lehigh University, June 1962.

33. B. Dowswell. Effective length factors for gusset plate buckling. *Engineering Journal*, pages 91–101, November 2006.

34. FHWA. *Load Rating Guidance and Examples For Bolted and Riveted Gusset Plates in Truss Bridges*. U.S. Department of Transportation Federal Highway Administration, 4th edition, 2009.

35. John W. Fisher. The analysis of bolted plate splices. Technical Report 288.10, Fritz Engineering Laboratory Report, 1964.

36. John W. Fisher and L. John Rumpf. The analysis of bolted butt joints. Technical Report 228.17, Fritz Engineering Laboratory Report, 1967.

37. John W. Fisher and John H.A. Struik. *Guide to Design Criteria for Bolted and Riveted Joints*. John Wiley & Sons, Inc, 1 edition, 1974.

38. W. John Fisher, O. Paul Ramseier, and S. Lynn Beedle. Strength of a440 steel joints fastened with a325 bolts. Technical Report 288.4, Fritz Engineering Laboratory Report, 1963.

39. Robert T. Foreman and John L. Rumpf. Static tension tests of bolted joints. Technical Report 271.1, Fritz Engineering Laboratory Report, 1958.

40. Michel Goossens, Frank Mittlebach, and Alexander Samarin. *The LaTeX Companion*. Addison-Wesley, Reading, Massachusetts, 1993.

41. J.L. Gross and G. Cheok. Experimental study of gusseted connections for laterally braced steel building. *National Institute of Standards and Technology, Gaithersburg,MD*, November 1988.

42. G. Anthony Hafner. Experimental research on the behavior and strength of large-scale steel gusset plates with sway-buckling response including effects of corrosion and retrofit options. Master's thesis, Oregon State University, March 2012.

43. Roger M. Hansen and John L. Rumpf. Further static tension tests of long bolted joints. Technical Report 271.15, Fritz Engineering Laboratory Report, 1960.

44. S.G. Hardash and R. Bjorhovde. New design criteria of gusset plate in tension. *Engineering Journal*, pages 77–94, 1985.

45. B.O. Hardin. Experimental investigation of the primary stress in gusset-plates of a double plan pratt truss joint with chord splice at the joint. *Bulletin No.49, University of Kentucky Engineering Experiment Station*, September 1958.

46. C. Higgins, E. Senturk, and O.T. Turan. Comparison of block-shear and whitmore

section methods for load rating existing steel truss gusset plate connections. *Journal of Bridge Engineering*, 15(2):160–171, March/April 2010.

47. C. Higgins, O.T. Turan, and R.J. Connor. Rapid ranking procedures for gusset plate connections in existing steel truss bridges. *Journal of Bridge Engineering*, 15(5):581–596, September/October 2010.

48. N.J. Hoff, B.A. Boley, and J.M. Coan. The development of a technique for testing stiff panels in edgewise compression. In *Proceedings of the Society for Experimental Stress Analysis*, volume 5, pages 14–24, 1948.

49. R. Holt and J. Hartmann. Adequacy of the u10 & l11 gusset plate design for the minnesota bridge no. 9340, interim report. Turner-Fairbank Highway Research Center Report,Federal Highway Administration, January 2008.

50. A. Hrennikoff. Work of rivets in riveted joints. *Transactions of the American Society of Civil engineers*, 99(1):437–449, January 1934.

51. A. Hrennikoff. Soultion of problems of elasticity by framework method. *Journal of Applied Mechanics*, December 1941.

52. S.Z. Hu and J.J.R. Cheng. Comprehensive behavior of gusset plate connections. *Structural Engineering Report, University of Alberta*, 1987.

53. W.G. Jr. Irvan. Experimental study of primary stresses in gusset-plates of a double plan pratt truss. *Bulletin Vol.12 No.2, University of Kentucky Engineering Experiment Station*, 1957.

54. M. Saura Jost. Behavior of riveted connections in steel truss bridges. Master's thesis, University of Washington, March 2012.

55. Sandor Kaliszky. *Plasticity (Theory and Engineering Applications)*. Elsevier, 1 edition, 1989.

56. Thomas S. Kay. Numerical modeling and analysis of steel bridge gusset plate connections. Master's thesis, Portland State University, June 2011.

57. Geoffrey L. Kulak, John W. Fisher, and John H.A. Struik. *Guide to Design Criteria for Bolted and Riveted Joints*. John Wiley & Sons, Inc, 1 edition, 1987.

58. G.L. Kulak and G.Y. Gordin. *Block Shear Failure in Steel Members - A Review of Design Practice*, volume 38. American Institute of Steel Construction, 2001.

59. M. Liao, T. Okazaki, R. Ballarini, A.E. Schultz, and T.V. Galambos. Nonlinear finite-element analysis of critical gusset plates in the i-35w bridge in minnesota. *Journal of Structural Engineering*, 137:59–68, 2011.

60. Yavuz Mentes. *Analytical and Experimental Assessment of Steel Truss Bridge Gusset Plate Connections*. PhD thesis, Georgia Institute of Technology, December 2011.

61. William H. Munse and Hugh L. Cox. The static strength of rivets subjected to combined tension and shear. Technical Report No. 437, University of Illinois Engineering Experiment Station, 1956.

62. J.M. Ocel and W.J. Wright. Finite element modeling of i-35w bridge collapse, final report. Turner-Fairbank Highway Research Center Report,Federal Highway Administration, October 2008.

63. J.M. Ocel, R. Zobel, D. White, and R. Leon. Fhwa full-scale testing of steel truss bridge gusset plate connections. In *International Association of Bridge Maintenance and Safety*. Taylor and Francis, 2012.

64. W. Aaron Olson. Triage evaluation of gusset plates in steel truss bridges. Master's thesis, University of Washington, December 2010.

65. P. Park and W.L. Gamble. *Reinforced Concrete Slab*. John Wiley & Sons, Inc, 1 edition, 1980.

66. J. Rhodes and J.M. Harvey. Examination of plate post-buckling behavior. *Journal of Engineering Mechanics Division*, 103(EM3):461–477, 1977.

67. A. E. Richard de Jonge. *Riveted Joints - A Critical Review of the Literature Covering*

their Development, with Bibliography and Abstracts of the Most Important Articles. American Society of Mechanical Engineers, 1945.

68. C.W. Roeder, D.E. Lehman, and J.H. Yoo. Improved seismic design of steel frame connections. *Steel Structures*, 5:141–153, 2005.

69. T.H. Rust. Specification and design of steel gusset plates. *Transactions of the American Society of Civil engineers*, 105, 1940.

70. Leo Schenker, G. Charles Salmon, and Bruce G. Johnston. Structural steel connections. Technical Report No. 352, University of Michigan Ann Arbor, 1954.

71. N. Sheng, C.H. Yam, and V.P. Iu. Analytical investigation and the design of the compressive strength of steel gusset plate connections. *Journal of Constructional Steel Research*, 58:1473–1493, 2002.

72. Dassault Systemes Simulia. *Abaqus Analysis User's Manual*, 2008.

73. J. Singer, J. Arbocz, M.Potier-Ferry, and V. Tvergaard. *Lecture Notes in Physics(Buckling and Post-Buckling*. Springer Berlin Heidelberg, 1 edition, 1985.

74. H. Gordon Sterling and W. John Fisher. Tests of long a440 steel bolted butt joints. Technical Report 288.26, Fritz Engineering Laboratory Report, 1965.

75. H. Gordon Sterling and W. John Fisher. A440 steel joints connected by a490 bolts. Technical Report 288.30, Fritz Engineering Laboratory Report, 1965.

76. Arthur N. Talbot and Herbert F. Moore. Tests for nickel-steel riveted joints. Technical Report No. 49, University of Illinois Engineering Experiment Station, 1911.

77. W.A. Thornton. Bracing connection for heavy construction. *Engineering Journal*, 21 (3):139–148, 1984.

78. Stephen Timoshenko. *Theory of Elasticity*. McGraw-Hill Companies, June 1970.

79. Corporation URS. Fatigue evaluation bridge 9340 35w over mississippi river. Minnesota Department of Transportation, Jun 2003.

80. D.D. Vasarhelyi. Test of gusset plate models. *Journal of Structural Division*, 97:665–678, February 1971.

81. R.E. Whitmore. Experimental investigation of stresses in gusset plates. *Bulletin No.16, University of Tennessee Engineering Experiment Station*, pages 1–33, May 1952.

82. M. Wilbur Wilson, H. Walter Bruckner, and H. Thomas Mccrackin. Tests of riveted and welded joints in low-alloy structural steels. Technical Report 337, University of Illionis Bulletin, September 1942.

83. Wilbur M Wilson and Frank P Thomas. Fatigue tests of riveted joints. Technical Report No. 302, University of Illinois Engineering Experiment Station, 1938.

84. WSDOT. *Bridge Design Manual LRFD*. Washington State Department of Transportation, 2010.

85. M.C.H. Yam. *Compressive Behavior and Strength of Steel Gusset Plate Connections*. PhD thesis, University of Alberta, 1994.

86. M.C.H. Yam and J.J Cheng. Experimental investigation of the compressive behavior of gusset plate connections. *Structural Engineering Report, University of Alberta*, (194), 1993.

87. M.C.H. Yam and J.J. Cheng. Behavior and design of gusset plate connections in compression. *Journal of Constructional Steel Research*, 58:1143–1459, 2002.

88. K. Yamamoto, N. Akiyama, and T. Okumura. Elastic analysis of gusseted truss joints. *Journal of Structural Engineering*, 111(12):2545–2564, December 1985.

89. K. Yamamoto, N. Akiyama, and T. Okumura. Buckling strengths of gusseted truss joints. *Journal of Structural Engineering*, 114(3):575–590, March 1988.